SPIN-NEMATIC SQUEEZING IN A SPIN-1 BOSE-EINSTEIN CONDENSATE

A Thesis
Presented to
The Academic Faculty

by

Christopher David Hamley

In Partial Fulfillment
of the Requirements for the Degree
Doctor of Philosophy in the
School of Physics

Georgia Institute of Technology
May 2012

SPIN-NEMATIC SQUEEZING IN A SPIN-1 BOSE-EINSTEIN CONDENSATE

Approved by:

Professor Michael S. Chapman, Advisor
School of Physics
Georgia Institute of Technology

Professor Chandra Raman
School of Physics
Georgia Institute of Technology

Professor Paul M. Goldbart
School of Physics
Georgia Institute of Technology

Professor Robert L. Whetten
School of Chemistry
Georgia Institute of Technology

Professor Carlos A. R. Sá de Melo
School of Physics
Georgia Institute of Technology

Date Approved: 15 December 2011

To the person most directly responsible for me choosing this path, CDR David Ruff, Captain USS Louisiana (SSBN 743) Gold Crew.

He asked the question that inspired me to pursue this new career as a physicist.

ACKNOWLEDGEMENTS

Mike Chapman gets a double acknowledgement, first for the time I worked in his lab as an undergraduate and second for being my graduate advisor after I had to return from Colorado. He still put up with me even though we can argue on something we agree about.

I have a rather lengthy history with Mike Chapman's lab. I first worked here as an undergraduate beginning fall 2001. I convinced him to hire me as an undergraduate researcher by having had electronics technician as a prior job title. I started out building circuit boards for laser current controllers and temperature controllers. I very briefly overlapped Murray Barrett, the graduate student who first developed the all-optical BEC. I started almost the same time as the next graduate student on that experiment, Ming-Shien Chang. Ming-Shien mentored me through a lot of optics alignment and was good guy to be around. I also worked with Jake Sauer, who was amazed anyone could put together a piece of electronics by hand and it work the first time. Jake was an enthusiastic friendly guy who loved what he did. The following summer we picked up Kevin Fortier and Sally Maddocks. I had a lot of fun that summer with those two doing a large scale plumbing project for the lab. Afterwards, Sally had to move on and for quite a while the lab was Jake, Ming-Shien, Kevin, and myself.

Next I started graduate school at the University of Colorado. There I had some wonderful instructors for my introductory courses of which two stand out. Tom DeGrand was the graduate quantum instructor who drilled into the class the phrase, "The same equations have the same solutions." For electro-dynamics (from Jackson) I had Chris Greene, who did a great job of elaborating on Jackson's proofs. I also enjoyed a math methods course he taught. I would also like to acknowledge Peter Bender, who I did LISA simulations for to earn my keep while looking for a permanent advisor. Part of that keep was assisting Jan

Hall, who made me learn a lot of control theory trying to improve the performance of simple temperature controllers. I worked on this project in the subbasement in JILA, a space shared with Jim Faller. He was always interesting to talk to. When I worked as a TA, the Lab Coordinator Jerry Leigh made the time instructing undergrads who thought physics lab was a waste of their time much more enjoyable. Finally I would like to acknowledge my classmates who along with their spouses were friends at Colorado; Jer Brown, Rob and Carolyn Hill, Jennifer McGee/Taylor and Bart Taylor. I greatly appreciate their commiseration and companionship.

Because of personnel decisions and sickness, graduate positions in cold atom physics became scarce around when I arrived. After two years this left me with the choice to do something entirely different or to go elsewhere. So I chose to leave Colorado and come back to Georgia Tech, where Mike Chapman took me back into the lab. Here back on the BEC experiment I worked with our post-docs Paul Griffin at first, followed by Peyman Ahmadi. Their dedication and work made thing go more smoothly. Gazal Aein-Behin worked as a research scientist on the BEC experiment and assisted in taking a lot of the photoassociation data. Of course there was my fellow graduate student on the BEC experiment, Eva Bookjans, who kept the BEC experiment alive through some challenging times and made a cottage industry out of realigning the trapping laser. I got to interact with people on the other projects in the lab as well such as Soo Kim, a bright physicist with a flair for fashion and a crazy hard worker. Michael Gibbons who I could count on for going out to lunch where we discussed our respective experiments. I have also has the pleasure of working with the graduate students Layne Churchill, Michael DePalatis, Chung-Yu Shih, and Adam Steel. Following me on the BEC experiment are Corey Gervin and Thai Hoang. Finally our two recent undergrads, Ben Land and Brian Rose. Ben's programing skills have really helped my simulations.

I would also like to acknowledge some of the faculty here at Georgia Tech. Jim Gole has been regaling me with his hallway humor ever since I had an undergraduate course with

him. I would very much like to thank T. A. Brian Kennedy, Carlos A. R. Sá de Melo, John Wood, and Li You for sharing their theoretical thoughts and insight. They have greatly aided me in my understanding of the theoretical aspects of this thesis.

TABLE OF CONTENTS

APPENDICES

LIST OF TABLES

LIST OF FIGURES

SUMMARY

The primary study of this thesis is spin-nematic squeezing in a spin-1 condensate. The measurement of spin-nematic squeezing builds on the success of previous experiments of spin-mixing together with advances in low noise atom counting. The major contributions of this thesis are linking theoretical models to experimental results and the development of the intuition and tools to address the squeezed subspaces. Understanding how spin-nematic squeezing is generated and how to measure it has required a review of several theoretical models of spin-mixing as well as extending these existing models. This extension reveals that the squeezing is between quadratures of a spin moment and a nematic (quadrapole) moment in abstract subspaces of the SU(3) symmetry group of the spin-1 system. The identification of the subspaces within the SU(3) symmetry allowed the development of techniques using RF and microwave oscillating magnetic fields to manipulate the phase space in order to measure the spin-nematic squeezing. Spin-mixing from a classically meta-stable state, the phase space manipulation, and low noise atom counting form the core of the experiment to measure spin-nematic squeezing. Spin-nematic squeezing is also compared to its quantum optics analogue, two-mode squeezing generated by four-wave mixing.

The other experimental study in this thesis is performing spin-dependent photo-association spectroscopy. Spin-mixing is known to depend on the difference of the strengths of the scattering channels of the atoms. Optical Feshbach resonances have been shown to be able to alter these scattering lengths but with prohibitive losses of atoms near the resonance. The possibility of using multiple nearby resonances from different scattering channels has been proposed to overcome this limitation. However there was no spectroscopy in the literature which analyzes for the different scattering channels of atoms for the same initial states.

Through analysis of the initial atomic states, this thesis studies how the spin state of the atoms affects what photo-association resonances are available to the colliding atoms based on their scattering channel and how this affects the optical Feshbach resonances. From this analysis a prediction is made for the extent of alteration of spin-mixing achievable as well as the impact on the atom loss rate.

CHAPTER I

INTRODUCTION

The experimental realization of a Bose-Einstein condensate (BEC) [1–3] and Fermi degeneracy [4–6] in dilute atomic vapors marked the beginning of a new era in atomic and condensed matter physics. Although the creation of a BEC is a uniquely quantum phenomena, the gross properties of the condensate can be described in the mean-field by a classical matter wave field having a coherent macroscopic phase [7, 8] similar to the coherent light field of a laser. Many of the first experiments with degenerate gases focused on phenomena associated with coherent matter waves. In these early experiments, coherence properties were observed in the interference of expanding condensates [7], atom lasers [9, 10], and the momentum distribution of a Mott insulator made by putting the BEC in a lattice [11]. The earliest BECs were confined in a magnetic trap, freezing their internal degrees of freedom. However shortly after these early experiments, a ^{23}Na BEC with spin-1 was transferred to an optical trap which freed its spin degrees of freedom from the trapping potential. Since the states were of the same hyperfine manifold, interconversion of spin states was possible. This interconversion allows the system to have dynamics in both amplitude and phase of its hyperfine components making this the first spinor BEC [12]. Later, the first ^{87}Rb spinor BECs were directly formed in optical traps [13].

Spinor condensates offer a form of multi-component coherent matter with internal spin degrees of freedom in addition to the external ones. In ultra-cold gases, multi-component systems can be realized simply by trapping multiple atomic species in the same trap. However spinor condensates are composed of multiple spin components of the same isotope. These spinor condensates are unique because while they are generally capable of exploring

the full range of phenomena accessible to mixtures of distinguishable condensates including phase separation, modulation instability, and domain formation, spinor condensates also offer qualitatively new phenomena deriving from their ability to interconvert the internal states of the atoms [14]. These phenomena are explained by a rich theoretical literature primarily using mean-field theory.

Currently there is growing emphasis on explorations beyond the mean-field limit and the creation and detection of non-classical, quantum correlated states of the atomic fields. Besides giving insight into fundamental principles of many-particle quantum mechanics, correlated atomic states are predicted to have a wide range of applications in quantum metrology, foundational studies of quantum mechanics, quantum information, and quantum simulations. In quantum metrology for example, certain types of quantum correlated states known as squeezed states are capable of providing enhanced precision beyond the standard quantum limit (SQL) that fundamentally limits the precision of measurements for ensembles of independent (uncorrelated) atoms.

The investigations in this thesis build upon previous work in this lab on multi-component, spinor condensates confined in optical traps, in which the first ferromagnetic condensate was realized [13], the first quantitative validation of the mean-field theory of spin-1 condensates was provided [15], coherent spin oscillations and coherent control of spinor dynamics were demonstrated [16], and sub-Poissonian fluctuations of the magnetization from spin-mixing were observed [17]. The main goal of this thesis is to further explore spin-1 condensates, their evolution from an initial classically meta-stable state, and to measure the squeezing this evolution is predicted to generate. Along the way new insight into the theory and symmetry describing the condensate is developed. Another goal explored is to use external light fields to modulate the spinor interaction.

1.1 Spinor BEC

There is an extensive literature devoted to spinor BEC, more than 300 papers, covering too many topics to summarize here. However, since this is primarily an experimental thesis a brief summary of experimental efforts is in order. Investigations of spinor condensates began with the pioneering MIT experiments with sodium condensates confined in optical traps [12]. In their studies, they observed spin-mixing of initially excited spin states [18] and studied the formation and dynamical evolution of spin domains in large extended condensates [19–21]. From the component miscibility properties observed, it was determined that $f = 1$ spinor condensates of ^{23}Na exhibit anti-ferromagnetic ordering of the spins in low magnetic fields and thus sodium has a positive sign for the spinor dynamical energy [18].

The first condensates with ferromagnetic ordering were realized by our group using ^{87}Rb condensates created directly in optical traps [13]. The focus of these initial investigations was on verifying the sign of the spinor dynamical energy for the $f = 1$ ^{87}Rb spinor, which had been predicted to be negative. Adapting methods used in the MIT experiments, the condensate atoms initially were prepared in the $m_f = 0$ state in a high magnetic field, which was then suddenly lowered (a 'quantum quench') [22] to study the subsequent evolution [15]. The equilibrium populations measured were in good agreement with the phase diagram of the ground states [18] and in particular exhibited the predicted quantum phase transition at a critical point of magnetic field versus spinor dynamical energy [15,22]. Similar results were reported by the Hamburg group [23], but for $f = 2$.

In subsequent work [16], our group demonstrated for the first time the coherent evolution and control of the spinor system, which provided the first convincing validation of the mean-field theoretical treatment of the system dynamics. Both low-field periodic phase oscillations as well as high-field running phase oscillations were demonstrated. Modification of spinor dynamics by short magnetic field pulses was also demonstrated. Similar work was performed with $f = 2$ ^{87}Rb by the Hamburg group [24, 25] and with $f = 1$ ^{23}Na by

the NIST group [26]. Spinor dynamics were also demonstrated for atom pairs in doubly occupied Mott insulator lattice sites by the Mainz group [27].

Spatial excitations and structures unique to spinor condensates have also been studied. Using large ^{87}Rb condensates in a quasi 2-D extended system, the Berkeley group observed spontaneous symmetry breaking across the phase transition in measurements of the transverse magnetization [28], and later showed that dipolar effects could be observed in the formation of helical spin textures [29]. Other fascinating studies of extended spinor condensates include the demonstration of spontaneous breaking of spatial and spin symmetries by the Hannover group [30], the demonstration of skyrmions by the Rochester group [31], and studies of a quantum phase transition in Na [32].

Most spinor BEC experimental work has focused on the mean-field limit, but the first explorations beyond the mean-field have also begun. Super-Poissonian noise ascribed to the effects of vacuum fluctuations was observed in several groups [33–35]. Until recently though, these experiments have not had the low noise atom detection capabilities necessary to detect sub-Poissonian quantum correlations. In this past year, both our group [17, 36] and the Hannover group [37] have developed these techniques and observed sub-Poissonian fluctuations (a.k.a. *relative number squeezing*).

1.1.1 Spinor Theory

Underlying the interesting dynamics of spinor BECs are the collisional interactions of the atoms. In a spinor BEC [12–14,38], the interplay between different atomic spin orientations results in a small spin dependence of the collisional interaction energy [39, 40]. The spin dependence is small relative to the total interaction energy (*e.g.* $\sim 0.5\%$ in ^{87}Rb) and arises from the small difference in the s-wave scattering lengths of the allowed angular momentum channels (Total spin $F = 0, 2$). This difference manifests itself as anti- or ferromagnetic properties for a spin-1 condensate, depending on the algebraic sign of the difference. The equilibrium state of the system is determined by the relative energies of

the collective spinor energy and the per particle energy due to a finite magnetic field. For high magnetic fields the ground state is the $m_f = 0$ polar state having nematic ordering of the spins with the director aligned with the magnetic field. Lowering the magnetic field, the system undergoes a quantum phase transition where in the thermodynamic limit the ground state order parameter abruptly changes at a critical magnetic field [22] and the sign of the spinor interaction energy determines the preferred order parameter, ferromagnetic or anti-ferromagnetic for negative or positive spinor energy. For a ferromagnet, this critical field is given by $q = 2|c|$ where q is the quadratic Zeeman energy per atom and c is the mean-field spinor energy parameter to be defined later. For an anti-ferromagnet the critical field is $q = 0$.

One of the key consequences of the spin-dependent collisional interactions is that the spin components can coherently exchange population in a process known as spin-mixing. For example, two atoms with spin components $m_f = -1$ and $+1$ can collide and become two atoms with spin component $m_f = 0$ and vice-versa. This process is closely analogous to optical four-wave mixing, which is a third-order non-linear process involving four optical fields. Spin-mixing is central to much of the experimental and theoretical investigations of spin-1 condensates (and larger spin systems) and underlies most of the proposals for generating squeezing and entanglement in spinor condensates. Note that spin-mixing is a feature unique to large spin systems ($S \geq 1$) and cannot occur in real or pseudo spin-1/2 systems.

The dynamics of spinor condensates have been explored theoretically both in the mean-field limit [41–43] and with fully quantum approaches [44–46]. Both approaches have been successful in explaining dynamics in a variety of situations. The mean-field approach has been particularly useful for calculating spatial excitations of the spinor order parameter. For dynamics of the internal modes, the mean field approach works well for classical states which evolve periodically [42, 45, 47]. Mean-field calculations also exhibit non-evolving meta-stable states. However, these states do evolve using quantum theoretical approaches.

Our most common spin-mixing experiment, evolution of a ferromagnetic condensate starting in $m_f = 0$, is an example of this. In this classically meta-stable state, dynamics are driven purely by quantum fluctuations and allow purely quantum effects to surface. These non-equilibrium quantum dynamics can generate non-classical states such as squeezing. The fluctuations can be recovered semi-classically using a quasi-probability distribution in the mean-field dynamical equations which will be shown in this thesis.

Recently there has been efforts to go beyond the mean-field theory in order to account for quantum effects [48–50]. Among these are the efforts for more complete quantum models to account for discrepancies with experimental results by investigating the effects of particle number and magnetic fields [50, 51]. In order to understand the measurements of this thesis, it has been necessary to learn from both mean-field and quantum theoretical approaches as well as their extensions. Furthermore it has been necessary to find agreement between the approaches by finding common ground through the underlying SU(3) group symmetry of the spin-1 system. This work is a major topic of this thesis.

1.1.2 Optical Feshbach Resonances

The ferromagnetic or anti-ferromagnetic properties of a spin-1 condensate depend on the sign of the spinor dynamical energy which in turns depends on the difference of the two s-wave scattering lengths. The difference of scattering lengths has largely been treated as fixed, however individual scattering lengths are known to be tunable by both magnetic and optical Feshbach resonances [52–54]. The ability to manipulate the magnetic properties of spinor condensates could open up new avenues of research. One possible technique, which is studied in this thesis, is to use nearby optical Feshbach resonances of different scattering channels [54–57]. Experimental identification of the necessary spectral structure and the assessment of a known photo-association level for use towards this goal is one result in this thesis.

1.1.3 Nematic Ordering

Spin-1 condensates can exhibit complex quantum magnetic order beyond that of real or pseudo spin-1/2 systems. Exotic types of magnetic order and phases resulting from collective behavior of quantum spins are an important focus of many-body physics. Nematic or quadrupolar ordering of spins is one such example [58], which breaks rotational symmetry, but has no magnetic moment. This ordering is analogous to the well-known ordering of molecules in nematic phases of liquid crystals [59]. Spin-nematic phases have been posited for a variety of condensed matter systems including frustrated quantum magnets [60–62], and heavy-fermion [63] and iron-based superconductors [64], although they are challenging to detect directly [65]. Spin-1 atomic Bose-Einstein condensates provide a natural system to investigate spin-nematic quantum phases that feature well-understood underlying microscopic models, controllable interaction parameters, and flexible defect-free geometries. Importantly, the ability to manipulate the atomic spins with electro-magnetic fields provides tools to initialize equilibrium or excited states of the system and to directly measure both the spin vector and the nematic tensor.

1.2 Squeezing

The study of quantum correlated states including squeezed and entangled states is an important frontier. In addition to being intrinsically fascinating, such states have important applications in precision measurements, quantum information and fundamental tests of quantum mechanics. Much of the early research in this area focused on quantum optical systems [66], motivated originally by the suggestion that squeezed states could be used in gravity wave detectors to surpass the standard quantum limit [67, 68]. There has also been significant progress in realizing squeezing and other quantum correlated (non-classical) states in atomic systems, using either non-linear atom-light interactions [69], or more recently, collisional interactions in ultra-cold atomic gases [70, 71]. Sub-Poissonian number fluctuations have been directly observed in a BEC [72–75], in a Mott insulator [11, 76–78], and in

a degenerate Fermi gas [77,78]. Measurements of spatial density correlations of expanding degenerate gases have enabled demonstration of the the Hanbury-Brown-Twiss effect for bosons [79, 80], anti-bunching for fermions [81, 82], correlations in a Mott-insulator [78], and atom pair correlations from molecular dissociation [77] and from colliding BECs [83].

Spin squeezing has been a topic of interest for atom optics for a number of years now. It is an analogue of single mode quadrature squeezing of light [84]. The typical realization is in a pseudo-spin-$\frac{1}{2}$ or two-level system either through two internal states or two interacting lattice sites [73]. Methods of generation have included transferring the squeezing from squeezed light [85], repeated quantum non-demolition (QND) measurements [86, 87], and interactions with an optical cavity [88, 89]. Spin squeezing in a BEC has also been observed in pseudo spin-1/2 systems where the nonlinear interaction was two-body collisions controlled either by a Feshbach resonance [70] or by controlling the overlap of the two spin components [71]. Spin squeezing has been demonstrated to enhance the sensitivity of atomic magnetometers [90, 91] and the accuracy of atomic clocks [92, 93].

1.2.1 Quadrature and Spin Squeezing

The standard quantum limit (SQL) of measurement uncertainty is a consequence of Heisenberg's uncertainty principle and corresponds to measurement uncertainty shared equally between two complementary properties. It is possible to do better using 'squeezed states' that reduce the measurement uncertainty of one property at the expense of another [67]. The uncertainty principle is defined in terms of the commutator of an operator pair. For general operators the uncertainty relation is given by $\langle(\Delta\hat{A})^2\rangle\langle(\Delta\hat{B})^2\rangle \geq \frac{1}{4}|\langle[\hat{A},\hat{B}]\rangle|^2$ with the expression $\frac{1}{2}|\langle[\hat{A},\hat{B}]\rangle|$ as the SQL for the variance of measured quantities of each of the observables. At a fundamental level, only operator pairs with non-zero expectation values for their commutation relations can exhibit squeezing of their uncertainty relationship.

For spin-1/2 particles, the complementary properties are the different components of the total spin vector $\langle \boldsymbol{S} \rangle$, uniquely specified on an SU(2) Bloch sphere. Building from the

foundations of optical squeezing, early theoretical work by Kitagawa and Ueda [94] and Wineland *et al.* [95] showed that certain classes of correlated spin states defined in terms of collective spin operators could have fluctuations of a spin component below the SQL. For a collection of N 2-level systems, the collective spin operators $\boldsymbol{S} = \sum_i \boldsymbol{s}_i$ where $\boldsymbol{s}_i$ is the spin of the i^{th} particle satisfy the usual angular momentum commutation rules, $\left[S_i, S_j\right] = i\varepsilon_{ijk}S_k$, and obey the uncertainty relationship, $\langle(\Delta S_i)^2\rangle\langle(\Delta S_j)^2\rangle \geq \frac{1}{4}|\langle S_k\rangle|^2$. The eigenvectors of the collective spin component in the (θ, ϕ) direction, $S_{\theta,\phi}$, are coherent spin states (CSS) or Bloch states and are direct product states of the individual spins. A state of spin S is squeezed if the variance of a spin component normal to the mean spin vector is less than the SQL:

$$\xi^2 = \frac{2\langle(\Delta S_\perp)^2\rangle}{\left|\left\langle S_{\theta,\phi}\right\rangle\right|} < 1 \tag{1.1}$$

where $S_\perp$ is a spin component orthogonal to the mean spin direction (θ, ϕ). For a CSS, the constituent spins are uncorrelated, and $\xi = 1$.

1.2.2 Sub-Poissonian Number Fluctuations

Optical four-wave mixing (FWM) was employed in the first demonstration of squeezed states of light in the pioneering experiments by Slusher *et al.* 25 years ago [96]. In spontaneous FWM, a strong pump field interacting with medium with a $\chi^{(3)}$ non-linearity generates two correlated optical beams known as the signal and idler modes that are exactly correlated in photon number, anti-correlated in phase [97]. This number correlation results in sub-Poissonian number statistics of the signal and idler photons. Similarly, in optical parametric amplification (OPA), the signal and idler photons are always created in pairs, enforced by energy conservation, leading to strong number correlations between the two. This was first studied by Mollow and Glauber [98]. These correlations are now commonly referred to as relative photon number or intensity squeezing. The observation of relative number squeezing is completely independent of the relative phases between the photons.

In ultra-cold atomic gases, the binary *s*-wave collisions between atoms naturally provide strong third-order non-linear interactions capable of producing analogous four-wave mixing of atomic matter waves. Indeed, both stimulated and spontaneous atomic four-wave mixing have been observed with colliding condensates [83, 99–102], and in the spin dynamics of spinor condensates [15, 16, 18, 23, 28, 103]. There have been many measurements of relative number squeezing [11,17,72–77,104] and other non-classical correlations in ultra-cold atoms [77–82].

While sub-Poissonian fluctuations are often a necessary consequence of quadrature squeezing, they are not sufficient to demonstrate it. Although there have been many measurements of sub-Poissonian number fluctuations, only a few experiments [37, 70, 71], including the results in this thesis, have demonstrated quadrature squeezing. Metrologists draw a strong distinction between the two. While quadrature squeezing can be used for quantum enhanced measurements in interferometry (e.g. for applications for gravity-wave detection, atomic frequency measurement and magnetometry), relative number squeezing cannot. Nonetheless, the measurement of relative number squeezing in our experiment [17] was an important demonstration since it shares several of the tools necessary to measure quadrature squeezing and paves the way for its demonstration.

1.2.3 Squeezing in a Spin-1 System

While criteria for squeezing and entanglement have by now been well established for spin-$\frac{1}{2}$ particles within an SU(2) framework, there has been much less work for higher spin particles with correspondingly higher symmetries and degrees of freedom. The intuition developed for SU(2) systems does not immediately illuminate squeezing in these systems with the exception of squeezing in the spin subspace. But not all squeezing is necessarily spin-squeezing. For spin-1 particles, the underlying SU(3) symmetry requires the rank-2 nematic tensor $\langle N_{ij} \rangle$ in addition to the vector spin to fully characterize the state, which leads naturally to the possibility of observing squeezing in these properties. Squeezing in

spin-1 systems has been studied from the perspective of multi-mode squeezing [105], in terms of the Gell-Mann (quark) framework of the SU(3) algebra [106], and in terms of dipole-quadrupole measurables [107]. Although in each study appropriate phase spaces for squeezing were identified, a comprehensive picture remains elusive. It is necessary to develop new intuitions for squeezing in higher spin particles. Further steps of developing these intuitions using the SU(3) symmetry group as a guide is a major topic of this thesis.

1.3 Thesis Contributions and Organization

This thesis describes two sets of experimental results along with theory that is critical to understand both. The first set of experimental results described is the measurement of spin-nematic squeezing for a spin-1 ferromagnetic ^{87}Rb condensate. This work draws heavily on the work of previous doctoral students. The original all-optical BEC experiment and the extremely flexible control system employed were developed for the thesis work of Dr. Murray Barrett [108]. This system was used for the explorations of coherent spin-mixing done by Dr. Ming-Shien Chang [109]. In that work the underlying spinor theory was developed along with the basis spin-mixing measurement tools and the microwave system for state manipulation. The coherent spin-mixing generated the relative number squeezing measured by Dr. Eva Bookjans [110]. That thesis contributes the low-noise imaging necessary to detect these quantum correlations and our first use of RF rotations to calibrate the atom counting. This thesis contributes a deeper theoretical understanding of the spin-mixing process and how it generates the squeezing. It also contributes a measurement protocol which uses the microwaves and RF manipulations combined in a new way to bring the state to the measurement basis. This was enabled by the deeper understanding provided from the SU(3) analysis of the phase space including a new visualization of the space using multiple Bloch spheres to represent different SU(2) subspaces.

The second set of experimental results describes an assessment of using optical Feshbach resonances to change the value and sign of the spinor dynamical energy. This builds on

the extensive photo-association literature. This thesis contributes a spinor analysis which allows more information about the molecular states to be extracted and shows for the first time photo-association spectra which depend solely on the scattering channel of the atoms involved.

The order of these two experiments are chronologically reversed, but the first set of experiments described have a much more significant result. As such the theory sections of the thesis focus more on this set of experiments, but the basic spinor theory is also applicable to the second, earlier experiment. The thesis is organized as follows. Chapter 2 gives a brief description of the experimental apparatus. This has been covered extensively before and so this thesis only contains an overview of the all-optical BEC technique. The tools used to manipulate and observe the BEC will be expounded on in more detail. In Chapter 3, spinor BEC theory and spin-mixing dynamics are discussed. Here quantum and mean-field theoretical approaches are developed following examples from several of the seminal papers. Throughout the results of the two major approaches are compared. In the final sections of this chapter a reconciliation between the quantum and mean-field approaches is found by using a semi-classical approach composed of the mean-field dynamic equations acting on a quasi-probability distribution of classical field variables. These dynamical equations are used for simulations of dynamics. In Chapter 4, the theory of squeezing is studied through a discussion of the squeezing of a single optical mode, spin squeezing, and spin-nematic squeezing. These ideas are applied to the spinor BEC along with a comparison to the two-mode squeezing of quantum optics. Finally the simulations of Chapter 3 are used in order to simulate and analyze the squeezing. In Chapter 5, the theoretical predictions are compared to the measured results. Using the understanding of the spin-1 phase space from Chapters 3 and 4, a measurement protocol is developed to access the squeezing quadratures. Several details of the measurement protocol and calibration for data analysis are discussed. Also the squeezed portion of the phase space is reconstructed. Chapter 6 describes measurements of spin-dependent photo-association spectroscopy. Here there is a brief overview of

the relevant molecular theory, but from a spinor viewpoint. This approach allowed for the spinor analysis of the spectra and to make predictions of the possibility of changing spinor properties using optical Feshbach resonances. Finally Chapter 7 contains some concluding remarks and possible future directions.

The information necessary for the explorations described in this thesis more resembles a web rather than a linear narrative in that the actual path of the exploration jumps from one major topic to another several times. Because of this, the topic of the underlying SU(3) symmetry of the spin-1 system has been broken up into a few smaller discussions spread throughout Chapters 3-5 in order to give the information more context with the spinor theory, squeezing theory, and measurement protocol.

CHAPTER II

EXPERIMENTAL APPARATUS

The all-optical BEC apparatus used in our lab has been well described in previous theses and papers [13, 15, 16, 108–110]. An overview of the major features is presented here along with a description of new features that are relevant to the experiments in this thesis.

Figure 2.1 gives a top view of the basic schematic of the experimental apparatus. The gravity direction is into the page. The rubidium atoms are trapped inside of an ultra-high vacuum (UHV) chamber designed for a large amount of optical access. The optics to direct and focus the dipole force trapping lasers, a CO_2 laser and an 852 nm wavelength laser (out of the schematic plane), surround the chamber. Near resonant laser light for the magneto-optical trap (MOT) is sent through different ports intersecting the dipole trapping lasers. The MOT beam axis which goes into and out of the page is not shown. There are three lenses inside the chamber. Two are for focusing the CO_2 trapping laser, and one is for imaging. The chamber has three axes of magnetic bias coils wrapped directly on it. These are used for trimming out the Earth's magnetic field and applying the desired bias fields. There are also three sets of gradient coils. One set is for the MOT, but is not shown since they are above and below the chamber. The gradient coil shown in the figure is for applying gradients along the main trapping beam axis for Stern-Gerlach separation of the m_f states. The third set of gradient coils is on top of the bias coils along the CO_2 laser axis and is used to zero a gradient along the CO_2 laser axis. A microwave horn points into the chamber at an angle from above and the RF coil sits on the top window (not shown).

2.1 Vacuum System

The experiments are performed inside of an ultra-high vacuum (UHV) chamber of an octagonal design from Kimball physics. The chamber has two large glass windows on 6”

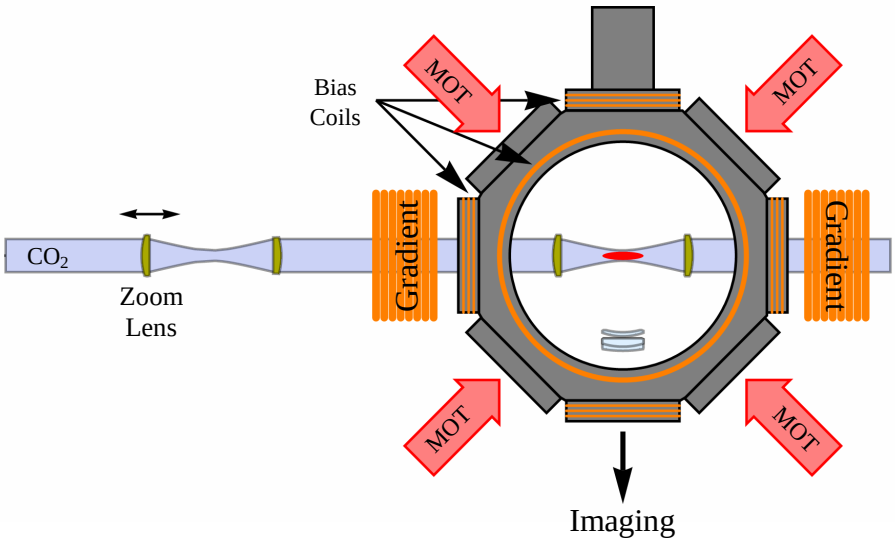

Figure 2.1: Diagram of the experimental setup.

flanges and five smaller glass windows on 2.75" ports. These glass windows are all broad-band anti-reflection coated for the near infra-red wavelengths. There are two zinc selenide (ZnSe) windows to pass the 10.6 μm of the main trapping laser mounted on two more 2.75" ports. On the final 2.75" port there is a connection to the vacuum pumps which has another glass window on the far side of the apparatus. Mounted in the chamber are two ZnSe lenses which focus the trapping laser and a high-aperture laser objective (HALO) lens for imaging (Figure 2.1). The chamber is maintained at UHV pressures using an ion pump and a titanium sublimation pump.

The source of rubidium comes from getters mounted on an electrical feed-through. The electrical feed-through is used to run current through the getter which heats them causing the release rubidium into the chamber. Also the rubidium already in the chamber is recycled by using light intensity assisted de-adsorption (LIAD) [111] which is accomplished by shining bright blue ($\sim$ 455 nm wavelength) LEDs onto the windows of the chamber. These are very efficient at de-adsorbing the rubidium from the glass windows and provides a strong controllable source to load the magneto-optical trap (MOT). While this de-adsorption of the rubidium affects the vacuum pressure during loading, upon extinguishing

the LEDs the excess rubidium rapidly re-adsorbs and brings the pressure back down.

2.2 ^{87}Rb Energy Level Structure

The relevant energy levels of ^{87}Rb for laser cooling and imaging are shown in Figure 2.2. The electronic structure of rubidium, [Kr]$5s^1$, has a single valence electron. The remaining electrons are in closed shells and therefore contribute nothing to the total angular momentum of the atom. So rubidium has a hydrogen-like electronic structure. The fine structure from spin-orbit coupling splits the excited $5p$ state into two levels with the total electronic angular momentum, $\boldsymbol{j} = \boldsymbol{l} + \boldsymbol{s}$, having values of $\frac{1}{2}$ and $\frac{3}{2}$ where $\boldsymbol{l}$ is the electronic orbital angular momentum and $\boldsymbol{s}$ is the electronic spin angular momentum. In the Russell-Saunders notation these are designated $5^2P_{1/2}$ and $5^2P_{3/2}$. The transitions to these states are known as the D lines (for doublet) since they are clearly split even in simple spectrographs. The transition to the $5^2P_{3/2}$ is known as the D_2 line, and its wavelength is 780.241 nm.

Both the $5^2S_{1/2}$ and $5^2P_{3/2}$ states have hyperfine structure which couples the nuclear spin, $\boldsymbol{i}$, with the total electronic angular momentum causing the states to split further into states of total atomic angular momentum, $\boldsymbol{f} = \boldsymbol{i} + \boldsymbol{j}$. The nuclear spin of ^{87}Rb is $\frac{3}{2}$ which gives the $5^2S_{1/2}$ electronic ground state two hyperfine states with a total atomic spin of $f = 1$ and $f = 2$. Details of this splitting are in Appendix A. The hyperfine splitting of the $5^2P_{3/2}$ state gives $f' = 0, 1, 2, 3$ [112, 113].[1] Dipole-allowed transitions between the ground and excited state hyperfine manifolds are used for laser cooling. Most important is the σ^+ polarization transition connecting the $|f = 2, m_f = 2\rangle$ state to the $|f' = 3, m'_f = 3\rangle$. This is the strongest transition of the manifold and more importantly atoms in the $|f' = 3, m'_f = 3\rangle$ can only decay to the $|f = 2, m_f = 2\rangle$ state. This allows continuous cycling on this transition which is thus called the cycling transition. Through optical pumping the atomic states tend to move towards the cycling transition in m_f states. The cycling on this transition is not perfect since there is some probability of off-resonant excitation to the

[1] Excited state f numbers are typically denoted with primes.

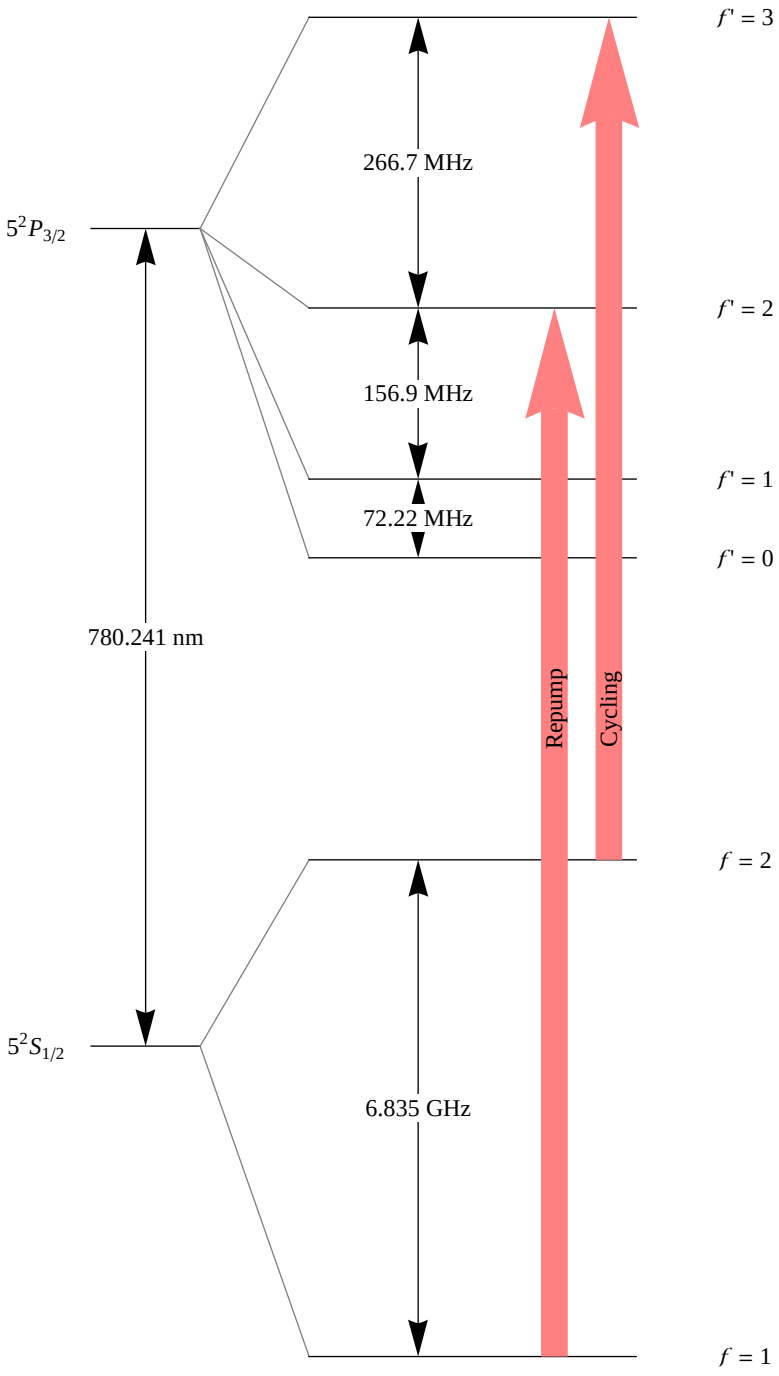

Figure 2.2: D_2 line for ^{87}Rb.

$f' = 2$ state which has a 50% probability of decaying to the $f = 1$ ground state. Once the atom decays to this state the off-resonant transition probability for the frequency of the cycling transtion to excite the atom back to the excited state manifold is negligible. Because of this off-resonant excitation, light is needed on the $f = 1$ to $f' = 2$ transition to repump the lost atoms back into the optical pumping scheme leading to the cycling transition. The transition which was off-resonantly excited by the cycling transition light is sometimes called the depumping transtion since it removes atoms from the cycling transition. The cycling transition and the repump transtion are the two most important laser frequencies needed for the MOT and for imaging.

Saturated-absorption spectroscopy is used to stabilize the lasers to the frequencies of the atomic transitions [114]. This non-linear spectroscopy technique uses a strong pump beam counter-propagating with a weak probe beam to overcome the Doppler broadening in a room temperature vapor cell used as the atomic reference. This technique generates a narrow peak for each transition frequency on top of the broad Doppler absorption feature.[2] Another feature of saturated-absorption spectroscopy is that halfway between each pair of transitions is a cross-over peak. These cross-over peaks are usually larger in amplitude than the peaks of the actual transitions and provide excellent locking points. The laser light used in the spectroscopy is also frequency modulated (FM) in order to generate an error signal used to lock the laser directly on the peaks of the spectroscopy [114].

2.3 Magneto-Optical Trap

The MOT is formed using a set of anti-Helmholtz coils and lasers near the rubidium D_2 line cycling transition. These lasers are in a $\sigma^+ - \sigma^-$ configuration on three orthogonal axes using retro-reflected beams [112]. These typically have $30 - 35$ mW per beam, collimated with an ~ 15 mm waist which is clipped into a top-hat profile with a diameter of ~ 25 mm.

[2]The narrowness of the saturated-absorption peak is limited by the transition linewidth of ~ 6 MHz but is typically a few times larger. This is still much narrower than the Doppler profile which is ~ 1 GHz for rubidium at room temperature.

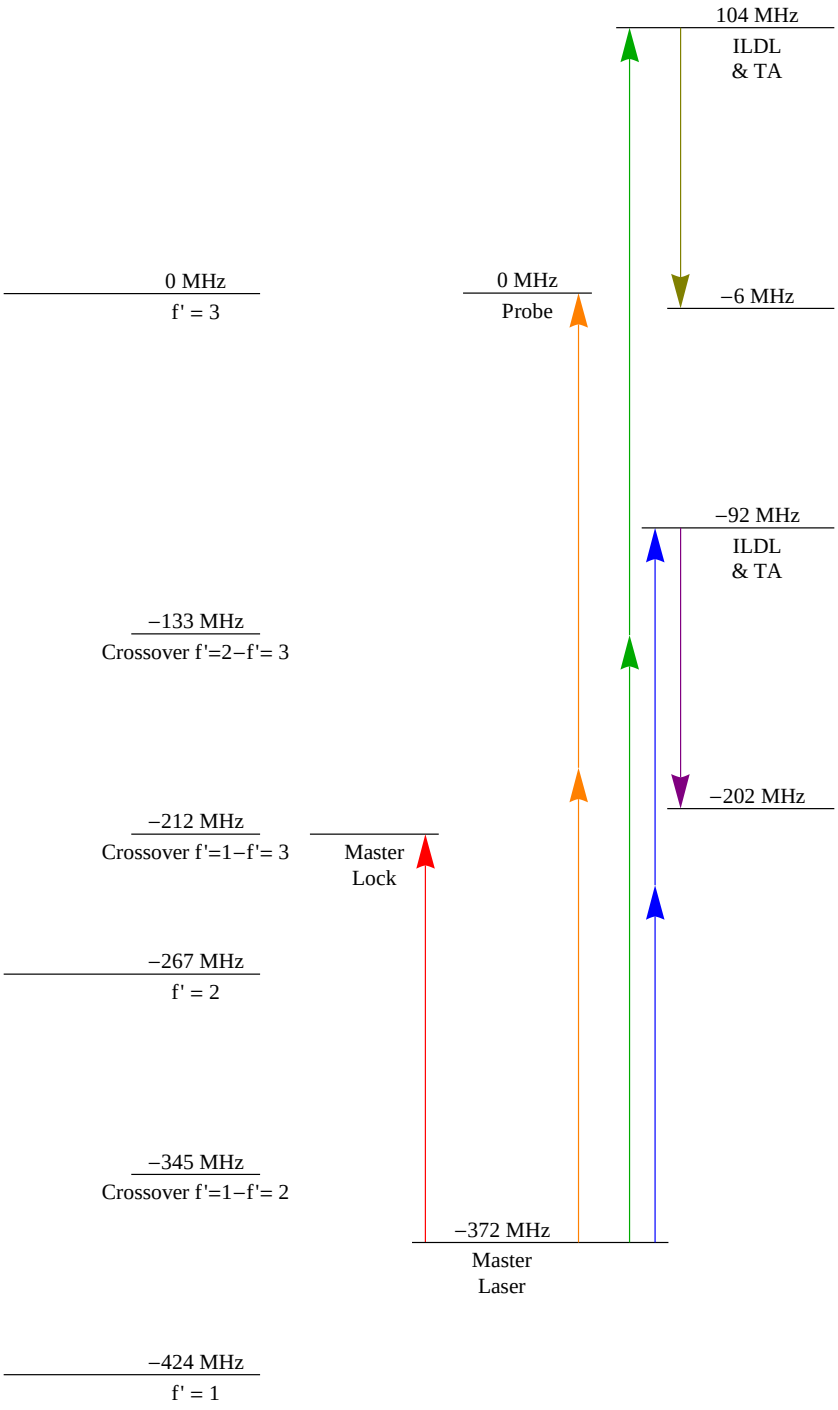

Figure 2.3: Frequency shifts for the MOT laser lock.

There is also a repump laser with the same top-hat profile which is only on the up/down axis of the MOT beam configuration and has up to 15 mW in its beam. The repump has the opposite circular polarization of the cycling transition lasers due to using a polarizing beam cube to combine the beams. The lasers for the cycling transition use a complicated frequency shifting scheme using an optics setup described in detail in Ref. [109, 110] in order to produce the relatively large range of detunings required by the experiment. Laser light from an external cavity diode laser (ECDL) master oscillator is frequency shifted up 160 MHz by an AOM (Figure 2.3 red arrow) which is used to offset the lock of the master laser from the lock point of the $f' = 1 - f' = 3$ crossover resonance. The light from the master laser is then double-passed through a variable frequency AOM (Figure 2.3 green and blue arrows) to seed an injection locked diode laser (ILDL). The frequency shift from this AOM varies from 2×140 MHz to 2×238 MHz. The ILDL is in turn used as the seed for the tapered amplifier (TA). Finally the output of the TA is passed through a final AOM to control power and is divided into three fibers going to the experiment. This AOM also shifts the frequency of the light back down 110 MHz (Figure 2.3 gold and purple arrows). A low power probe beam for absorptive imaging is also derived from frequency shifting the master oscillator and is switched on and off with a double-passed AOM operating at 186 MHz (Figure 2.3 orange arrows). Finally a second ECDL master oscillator (not shown) seeds another ILDL used for repump laser light. The power from this ILDL delivered to the experiment is also controlled by an AOM. The frequency manipulation of the repump is much simpler in that the lock is used to offset the laser frequency by 80 MHz from the resonance and the control AOM shifts the laser light 80 MHz back to resonance. All of the resonant light beams also have a shutter to eliminate any light leakage through the AOMs from getting to the experiment when not desired. This setup is essentially unchanged since the work of Murray Barrett and Ming-Shien Chang [108, 109]. The final result is a set of lasers that provide light on the ^{87}Rb D_2 manifold connecting the ground electronic state $5^2S_{1/2}$ to the excited electronic state $5^2P_{3/2}$. The laser light derived from the MOT master

varies from $\sim$ 6 MHz red of the cycling transition $5^2S_{1/2}$ $f = 2 \rightarrow 5^2P_{3/2}$ $f' = 3$ to $\sim$ 200 MHz to the red, or 65 MHz blue of the depumping transition $5^2S_{1/2}$ $f = 2 \rightarrow 5^2P_{3/2}$ $f' = 2$. The weak absorptive probe is on the cycling transition to within 0.1 MHz. The repump laser light stays on resonance for the $5^2S_{1/2}$ $f = 1 \rightarrow 5^2P_{3/2}$ $f' = 2$.

2.4 Dipole Force Trapping

The dipole force trapping laser is provided by an industrial CO_2 laser at 10.6 μm with 100 W continuous output power. This is in the regime of the quasi-electrostatic trap (QUEST) where the AC polarizability of the trapped atom is approximately the DC polarizability [108, 109, 115]. The CO_2 laser power delivered to the experiment is controlled by two AOMs after a 90/10 beam-splitter. The high power beam is used by the basic single focus trap and the low power beam is used for a counter-propagating lattice. These beams are aligned through the ZnSe optics of the chamber in a horizontal direction. The AOM control of the laser power is carefully calibrated in order to control the main trapping beam power from 5 mW to 50 W of power going to the chamber. The main high power beam path incorporates a telescope with an motor-actuated zoom lens. Moving this lens allows the size of the waist at the focusing lens in the chamber to be varied and thus the waist at the focus. The waist size of the focus is variable from $\sim 20 - 120$ μm. Details of dipole force trapping with the CO_2 laser are described extensively in Ref. [109].

In order to create the tightly confined traps used in most of this thesis, a secondary laser is used to make another dipole force trap crossed with the main dipole force trap. The secondary dipole force trap comes from a diode laser at 852 nm with up to 30 mW of power delivered to the experiment. This light is in the regime of the far off resonant trap (FORT) [115]. The power is also controlled by an AOM and has a shutter since its leakage is detected as scattered light during imaging. This laser light is fiber coupled to a fixed focus setup aligned as a cross with the main trapping beam. This beam requires delicate alignment since its 20 μm waist must intersect the 20 μm waist of the main dipole force

trap, with each one intersecting at the focus of the other beam. This dipole trap can be used with the main trapping laser to make a cross trap or it can be used to load only 1-2 lattice sites of the lattice configuration.

2.5 Photo-association Laser

In Chapter 6, photo-association (PA) is investigated. Since the photo-association lines are not amenable to the spectroscopic techniques typically used for locking lasers, a transfer lock is used to stabilize this laser (See Figure 2.4). The cycling transition master oscillator is used as the frequency reference. Light from this laser is shifted by an electro-optic modulator (EOM) which gives the light sidebands 25 MHz to 4 GHz offset from the carrier. By locking the cavity to one of these sidebands the length of the cavity can still be locked while scanning the EOM frequency shifts the transfer lock hundreds of MHz in 5 MHz steps. The frequency modulation that is already on the master laser is also used to generate the locking signal for the cavity. The cavity is a Fabry-Perot cavity with a free-spectral range (FSR) of 5.775 GHz and a linewidth of $\sim$ 25 MHz. The signal generated from the FM spectroscopy using the master laser is used in a controller to feedback to the piezo-electric element which controls the length of the cavity. The PA laser is another ECDL master oscillator. A small portion of the PA laser light is frequency modulated by a dithered AOM and combined with the master oscillator on a polarizing beam splitter to go through the cavity. The frequency modulation of the PA laser is at a different frequency than the modulation of the master laser. This allows using the same photo-detector for both signals where the demodulation frequency determines which error signal is being produced. The error signal demodulated with the same frequency as the PA FM is used to lock the PA laser to a cavity resonance 723 GHz (125 FSRs) away from the resonance used to lock the cavity. By varying the frequency of the EOM, the cavity lock is scanned which in turn scans the lock of the PA laser. Light from the PA laser is also sent to a wavemeter to verify the wavelength of the photo-association line. The majority of the laser power from the PA

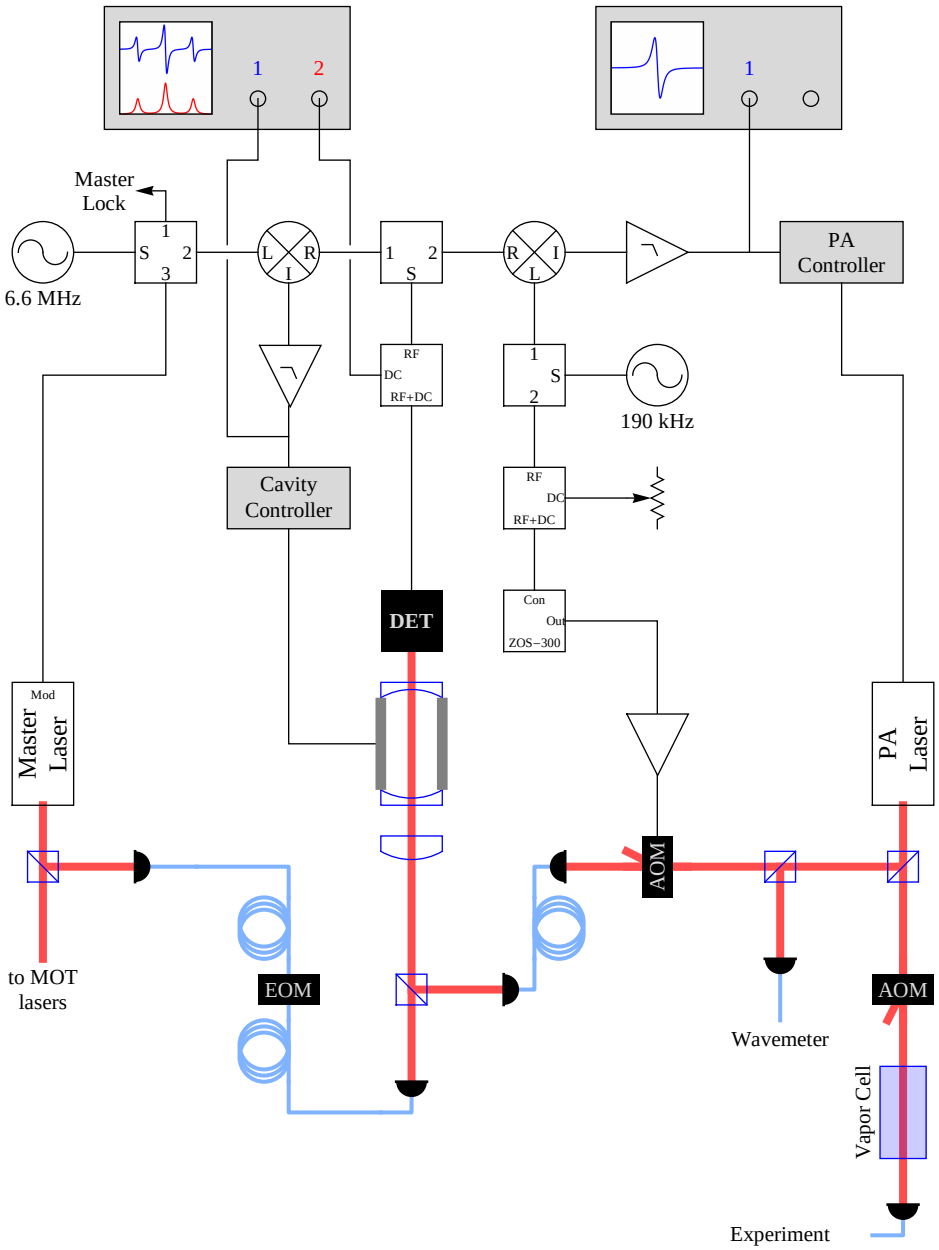

Figure 2.4: Photo-Association Laser Transfer Lock.

laser is sent through an AOM to control the power delivered to the experiment. The light controlled by the AOM is also sent through a heated rubidium vapor cell to filter out any light resonant with the atomic transitions.

2.6 Microwave and RF Systems

Whereas the lasers primarily interact with the electric dipole moment of the valence electron, oscillating magnetic fields can be used to interact with the magnetic dipole moment of the valence electron and to a much lesser extent with the nuclear magnetic moment. Within the electronic ground state hyperfine manifold ($5^2S_{1/2}$), the magnetic dipole transitions are broken up by microwaves which connect $f = 1$ to $f = 2$ (red, green, and blue arrows in Figure 2.5) and RF which connect Zeeman sub-levels within the same f state (gray arrows in Figure 2.5). The theoretical details are worked out in Appendix A. Access to these transitions is useful for magnetic field measurement, state preparation, and the measurement protocol used to measure squeezing.

The microwave system takes its frequency reference from a GPS receiver which produces a 10 MHz reference signal. Two frequency synthesizers are set to half the microwave frequency of 6.835 GHz because the generators are limited to 4 GHz in output and the RF switch used to control them leaks above 5 GHz. Two generators are used since it is sometimes necessary to have two microwave pulses of different frequencies during the experimental run and the generators cannot change frequency fast enough. After the switch, the frequency is doubled using a passive doubler. Signals from the two generators are combined and amplified up to 12 W to drive the microwave horn. The amplitude of the microwaves is controlled by adjusting the power output of the generators. The microwave horn was designed to work with a previous welded metal tube chamber. It is a right circular cylinder of diameter (1.5”) matching that of a standard vacuum nipple for a 2.75” flange in order to optimize coupling. Propagating waves along this type of waveguide is a standard electromagnetism problem [116]. This size supports the lowest transverse electric (TE)

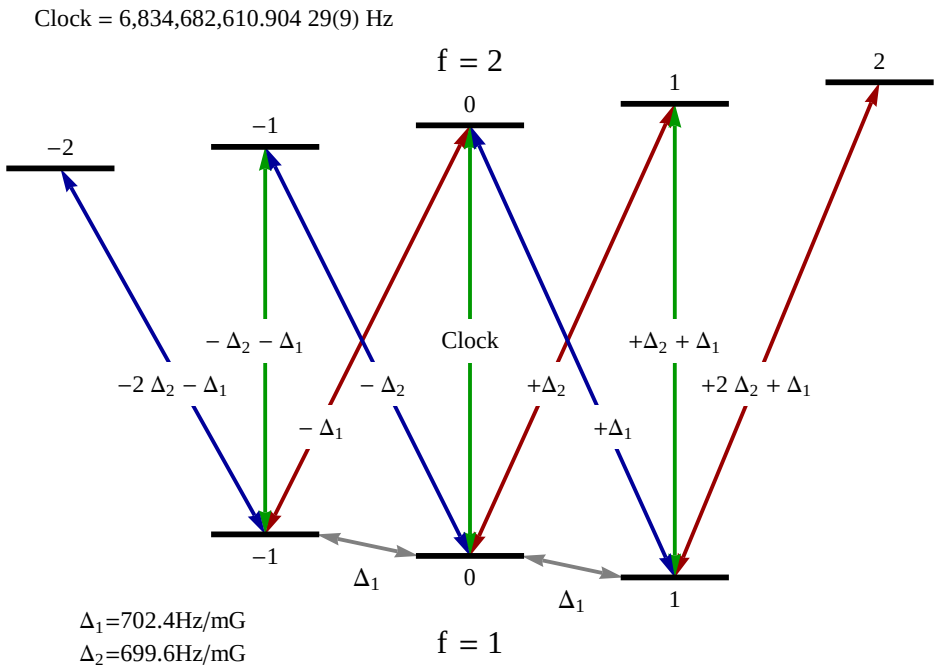

Figure 2.5: Microwave and RF transitions.

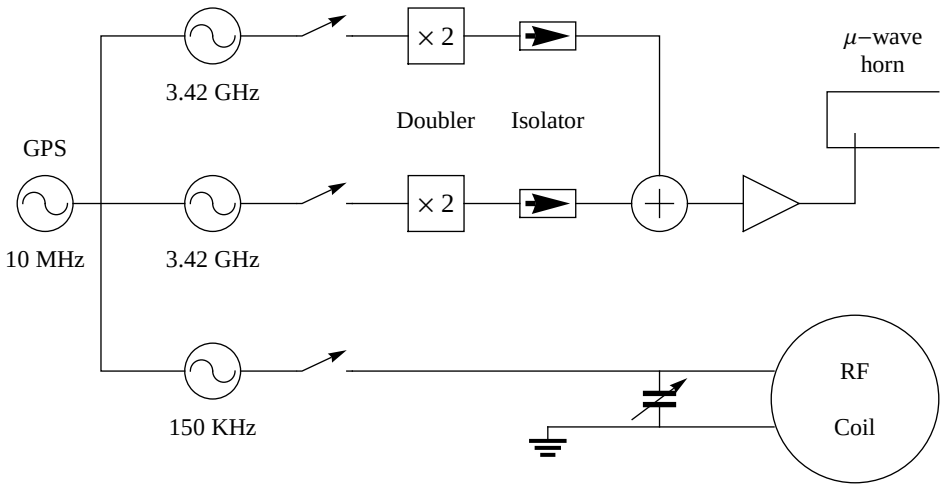

Figure 2.6: Microwave and RF control system.

and transverse magnetic (TM) modes for the microwave frequency. The injection probe is a quarter wave antenna in the guide which should only excite the TE mode. For the chamber used for the experiments in this thesis, the coupling is no longer waveguide-to-waveguide but waveguide-to-free-space and operates more in a far-field regime. Since the horn is not flared, its aperture is slightly smaller than the free space wavelength of 4.4 cm making the lobe of the output mode diverge considerably and reducing the amplitude at the atoms. In the previous chamber the system was capable of Rabi rates of 55 kHz but in this setup the system is limited to 20 kHz when driven with the maximum microwave amplifier output power of 12 W.

The RF system also uses the GPS 10 MHz reference for its function generator. The generator drives the RF coil directly through an RF switch. The power is limited to 100 mW by the switch, but this is sufficient to achieve Rabi rates of 2.5 kHz. The RF is coupled to the atoms by a simple 2 turn coil placed on top of the chamber centered on the large window. The required frequency to excite the RF transitions varies with the magnetic field, but is typically 50-300 kHz. This coil operates entirely in the near field regime since the coil is 3.5" in diameter, much smaller than the wavelength of about 1-6 km. In order to increase the amplitude of the oscillating magnetic field it is operated in parallel with a capacitor tuned such that the coil and capacitor form a resonator at the desired operation frequency. This results in a ring up/down time of $\sim 10\,\mu$s which is much shorter than the typical pulse times of $\sim 100\,\mu$s. For a 150 kHz drive frequency the required capacitance is 750 nF indicating that the inductance of the coil is 1.5 μH.

2.7 Imaging System

The imaging configuration used to take all the data in this thesis has been a $4f$ imaging system. Two basic types of imaging were used, absorptive and fluorescence, each with distinct advantages and disadvantages. The $4f$ configuration is required by absorptive imaging, but also minimizes aberrations for fluorescence imaging. If different focal lengths are used

for the lenses, then the system can magnify or reduce the imaging plane. Then the actual length of the system is $2f_1 + 2f_2$ but it is still called a $4f$ imaging system. These techniques along with their noise and calibration are covered extensively in Ref. [110].

For absorptive imaging shown in Figure 2.7(a), a probe beam of resonant laser light is directed towards the imaging system from behind the atoms which absorb the light and cast a shadow. This shadow propagates as a combination of modes subtracted from the probe beam. The ultimate resolution is determined by how many of these modes make it through the aperture of the first lens. These shadow modes are collimated by the first lens which also focuses the probe beam. The second lens is placed to re-collimate the probe beam and to focus the shadow modes onto the CCD camera. The two lenses act as a telescope for the probe beam and as an imaging lens for the shadow. The need to do both of these is why absorptive imaging requires a $4f$ imaging system. The image of the shadow of the atomic cloud is compared to a reference image of the probe light when no atoms are there in order to determine the optical depth which is related to the column density of the atomic cloud which can be summed to determine the number. However the determination of the optical depth is nonlinear in the column density and depends on the probe beam intensity. The absorptive imaging technique has a high spatial resolution because the atoms do not move much during the imaging since only short pulses are needed to provide sufficient light for the camera. However the use of laser light through multiple optical elements usually results in interference patterns which can affect the final image quality especially if they change between the signal and reference shots.

For fluorescence imaging shown in Figure 2.7(b), resonant or near resonant laser beams directed from the side of the imaging path illuminate the atoms causing them to fluoresce. The fluorescence is collected by the imaging system so that the scattered photons can be counted. Here the two lenses merely act to image the fluorescing atoms onto the CCD camera. The collection efficiency is limited by the apertures of the system. Resolution is primarily limited by atomic motion due to heating and pushing from the beams used to

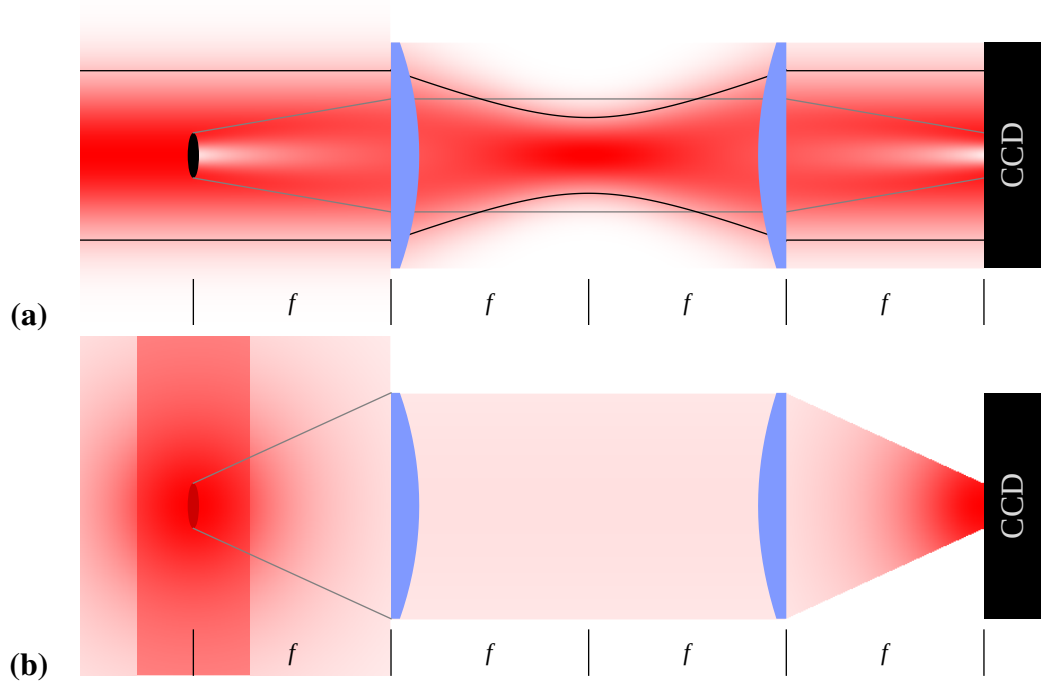

Figure 2.7: Imaging Configurations. **a.** Absorptive Imaging. **b.** Fluorescence Imaging.

fluoresce the atoms. This is a more significant problem for fluorescence versus absorptive imaging since the exposure usually needs to be longer than absorptive imaging to collect enough photons. Also the fluorescence technique is more sensitive to light scattering into the imaging path that is not from fluorescence of the atoms. However this technique does not suffer from interference since the fluoresced light is not phase coherent. This technique is very good at counting atoms due to its linear response to number of atoms.

Both of these techniques use resonant light on the cycling transition. However typically the atoms imaged are in the $f = 1$ state. Because of this the repump beam is also turned on simultaneously to transfer the atoms to the $f = 2$ state so that they will absorb and fluoresce with the cycling transition. The need for this has a useful side effect; the atoms can also be transferred to the $f = 2$ level with microwaves. Therefore microwave spectroscopy used to determine the magnetic field relies on this imaging distinction between $f = 1$ and $f = 2$ atoms by leaving off the repump beam during imaging.

2.8 The Control System

The experimental sequence is automated using computer control through National Instruments output boards and Labview programming. The system has 16 analog output channels to control such signals as bias and gradient coil currents, laser detuning and power, and getter current. There are also 24 digital channels to control various RF switches, shutters, and triggers for cameras and pulse generators. GPIB and RS-232 are used to update values for various function generators, pulse generators, and the lens mover. A frame grabber is used to digitize the analog signal from a CCTV camera for trap loading diagnostics. It is this complex control apparatus that allows such flexibility in the variety of experiments that are ran.

2.9 Basic Experimental Sequence

The experimental sequence begins by loading the main optical dipole force trap. This starts with the MOT laser light and coils on, the blue LED lights on, and the CO_2 trapping laser on at full power with the zoom lens positioned such that the dipole trap has a large waist to maximize overlap. The MOT loads for 15 s at which point the number of atoms in the MOT saturates. Once this is done, the atoms are loaded into the optical dipole trap using a temporal dark MOT sequence. The MOT gradient coil current is halved, the cycling transition laser power is halved, the repump power is lowered to a few tens of μW, and the detuning of the cycling transition laser is detuned as far to the red as the control system will allow.[3] While in this transient condition, the MOT collapses along the direction of the repump light into a pancake shape. The exact location it collapses to is sensitively dependent on the final repump power. The final cloud loads the optical dipole force trap

[3]The optimization of the temporal dark MOT sequence is empirically determined. The final gradient and cycling transition intensity both have some effect on loading and the optimum values vary from no change to half their MOT loading values. The effect on the loading from the detuning is stronger and has always been optimized for the farthest red from the cycling transition as the control system can reliably produce. The efficiency of the loading is very sensitive to the final power for the repump laser which has to be checked daily.

with 10-15 million atoms at $\sim$ 30 μK with an equal distribution of m_f states within the $f = 1$ manifold.

Now with the optical dipole force trap loaded, all resonant laser light is extinguished and evaporative cooling begins. Evaporation is accomplished in two ways. Foremost the trap power is simply lowered adiabatically allowing the hotter atoms to escape lowering the overall temperature. If this were the only evaporation technique used for a dipole force trap with a large waist, the re-thermalization rate and hence evaporative cooling rate would slow too much and there would be insufficient cooling to reach the BEC transition temperature. So the zoom lens moves simultaneously changing the geometry of the trap to a smaller waist which maintains the radial trap frequencies and thus re-thermalization rate. This creates a BEC with over 100 thousand atoms after 2 s of evaporative cooling. During evaporation, we typically apply magnetic biases and gradients to influence the m_f populations of the final BEC. In order to create a $m_f = 0$ condensate, a relatively large gradient of 20 G/cm is applied along the weak trapping direction of the main trapping laser. This pulls the $m_f = \pm 1$ components towards more weakly trapped regions causing them to be lost preferentially while maintaining thermal equilibrium with the other m_f states. To create a condensate of $m_f = \pm 1$, the gradient is oriented along the gravity direction and depending on its direction one of the states is levitated against gravity and the other is pushed with it causing the levitated state to be kept preferentially. In this case the $m_f = 0$ component is neither levitated or pushed down and usually leaves some residual amount. It is possible to selectively push out this residual component using microwave transitions and resonant light. After the gradient is ramped down, the secondary dipole force trap, if used, is ramped up. If the lattice configuration is to be used, the counter propagating beam for the primary dipole trap is then ramped up and the secondary dipole force trap is ramped back down. For the cross trap configuration, the secondary dipole force trap remains on throughout the experiment. Further evaporation cools the atoms to well below the BEC transition temperature whereby the ground state of the trapping potential is macroscopically occupied.

Dynamical evolution of the internal states of the BEC would occur even before evaporation is complete unless it is prevented. During the creation of the BEC a bias field of 2 G is applied to prevent this dynamical evolution. Evolution of the condensate is initiated by bringing down the bias field. After the bias is ramped down, the initial state can be further prepared by performing microwave and RF manipulations as necessary. These manipulations are not performed until the ramp is complete since the microwave and RF frequencies are magnetic field dependent. The field ramp takes $10 - 15$ ms to reach the necessary stability to use the microwaves and RF. The manipulations themselves take a few hundred microseconds. Most of the experiments in this thesis use an initial state of $m_f = 0$ with no state preparation. After the preparation the BEC is allowed to evolve freely for some amount of time from no evolution time to a couple of seconds. Following this evolution, the microwaves and RF are again used to prepare the state for measurement. At this point the trapping lasers are shut off and the atoms are allowed to fall and expand for $5 - 20$ ms. During this time of flight (TOF) a gradient is turned on again to spatially separate the final m_f projections. At the end of this expansion one of the two imaging techniques is used to count and spatially resolve the expanded atom clouds. Finally everything is reset for another run.

CHAPTER III

SPINOR BOSE-EINSTEIN CONDENSATE THEORY

Spinor theory has taken two major approaches, mean-field and quantum. In this chapter, some of the key results from early seminal papers ([39,40,42,44,45,47,117,118]) are built upon to review both approaches. This review is focused on one of our most common experiments, evolution of a ferromagnetic condensate from the classically meta-stable initial state of $m_f = 0$. Throughout the results of both approaches are compared to each other through ground state and dynamical predictions. They are also compared to the experimental signature of an initial pause of no apparent evolution followed by under-damped oscillations to the ground state populations established in Ref. [15]. The mean-field approach predicts there to be no evolution from the exact $m_f = 0$ state. The fact that the state nonetheless evolves has been attributed to seeding either from quantum fluctuations or technical noise. The quantum approach predicts immediate evolution with almost critical damping to the ground state populations [44–46]. As part of the discussion, the original theoretical analyses are extended to include finite magnetic fields and their effects as well as the effects of the number of atoms. These extensions are explored through their effects on the ground states and spinor dynamics. This extension along with a semi-classical extension of the mean-field to account for quantum fluctuation as determined by an SU(3) analysis of the system allows an agreement to be found between the two theoretical approaches and with the experiment as well as shown in later chapters.

3.1 Theoretical Model of Spinor Interactions

3.1.1 Gross-Pitaevskii Equation

The Gross-Pitaevskii equation derives the Hamiltonian for a quantum system of identical bosons by making the Hartree-Fock approximation (treating the total wave-function as a

product of single particle states) and using a pseudo-potential to describe the interaction between particles using the scattering lengths. The pseudo-potential coupling strength is given by $g = 4\pi\hbar^2 a/m$ where a is the s-wave scattering length and m is the particle mass. The Gross-Pitaevskii equation reduces to the non-interacting BEC Hamiltonian as the s-wave scattering lengths goes to zero. For a scalar BEC, such as a $|f = 1, m_f = -1\rangle$ condensate in a magnetic trap, there is only one scattering length. This has the Hamiltonian

$$H = \sum_{i=1}^{N} -\frac{\nabla^2}{2m} + V_T(\mathbf{r}_i) + \sum_{i<j} g\,\delta(\mathbf{r}_i - \mathbf{r}_j) \tag{3.1}$$

with V_T being the trapping potential [119, 120]. However for a spinor BEC with spin-1, there are two scattering lengths corresponding to scattering through the total spin $F = 0$ and $F = 2$ scattering channels. For the low-temperature limit where there is only s-wave scattering, the spin-mixing interaction is modeled as a contact pseudo-potential in two body collisions [44–46]. The interaction between two atoms in a collision is given by [44, 45]:

$$U(\mathbf{r}_i, \mathbf{r}_j) = \delta(\mathbf{r}_i - \mathbf{r}_j) \sum_{F=0}^{2} g_F \sum_{M_F=-F}^{F} |F, M_F\rangle\langle F, M_F| \tag{3.2}$$

where g_F is the coupling strength of the total spin F scattering channel. The scattering channels can be expanded into the $|f = 1, m_f\rangle_1 \otimes |f = 1, m_f\rangle_2$ basis of the colliding atoms [44]. Thus the sums of Eq. (3.2) become

$$\begin{aligned}
&\sum_{F=0}^{2} g_F \sum_{M_F=-F}^{F} |F, M_F\rangle\langle F, M_F| \\
&= g_2\Big(\hat{\Psi}_1^\dagger\hat{\Psi}_1^\dagger\hat{\Psi}_1\hat{\Psi}_1 + 2\hat{\Psi}_1^\dagger\hat{\Psi}_0^\dagger\hat{\Psi}_1\hat{\Psi}_0 + \frac{2}{3}\hat{\Psi}_1^\dagger\hat{\Psi}_{-1}^\dagger\hat{\Psi}_1\hat{\Psi}_{-1} + \frac{2}{3}\hat{\Psi}_0^\dagger\hat{\Psi}_0^\dagger\hat{\Psi}_0\hat{\Psi}_0 \\
&\quad + \frac{2}{3}\hat{\Psi}_1^\dagger\hat{\Psi}_{-1}^\dagger\hat{\Psi}_0\hat{\Psi}_0 + \frac{2}{3}\hat{\Psi}_0^\dagger\hat{\Psi}_0^\dagger\hat{\Psi}_1\hat{\Psi}_{-1} + 2\hat{\Psi}_0^\dagger\hat{\Psi}_{-1}^\dagger\hat{\Psi}_0\hat{\Psi}_{-1} + \hat{\Psi}_{-1}^\dagger\hat{\Psi}_{-1}^\dagger\hat{\Psi}_{-1}\hat{\Psi}_{-1}\Big) \\
&\quad + g_0\Big(\frac{4}{3}\hat{\Psi}_1^\dagger\hat{\Psi}_{-1}^\dagger\hat{\Psi}_1\hat{\Psi}_{-1} + \frac{1}{3}\hat{\Psi}_0^\dagger\hat{\Psi}_0^\dagger\hat{\Psi}_0\hat{\Psi}_0 - \frac{2}{3}\hat{\Psi}_1^\dagger\hat{\Psi}_{-1}^\dagger\hat{\Psi}_0\hat{\Psi}_0 - \frac{2}{3}\hat{\Psi}_0^\dagger\hat{\Psi}_0^\dagger\hat{\Psi}_1\hat{\Psi}_{-1}\Big)
\end{aligned} \tag{3.3}$$

where $|f = 1, m_f = \alpha\rangle \to \hat{\Psi}_\alpha^\dagger$ has been substituted for compactness. It is useful to rearrange this sum such that the portions of the pseudo-potential associated with each s-wave scattering channel are recombined into a spin-independent part which is symmetric under change

of indices and has a coupling strength which is the weighted mean of the channel strengths ($\lambda_s = (2g_2 + g_0)/3$), and a spin-dependent part which is asymmetric under exchange of indices and has a coupling strength which is proportional to the difference of the channel strengths ($\lambda_a = (g_2 - g_0)/3$). The kinetic energy term of the Hamiltonian is also symmetric under exchange of indices and for now we will assume the trapping potential is as well. The symmetric and asymmetric parts of the Hamiltonian are given by: [44]

$$\mathcal{H}_S = \sum_i \int d^3r \hat{\Psi}_i^\dagger \left(-\frac{\hbar^2\nabla^2}{2m} + V_T \right) \hat{\Psi}_i + \frac{\lambda_s}{2} \sum_{ij} \int d^3r \hat{\Psi}_i^\dagger \hat{\Psi}_j^\dagger \hat{\Psi}_i \hat{\Psi}_j \tag{3.4a}$$

$$\begin{aligned} \mathcal{H}_A = \frac{\lambda_a}{2} \int d^3r \Big(& \hat{\Psi}_1^\dagger \hat{\Psi}_1^\dagger \hat{\Psi}_1 \hat{\Psi}_1 + \hat{\Psi}_{-1}^\dagger \hat{\Psi}_{-1}^\dagger \hat{\Psi}_{-1} \hat{\Psi}_{-1} - 2\hat{\Psi}_1^\dagger \hat{\Psi}_{-1}^\dagger \hat{\Psi}_1 \hat{\Psi}_{-1} \\ & + 2\hat{\Psi}_1^\dagger \hat{\Psi}_0^\dagger \hat{\Psi}_1 \hat{\Psi}_0 + 2\hat{\Psi}_{-1}^\dagger \hat{\Psi}_0^\dagger \hat{\Psi}_{-1} \hat{\Psi}_0 + 2\hat{\Psi}_0^\dagger \hat{\Psi}_0^\dagger \hat{\Psi}_1 \hat{\Psi}_{-1} + 2\hat{\Psi}_1^\dagger \hat{\Psi}_{-1}^\dagger \hat{\Psi}_0 \hat{\Psi}_0 \Big) \end{aligned} \tag{3.4b}$$

So the spin-mixing Hamiltonian is composed of a spin-independent symmetric part which will determine the overall spatial and motional wavefunction and a spin-dependent asymmetric part which allows interchange of hyperfine states during collisions while preserving the overall spin. It is this collisional interchange that drives spin-mixing.

3.1.2 Single Mode Approximation

Although the Hamiltonian has been separated into spin independent spatial modes portion and spin dependent internal modes portion, nothing done so far precludes the exchange of energy between them. This thesis seeks to study the internal dynamics alone, uncomplicated by spin waves, vortices, skyrmions, etc. So the single mode approximation will be used to remove the complications of energy exchange with a spatial/motional mode structure. The two interaction strengths provide two length scales for the BEC, $\xi_i = 2\pi\hbar/\sqrt{2m|\lambda_i|n}$ where n is the density. For ^{87}Rb (and ^{23}Na as well) $\lambda_s \gg \lambda_a$ making the spin independent length scale much smaller. This sets the scale over which the total density of the condensate can vary. The larger spin dependent length scale sets the scale of spin excitations. This disparity has an important consequence, that it is possible to create a condensate where the density drops to zero in a region smaller than the spin modes can

vary. In a shallow linearly polarized dipole force trap, the trapping potential generated is not dependent on the spin component. If the magnetic field gradient is also sufficiently small such that the overall trapping potential is the same for all three spin components, then the assumption of the trapping potential being symmetric is validated and furthermore the spatial structure can be decoupled from the internal dynamics. The dominant symmetric part of the Hamiltonian determines the overall spatial wavefunction $\phi(\boldsymbol{r})$ which is the solution to the mean-field scalar Gross-Pitaevskii equation for $\mathcal{H}_S$

$$\left(-\frac{\nabla^2}{2m} + V_T + \lambda_s N|\phi|^2\right)\phi = \mu\phi, \qquad \int d^3r|\phi(\boldsymbol{r})|^2 = 1 \tag{3.5}$$

with μ the chemical potential. This spatial wavefunction is common to all m_f projections. This simplification is known as the single mode approximation (SMA) which allows the focus to be only the internal dynamics independent of the spatial dynamics. The required conditions are fairly easy to achieve in optical traps having tight confinement in all three dimensions such as cross traps and lattices.

For large numbers of atoms, the scalar Gross-Pitaevskii equation is typically solved using the Thomas-Fermi approximation. Here the kinetic energy term is neglected and $\phi(\boldsymbol{r}) = \sqrt{\frac{\mu - V(\boldsymbol{r})}{N\lambda_s}}$. For a trapping potential approximated by a three dimensional simple harmonic oscillator potential, the chemical potential is given by [109]

$$\mu = \left(\frac{15\hbar^2 m^{1/2}}{2^{5/2}} N\bar{\omega}^3 \bar{a}\right)^{2/5} \tag{3.6}$$

where $\bar{\omega}$ is the geometric mean of the harmonic oscillator frequencies and $\bar{a} = (2a_2 + a_0)/3$ is the mean scattering length. The density is given by

$$N|\phi(\boldsymbol{r})|^2 \approx n_{TF}(\boldsymbol{r}) = \frac{15N}{8\pi R_1 R_2 R_3} \max\left[1 - \sum_{i=1}^{3} \frac{r_i^2}{R_i^2}, 0\right] \tag{3.7}$$

where $R_i = \sqrt{\frac{2\mu}{m\omega_i^2}}$ are the Thomas-Fermi radii with ω_i the characteristic frequencies of the three dimensional harmonic oscillator potential. From this a peak density, $n_0 = \frac{15N}{8\pi R_1 R_2 R_3}$, is also determined.

The SMA allows the internal modes to be approximated as $\hat{\Psi}_\kappa \approx \hat{a}_\kappa \phi(\boldsymbol{r})$, where $\kappa = 0, \pm 1$. The annihilation operator $\hat{a}_\kappa$ follows the usual bosonic commutation relation, $\left[\hat{a}_\kappa, \hat{a}_\iota^\dagger\right] = \delta_{\kappa\iota}$. With this approximation integration over the spatial portion simplifies the symmetric and asymmetric parts of the Hamiltonian to [44]

$$\hat{H}_s = \mu\hat{N} - \lambda_s'\hat{N}\left(\hat{N} - 1\right) \tag{3.8a}$$

$$\begin{aligned}\hat{H}_a &= \lambda_a' \left(\hat{a}_1^\dagger\hat{a}_1^\dagger\hat{a}_1\hat{a}_1 + \hat{a}_{-1}^\dagger\hat{a}_{-1}^\dagger\hat{a}_{-1}\hat{a}_{-1} - 2\hat{a}_1^\dagger\hat{a}_{-1}^\dagger\hat{a}_1\hat{a}_{-1}\right. \\ &\quad + 2\hat{a}_1^\dagger\hat{a}_0^\dagger\hat{a}_1\hat{a}_0 + 2\hat{a}_{-1}^\dagger\hat{a}_0^\dagger\hat{a}_{-1}\hat{a}_0 \\ &\quad \left. + 2\hat{a}_0^\dagger\hat{a}_0^\dagger\hat{a}_1\hat{a}_{-1} + 2\hat{a}_1^\dagger\hat{a}_{-1}^\dagger\hat{a}_0\hat{a}_0\right).\end{aligned} \tag{3.8b}$$

Here $2\lambda_i' = \lambda_i \int |\phi(\boldsymbol{r})^4| d^3r$ and $\hat{N} = \hat{a}_1^\dagger\hat{a}_1 + \hat{a}_0^\dagger\hat{a}_0 + \hat{a}_{-1}^\dagger\hat{a}_{-1}$ are the spatially integrated interaction strength and total number of atoms respectively. With the Thomas-Fermi approximation, the density squared integral, $\int |\phi(\boldsymbol{r})^4| d^3r$ evaluates to $\frac{4}{7}\frac{n_0}{N}$ and so for the same harmonic trapping potential λ_i' scales with number of atoms as $N^{-3/5}$. Clearly with no atom loss or change in the trapping potential $\hat{H}_s$ is a constant and all of the dynamics happen with $\hat{H}_a$.

3.1.3 Using Angular Momentum Algebra

The second quantized form of the components of the total spin angular momentum are defined by by

$$\hat{L}_x = \frac{1}{\sqrt{2}}\left(\hat{a}_1^\dagger\hat{a}_0 + \hat{a}_0^\dagger\hat{a}_{-1} + \hat{a}_0^\dagger\hat{a}_1 + \hat{a}_{-1}^\dagger\hat{a}_0\right) \tag{3.9a}$$

$$\hat{L}_y = \frac{i}{\sqrt{2}}\left(-\hat{a}_1^\dagger\hat{a}_0 - \hat{a}_0^\dagger\hat{a}_{-1} + \hat{a}_0^\dagger\hat{a}_1 + \hat{a}_{-1}^\dagger\hat{a}_0\right) \tag{3.9b}$$

$$\hat{L}_z = \left(\hat{a}_1^\dagger\hat{a}_1 - \hat{a}_{-1}^\dagger\hat{a}_{-1}\right). \tag{3.9c}$$

The spin dependent part of the Hamiltonian (Eq. (3.8b)) can be recast into an eigenbasis of angular momentum states [45]. This simplifies Eq. (3.8b) to:

$$\hat{H}_a = \lambda_a'\left(\hat{L}^2 - 2\hat{N}\right) \tag{3.10}$$

which can be seen to be equivalent to Eq. (3.8b) by expanding out $\hat{L}^2 = \hat{L}_x^2 + \hat{L}_y^2 + \hat{L}_z^2$ and $\hat{N}$ into their respective mode annihilation and creation operators and then normally ordering the mode operators. From Eq. (3.10) it is clear that the eigenstates of the spin-mixing Hamiltonian are total spin angular momentum states $|L, M_L\rangle$ with energy:

$$E_L^a = \lambda_a' \left[L(L+1) - 2N\right]. \tag{3.11}$$

The ground state of the system depends on the sign of λ_a'. For an anti-ferromagnetic condensate such as ^{23}Na, $\lambda_a' > 0$ and the energy is minimized by minimizing L which is globally $L = 0 (L = 1)$ for even(odd) N. The populations of the m_f states for the ground state are $\langle N_1\rangle = \langle N_0\rangle = \langle N_{-1}\rangle = N/3$. For a ferromagnetic condensate such as ^{87}Rb, $\lambda_a' < 0$ and the energy is minimized by maximizing L which has a maximum value of N. This has $2N + 1$ degenerate ground states, one for each value of the conserved magnetization. For $M_L = 0$ the populations of the m_f states for the ground state are $\langle N_1\rangle = \langle N_{-1}\rangle = N/4$ and $\langle N_0\rangle = N/2$.

To find the evolution of an initial state, simply find the initial state's projection onto each of the eigenstates by $C_L = \langle\psi(0)|L, M_L\rangle$ and evolve their phases for each eigenvalue $e^{-iE_L^a t/\hbar}$.

$$|\psi(t)\rangle = \exp^{-i\theta_N(t)} \sum_{L=0}^{N} C_L \exp^{-i\lambda_a' L(L+1)t} |L, M_L\rangle \tag{3.12}$$

Here the common part of the eigenvalue due to the number of atoms is pulled from the sum with $\theta_N(t) = -2N\lambda_a' t/\hbar$. Since the Hamiltonian commutes with N and $\hat{L}_z$, number of atoms and magnetization is conserved.

The initial state for most of our spin-mixing experiments is all atoms in the $m_f = 0$ state which is represented as the Fock state ($|N_1, N_0, N_{-1}\rangle$) where $N_1 = N_{-1} = 0$ and $N_0 = N$. To analyze the evolution the angular momentum states are expanded into the Fock basis. This basis can be constructed by taking a maximal state, $|L = N, M_L = -N\rangle \equiv |0, 0, N\rangle$, and applying the raising operator, $\hat{L}_+ = \sqrt{2}\left(\hat{a}_1^\dagger \hat{a}_0 + \hat{a}_0^\dagger \hat{a}_{-1}\right)$, until $M_L = 0$.[1] For lower values

[1]Proper normalization also requires applying the angular momentum basis raising operator, $\hat{L}_+|L, M\rangle =$

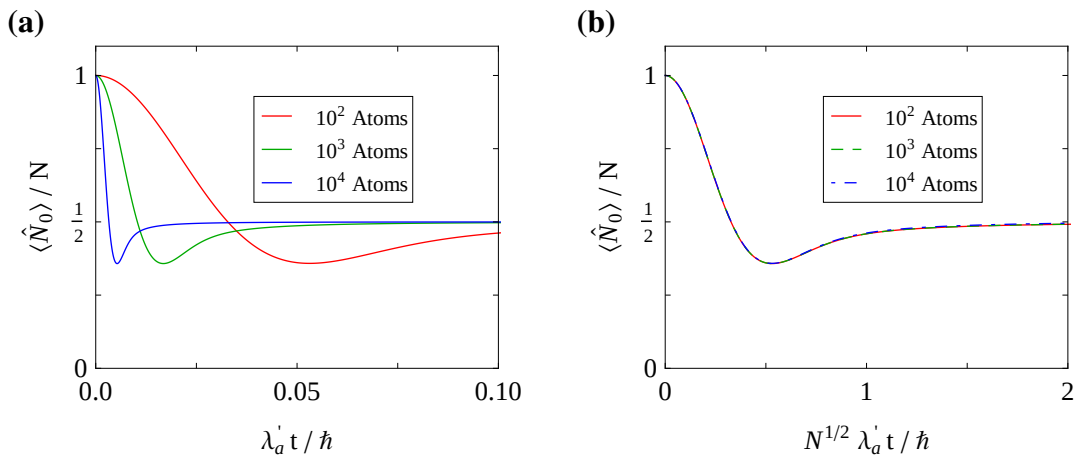

Figure 3.1: Quantum time evolution of $n_0 = \langle N_0 \rangle / N$ for 10^2, 10^3, and 10^4 atoms. **(a)** Time is scaled by λ_a'. **(b)** Time is scaled by $\sqrt{N}\lambda_a'$.

of L, the maximum M_L is constructed by orthogonality whenever possible. This occurs for every two applications of the raising operator. An example of this construction for four atoms is in Appendix B. A combinatoric form of the coefficients for the $|0, N, 0\rangle$ Fock state is provided in Ref. [50].

In Figure 3.1 the results of these dynamics for the population in $m_f = 0$ is shown. Since $M = 0$ and is conserved, $N_{\pm 1} = (N - N_0)/2$. The dynamics show an immediate evolution out of the $m_f = 0$ state with one overshoot before converging to the ground state populations. This is qualitatively similar to the experimental measurements in Ref. [15]. Figure 3.1(a) shows the quantum evolution for 10^2, 10^3, and 10^4 atoms, with the time scale by λ_a'. Figure 3.1(b) shows the same evolution but with time scaled by $\sqrt{N}\lambda_a'$ to illustrate the common time at which the minimum population of $m_f = 0$ occurs. This minimum occurs at a time $\hbar/(2\sqrt{N}|\lambda_a'|)$. Using the parameters from Ref. [15] of 30000 atoms with trap frequencies of $2\pi \times (120, 120, 2550)$ Hz and the ^{87}Rb value $\Delta a = -1.45\ a_B$, the interaction strength is calculated to be $\lambda_a' = -\hbar \times 1.3 \times 10^{-3}\ \mathrm{s}^{-1}$. This gives the time for the minimum to be 2.25 s, an order of magnitude larger than the experimental value of 250 ms in Ref. [15].

$\sqrt{L(L+1) - M(M+1)}\,|L, M+1\rangle$ to the LHS as well.

So while the theoretical evolution is qualitatively similar to experimental measurements, there is a serious discrepancy in the time scale. This discrepancy will be returned to in Section 3.2.1.

3.1.4 Mean Field Approach

Another way to evaluate the Hamiltonian is to use a mean-field approach. A mean-field approximation has already been made to calculate the spatial modes in the SMA. Another mean-field approximation can be made for the internal states as well. From the spinor portion of the Hamiltonian ($\hat{H}_a$) a set of coupled dynamical equations can be derived using the Heisenberg equation of motion. Inserting the spin dependent Hamiltonian (Eq. (3.8b)) into the Heisenberg equation of motion for each m_f state gives the coupled equations

$$i\hbar\frac{\partial\hat{a}_1}{\partial t} = 2\lambda'_a\left(\hat{a}_1^\dagger\hat{a}_1\hat{a}_1 - \hat{a}_{-1}^\dagger\hat{a}_1\hat{a}_{-1} + \hat{a}_0^\dagger\hat{a}_1\hat{a}_0 + \hat{a}_{-1}^\dagger\hat{a}_0\hat{a}_0\right) \tag{3.13a}$$

$$i\hbar\frac{\partial\hat{a}_0}{\partial t} = 2\lambda'_a\left(\hat{a}_1^\dagger\hat{a}_1\hat{a}_0 + \hat{a}_{-1}^\dagger\hat{a}_0\hat{a}_{-1} + 2\hat{a}_0^\dagger\hat{a}_1\hat{a}_{-1}\right) \tag{3.13b}$$

$$i\hbar\frac{\partial\hat{a}_{-1}}{\partial t} = 2\lambda'_a\left(\hat{a}_{-1}^\dagger\hat{a}_{-1}\hat{a}_{-1} - \hat{a}_1^\dagger\hat{a}_1\hat{a}_{-1} + \hat{a}_0^\dagger\hat{a}_0\hat{a}_{-1} + \hat{a}_1^\dagger\hat{a}_0\hat{a}_0\right) \tag{3.13c}$$

For large numbers of atoms the quantum fluctuations can be ignored and the mean field approximation made for the internal states. In the mean field limit, the field operators can be replaced by complex numbers ($\hat{a}_\kappa \rightarrow \sqrt{N}\zeta_\kappa$, $\hat{a}_\kappa^\dagger \rightarrow \sqrt{N}\zeta_\kappa^*$ with $\zeta_\kappa = |\zeta_\kappa|e^{i\theta_\kappa}$ and $\sum_\kappa \zeta_\kappa^*\zeta_\kappa = 1$) to represent the classical field amplitudes and phases of the internal modes. This replacement and dividing through by a common factor of $\sqrt{N}$ gives

$$i\hbar\dot{\zeta}_1 = c[(\rho_1 + \rho_0 - \rho_{-1})\zeta_1 + \zeta_0^2\zeta_{-1}^*] \tag{3.14a}$$

$$i\hbar\dot{\zeta}_0 = c[(\rho_1 + \rho_{-1})\zeta_0 + 2\zeta_1\zeta_{-1}\zeta_0^*] \tag{3.14b}$$

$$i\hbar\dot{\zeta}_{-1} = c[(\rho_{-1} + \rho_0 - \rho_1)\zeta_{-1} + \zeta_0^2\zeta_1^*] \tag{3.14c}$$

where $c = 2\lambda'_aN$ and $\rho_i = |\zeta_i|^2 = N_i/N$. The vector order parameter of three complex numbers representing the classical fields for the three components, $\psi = (\zeta_1, \zeta_0, \zeta_{-1})^T$, has six parameters. The constraint that $|\zeta_1|^2 + |\zeta_0|^2 + |\zeta_{-1}|^2 = 1$ reduces this to four parameters. A

useful parameterization of this is $\zeta_1 = \sqrt{\frac{1-\rho_0+m}{2}}e^{i\chi_+}$, $\zeta_0 = \sqrt{\rho_0}$, and $\zeta_{-1} = \sqrt{\frac{1-\rho_0-m}{2}}e^{i\chi_-}$, with $\chi_\pm = \theta_{\pm1} - \theta_0 = \frac{\theta_s \pm \theta_m}{2}$, and $m = (N_1 - N_{-1})/N$. The phase combinations θ_s and θ_m are called the spinor phase and magnetization phase (also known as the Larmor precession phase) respectively. This recombination is useful since the mean field spinor energy depends on the spinor phase but not the magnetization phase. Using this parameterization and changing to a rotating frame to remove the magnetization phase ($\zeta'_{\pm1} \to e^{\mp i\theta_m/2}\zeta_{\pm1}$), the equations can be further simplified to just two dynamical variables, ρ_0 and θ_s.

$$\dot{\rho}_0 = \frac{2c}{\hbar}\rho_0\sqrt{(1-\rho_0)^2 - m^2}\sin\theta_s \tag{3.15a}$$

$$\dot{\theta}_s = \frac{2c}{\hbar}\left[(1-2\rho_0) + \frac{(1-\rho_0)(1-2\rho_0) - m^2}{\sqrt{(1-\rho_0)^2 - m^2}}\cos\theta_s\right] \tag{3.15b}$$

These two coupled equations are the same as those of a classical non-rigid pendulum [42]. The corresponding mean-field spinor energy functional can be derived by making the same mean field substitutions into Eq. (3.8b), and dividing by N to get the spinor energy per particle:

$$\mathcal{E} = \frac{c}{2}m^2 + c\rho_0\left[(1-\rho_0) + \sqrt{(1-\rho_0)^2 - m^2}\cos\theta_s\right]. \tag{3.16}$$

Figure 3.2 is a plot of the energy contours in all three variables. Using this energy functional Eq. (3.15) can also be derived using the Hamiltonian equations of motion, $\dot{\rho}_0 = \frac{2}{\hbar}\frac{\partial\mathcal{E}}{\partial\theta_s}$ and $\dot{\theta}_s = \frac{2}{\hbar}\frac{\partial\mathcal{E}}{\partial\rho_0}$. This demonstrates that ρ_0 and θ_s are canonically conjugate variables. The parameterization has another pair of canonically conjugate variables, m and θ_m. However since the energy functional does not depend on θ_m, $\dot{m} = 0$ and the magnetization is conserved [47, 121].

The mean field energy functional can be minimized to find ground states. For the antiferromagnetic case with $c > 0$, the functional is minimized when $m = 0$ and either $\theta_s = \pm\pi$ or $\rho_0 = 0, 1$. This indeterminacy does not lend itself to comparison with the quantum ground state. For the ferromagnetic case where $c < 0$, the functional is minimized when $\theta_s = 0$ and $\rho_0 = (1 - m^2)/2$. This is the relationship of expectation values for a rotation of

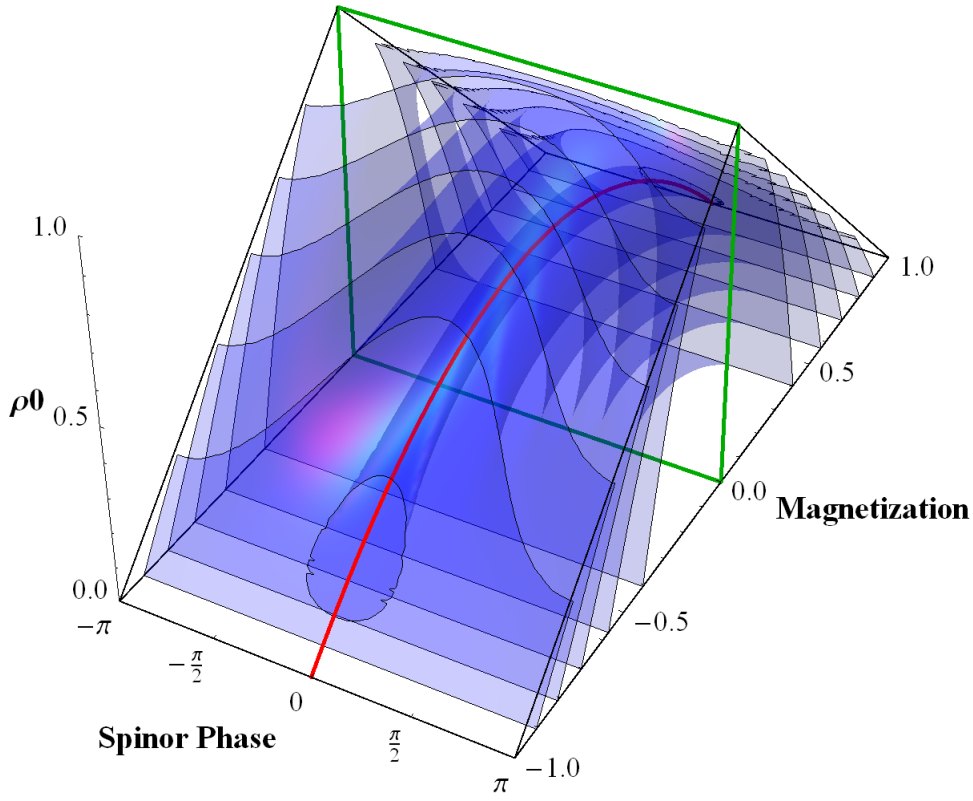

Figure 3.2: Representation of the spinor phase space in ρ_0, m, and θ_s with energy contours. Ferromagnetic ground states are shown in red. Anti-ferromagnetic ground states are shown in green.

quantum state $|L = N, M_L = -N\rangle$.

The mean-field dynamical equations have oscillatory solutions, without the apparent damping seen in the experiment. A general solution using Jacobian elliptic functions is given in Ref. [42]. The period is dependent on the displacement from the ferromagnetic ground state, and for small perturbations from the ground state it is approximately $T = 1/(2|c|)$. For the simplified dynamical equations (Eq. (3.15)), any time one of the populations is zero, the spinor phase is undefined. However Eq. (3.14) does not have this problem. Even so, starting with our initial state of $m_f = 0$, $\zeta_{\pm 1} = 0$ and $\zeta_0 = 1$, it is found that all the time derivatives are zero and thus the period goes to infinity. The exact $m_f = 0$ state does not evolve from the mean-field dynamical equations. This is inconsistent with the quantum solution and experimental measurements. Initial states arbitrarily close

to the $m_f = 0$ state do evolve, though with increasing slowness with greater proximity. A better understanding of the states of the system is needed. An overview initial is given in Section 3.1.5 and the $m_f = 0$ state in particular will be discussed in detail in Section 3.2.3

3.1.5 Decomposing the Spin-1 Density Matrix

In order to better understand the states of the system, it is necessary to look at the group structure of the spin-1 system. For spin-1, the order parameter is a rank-1 tensor or a vector of complex numbers. The density matrix can be decomposed into monopole, dipole, and quadrupole moments [122, 123]. Fixing the overall number and phase leaves the dipole (spin vector) and quadrupole irreducible tensors. The combination of the components of the spin vector and the components of the quadrupole tensor form a basis of infinitesimal generators for the Lie algebra su(3) [124]. The su(3) Lie algebra is related to the SU(3) group by the exponential map. For example the SU(3) group element for a $\pi/2$ rotation about L_y is given by $\exp\left(i\frac{\pi}{2}\hat{L}_y\right)$ where $\hat{L}_y$ is an element of the su(3) Lie algebra. There are three dipole (or angular momentum) operators L_a (Table 3.1), and five quadrapole operators N_{ab} which are moments of the quadrapole tensor (Table 3.2)[2]. These are defined as:

$$L_a = -i\hbar\epsilon_{abc}c_{bc} \tag{3.17}$$

$$N_{ab} = -c_{ab} - c_{ba} + \frac{2}{3}\delta_{ab}c_{cc} \tag{3.18}$$

summing over repeated indices. Here c_{ab} is the outer product $|\phi_a\rangle\langle\phi_b|$ for the matrix form of the tensor and the bilinear operator $b_a^\dagger b_b$ for the second quantized form. We use a basis of polar states (defined below) given by:

$$\begin{aligned}
|\phi_x\rangle &= \left(-|m_z = 1\rangle + |m_z = -1\rangle\right)/\sqrt{2} \quad & b_x^\dagger &= \left(-a_{+1}^\dagger + a_{-1}^\dagger\right)/\sqrt{2} \\
|\phi_y\rangle &= i\left(|m_z = 1\rangle + |m_z = -1\rangle\right)/\sqrt{2} \quad & b_y^\dagger &= i\left(a_{+1}^\dagger + a_{-1}^\dagger\right)/\sqrt{2} \\
|\phi_z\rangle &= |m_z = 0\rangle & b_z^\dagger &= a_0^\dagger
\end{aligned}$$

[2]While there are a total of nine quadrapole operators, only five of them are linearly independent since the quadrapole tensor is symmetric ($N_{ab} = N_{ba}$) and traceless ($N_{aa} + N_{bb} + N_{cc} = 0$).

For the matrix form only, there is also the relationship $N_{ab} = L_a L_b + L_b L_a - \frac{4}{3}\delta_{ab}$ [107].

States for which the density matrix can be brought to diagonal form by real space rotations (operators which are exponentiations of the dipole operators) are know as 'oriented' states [125, 126]. Spin-1 has two general classes of 'oriented' states which are real space rotations of $|m_f = 1\rangle$ and $|m_f = 0\rangle$. Rotations of $|m_f = 1\rangle$ are known as ferromagnetic states since the spins are all oriented the same up to quantum fluctuations. They are also states of maximal total spin or just spin states and belong to an SO(3) (SU(2)) symmetry group [39]. These states have $\langle L^2 \rangle = N(N+1)$ and the values of $\langle L_x \rangle$, $\langle L_y \rangle$, and $\langle L_z \rangle$ are such that the length of $\boldsymbol{L}$ is N. These spin states have an orientation vector which is just the coherent spin vector. From the mean-field parameterization, these states have $\theta_s = 0$ and $\rho_0 = (1 - m^2)/2$ and so are the ground states of a ferromagnetic condensate.

Rotations of $|m_f = 0\rangle$ are known as polar states. These states have $\langle L^2 \rangle = 2N$ but have $\langle L_x \rangle = \langle L_y \rangle = \langle L_z \rangle = 0$. The polar states do not have a net spin vector but can be characterized by their alignment of the minimum fluctuation of the spin components. The alignment is defined by a director to which the fluctuations are transverse. The polar states belong to a $\mathrm{U}(1)\times\mathrm{S}^2$ symmetry group [39]. These states have $\theta_s = \pm\pi$ and can have ρ_0 from 0 to 1. These conditions match the constraints on the mean-field anti-ferromagnetic ground state. They do not match the quantum ground state of $L = 0$, which remains a question to be answered later in this chapter.

The two classes of 'oriented' states together complete the SU(3) symmetry group. The connection between the polar and ferromagnetic states is the spinor phase shift, an SU(3) rotation, $\exp\left(i\Delta\theta_s \hat{N}_{zz}\right)$. The connection is simplest to see at a point where the two rotations give the same populations of $(\frac{1}{4}, \frac{1}{2}, \frac{1}{4})$ (Figure 3.2).

Table 3.1: Spin-1 dipole operators. Expectation values of these operators are components of the angular momentum vector. Matrices in spherical polar basis $|f, m_f\rangle$.

$$L_x = \frac{1}{\sqrt{2}} \begin{pmatrix} 0 & 1 & 0 \\ 1 & 0 & 1 \\ 0 & 1 & 0 \end{pmatrix} \qquad \hat{L}_x = \frac{1}{\sqrt{2}} \left(\hat{a}_1^\dagger \hat{a}_0 + \hat{a}_0^\dagger \hat{a}_{-1} + \hat{a}_0^\dagger \hat{a}_1 + \hat{a}_{-1}^\dagger \hat{a}_0 \right)$$

$$L_y = \frac{i}{\sqrt{2}} \begin{pmatrix} 0 & -1 & 0 \\ 1 & 0 & -1 \\ 0 & 1 & 0 \end{pmatrix} \qquad \hat{L}_y = \frac{i}{\sqrt{2}} \left(-\hat{a}_1^\dagger \hat{a}_0 - \hat{a}_0^\dagger \hat{a}_{-1} + \hat{a}_0^\dagger \hat{a}_1 + \hat{a}_{-1}^\dagger \hat{a}_0 \right)$$

$$L_z = \begin{pmatrix} 1 & 0 & 0 \\ 0 & 0 & 0 \\ 0 & 0 & -1 \end{pmatrix} \qquad \hat{L}_z = \left(\hat{a}_1^\dagger \hat{a}_1 - \hat{a}_{-1}^\dagger \hat{a}_{-1} \right)$$

Table 3.2: The spin-1 quadrapole operators. Expectation values of these operators are moments of the symmetric traceless quadrapole tensor. Matrices in spherical polar basis $|f, m_f\rangle$.

$$N_{yz} = \frac{i}{\sqrt{2}} \begin{pmatrix} 0 & -1 & 0 \\ 1 & 0 & 1 \\ 0 & -1 & 0 \end{pmatrix} \qquad \hat{N}_{yz} = \frac{i}{\sqrt{2}} \left(-\hat{a}_1^\dagger \hat{a}_0 + \hat{a}_0^\dagger \hat{a}_{-1} + \hat{a}_0^\dagger \hat{a}_1 - \hat{a}_{-1}^\dagger \hat{a}_0 \right)$$

$$N_{xz} = \frac{1}{\sqrt{2}} \begin{pmatrix} 0 & 1 & 0 \\ 1 & 0 & -1 \\ 0 & -1 & 0 \end{pmatrix} \qquad \hat{N}_{xz} = \frac{1}{\sqrt{2}} \left(\hat{a}_1^\dagger \hat{a}_0 - \hat{a}_0^\dagger \hat{a}_{-1} + \hat{a}_0^\dagger \hat{a}_1 - \hat{a}_{-1}^\dagger \hat{a}_0 \right)$$

$$N_{xy} = i \begin{pmatrix} 0 & 0 & -1 \\ 0 & 0 & 0 \\ 1 & 0 & 0 \end{pmatrix} \qquad \hat{N}_{xy} = i \left(-\hat{a}_1^\dagger \hat{a}_{-1} + \hat{a}_{-1}^\dagger \hat{a}_1 \right)$$

$$N_{xx} = \begin{pmatrix} -\frac{1}{3} & 0 & 1 \\ 0 & \frac{2}{3} & 0 \\ 1 & 0 & -\frac{1}{3} \end{pmatrix} \qquad \hat{N}_{xx} = -\frac{1}{3} \hat{a}_{+1}^\dagger \hat{a}_{+1} + \frac{2}{3} \hat{a}_0^\dagger \hat{a}_0 - \frac{1}{3} \hat{a}_{-1}^\dagger a_{-1} + \hat{a}_{+1}^\dagger \hat{a}_{-1} + \hat{a}_{-1}^\dagger \hat{a}_{+1}$$

$$N_{yy} = \begin{pmatrix} -\frac{1}{3} & 0 & -1 \\ 0 & \frac{2}{3} & 0 \\ -1 & 0 & -\frac{1}{3} \end{pmatrix} \qquad \hat{N}_{yy} = -\frac{1}{3} \hat{a}_{+1}^\dagger \hat{a}_{+1} + \frac{2}{3} \hat{a}_0^\dagger \hat{a}_0 - \frac{1}{3} \hat{a}_{-1}^\dagger \hat{a}_{-1} - \hat{a}_{+1}^\dagger \hat{a}_{-1} - \hat{a}_{-1}^\dagger \hat{a}_{+1}$$

$$N_{zz} = \begin{pmatrix} \frac{2}{3} & 0 & 0 \\ 0 & -\frac{4}{3} & 0 \\ 0 & 0 & \frac{2}{3} \end{pmatrix} \qquad \hat{N}_{zz} = \frac{2}{3} \hat{a}_{+1}^\dagger \hat{a}_{+1} - \frac{4}{3} \hat{a}_0^\dagger \hat{a}_0 + \frac{2}{3} \hat{a}_{-1}^\dagger \hat{a}_{-1}$$

3.1.6 Magnetic Fields

We have not yet considered the effects of magnetic fields. The Zeeman energy is simple to calculate (See Appendix A) resulting in the well known *Breit-Rabi* formula for the hyperfine ground states [113]. For low fields, it is typically expanded into a power series giving the linear Zeeman effect and a quadratic Zeeman effect. In the SMA only the energy difference of the m_f states affects dynamics. The energy relative to the energy for $m_f = 0$ is given by $E_\kappa - E_0 = p\kappa + q\kappa^2$, where $p = \mu_B B_z g_f$, $q = \mu_B^2 B_z^2 / \left(\hbar^2 E_{HFS}\right)$, g_f is the Landé g-factor, and E_{HFS} is the ground state hyperfine splitting [45, 46, 105]. The total magnetic field energy is given by

$$\begin{aligned} E_B &= E_1 N_1 + E_0 N_0 + E_{-1} N_{-1} \\ &= p(N_1 - N_{-1}) + (q + E_0)(N_1 + N_{-1}) + E_0 N_0 \\ &= p(N_1 - N_{-1}) + q(N_1 + N_{-1}) + E_0 N. \end{aligned} \tag{3.19}$$

The final term $E_0 N$ is a constant offset of the energy which does not affect dynamics. The linear Zeeman effect is simply proportional to $L_z = N_1 - N_{-1}$ with each atom having energy pm_f. The matrix form of pL_z gives the energy per particle. However the quadratic Zeeman causes a difficulty. The energy is often listed as qL_z^2 which works perfectly well for the energy per particle in the matrix form, but not for the second quantized form. This problem can be avoided by summing directly over the atoms giving the total quadratic Zeeman energy, $E_q = q \sum_i m_i^2$, but this basis dependent form can be cumbersome to calculate. A similar way to express the quadratic Zeeman energy is $E_q = q(N - N_0)$. A basis independent operator that gives the energy as $q\,(N_1 + N_{-1})$ (or $q(N - N_0)$) is needed. This leads to the energy being $\frac{q}{2} N_{zz}$ which works well for the matrix form and the second quantized form.

The equivalence of using N_{zz} as the quadratic Zeeman operator is shown as follows

$$\begin{aligned} N_{zz} &= \frac{2}{3}N_1 + \frac{2}{3}N_{-1} - \frac{4}{3}N_0 \\ &= \frac{2}{3}(N_1 + N_{-1}) - \frac{4}{3}(N - N_1 - N_{-1}) \\ &= 2(N_1 + N_{-1}) - \frac{4}{3}N. \end{aligned} \tag{3.20}$$

So $\frac{q}{2}N_{zz} = q(N_1 + N_{-1}) - \frac{2}{3}qN$ which again has constant final term. This presents the interesting picture that the linear Zeeman energy depends on the z projection of the spin, while the quadratic Zeeman depends on the z projection of the quadrupole moment.[3]

3.1.7 Quantum Approach with Finite Magnetic Field

Combining Eq. (3.10) with the appropriate operators for the magnetic field, the full Hamiltonian in a finite magnetic field takes on a compact basis independent form.

$$\hat{H}_{SMA} = \lambda_a' \left(\hat{L}^2 - 2\hat{N}\right) + p\hat{L}_z + \frac{q}{2}\hat{N}_{zz}. \tag{3.21}$$

$\hat{L}_z$ commutes with the entire Hamiltonian, but $\hat{N}_{zz}$ and $\hat{L}^2$ do not commute. This makes adding the effects a finite magnetic to the angular momentum formulation somewhat difficult in terms of solving the evolution. However Fock states are eigenstates of both L_z and N_{zz} and the angular momentum basis has already been projected onto the Fock basis.

An alternative route to evaluate the asymmetric spin-mixing Hamiltonian (Eq. (3.8b)) is found in Refs. [46, 48, 51] which gives a Fock state basis as a number of pairs of $m_f = \pm 1$ in a vacuum state of atoms with $m_f = 0$. While one enumeration of the Fock state is $|N_{-1}, N_0, N_1\rangle$, it can also be equivalently enumerated by $|N, M, k\rangle$ where $N = N_{-1} + N_0 + N_1$ is the total number of atoms, $M = N_1 - N_{-1}$ is the magnetization, and k is the number of ± 1 pairs. The spin-mixing Hamiltonian conserves both N and M and so the only evolution is in k. Using this form the spin-mixing portion then acts as a hopping Hamiltonian jumping between numbers of pairs and can be represented by a tridiagonal

[3] L_z is the zero projection of the rank-1 dipole spherical tensor while N_{zz} is the zero projection of the rank-2 quadrupole spherical tensor.

matrix. Rewriting Eq. (3.8b) by pairing up mode operators into number operators gives

$$\hat{H}_a = \lambda_a' \left((\hat{N}_1 - \hat{N}_{-1})^2 + (2\hat{N}_0 - 1)(\hat{N}_1 + \hat{N}_{-1}) + 2\hat{a}_1^\dagger \hat{a}_{-1}^\dagger \hat{a}_0 \hat{a}_0 + 2\hat{a}_0^\dagger \hat{a}_0^\dagger \hat{a}_1 \hat{a}_{-1} \right). \tag{3.22}$$

Now adding in the effects from a finite magnetic field is trivial since it is diagonal in this basis. The magnetic field portion is just $p\left(\hat{N}_1 - \hat{N}_{-1}\right) + q\left(\hat{N}_1 + \hat{N}_{-1}\right)$.[4] Setting $M_L = 0$ and evaluating this equation for numbers of pairs gives us the matrix elements (similar to Ref. [46]):[5]

$$\begin{aligned} \tilde{H}_{k,k'} &= \{2\lambda_a' k(2(N-2k)-1) + 2q\}\delta_{k,k'} \\ &+ 2\lambda_a' \{(k'+1)\sqrt{(N-2k')(N-2k'-1)}\delta_{k,k'+1} \\ &+ k'\sqrt{(N-2k'+1)(N-2k'+2)}\delta_{k,k'-1}\} \end{aligned} \tag{3.23}$$

The eigenvalues of this matrix for $q = 0$ are the same as Eq. (3.11) and the eigenvectors are just the projections of the angular momentum states onto the Fock basis as generated by the raising operator method seen previously. Using these eigenvalues and eigenvectors, it is once again possible to solve for the exact evolution. Setting $q \neq 0$ gives eigenstates that are mixed between the angular momentum basis and the Fock pairs basis which can also be diagonalized to get an exact solution [51]. Figure 3.3 shows the eigenspectrum for both a ferromagnetic and anti-ferromagnetic condensate. For low magnetic fields the eigenenergies vary quadratically with index because the eigenstates are angular momentum states. For high magnetic fields the eigenenergies vary linearly with index because the eigenstates are Fock states. The ground state in high magnetic fields is the lowest energy eigenstate of N_{zz} which is the $|0, N, 0\rangle$ Fock state equivalent to the $m_f = 0$ polar state. This is true regardless of the sign of λ_a' [41].

[4] For simplicity E_0 is chosen as the zero point for the quadratic Zeeman energy.

[5] There is a typographical error in Eqn. (26) of Ref. [46] in the coefficients of the off diagonal terms. This error causes the contribution to the coefficients of the annihilation and creation operators for the ±1 modes to be neglected.

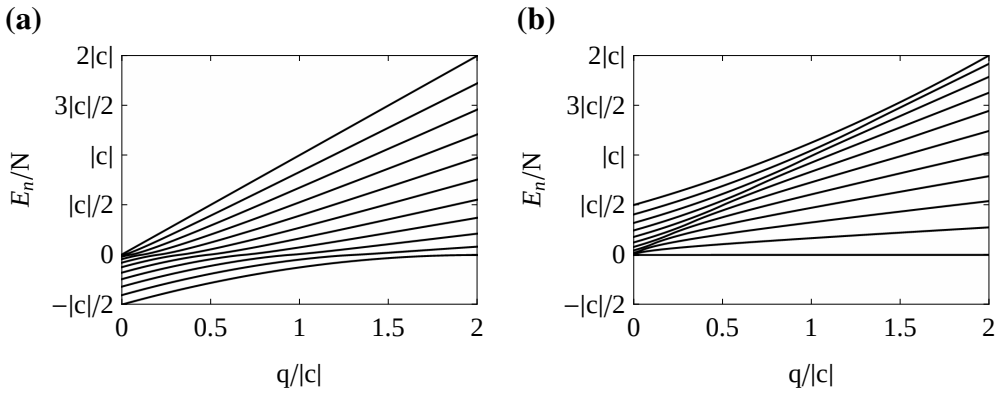

Figure 3.3: Plot of the eigenspectrum normalized to N versus the quadratic Zeeman energy for **(a)** a ferromagnetic condensate and **(b)** an anti-ferromagnetic condensate. This plot is for 1000 atoms with every fiftieth eigenvalue of 501 shown.

3.1.8 Mean-Field Equations with a Finite Magnetic Field

For the mean-field equations the magnetic field is simple to add to the dynamical equations (Eq. (3.14)). This gives

$$i\hbar\dot{\zeta}_1 = E_1\zeta_1 + c[(\rho_1 + \rho_0 - \rho_{-1})\zeta_1 + \zeta_0^2\zeta_{-1}^*] \tag{3.24a}$$

$$i\hbar\dot{\zeta}_0 = E_0\zeta_0 + c[(\rho_1 + \rho_{-1})\zeta_0 + 2\zeta_1\zeta_{-1}\zeta_0^*] \tag{3.24b}$$

$$i\hbar\dot{\zeta}_{-1} = E_{-1}\zeta_{-1} + c[(\rho_{-1} + \rho_0 - \rho_1)\zeta_{-1} + \zeta_0^2\zeta_1^*]. \tag{3.24c}$$

Making the same parameterization and change of variables as before, the simplified equations are

$$\dot{\rho}_0 = \frac{2c}{\hbar}\rho_0\sqrt{(1-\rho_0)^2 - m^2}\sin\theta_s \tag{3.25a}$$

$$\dot{\theta}_s = -\frac{2q}{\hbar} + \frac{2c}{\hbar}\left[(1-2\rho_0) + \frac{(1-\rho_0)(1-2\rho_0) - m^2}{\sqrt{(1-\rho_0)^2 - m^2}}\cos\theta_s\right]. \tag{3.25b}$$

The energy functional is now

$$\mathcal{E} = \frac{c}{2}m^2 + c\rho_0\left[(1-\rho_0) + \sqrt{(1-\rho_0)^2 - m^2}\cos\theta_s\right] + pm + q(1-\rho_0). \tag{3.26}$$

Because of the extra complexity, only the phase space with $m = 0$ is analyzed. Figure 3.4 shows the $m = 0$ slice of the spinor energy contours for several values of magnetic field

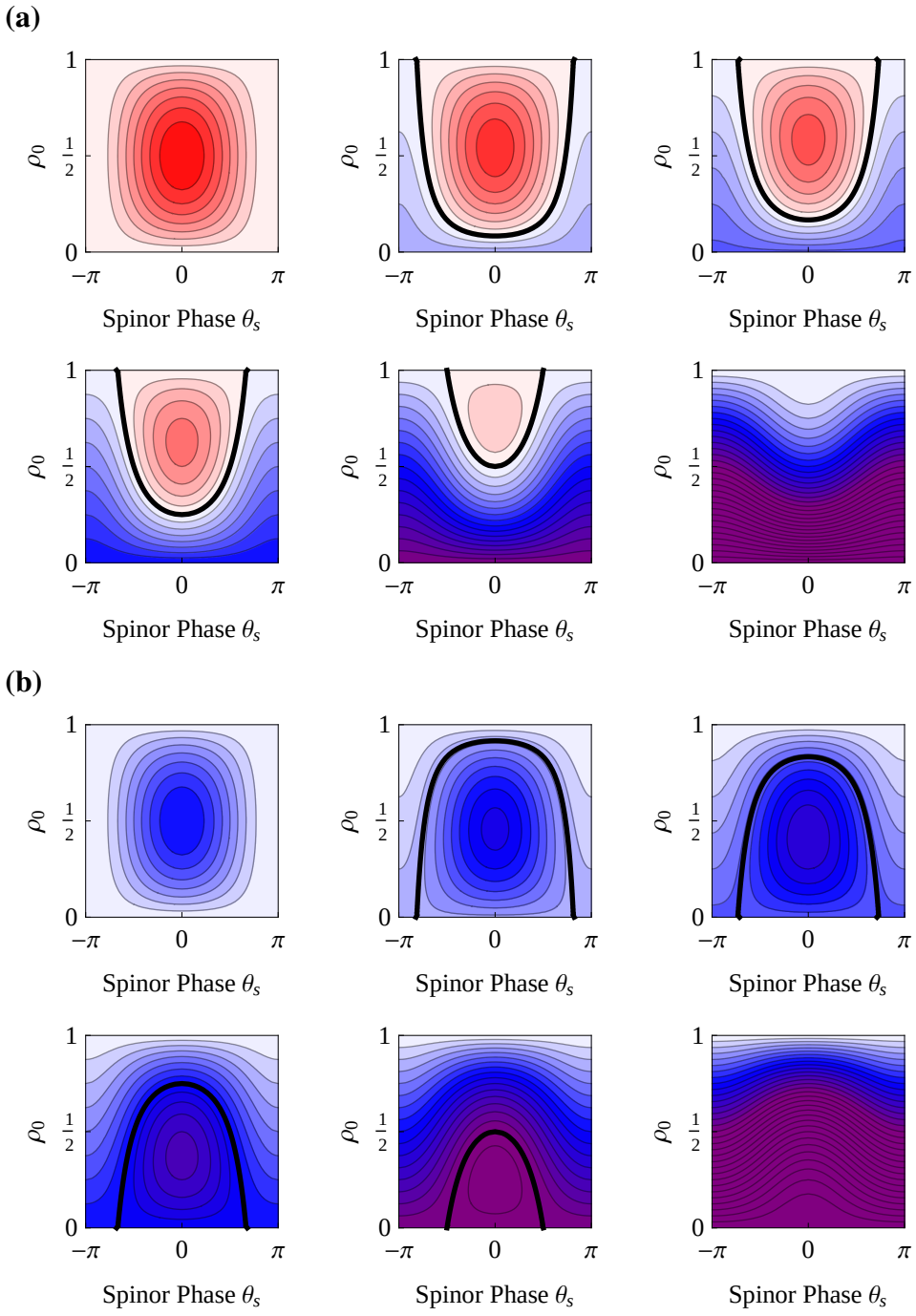

Figure 3.4: Mean-field energy contours for no and finite magnetic field for **(a)** a ferromagnetic condensate and **(b)** an anti-ferromagnetic condensate. Magnetic field energy q is 0, $|c|/6$, and $|c|/3$ in the top row and $|c|/2$, $|c|$, and $2|c|$ in the bottom row of each.

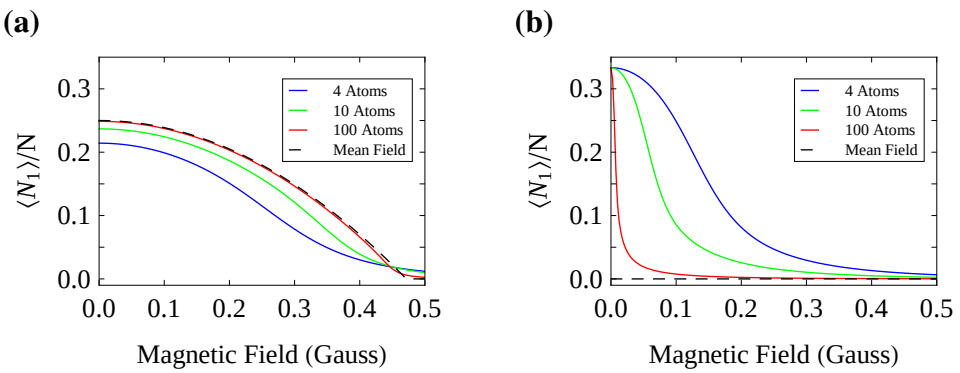

Figure 3.5: Plot of the expectation value of ρ_1 of the spinor ground state in the mean-field and Fock calculation for the indicated atom numbers as a function of magnetic field for a spinor energy of **(a)** $-2\pi\hbar \times 8$ Hz for the ferromagnet and **(a)** $2\pi\hbar \times 8$ Hz for the anti-ferromagnet. The quadratic Zeeman energy per atom of $2\pi\hbar \times 72$ Hz/G^2 for ^{87}Rb is used for both.

energy for both a ferromagnetic condensate and an anti-ferromagnetic condensate. For zero magnetic field the energy contours are identical with the border being zero energy, but differ in that the inner region is lower energy (red) for a ferromagnetic condensate and higher energy (blue) for an anti-ferromagnetic condensate. Dynamical evolution follows the energy contours and oscillate around the central point. As the magnetic field is increased, both ferromagnetic and anti-ferromagnetic phase spaces split into two regions; one with dynamical solutions the spinor phase oscillates about zero and one where the spinor phase winds around the phase space. These will be called oscillating solutions and phase-winding solutions. In both cases the fractional population of $m_f = 0$ oscillates up and down. Separating these two types of dynamical solutions is an energy contour with infinite period [42], known as the separatrix. For the ferromagnetic condensate the separatrix always occurs at the $\mathcal{E} = 0$ energy contour. For the anti-ferromagnetic condensate the separatrix occurs along the contour defined by $\mathcal{E} = c$. As the field increases further, the solution at the middle of the contours, which is the ground state for the ferromagnetic condensate, moves towards $\rho_0 = 1$ for the ferromagnet and $\rho_0 = 0$ for the anti-ferromagnet. When $q = 2|c|$

the oscillatory solutions no longer exist for either the ferromagnetic condensate or the anti-ferromagnetic condensate.

The indeterminacy of the mean-field anti-ferromagnetic ground state discussed in Section 3.1.4 disappears for any finite magnetic field. For $c > 0$ the ground state is always $\rho_0 = 1$ which is the polar state with $m_f = 0$. For the ferromagnetic ground state we have the relationship $\rho_0 = \frac{1}{2} - \frac{q}{4c}$ which is valid up to $q = 2|c|$. Above this value we are once again left with the polar state $\rho_0 = 1$ as the ground state. Figure 3.5 compares these mean-field ground states to the quantum ground states in terms of the expectation value of the $m_f = 1$ population of the ground state as a function of magnetic field. These values are obtained by diagonalizing Eq. (3.23) and calculating the expectation value of the number of pairs for the lowest energy eigenstate. For the ferromagnetic condensate, the quantum calculation smooths out the abrupt transition at $q = 2|c|$. Also the expectation value at zero field is somewhat below the mean-field value, but this is expected for the angular momentum state. For the anti-ferromagnetic condensate, the zero field ground state is the angular momentum state, but this quickly goes to the polar state in a magnetic field even with very few atoms. This plot shows that the quantum expectation values converge to the mean field calculations as the number of atoms increases and for as few as 100 atoms, the mean field solution closely approximates the quantum solution.

3.2 Dynamical Simulations

The equations developed in the sections above provide the tools to simulate the experiment and make qualitative and quantitative predictions. In this section, details of the dynamical simulations will be discussed. The simulations will be used to make several qualitative predictions of population dynamics and illustrate some basic characteristics of spin-mixing in a finite magnetic field. The primary focus will be for the starting state of $m_f = 0$, the starting state primarily used in our experiment and whose evolution is predicted to generate squeezing. The simulations described in this section will be used again in the next chapter

to illustrate spin-nematic squeezing.

3.2.1 Quantum Dynamical Simulations

To simulate the dynamics of the system, a ferromagnetic condensate starting in $m_f = 0$ in a finite magnetic field will be used. The quantum Hamiltonian in the pairs basis given in Eq. (3.23) could simply be diagonalized finding the eigenenergies and eigenvectors and come up with an exact solution [50, 51]. However this approach becomes impractical for large atom numbers. An advantage of this form of the Hamiltonian is that it is simple to numerically integrate the Schrödinger equation for the initial state using the tridiagonal matrix without ever solving the exact eigenvalue problem. Numerical integration also allows simulation of a time varying magnetic field, such as the ramp used in the experiment.

For the simulation the state ψ is represented as a vector of the complex coefficients of the Fock states starting with the coefficient for $\psi_0 = 1$ and all others zero to represent the initial $m_f = 0$ state. Evolution is accomplished by numerical integration of the Schrödinger equation using Eq. (3.23) for $\tilde{H}$

$$\dot{\psi}(t) = -\frac{i}{\hbar}\tilde{H}\cdot\psi(t) \tag{3.27a}$$

$$\begin{pmatrix} \dot{\psi}_0 \\ \vdots \\ \dot{\psi}_k \\ \vdots \\ \dot{\psi}_{k_{max}} \end{pmatrix} = -\frac{i}{\hbar}\begin{pmatrix} \tilde{H}_{00}\cdot\psi_0 + \tilde{H}_{01}\cdot\psi_1 \\ \vdots \\ \tilde{H}_{k(k-1)}\cdot\psi_{k-1} + \tilde{H}_{kk}\cdot\psi_k + \tilde{H}_{k(k+1)}\cdot\psi_{k+1} \\ \vdots \\ \tilde{H}_{k_{max}(k_{max}-1)}\cdot\psi_{k_{max}-1} + \tilde{H}_{k_{max}k_{max}}\cdot\psi_{k_{max}} \end{pmatrix} \tag{3.27b}$$

$$\psi(t+\Delta t) = \psi(t) + \Delta t\cdot\dot{\psi}(t) \tag{3.27c}$$

This is iterated as many times as needed to get the desired evolution time. The Δt is chosen sufficiently small such that several iterations occur for a cycle of the highest eigenfrequency in order to prevent aliasing. This set of equations is simply numerical integration using Newton's method. Our actual simulation code takes the numerical integration further and

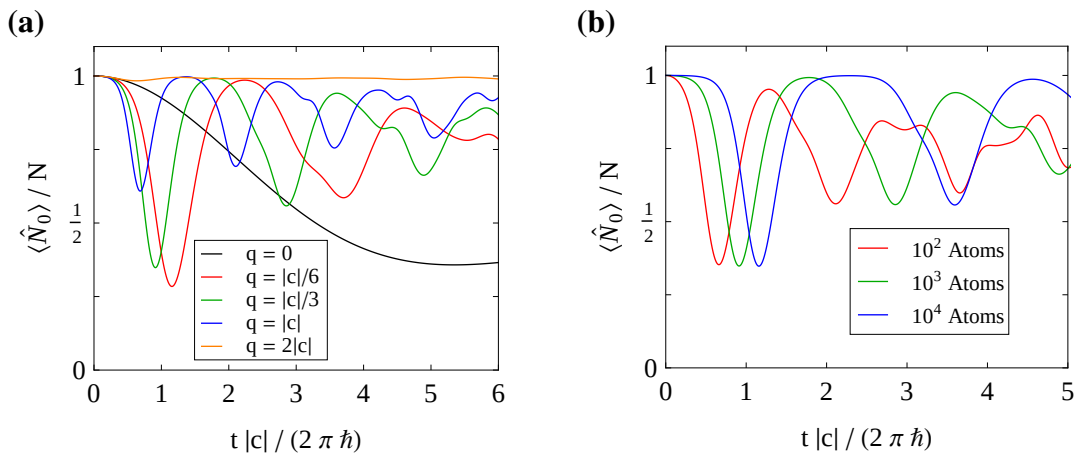

Figure 3.6: Time evolution of n_0 from the quantum simulation for several conditions. **(a)** Simulation with 10^3 atoms for $q = 0$, $q = |c|/6$, $q = |c|/3$, $q = |c|$, and $q = 2|c|$. **(b)** Simulation with $q = |c|/3$ for 10^2, 10^3, and 10^4 atoms.

uses a fourth order Runge-Kutta numerical integration algorithm. The size of the vector scales with N while the Hamiltonian matrix scales with N^2. However the number of non-zero matrix elements also scales with N because the matrix is tridiagonal. This greatly simplifies the numerical integration because it is only necessary to evaluate the non-zero matrix elements. A sample of the simulation code is provided in Appendix C.

Figure 3.6 shows the results of these simulations for several conditions. Time and magnetic field are scaled by the mean-field spinor dynamical rate. In part (a) the dynamical evolution of 1000 atoms is shown for several different magnetic fields. The black line is the same zero field dynamics from Figure 3.1. Even for the relatively small field of $q = |c|/6$, which for $c = -2\pi\hbar \times 8$ Hz and $q = 2\pi\hbar \times 72$ Hz/G^2 is 136 mG, a major change is seen in the dynamics. Initially the population evolves slowly like the zero field case. However at approximately $t|c|/(2\pi\hbar) = 1/2$ rapid population dynamics begin with one oscillation followed by seemingly damped oscillations. For larger magnetic fields, the beginning of the oscillation occurs sooner, but the depth is reduced until at $q = 2|c|$ (orange line in Figure 3.6(a)) there is almost no population dynamics. This is the magnetic field determined earlier where the mean-field separatrix moves up until there are no more oscillating

solutions, only phase winding solutions. In part (b) the dynamics of 10^2, 10^3, and 10^4 atoms are compared for the same $q = |c|/3$. These all have the signature of an initial pause, followed by a quick oscillation leading to apparently damped oscillations. The length of the initial pause is related to the number of atoms and the location of the first minimum of ρ_0 appears to vary approximately as $\log N$. As the number of atoms increases the damping appears less. For 10^4 atoms, after the first quick oscillation, there is another lengthy pause.

In Section 3.1.3 we noted that the quantum calculation for $q = 0$ predicted a time for the first minimum of $m_f = 0$ much longer than the experimental value in Ref. [15]. The simulation predicts for a finite magnetic field the time varies as $\log N$, but varies as $\sqrt{N}$ for no field. So the timing of the initial minimum compared to measurements will be reanalyzed. Note in Figure 3.6(a) that for 10^3 atoms and the experimental value of $q = |c|/6$ that the minimum time changes by a factor of five. Scaling the number of atoms to the experimental value of 30000 using the $\sqrt{N}$ relationship for no field the expected factor is now ~ 18 which is roughly the disparity factor calculated earlier. So the time scale disparity is explained by a finite magnetic field.

3.2.2 Mean-Field Dynamical Simulations

The quantum dynamical simulations provide moments of measurables such as the mean and standard deviation, but lack the intuitive phase space given by mean-field dynamics. The mean-field approach is also simpler in terms of scaling with atom number and operations such as RF rotations. Of course the mean-field solutions as presented cannot capture uniquely quantum features, namely fluctuations and evolution from classically meta-stable states. Even with the addition of a finite magnetic field, all atoms in $m_f = 0$ is still a meta-stable state. Points arbitrarily close to the $m_f = 0$ state do evolve, though the periods are longer the closer to this state the initial state is chosen to be.

The mean-field equations are non-linear equations for classical fields which have no distribution. However the initial state for the quantum simulation was a Fock state. This

Fock state can be represented by a distribution of classical field states. So to borrow a technique used in quantum optics, a distribution of states is used with the classical evolution of the mean-field dynamical equations performed on each one [97]. In the relationships of the SU(3) group structure, we can find the approximate quasi-probability distribution to represent the initial state.

3.2.3 Quasi-Probability Distribution

We use the commutator table of the su(3) operators the dipole-quadrupole basis (Table 3.3) to find the quantum fluctuations of the initial state. Commutators of these operators have the same structure as the three dimensional isotropic harmonic oscillator in Heisenberg form. From the table it can be seen that the commutator of two spin moments or of two nematic moments is a spin moment. The commutator of a spin moment with a nematic moment is another nematic moment. There are seven triples of operators where the commutation of two of them is the third up to constant factors. These correspond to seven SU(2) subgroups of the SU(3) Lie group.[6] A useful property of the subgroups is that they are closed (combinations of subgroup elements will produce another element within the same subgroup) and so operations on the subspace consisting of exponentiations of the basis elements of that subspace's Lie algebra will appear as rotations within that subspace.

These commutators enable the analysis of the fluctuations about the initial $m_f = 0$ state. The generalized uncertainty relations, $\langle(\Delta\hat{A})^2\rangle\langle(\Delta\hat{B})^2\rangle \geq \frac{1}{4}|\langle[\hat{A},\hat{B}]\rangle|^2$, give the product of the variances of the operators $\hat{A}$ and $\hat{B}$. Looking through Table 3.3, there are only two pairs of operators where the commutator has a non-zero expectation value for their commutator. These are $\langle 0,N,0|[L_x,N_{yz}]|0,N,0\rangle = -2iN$ and $\langle 0,N,0|[L_y,N_{xz}]|0,N,0\rangle = 2iN$ and therefore there are the relationships $\langle(\Delta\hat{L}_x)^2\rangle\langle(\Delta\hat{N}_{yz})^2\rangle \geq N^2$ and $\langle(\Delta\hat{L}_y)^2\rangle\langle(\Delta\hat{N}_{xz})^2\rangle \geq N^2$. The initial state is uncorrelated and therefore the variance is split equally between each operator in the pair. The expectation values of L_x, L_y, N_{yz}, and N_{xz} are all zero for the

[6] These seven subspaces are not unique. There are infinitely many ways to do this decomposition, this one merely corresponds to the commutators of the Cartesian dipole-quadrapole basis.

Table 3.3: Commutators of the dipole-quadrapole basis. The seven triple operator combinations of this table are used to define SU(2) subspaces: $\{L_x, L_y, L_z\}$, $\{N_{xz}, N_{yz}, L_z\}$, $\{L_x, N_{yz}, (N_{zz} - N_{yy})\}$, $\{L_x, N_{xz}, N_{xy}\}$, $\{L_y, N_{xz}, (N_{xx} - N_{zz})\}$, $\{L_y, N_{yz}, N_{xy}\}$, and $\{L_z, N_{xy}, (N_{yy} - N_{xx})\}$. These SU(2) projections can be used to illustrate the SU(3) space on multiple Bloch spheres.

$[\downarrow, \rightarrow]$	L_y	L_z	N_{yz}	N_{xz}	N_{xy}	N_{xx}	N_{yy}	N_{zz}
L_x	iL_z	$-iL_y$	$i(N_{zz} - N_{yy})$	$-iN_{xy}$	iN_{xz}	0	$2iN_{yz}$	$-2iN_{yz}$
L_y		iL_x	iN_{xy}	$i(N_{xx} - N_{zz})$	$-iN_{yz}$	$-2iN_{xz}$	0	$2iN_{xz}$
L_z			$-iN_{xz}$	iN_{yz}	$i(N_{yy} - N_{xx})$	$2iN_{xy}$	$-2iN_{xy}$	0
N_{yz}				$-iL_z$	iL_y	0	$-2iL_x$	$2iL_x$
N_{xz}					$-iL_x$	$2iL_y$	0	$-2iL_y$
N_{xy}						$-2iL_z$	$2iL_z$	0
N_{xx}							0	0
N_{yy}								0

$m_f = 0$ state. These commutation relationships show how to represent the $|0, N, 0\rangle$ Fock state semi-classically as a normal distribution in L_x, L_y, N_{yz}, and N_{xz} each with a mean value 0 and a variance N. These are used to generate a quasi-probability distribution (QPD) of the classical field variables, ρ_0, m, χ_+, and χ_-, needed for semi-classical simulations. Using $\psi = \left(\sqrt{\rho_1}e^{i\chi_+}, \sqrt{\rho_0}, \sqrt{\rho_{-1}}e^{i\chi_-}\right)^T$ and the matrix form of the operators (Table 3.1 and Table 3.2), the expectation values in terms of these classical field variables are given by:

$$\begin{aligned}
\langle L_x \rangle &= \sqrt{2\rho_0\rho_1}\cos\chi_+ + \sqrt{2\rho_0\rho_{-1}}\cos\chi_- \\
\left\langle N_{yz} \right\rangle &= -\sqrt{2\rho_0\rho_1}\sin\chi_+ - \sqrt{2\rho_0\rho_{-1}}\sin\chi_- \\
\left\langle L_y \right\rangle &= -\sqrt{2\rho_0\rho_1}\sin\chi_+ + \sqrt{2\rho_0\rho_{-1}}\sin\chi_- \\
\langle N_{xz} \rangle &= \sqrt{2\rho_0\rho_1}\cos\chi_+ - \sqrt{2\rho_0\rho_{-1}}\cos\chi_-.
\end{aligned} \tag{3.28}$$

These equations can be inverted to give the values for the vector order parameter from an uncorrelated distribution of L_x, L_y, N_{yz}, and N_{xz}.

$$\begin{aligned}
\tan\chi_+ &= -\frac{L_y + N_{yz}}{L_x + N_{xz}} \\
\tan\chi_- &= \frac{L_y - N_{yz}}{L_x - N_{xz}} \\
\rho_0 &= \frac{1}{2} + \sqrt{\frac{1}{4} - \frac{1}{8}\left(\left(\frac{L_x + N_{xz}}{\cos\chi_+}\right)^2 + \left(\frac{L_x - N_{xz}}{\cos\chi_-}\right)^2\right)} \\
m &= \frac{1}{8\rho_0}\left(\left(\frac{L_x + N_{xz}}{\cos\chi_+}\right)^2 - \left(\frac{L_x - N_{xz}}{\cos\chi_-}\right)^2\right)
\end{aligned} \tag{3.29}$$

The results of this are shown in Figure 3.7 for a Fock state $|0, 45000, 0\rangle$. Looking just at the distribution of ρ_0 in part (a) it appears similar to a half normal distribution multiplied by a linear function that goes to zero at N. In (b) the distribution for m is shown. It appears as a spike which resembles a Laplace distribution function. The distributions for χ_+ and χ_- are not shown since they are both completely random on their range. The appearance of the distributions for ρ_0 and m are explained by looking at their two dimensional distribution (Figure 3.7(c)). The result is a half-normal distribution in ρ_0 but filling every physical value of χ_+, χ_-, and m. The physical values of m are constrained such that $|m| \leq 1 - \rho_0$ leading

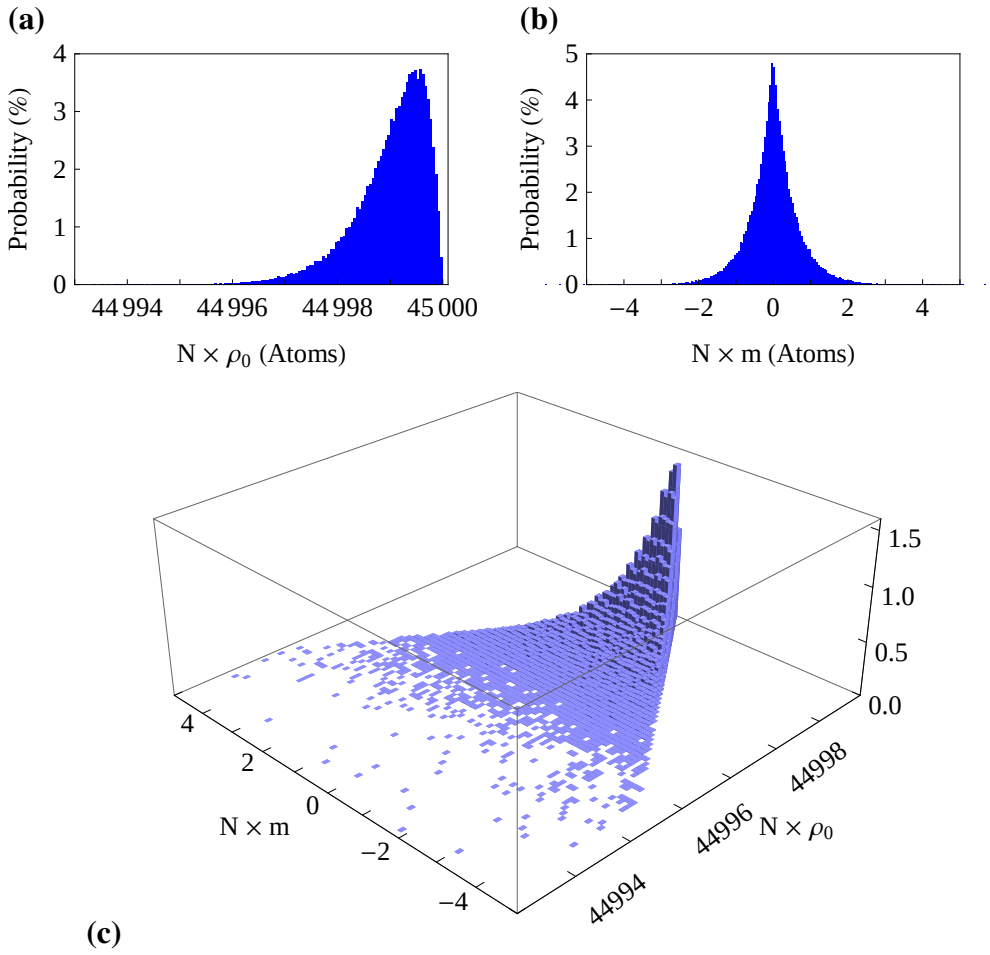

Figure 3.7: Distributions of ρ_0 and m for $m_f = 0$ with 45000 atoms.

to its pointed and narrow distribution about zero. The ρ_0 distribution always represents a mean $\bar{N}_0 = N - 1$ with a standard deviation of $1/\sqrt{2}$ atoms. The m distribution always has a mean of zero with a standard deviation of $1/\sqrt{2}$ atoms.

3.2.4 Semi-Classical Evolution and Dispersion

The QPD for the initial $m_f = 0$ state shown in Figure 3.7 is used to perform semi-classical simulations. An ensemble of initial states distributed according to the QPD is created each consisting of the three complex numbers, ζ_i, of the order parameter. These states are numerically integrating using the mean-field dynamical equations (Eq. (3.24)) for each state of the ensemble. In order to find the evolution of the parameters at a given point in the

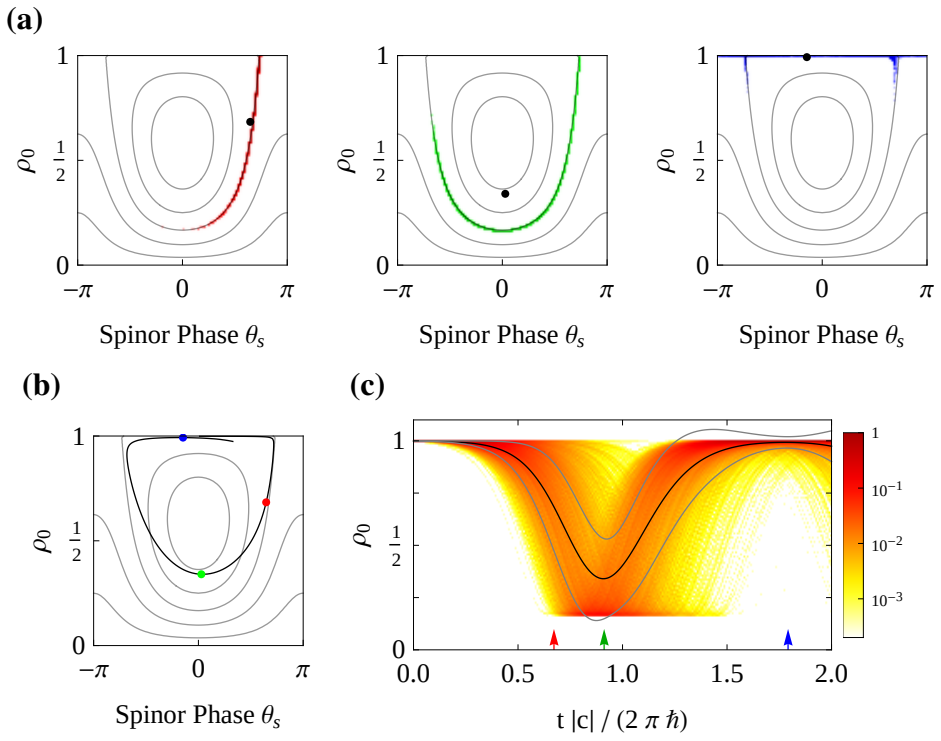

Figure 3.8: Mean field dynamics using a Quasi-Probability Distribution. **a.** Plots of the mean field phase space with the QPD evolution at different times with the mean value shown as a black dot. **b.** Plot of the evolution of the mean value with colored dots corresponding to the mean values in part (**a**). **c.** Time plot of the evolution of the probability density of ρ_0. The mean is shown in black with the mean plus and minus the standard deviation in gray. The times for of the phase space distributions is shown with an arrow in corresponding color.

evolution, the matrix form of the operators is used to take the expectation values[7] for each state of the ensemble. From these values, it is straightforward to calculate the mean, the standard deviation, or a histogram of the ensemble. For these simulations, a fourth order Runge-Kutta algorithm is used for the numerical integration. A sample of the simulation code which also calculates the quasi-probability distribution is provided in Appendix C.

An example simulation is shown in Figure 3.8. Here a simulation is done for 1000 atoms starting in $m_f = 0$ state. The spinor energy is $c = -2\pi\hbar \times 8$ Hz and the magnetic field energy is $q = |c|/3$. An ensemble of 1000 states is produced according to the formulation

[7]For example, $\langle L_x \rangle = (\zeta_1^*, \zeta_0^*, \zeta_{-1}^*) \cdot L_x \cdot (\zeta_1, \zeta_0, \zeta_{-1})^T$.

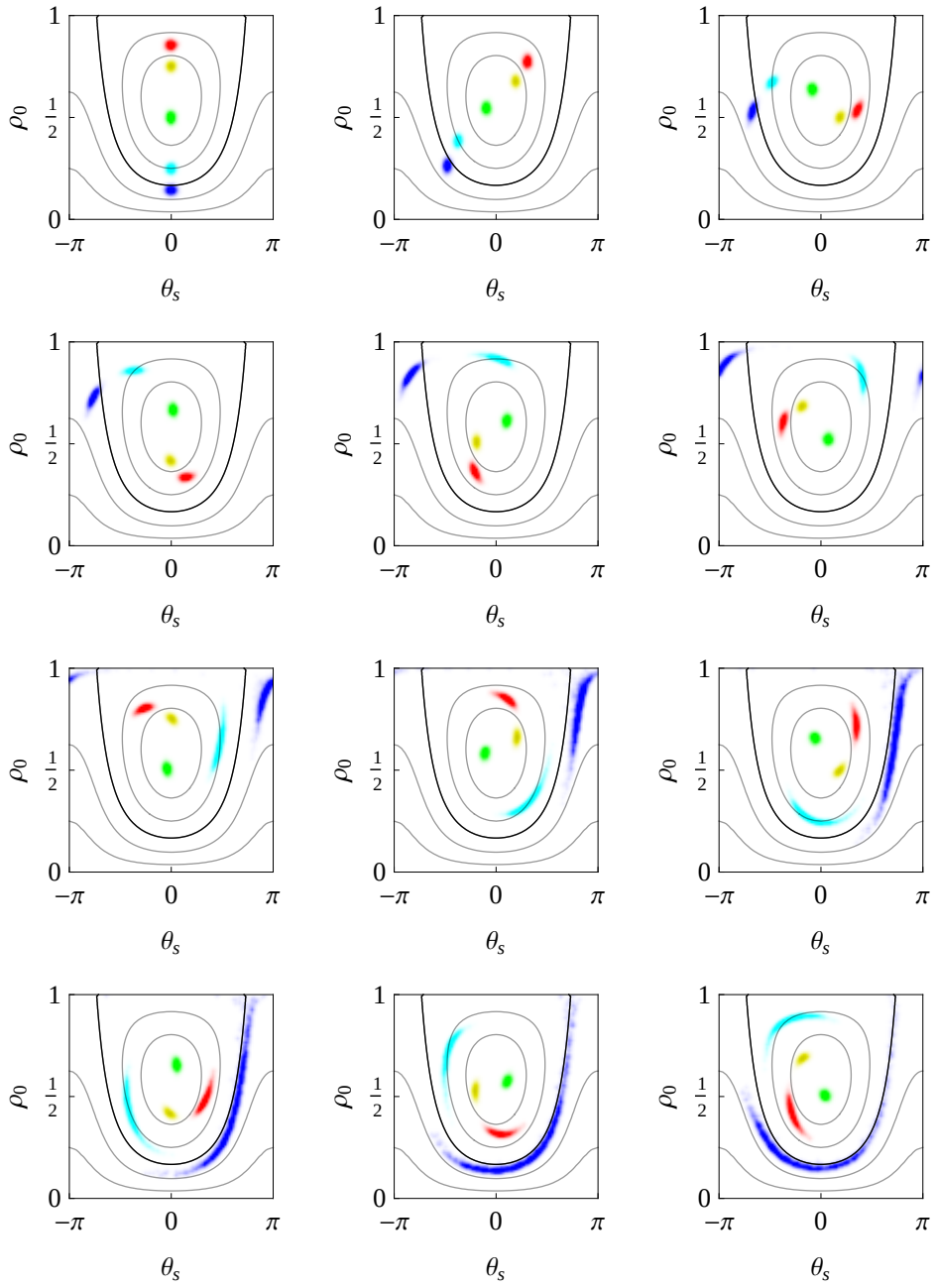

Figure 3.9: Dispersion across the energy contours for several initial state preparations of 1000 atoms.

in the previous section and this ensemble is evolved. In part (a) the distribution in the phase space of the ρ_0 and θ_s is shown for three different evolution times. Initially the distribution in ρ_0 is tightly packed at the top of the phase space with random spinor phase (not shown). As evolution proceeds, the phase converges towards the separatrix, and the population starts to evolve along it seen in the first panel (red). In the second panel (green) the state wraps around the phase space, dispersed along the separatrix. In the final panel (blue), the majority of the distribution has returned to the top of the phase space near $\rho_0 = 1$. The states disperse due to the different evolution rates of nearby energy contours. The mean is shown as a black dot in each panel. In part (b) the mean trajectory is plotted. While each state of the ensemble travels along its starting energy contour, the mean does not. In part (c) the evolution of the expectation value and standard deviation of ρ_0 is shown with the times of the distributions in part (a) marked by arrows. The mean is shown as a black line and the mean plus and minus the standard deviation is shown as gray lines. These agree quantitatively with the quantum dynamical simulation. These calculations provide an amazing insight into the evolution of the system. It is clear that simply measuring the mean value and the variance of the system is only the coarsest view of the dynamics and not sufficient to capture the highly non-Gaussian nature of the evolved states. Exploration of these population distributions generated by the dynamics is grounds for future work.

Figure 3.8 is an extreme example of dispersion since the starting state is right on the separatrix which has infinite period of oscillation, and the period falls off rapidly for nearby contours. In Figure 3.9, the evolution is shown for different initial states that are not meta-stable to better illustrate the importance of dispersion even for these states. This plot is for the same values of c and q and thus energy contours (the separatrix here is highlighted as the black contour) as Figure 3.8. The initial states are prepared by an RF rotation of an $m_f = 0$ condensate followed by a spinor phase shift of $-\pi$. The results are initial states with mean values of the spinor phase being zero and ρ_0 of 0.85 (red), 0.75 (yellow), 0.5 (green), 0.25 (cyan) and 0.15 (blue). The apparent disparity in their shapes at the initial time is

due to this plot being essentially a Mercator projection from one hemisphere which will be seen in the next chapter when this space is mapped onto a Bloch sphere representation. They are all minimum uncertainty states with equal quadrature variances. Time advances left to right, top to bottom until in the last plot the slowest oscillation (blue) has completed approximately one period. The fastest (green) completes approximately two oscillations in the time. The green ensemble is near the ferromagnetic spinor ground state where the oscillation periods are all nearly the same at $1/(2|c|)$ and retains its shape. Next further out in energy contours are the yellow, red, and cyan ensembles which clearly show more and more dispersion as they get farther from the spinor ground state and more towards the separatrix. Finally the blue ensemble is nearest the separatrix and has considerable dispersion. It is also centered on the other side of the separatrix from the other four ensembles and thus executes phase winding trajectories. From this figure it is seen that dispersion clearly has an effect on the noise statistics of the evolution.

The source of the dispersion is that different energy contours have different periods of oscillation [42]. This is shown in Figure 3.10 as a function of the spinor energy contour for values of magnetic field from $q = 0$ to $q = 2|c|$. For the ferromagnetic case analyzed here, the separatrix is the zero energy contour where the periods rise rapidly to infinity. The ground state (lower edge in Figure 3.10) has a period of $1/(2|c|)$ while the $\rho_0 = 0$ state (upper edge) approaches a period of $1/(2q)$ for large magnetic fields. This plot has the same boundaries as Figure 3.3(a) where the separatrix is visible as the kink in eigenspectrum. The quasi-probability distribution samples many different nearby mean-field spinor energy contours. A given state evolves along its contour, but different contours have different periods of oscillation with the separatrix having an infinite period. When taking statistics across the ensemble of states, this smears out the initial state increasing the noise while damping the mean dynamics. The apparent dissipation is adequately described by the dispersion across energy contours. States close to the ground state have less dispersion than states close to the separatrix, such as the $m_f = 0$ state which straddles the separatrix.

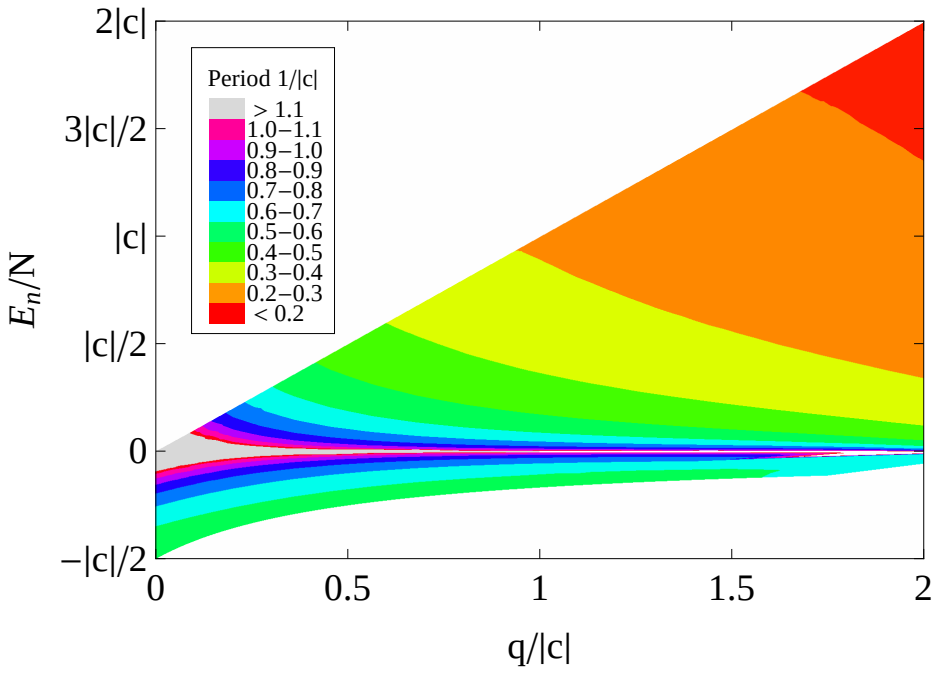

Figure 3.10: Period of mean field spinor orbit versus spinor energy.

3.3 Convergence of the Mean Field and Quantum Approaches

In Figure 3.11, a comparison of the quantum and the mean-field with QPD dynamical simulations is shown. The simulations are for experimental parameters of 45000 atoms starting in $m_f = 0$ at a field of 2 G. At time zero the system is quenched by ramping the magnetic field with a decay constant, $\tau_B = 1$ ms, that matches the experimentally measured value. The final field is 210 mG, and the spinor dynamical rate is $c = -2\pi\hbar \times 7.5$ Hz. The mean value of ρ_0 shown as a blue line with the shaded region being the mean plus and minus the standard deviation. The difference in results between the two simulations is $< 0.5\%$ in the mean and $< 1\%$ in the standard deviation over the entire time of the simulation. The primary reason for this deviation is the finite number of samples in the ensemble (5000) used for the semi-classical simulation.

The dynamical simulation techniques developed in this chapter provide the tools needed for the analysis and simulation of spin-nematic squeezing. The quantum techniques are merely a review of the extensive literature on the topic. The semi-classical mean-field

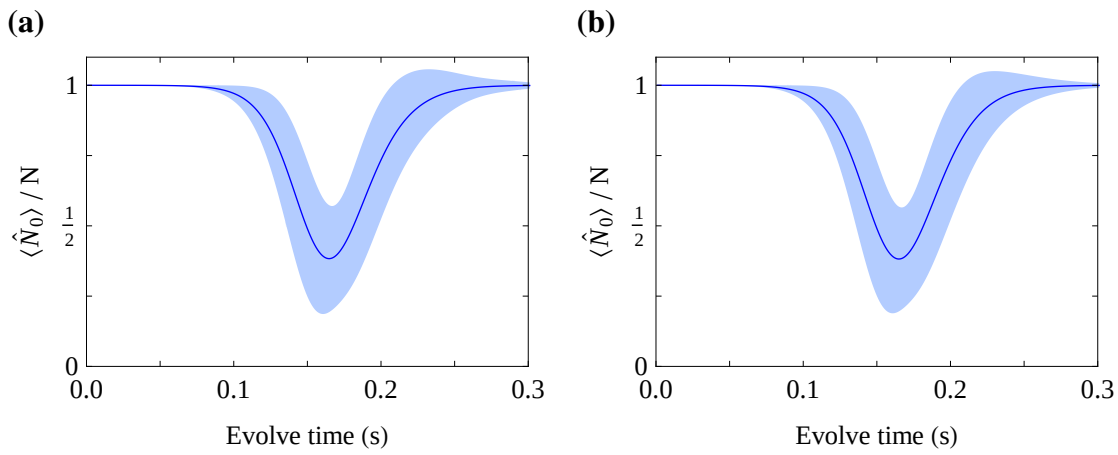

Figure 3.11: Comparison of the theoretical mean and standard deviation of ρ_0 for the semi-classical mean field (**a**) and quantum simulations (**b**).

technique is also largely a review, but with the addition of a quasi-probability distribution determined by the commutation relations of the su(3) Lie algebra of the spin-1 system. This semi-classical approach is validated by comparison to the exact quantum technique. These tools will be used in later chapters to visually represent the spin-1 phase space, predict and visualize spin-nematic squeezing, and make quantitative predictions for population dynamics and squeezing parameters.

CHAPTER IV

THEORY OF SQUEEZING IN A SPIN-1 BOSE-EINSTEIN CONDENSATE

Entanglement and squeezing are hallmarks of a quantum system and its evolution that are fundamentally non-classical. They allow overcoming of the classical limits for quantum metrology and quantum computation [127]. Squeezing in optical modes can be generated by the squeezing of vacuum, parametric amplification, and four-wave mixing (FWM). Squeezed light for each mode is described on the complex plane spanning two quadrature amplitudes with U(1) symmetry. Spin-squeezing is typically considered on two-level atomic systems with SU(2) symmetry. Spin-squeezing has been generated using interactions with squeezed light [85], repeated Quantum Non-Demolition measurements [86, 87], light in cavity modes [88, 89], and by collisional interactions in a BEC [70, 71]. Both squeezed light and spin-squeezing are well understood theoretically [94, 97, 127] and have many experimental demonstrations. We begin by reviewing squeezing in a single optical mode and the spin-$\frac{1}{2}$ system in order to introduce some concepts. These systems can exhibit quadrature squeezing of a single optical mode and spin-squeezing in the spin-$\frac{1}{2}$ system.

We will next consider squeezing in the spin-1 system. Spin-mixing in a spin-1 system has been predicted to generate squeezing as has been discussed by several authors [105–107]. Operators from the spin-mixing Hamiltonian such as L_x^2 and L_y^2 are well known to generate squeezing in a spin-$\frac{1}{2}$ system through twisting of an axis in the SU(2) phase space consisting of three spin moments [94]. However, generalizing this to a spin-1 system with SU(3) symmetry is not trivial [106]. Squeezing in spin-1 systems has been studied from the perspective of multi-mode squeezing [105], in terms of the Gell-Mann (quark) framework of the SU(3) algebra [106], and in terms of dipole-quadrupole measurables [107]. Although

in each study appropriate phase spaces for squeezing were identified, it is fair to say that a comprehensive picture remains to be developed. Additionally, it is necessary to develop new intuitions for squeezing in higher spin particles. For example, the squeezing generated by spin-mixing from $m_f = 0$ is not developed in the spin space along any direction, but rather in a joint spin-nematic space. We will discuss squeezing in the spin-1 system in terms of a dipole-quadrupole basis of the su(3) Lie algebra in order to provide a comprehensive picture and develop intuition for the phase space. We will also discuss squeezing of the spin-1 system from the perspective of four-wave mixing as a comparison.

Finally we will use simulations based on the previous chapter to demonstrate spin-nematic squeezing for spin-mixing of a ferromagnetic condensate from $m_f = 0$. For a visual representation of the simulations, multiple subspaces of SU(3), each with SU(2) symmetry, are represented simultaneously on corresponding Bloch spheres. How spin-mixing affects the phase space and the time evolution of the squeezing parameters is explored through the simulations. A brief analysis of spin-nematic squeezing in an anti-ferromagnetic condensate is also presented.

4.1 Squeezing in a Single Optical Mode

Early work in squeezing focused on quantum optics systems. The simplest form of squeezing in quantum optics is that of a single optical mode. In classical electromagnetic theory the field is represented by the complex Fourier amplitude of the spectral mode. This is quantized for a mode k using the bosonic mode operators $\hat{a}_k$ and $\hat{a}_k^\dagger$ which are the annihilation and creation operators for the quanta of the mode (photons). These operators make up the Lie algebra u(1) and the field is described by its corresponding Lie group U(1). These have the standard bosonic commutation relationship $\left[\hat{a}_k, \hat{a}_{k'}^\dagger\right] = \delta_{kk'}$ and the number of quanta in the mode is given by $\hat{N}_k = \hat{a}_k^\dagger \hat{a}_k$.

The bosonic mode operators can be combined into two field quadrature operators that describe the real and imaginary parts of the electric field amplitude of a mode [97]. Ignoring

overall constants these quadratures and their commutator are given by

$$\begin{aligned} \hat{X}_1 &= \left(\hat{a} + \hat{a}^\dagger\right) \\ \hat{X}_2 &= -i\left(\hat{a} - \hat{a}^\dagger\right) \\ \left[\hat{X}_1, \hat{X}_2\right] &= 2i. \end{aligned} \tag{4.1}$$

These quadrature operators have the same form as the position and momentum operators of the simple harmonic oscillator. From the generalized uncertainty principle

$$\langle(\Delta\hat{A})^2\rangle\langle(\Delta\hat{B})^2\rangle \geq \frac{1}{4}|\langle[\hat{A}, \hat{B}]\rangle|^2, \tag{4.2}$$

therefore the uncertainty relationship of the mode is given by

$$(\Delta\hat{X}_1)^2(\Delta\hat{X}_2)^2 \geq 1. \tag{4.3}$$

We consider three important types of states, the Fock state, the coherent state, and the squeezed state. Fock states are simply the eigenstates of the number operator. They have a sharp amplitude, but are completely random in phase. Coherent states are eigenstates of the annihilation operator. These are the states that most closely approximate the classical amplitude while still satisfying the uncertainty principle. Where the classical field is represented by a single complex number defining a definite field amplitude and phase, the coherent state corresponds to a distribution with minimum uncertainty about this classical point. The coherent state has the uncertainty equally distributed in each quadrature, so each has a variance of 1, which is the standard quantum limit (SQL).[1] Any time the variance of a field quadrature is less than one, then the state is squeezed. If the minimum uncertainty product is maintained, then it is an ideal squeezed state. Discussions of how to generate single mode squeezing of the electric field can be found in Ref. [97]. In order to detect the squeezed state, the standard detection technique is to interfere the state with a local oscillator (usually a coherent state with a variable phase) and count photons on a detector. The

[1] The value of 1 is due to the normalization convention of the quadratures. The photon SQL is often cited as $\frac{1}{4}$ due to a different normalization convention.

detector counts are related to the complex square of the field operators for the combined input field and the local oscillator. Information about the field quadratures is determined from the mean and variance of the counts as the phase of the local oscillator is varied.

4.2 The Spin-$\frac{1}{2}$ Phase Space

It is also possible to create squeezing in more complicated phase spaces. The next more complicated phase space is two modes, each of which can be represented classically with a complex number. This pair of complex numbers constitute a vector order parameter, $\psi = (\zeta_+, \zeta_-)^T$. This is of course corresponds to the Lie group U(2). The u(2) Lie algebra is composed of annihilation and creation operators for each mode: $\hat{a}_+$, $\hat{a}_-$, $\hat{a}_+^\dagger$, and $\hat{a}_-^\dagger$. However for particles, the number of particles is conserved even though they can change modes. So the operators are combined into number conserving bilinear operators, which combine a creation operator and an annihilation operator. Adding these constraints gives SU(2), the group which represents spin-$\frac{1}{2}$ particles. The density matrix can be constructed from the outer product of the order parameter and can be represented in a tensor matrix form ($m = \sum_{i,j} |\psi_i\rangle\langle\psi_j|$) or in second quantized form ($\hat{m} = \sum_{i,j} \hat{\psi}_i^\dagger \hat{\psi}_j$). The density matrix is a tensor and can be decomposed into multipoles which are irreducible tensors [122]. For the SU(2)/spin-$\frac{1}{2}$ system there is only a rank-1 dipole or vector spin.[2]

The spin-$\frac{1}{2}$ phase space has been extensively studied and is included in elementary texts [128, 129]. The entire space is the vector spin space with the Lie algebra spanned by the operators S_x, S_y, and S_z (Table 4.1). This decomposition is not unique and often $S_\pm = S_x \pm iS_y$ are substituted [128]. A faithful representation of the Cartesian form is the familiar Pauli spin matrices that operate on the vector order parameter. The phase space can be represented on the well known Bloch sphere (Figure 4.1) [112]. The Lie algebra basis for su(2) has a particularly simple commutator structure, $\left[S_i, S_j\right] = i\epsilon_{ijk} S_k$. A coherent spin state (CSS) only requires two parameters which can be seen on the Bloch

[2]The monopole is constrained by number conservation when going from U(2) to SU(2).

Table 4.1: Spin operators for spin-$\frac{1}{2}$. Expectation values of these operators are components of the total spin angular momentum vector and are represented by the Pauli spin matrices.

$$
\begin{aligned}
S_x &= \tfrac{1}{2}\begin{pmatrix} 0 & 1 \\ 1 & 0 \end{pmatrix} & \hat{S}_x &= \tfrac{1}{2}\left(\hat{a}_+^\dagger \hat{a}_- + \hat{a}_-^\dagger \hat{a}_+\right) \\
S_y &= \tfrac{i}{2}\begin{pmatrix} 0 & -1 \\ 1 & 0 \end{pmatrix} & \hat{S}_y &= \tfrac{i}{2}\left(-\hat{a}_+^\dagger \hat{a}_- + \hat{a}_-^\dagger \hat{a}_+\right) \\
S_z &= \tfrac{1}{2}\begin{pmatrix} 1 & 0 \\ 0 & -1 \end{pmatrix} & \hat{S}_z &= \tfrac{1}{2}\left(\hat{a}_+^\dagger \hat{a}_+ - \hat{a}_-^\dagger \hat{a}_-\right)
\end{aligned}
$$

sphere. Starting with a coherent state at one of the eigenvalues of S_z, the first parameter is a rotation about a transverse spin component (S_x or S_y) to get the azimuthal angle followed by a rotation about S_z to get the longitudinal angle. Since the initial coherent state has symmetric fluctuations transverse to the mean spin vector, rotation about the mean spin vector has no effect.

4.3 Spin Squeezing in Spin-$\frac{1}{2}$

The first key difficulty in discussing spin squeezing is answering the question, what is a spin squeezed state? Going from optical type squeezing to spin squeezing was at first very confusing [130]. For the U(1) radiation field it is sufficient to say that it is squeezed if one quadrature amplitude is less than the SQL of 1 (or $\frac{1}{4}$) [94]. However, if one extrapolates this to spins, i.e a spin-$\frac{1}{2}$, system, then it is possible to meet this condition merely by the choice of the system coordinates and thus this is clearly not a fundamental definition. Indeed such a state can be accomplished by merely rotating a CSS. The initial coherent state was already a minimum uncertainty state, but with no correlations and hence identical quadrature amplitudes. For spin-squeezing, it is necessary to look at fluctuations in quadratures normal to the mean spin direction because the commutator between spin moments is not a constant like the single optical mode case, but another spin moment [94, 127, 130]. For any three orthogonal spin directions (indexed by i,j,k) the commutation relation $\left[S_i, S_j\right] = i\epsilon_{ijk}S_k$ holds and thus $\langle \Delta S_i^2 \rangle \langle \Delta S_j^2 \rangle \geq \frac{1}{4}|\langle S_k \rangle|$. With S_k being the mean spin direction of length

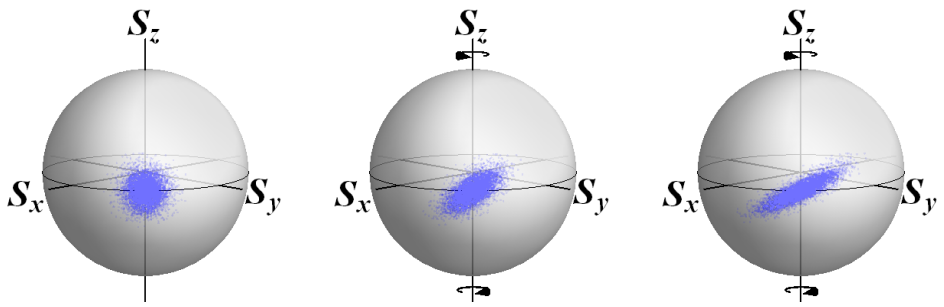

Figure 4.1: Representation of the spin-$\frac{1}{2}$ phase space for 100 atoms in S_x, S_y, and S_z. The second and third frames show single axis twisting generating spin squeezing.

S the balanced minimum uncertainty gives $\langle \Delta S_i^2 \rangle = \langle \Delta S_j^2 \rangle = \frac{S}{2}$. Thus the commutation relation of the su(2) Lie algebra trivially gives the SQL. A quadrature transverse to the mean spin direction having noise statistics below the SQL indicates a squeezed spin state (SSS) [94]. If the uncertainty product is maintained as an equality, then it is an ideal SSS. If the expectation value of the commutator is zero, there can be no squeezing in the transverse quadratures since the SQL is zero also.

A common way to generate squeezing in the spin-$\frac{1}{2}$ system is to use the one-axis twisting scheme [94]. This requires a non-linear Hamiltonian of the form S_i^2 where S_i is transverse to the mean spin direction S_k. This Hamiltonian will rotate one hemisphere clockwise and the other counterclockwise with the amount of rotation varying continuously with a maximum at the poles and being zero at the equator (Figure 4.1).

4.4 Spin-Nematic Squeezing in Spin-1

The extension of spin-squeezing from spin-$\frac{1}{2}$ to spin-1 is trivial; merely use the spin-1 vector magnetization operators. However the squeezing about $m_f = 0$ cannot be spin-squeezing since $\langle L_x \rangle = \langle L_y \rangle = \langle L_z \rangle = 0$. But spin-1 has other higher order spin moments which could exhibit squeezing. Previously squeezing in this system has been studied using two mode squeezing [105], using an SU(3) algebra in the quark basis [106], and for dipole-quadrupole measureables [107]. These analyses were the guide which led to the form

presented here. In the case of spin-mixing from the meta-stable $m_f = 0$ state, the squeezing is not developed in the spin subspace, but rather a joint spin-nematic subspace.

4.4.1 The Squeezing Observables

The source of squeezing in a spin-1 condensate is the non-linear collisional spin interaction of $\hat{H}_a = \lambda_a' \left(\hat{L}^2 - 2\hat{N}\right)$. The generalized uncertainty principle is again used in order to understand the squeezing sub-spaces in a spin-1 system. As noted earlier, only operator pairs with non-zero expectation values for their commutation relations can exhibit squeezing. In considering the commutation relations of the spin and nematic components, there are seven operator triplets with SU(2) commutation relations. For condensates with the atoms in the $m_f = 0$ state, there are only two commutators with non-zero expectation values: $\langle 0, N, 0|[L_x, N_{yz}]|0, N, 0\rangle = -2iN$ and $\langle 0, N, 0|[L_y, N_{xz}]|0, N, 0\rangle = 2iN$, leading to the relevant uncertainty relations $\Delta L_x \Delta N_{yz} \geq N$ and $\Delta L_y \Delta N_{xz} \geq N$. For each of these, the uncertainty relationship is between a spin operator and a quadrupole nematic operator, hence *spin-nematic squeezing*. These operators and their commutators define two subspaces, each with su(2) Lie algebra commutation relations. From these relations, two squeezing parameters are defined in terms of quadratures of the operators:

$$\xi^{\theta}_{x(y)} = \langle \left(\Delta \left(\cos\theta L_{y(x)} + \sin\theta N_{xz(yz)}\right)\right)^2 \rangle / N. \tag{4.4}$$

with θ as the quadrature angle [105, 107]. Squeezing within a given SU(2) subspace is indicated by the variance of the quadrature operator being less than the standard quantum limit (SQL) of N for some value of θ. In each SU(2) subspace, the squeezing is analogous to spin squeezing [105]. The important differences are that there are two such subspaces and that there is no squeezing in the familiar spin subspace $\{L_x, L_y, L_z\}$.

4.4.2 Four-Wave Mixing

Squeezing in a spinor condensate was first considered by Duan, *et. al.*, who discussed it in language of two-mode squeezing [105]. Spin-mixing has been identified as a type of atomic

FWM of the internal states [44, 117]. In optical systems, FWM is known to generate two-mode squeezing [97,131]. To calculate an analytic form for the generation of squeezing, an approach similar to Ref. [105, 131, 132] is used. The focus of the calculation will be solely on the spin-mixing Hamiltonian terms similar to the $\chi^{(3)}$ non-linearity of optical FWM. As done in the optical case, an undepleted[3] pump of $m_f = 0$ is used allowing this mode to approximated as a classical field and so $\hat{a}_0^\dagger$ is replaced with $\sqrt{N}e^{i\theta_0}$.

$$\begin{aligned}\hat{H}_{\chi^{(3)}} &= 2\lambda_a' \left(\hat{a}_0^\dagger \hat{a}_0^\dagger \hat{a}_1 \hat{a}_{-1} + \hat{a}_1^\dagger \hat{a}_{-1}^\dagger \hat{a}_0 \hat{a}_0\right) \\ &= c \left(e^{2i\theta_0} \hat{a}_1 \hat{a}_{-1} + e^{-2i\theta_0} \hat{a}_1^\dagger \hat{a}_{-1}^\dagger\right) \end{aligned} \tag{4.5}$$

Taking the Heisenberg equation of motion for $\hat{a}_{\pm1}$ and $\hat{a}_{\pm1}^\dagger$ gives:

$$\frac{\partial \hat{a}_{\pm1}}{\partial t} = -ie^{-2i\theta_0} \frac{c}{\hbar} \hat{a}_{\mp1}^\dagger \tag{4.6a}$$

$$\frac{\partial \hat{a}_{\pm1}^\dagger}{\partial t} = ie^{2i\theta_0} \frac{c}{\hbar} \hat{a}_{\mp1} \tag{4.6b}$$

These coupled linear equations have the solutions

$$\hat{a}_{\pm1}(t) = \hat{a}_{\pm1}(0) \cosh \frac{|c|}{\hbar} t - ie^{-2i\theta_0} \hat{a}_{\mp1}^\dagger(0) \sinh \frac{|c|}{\hbar} t \tag{4.7a}$$

$$\hat{a}_{\pm1}^\dagger(t) = \hat{a}_{\pm1}^\dagger(0) \cosh \frac{|c|}{\hbar} t + ie^{2i\theta_0} \hat{a}_{\mp1}(0) \sinh \frac{|c|}{\hbar} t \tag{4.7b}$$

where $\hat{a}_{\pm1}^\dagger(0)$ and $\hat{a}_{\mp1}(0)$ act on the initial state at $t = 0$. A similar solution for the more complete Hamiltonian of Eq. (3.22) is given in Ref. [46]. With these solutions and the initially unpopulated (vacuum) $m_f = \pm1$ modes, time evolutions can be calculated. The subsequent population of $m_f = \pm1$ is

$$\langle \hat{N}_{\pm1} \rangle = \langle \hat{a}_{\pm1}^\dagger \hat{a}_{\pm1} \rangle = \sinh^2 \frac{|c|}{\hbar} t. \tag{4.8}$$

Next the bosonic quadratures for the $m_f = \pm1$ modes are calculated.

$$\hat{Q}_{\pm1}^\phi = \hat{a}_{\pm1} e^{-i\phi} + \hat{a}_{\pm1}^\dagger e^{i\phi} \tag{4.9a}$$

[3]For low depletion, $N_0 \approx N$.

$$\langle \hat{Q}^{\phi}_{\pm 1} \rangle = 0 \tag{4.9b}$$

$$\begin{aligned} \langle (\Delta \hat{Q}^{\phi}_{\pm 1})^2 \rangle &= \cosh^2 \frac{|c|}{\hbar} t + \sinh^2 \frac{|c|}{\hbar} t \\ &= \cosh \frac{2|c|}{\hbar} t \end{aligned} \tag{4.9c}$$

The SQL for this quadrature is 1, similar to the single mode light field. Since $\cosh 2|c|t/\hbar \geq 1$ the quadratures of $m_f = \pm 1$ are never squeezed, just as the two output modes in optical FWM are not squeezed [97, 131]. However like the optical case, we look also for squeezing in the quadratures of the sum of the modes.[4]

$$\hat{b}_+ = (\hat{a}_{+1} + \hat{a}_{-1}) / \sqrt{2} \tag{4.10a}$$

$$\hat{Q}^{\phi}_{+} = \hat{b}_+ e^{-i\phi} + \hat{b}^{\dagger}_+ e^{i\phi} \tag{4.10b}$$

$$\langle \hat{Q}^{\phi}_{+} \rangle = 0 \tag{4.10c}$$

$$\begin{aligned} \langle (\Delta \hat{Q}^{\phi}_{+})^2 \rangle &= \cosh^2 \frac{|c|}{\hbar} t + \sinh^2 \frac{|c|}{\hbar} t - 2 \sin(2\theta_0 + 2\phi) \cosh(\frac{|c|}{\hbar} t) \sinh(\frac{|c|}{\hbar} t) \\ &= \cosh \frac{2|c|}{\hbar} t - \sin(2\theta_0 + 2\phi) \sinh \frac{2|c|}{\hbar} t \end{aligned} \tag{4.10d}$$

As ϕ is varied the quadrature variance goes between a maximum value of $e^{2|c|t/\hbar}$ and a minimum value of $e^{-2|c|t/\hbar}$. So there is squeezing for the minimum quadrature variance that evolves with a time constant of $2|c|/\hbar$ while the maximum quadrature variance also evolves with the same time constant. To compare this quadrature to the spin-nematic squeezing quadratures above, it is noted that if the classical treatment of $\hat{a}_0$ is taken into account, then $\hat{Q}^{\phi=0}_{+}$ is $\hat{L}_x$ and $\hat{Q}^{\phi=\pi/2}_{+}$ is $\hat{N}_{yz}$. An equivalent quantum optics experiment is given in Appendix D.

4.5 Squeezing as Determined by Simulations

In order to make the squeezing intuitively clear, a visualization of the SU(3) phase space is helpful, especially for understanding the subspaces where squeezing occurs. The Bloch

[4] This is the same as the y mode of the polar basis up to a phase. [105, 106]

(a)

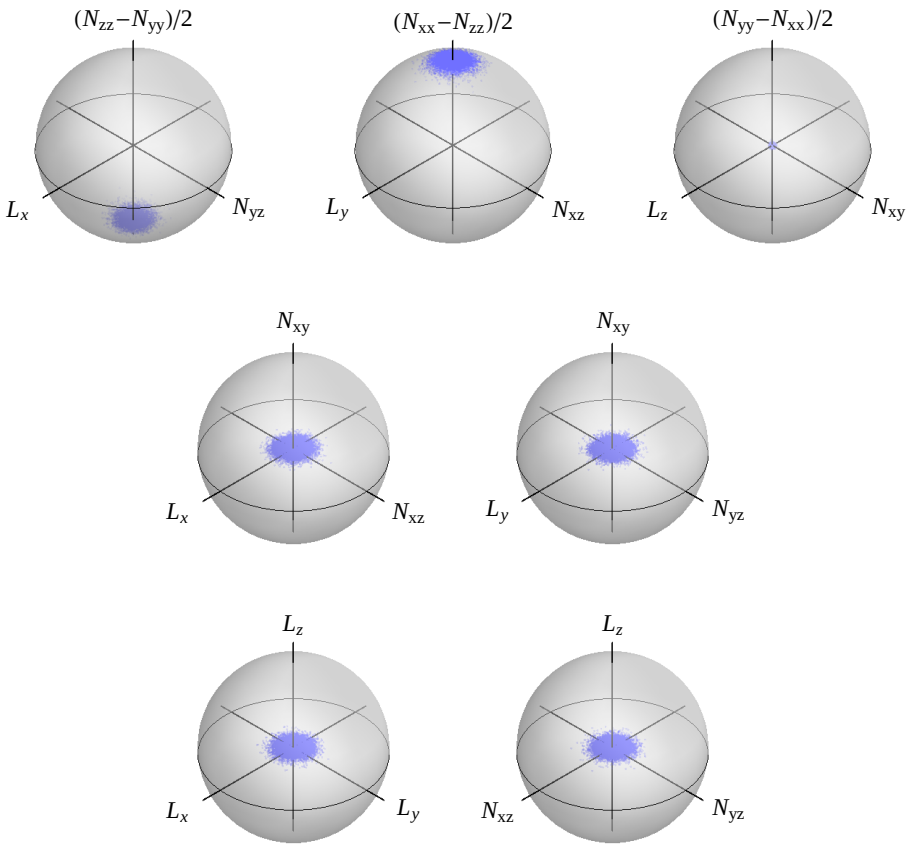

(b)

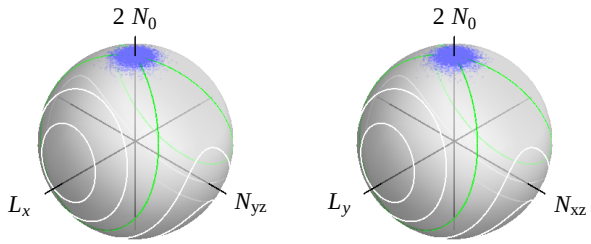

Figure 4.2: **(a)** The seven subspaces of SU(3) with the distribution for pure $m_f = 0$ of 100 atoms. **(a)** Approximate SU(2) subspaces when $N_0 \approx N$.

sphere provides an excellent visualization of the SU(2) system. The eight basis operators of SU(3) are more challenging to visualize, but taking the seven SU(2) subspaces (See Table 3.3) and placing them each on their own Bloch sphere allows a visual representation of the system (Figure 4.2(a)). It takes a minimum of three subspaces to span the space such as the first row of Figure 4.2(a). The first figure of the third row is the familiar spin subspace typically represented on a Bloch sphere. For the case here, the most important subspaces will be those that can exhibit squeezing (First two figures in the first row of Figure 4.2(a)). Unfortunately, two of the axes of each one is from the non-intuitive quadrupole tensor. For the starting state $m_f = 0$, about which the squeezing is centered, a simplification is possible. The off diagonal contributions of $\langle N_{zz} - N_{yy} \rangle$ and $\langle N_{xx} - N_{zz} \rangle$ are small, $\sim \sqrt{N_1 N_{-1}}$ and average to zero over a Larmor precession cycle. When the off diagonal terms are neglected, $N_{zz} - N_{yy} \approx -2N_0$ and $N_{xx} - N_{zz} \approx 2N_0$. Taking both of these as $2N_0$ gives two approximately SU(2) representations[5] shown in Figure 4.2(b). This has the benefit of allowing the spinor energy contours to be plotted on these spheres as shown in green and white lines. Using this visualization, the squeezing in the subspaces will become clear graphically. This visualization also will aid in understanding the manipulations that makeup the measurement protocol used to measure the squeezing generated by spin-mixing discussed in Chapter 5.

Mapping the spinor energy contours onto the Bloch spheres illustrates some interesting features. One of the first things to notice is that for the spinor phase going from $-\pi$ to π only goes halfway around the spheres in Figure 4.2(b). This is because the spinor phase cannot distinguish between $\langle L_x \rangle > 0$ or $\langle L_x \rangle < 0$ since the energy goes as $\langle L_x^2 \rangle$. So the quadrature phase is only half the spinor phase and distinguishes between signs of L_x and N_{yz}. Because of this phase degeneracy, what happens in one hemisphere is reflected across the 'z' axis into the other. Furthermore the $\{L_x, N_{yz}, 2N_0\}$ and $\{L_y, N_{xz}, 2N_0\}$ spaces are degenerate. Unlike what is normally seen for the spin-$\frac{1}{2}$ system, the energy contours are

[5]Using positive $2N_0$ for both has the effect of flipping over the $\left\{L_x, N_{yz}, (N_{zz} - N_{yy})\right\}$ subspace and so the labeled N_{yz} axis is actually the negative valued axis.

not simply lines of latitude in the basis of the squeezing operator (L_x^2 or L_y^2) associated with each squeezed subspace. In the single axis twisting scheme for the spin-$\frac{1}{2}$, the squeezing was generated by a shearing about the equator. Here the shearing is about the separatrix energy contour, which in this case divides the phase space into three regions instead of two. These richer energy contours are due to the quadrupole moment that does not exist in spin-$\frac{1}{2}$, but only spin-1 and higher. The effect of the quadratic Zeeman energy is a uniform rotation of the states about the $2N_0$ axis. At one pole it aids the twisting and at the other it opposes. In the limit of zero magnetic field, the energy contours reduce to the lines of latitude, but with degenerate lines mirrored across the equator which is also dissimilar to the normal SU(2) system for single axis twisting.

4.5.1 Illustrative Cartoon

In order to look at the phase space density on the Bloch spheres, the semi-classical simulation is used. For each pure state of the ensemble we calculate the necessary expectation values of the basis operators for su(3). For example $\langle L_x \rangle$, $\langle N_{yz} \rangle$ and $\langle N_0 \rangle$ for each state in the ensemble are calculated in order to get the coordinates of the distribution in the top row of Figure 4.3. For the illustration the semi-classical simulation is used with parameters similar to the experiment ($c = -2\pi\hbar \times 8$ Hz and $B = 210$ mG), but with only 30 atoms in order to be able to clearly visualize the fluctuations on the Bloch spheres.

The two subspaces where squeezing can occur along with the spin subspace are used to illustrate the dynamics. In Figure 4.3, the initial state is similar to that shown in Figure 4.2. It can be seen that during spin-mixing, the expectation values of L_x, L_y, N_{yz}, and N_{xz} remain zero, but their distributions and correlations evolve from their initial uncorrelated minimum uncertainty values. All of the distributions of these moments increase with time, with the nematic moments growing faster than the spin moments.[6] The distribution grows considerably along one branch of the separatrix (which will be called the descending branch),

[6]For $q = 0$, the distributions of spin moments remain constant. For $q > -c(1 + 1/\sqrt{2})$ the spin moments grow faster.

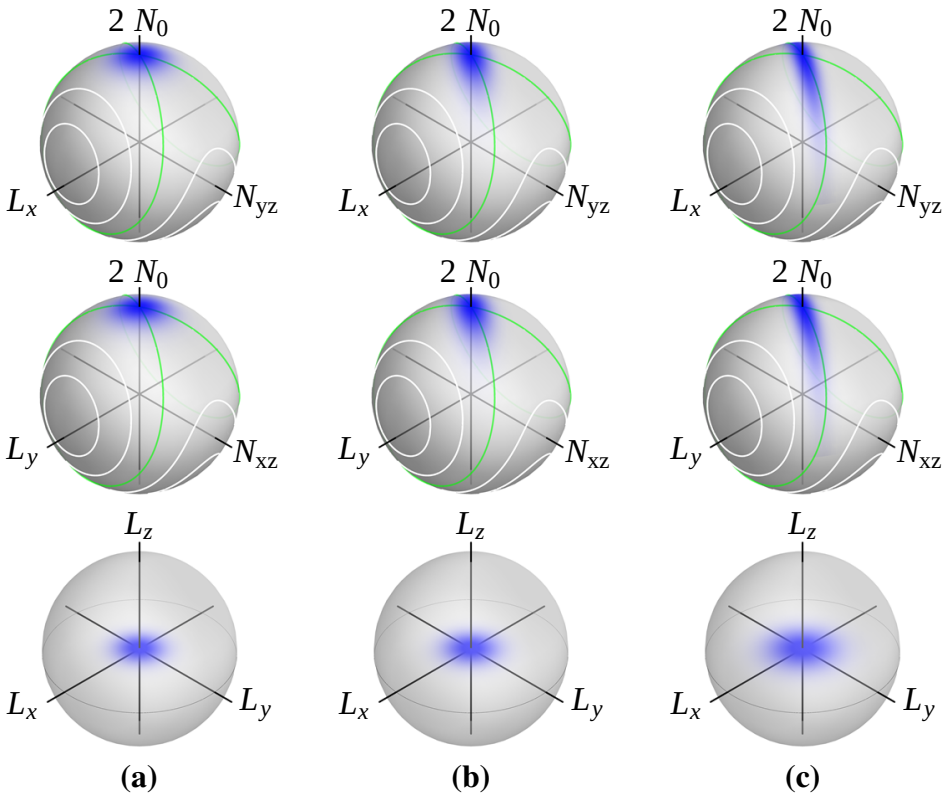

Figure 4.3: Squeezing Cartoon. **(a)** Initial distribution for 30 atoms with energy contours for $c = -2\pi\hbar \times 8$ Hz and $B = 210$ mG shown. **(b)** The phase space after 10 ms of evolution. **(c)** 20 ms.

while at the same time shrinking along the perpendicular direction. This is a clear graphical illustration of the squeezing generated by spin-mixing.

Under the spin mixing Hamiltonian, both of the degenerate SU(2) subspaces exhibit squeezing [105]. In the limit of zero magnetic field, each degenerate subspace undergoes its own single-axis twisting scheme until the $m_f = 0$ component begins to exhibit depletion. While L_x^2 or L_y^2 would normally twist the spin subspace as well, their combined action cancels in this subspace. Hence there is no squeezing in the spin subspace. In finite magnetic fields the system does not confine itself to either of the SU(2) subspaces but rather the Larmor precession rapidly shifts the states of the system back and forth between the two degenerate subspaces on simple orbits described by rotations about L_z in the SU(2) subspaces $\{L_x, L_y, L_z\}$ and $\{N_{yz}, N_{xz}, L_z\}$ (Second figure of the third row in Figure 4.2(a)). Thus

the two degenerate subspaces are connected by the action of the magnetic field portion of the Hamiltonian.

We now discuss how the minimum and maximum values of the quadrature variance or squeezing parameter (Eq. (4.4)) evolve in time. For both the semi-classical and quantum simulations, the squeezing parameter is calculated by performing the spinor phase shift operation ($\exp\left(i\Delta\theta_s\hat{N}_{zz}\right)$) and then calculating $\langle\hat{L}_x^2\rangle = \langle(\Delta\hat{L}_x)^2\rangle$. Semi-classically this is done by calculating $\langle L_x\rangle$ for each state of the ensemble and then calculating the variance of these numbers. For the quantum version $\hat{L}_x^2$ is converted to a tridiagonal matrix form to operate on the $N/2+1$ complex coefficients of the Fock basis. For a single magnetization value of zero this gives[7]

$$\begin{aligned}\left(\hat{L}_x^2\right)_{k,k'} &= (k(N-2k+1)+(k+1)(N-2k))\,\delta_{k,k'} \\ &+ (k+1)\sqrt{(N-2k)(N-2k-1)}\delta_{k,k'+1} \\ &+ k\sqrt{(N-2k+1)(N-2k+2)}\delta_{k,k'-1}. \end{aligned} \tag{4.11}$$

In Figure 4.4, these quadrature values are shown in dB relative to the SQL for evolution as calculated for 10^2, 10^3, and 10^4 atoms using the same parameters as Figure 3.6(b), $c = -2\pi\hbar \times 8$ Hz and $q = |c|/3$. According to the FWM approach these initially evolve exponentially with a time constant of $2|c|/\hbar$, shown as black lines in Figure 4.4. For all three atom numbers the maximum and minimum quadrature variance initially evolve with the FWM time constant. The main difference between number of atoms is when the low depletion approximation fails. At this time, the greatest degree of squeezing is reached and the minimum quadrature starts to increase. From the plots the maximum amount of squeezing appears to scale with $\sqrt{N}$, while the single axis twisting scheme in an SU(2) system is calculated to scale as $N^{1/3}$ [94]. After the extremal squeezing is reached, squeezing becomes difficult to interpret [106]. However, the maximum quadrature variance continues to grow after the minimum value turns and grows more quickly than the maximum variance.

[7]For any state, if the Fock state basis only has one value of magnetization, then $\langle L_x\rangle = 0$. The quantum form of $\hat{L}_x^2$ shown here neglects terms which have $\Delta M = \pm 2$ since only one value of M is expected.

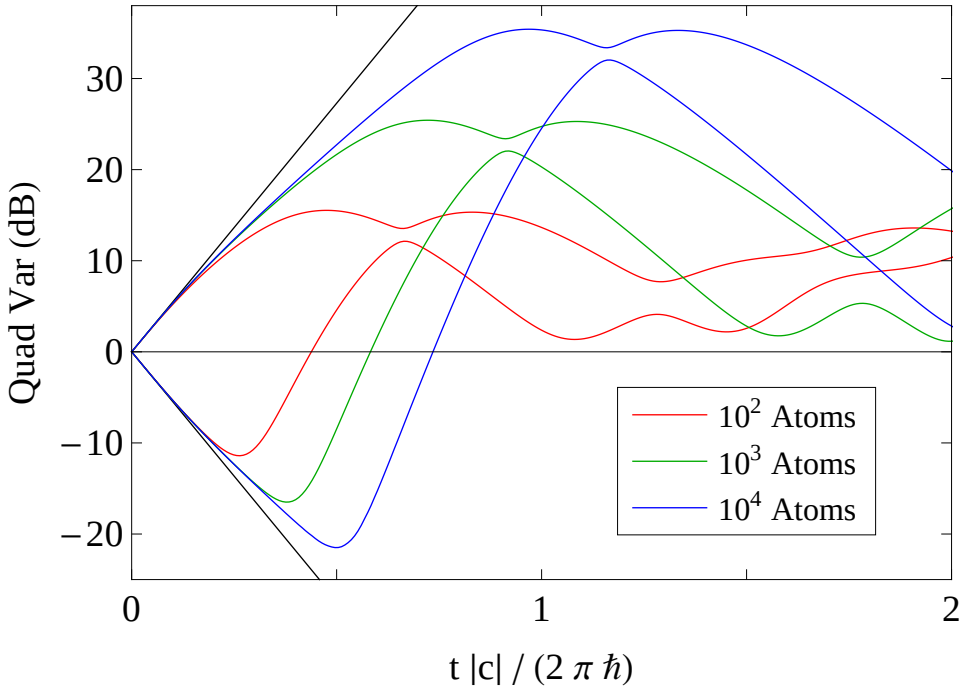

Figure 4.4: Ferromagnetic squeezing quadratures minimum and maximum as a function of time for different values of N.

The maximum variance also turns, with it and the minimum variance having nearly the same value well above the SQL before continued evolution separates them. The time of the closest approach of the quadratures corresponds to the minimum average value of N_0 during the first oscillation of the spin-mixing dynamics.

4.5.2 Simulation with experimental parameters

We now describe simulations to match the typical experimental conditions starting with an $m_f = 0$ condensate of 45000 atoms. This makes the initial distribution have a FWHM of $\sim$ 500 atoms or $\sim$ 0.5% diameter of the Bloch sphere. To see the dynamics it is necessary to zoom in onto the pole (Figure 4.5). For each plot a density plot from the semi-classical simulation is displayed along with the uncertainty ellipse from the quantum simulation and the separatrix for the final magnetic field. Evolution starts in a high magnetic field of 2 G. The magnetic field is brought down through a quench to the final value of 210 mG. The time dependence of the magnetic field has been measured using microwave spectroscopy and is

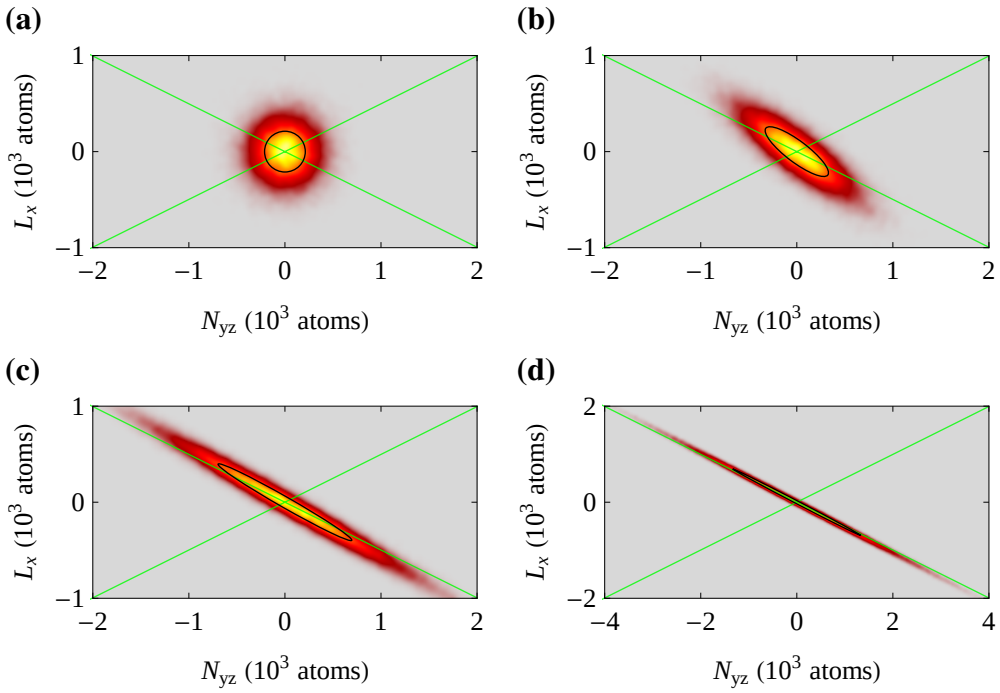

Figure 4.5: Quadratures of L_x and N_{yz} with experimental parameters zoomed in at the pole. The plot consists of a density plot generated using the semi-classical simulation and the uncertainty ellipse (black line) from the quantum simulation. The separatrix is shown in green. Simulation times are **(a)**, 0 ms; **(b)**, 15 ms; **(c)**, 30 ms; and **(d)**, 45 ms.

well modeled using the 2 ms long ramp of the control signal with a 1 ms decay constant. The simulation uses $c = -2\pi\hbar \times 8$ Hz. Similar to the cartoon in Figure 4.3, the initial state is the unsqueezed minimum uncertainty state shown in Figure 4.5(a). The magnetic field drops below $q = 2|c|$ at approximately 2 ms of evolution and the spin-mixing portion of the Hamiltonian starts to squeeze the initial state as seen in Figure 4.5(b). In Figure 4.5(c) the state continues to grow along an axis that is converging with the descending branch of the separatrix and shrinks perpendicular to this axis. By Figure 4.5(d) the state has squeezed until the long axis is approximately 10% of the diameter of the Bloch sphere. However, even for this value ρ_0 is still > 0.995.

Figure 4.6(a) plots the minimum and maximum quadrature variance as a function of time and Figure 4.6(b) plots the quadrature variance as a function of spinor phase for a few times. The point where the minimum and maximum quadratures are pinched together at

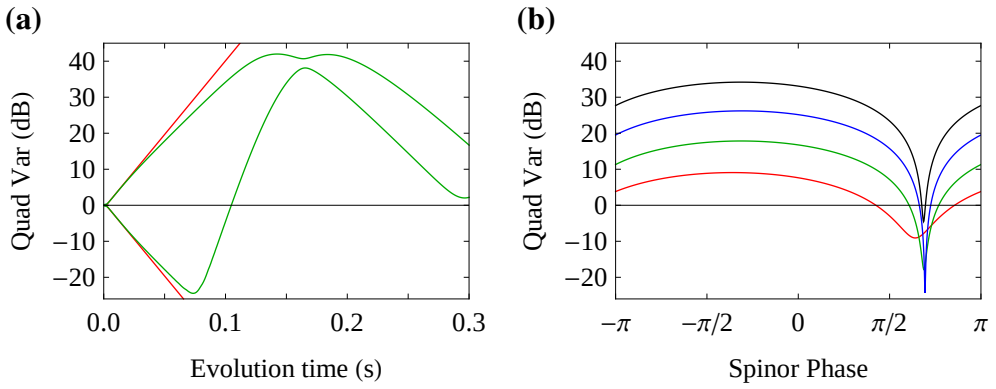

Figure 4.6: Time evolution of squeezing for 45000 atoms, $c = -2\pi\hbar \times 8$ Hz and a magnetic field of 210 mG. **(a)** Minimum and maximum quadrature variance as a function of time. **(b)** Plot of the variance of the quadrature as a function of spinor phase for evolution times 25 ms (red), 50 ms (green), 75 ms (blue), and 100 ms (black).

about 170 ms corresponds to the minimum ρ_0 of the first oscillation (See Figure 3.11). All of the squeezing in the spin-nematic quadratures occurs before there is noticeable evolution of the populations of the modes. The minimum and maximum of the quadrature variances in early times evolve with a time constant of $(2|c|/\hbar)^{-1} = 10$ ms as shown with the red lines in Figure 4.6(a). Figure 4.6(b) shows the quadrature variance as a function of spinor phase for several evolution times. The plots are the variance of the fluctuations transverse to a line defined by the spinor phase. For zero spinor phase the line aligns with the L_x axis and for $\pm\pi$ spinor phase it aligns with the N_{yz} axis. As the squeezing quadratures evolve, so does the spinor phase of maximum squeezing. This phase converges to the spinor phase of the descending branch of the separatrix.

4.6 Prediction for an Anti-Ferromagnetic Condensate

Simulations are also run for an anti-ferromagnetic condensate. The parameters used are similar to the previous section for comparison purposes except the sign of the spinor dynamical rate is changed. Looking at Figure 4.7(a), the squeezing parameter initially evolves

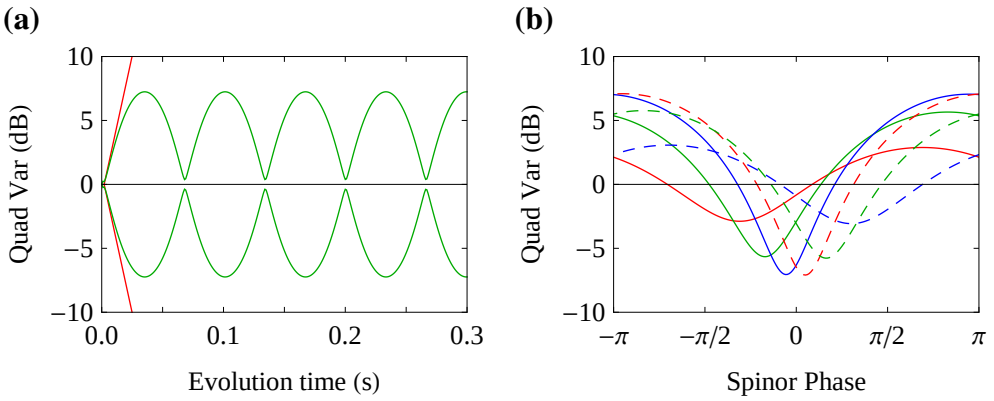

Figure 4.7: Time evolution of squeezing for an anti-ferromagnetic condensate 45000 atoms, $c = 2\pi\hbar \times 8$ Hz and a magnetic field of 210 mG. **(a)** Plot of the variance of the quadrature as a function of spinor phase for evolution times 10 ms (red), 20 ms (green), 30 ms (blue), 40 ms (dashed red), 50 ms (dashed green), and 60 ms (dashed blue). **(b)** Minimum and maximum quadrature variance as a function of time.

with a time constant of $2|c|/\hbar$ like the ferromagnetic case. However, the maximum squeezing attained is much less, ~ -7 dB, before the state starts to un-squeeze. What is particularly interesting is that this condensate never leaves the low depletion regime for a starting state of $m_f = 0$ but cyclically squeezes and un-squeezes. The reason for this can be seen in Figure 4.7(b). For the ferromagnetic case the twisting and rotations of the phase space oppose each other near $m_f = 0$ causing the spinor phase to converge, but in the anti-ferromagnetic case they aid each other causing the spinor phase to wind. So while the twisting is generating squeezing, the phase winding of the rotation is bringing the squeezed quadrature around until it is in the amplified fluctuation direction and the squeezing is undone only to have the cycle repeated indefinitely.

CHAPTER V

MEASUREMENT OF SPIN-NEMATIC SQUEEZING

The primary goal of this thesis is the measurement of squeezing generated by spin-mixing from the meta-stable $m_f = 0$ state. In the course of this thesis considerable effort has been devoted to theoretical predictions of this process to explain and guide these experiments. These predictions provide the model of spin-nematic squeezing which will now be applied to this measurement. In this chapter a measurement protocol is developed which provides access to the abstract subspaces where spin-nematic squeezing occurs. The measurement protocol makes use of the microwave and RF techniques previously developed for the experiment [15, 133]. Included in this discussion is the imaging calibration of the low noise fluorescence imaging required to make this measurement. Next the experimental measurement of spin-nematic squeezing is described and the data collected is presented. The acquired data is compared with the simulations in several ways including a reconstruction of the probability density of the phase space. Finally population dynamics for times past when the low-depletion limit is applicable are presented. These measurements, similar to previous measurements [15, 109], are also compared to the simulations.

5.1 Measurement Protocol and Atom Counting

5.1.1 Measurement Protocol

In order to understand how the squeezing can be measured, it is helpful to visualize the quantum states of the system on the spin SU(2) subspace, $\{L_x, L_y, L_z\}$, and the two subspaces that exhibit squeezing, $\{L_x, N_{yz}, 2N_0\}$ and $\{L_y, N_{xz}, 2N_0\}$. The squeezed state for 30 atoms from Figure 4.3(c) is shown in Figure 5.1(a). Measuring the squeezing requires state tomography involving two SU(3) rotations. The first is a rotation about $N_{zz} \sim 2N_0$ that aligns the squeezing quadrature to be measured with L_x (Figure 5.1(b)) in the $\{L_x, N_{yz}, 2N_0\}$

subspace. The second is a $\pi/2$ RF rotation about the L_y axis (in the lab frame) that rotates the fluctuations in L_x into the measurement basis, L_z (Figure 5.1(c)). Then measurement is simply a matter of counting m_f populations.

Identical squeezing also occurs in the degenerate $\{L_y, N_{xz}, 2N_0\}$ subspace, which leads to an important, but subtle point. In the lab frame, the system does not confine itself to either of the SU(2) subspaces but rather undergoes rapid Larmor rotations about L_z in two other SU(2) subspaces $\{L_x, L_y, L_z\}$ and $\{N_{yz}, N_{xz}, L_z\}$. However, because the squeezing is identical in both subspaces, and the Larmor precession of the spin vector and quadrapole are synchronized, it is not necessary to track the precession in order to measure squeezing. This has important experimental consequences in that it is not necessary to maintain synchronization with the Larmor rotation in order to perform quantum state tomography.

The spinor phase shift of the measurement protocol is a rotation generalized to the SU(3) symmetry of the spin-1 system. The Larmor precession from the linear Zeeman effect rotates the transverse magnetization about the z axis, which is simply a rotation of the spin vector in normal space (it also does rotations in the other two SU(2) subspaces containing L_z). However, the quadratic Zeeman portion produces a rotation about N_{zz}, and is a rotation in the 8-dimensional basis of su(3). This rotates L_x into N_{yz} and L_y into N_{xz}, the quadratures of the squeezing parameters. One way to effect the spinor phase shift of this rotation is to briefly increase the magnetic field such that the quadratic Zeeman is the dominant part of the Hamiltonian. Then the spinor phase simply winds, $\Delta\theta_s = \int dt\, q(t)/\hbar$, as was first demonstrated in Ref. [16, 109]. This approach poses experimental difficulties since there are limitations on the bias field magnitude and how quickly it can be changed. Alternately, the AC Zeeman shift due to a far off resonant microwave also provides energy shifts that are quadratic in m_f states and can quickly be changed with higher phase winding rates. This approach also allows a negative effective quadratic Zeeman shifts ($q < 0$) [34, 134, 135]. However because the transition frequencies depend on the magnetic field, it is sensitive to magnetic field fluctuations.

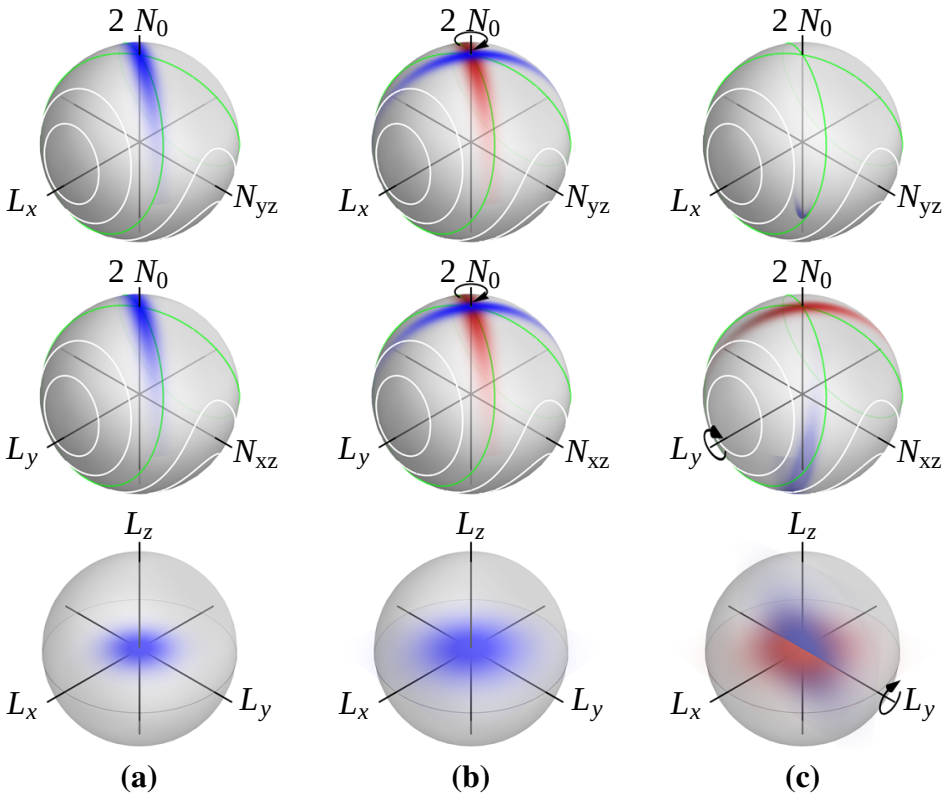

Figure 5.1: Measurement Protocol. **(a)** Same as the last part of the Figure 4.3. **(b)** The spinor phase shift rotates the quadratures of the squeezed subspaces from the before (red) to the after (blue). **(c)** The RF rotation about L_y which appear as rotations in the second squeezed subspace and the spin subspace. For those subspaces a before (red) and after (blue) are shown.

We have developed a variation on this technique. A microwave pulse just off resonant from the clock transition ($|f = 1, m_f = 0\rangle \leftrightarrow |f = 2, m_f = 0\rangle$) is used to shift the phase of the zero component, which is equivalent to shifting the $m_f = \pm 1$ phases equally relative to the $m_f = 0$ phase. The near resonant 2π pulse advances the phase of the zero component by a controllable amount depending on the detuning and the on-resonance Rabi rate. The phase shift of the zero component is $\Delta\theta_0 = \pi\left(1 + \Delta/\sqrt{1+\Delta^2}\right)$, where $\Delta = \delta/\Omega$ is the detuning normalized to the on-resonance Rabi rate. This technique has the advantage of being insensitive to magnetic field fluctuations since it employs the clock transition.

Using this technique, the quadratures of the squeezed subspaces can be rotated thus changing the alignment of the squeezed quadrature with the L_x axis. The second part of

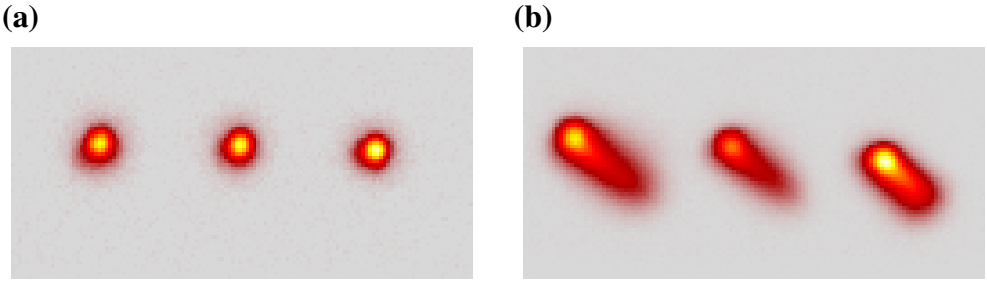

Figure 5.2: Sample false color images for **(a)** 100 μs and **(b)** 400 μs exposures.

the measurement protocol is simply a $\frac{\pi}{2}$ RF rotation about L_y. This is accomplished with a simple 2 turn coil on the experimental y-axis driven at the frequency splitting of the m_f states. Theoretical details of these manipulations are in Appendix A. A Stern-Gerlach gradient field is used to spatially separate the atoms into clouds of different m_f projections during time of flight (TOF). The atoms are then imaged using the fluorescence imaging technique.

5.1.2 Imaging Calibration

The measurements of L_z require low noise counting of the m_f states of the atoms which was developed for the experiment by Eva Bookjans [110, 133]. A sample of fluorescence images is shown in Figure 5.2 for 100 μs and 400 μs exposures. A primary limitation of the counting comes from the ability to separate the fluorescence of the different m_f states. The TOF, magnification (5×) and Stern-Gerlach all play a role in this. However the most limiting in our case was the imbalances of the MOT beams used to fluoresce the atoms. This is evident in the comet-like tails seen in the 400 μs image (Figure 5.2(b)). The forces induced from the imbalance moves the atoms during imaging causing this blurring.

For the most sensitive data, the atoms are fluoresced for 400 μs. After loading of the dipole trap, the magneto-optical trap (MOT) beams are apertured down to 12 mm diameter to reduce the background scattered light during imaging. For imaging, the MOT beams are detuned -6 MHz from the $f = 2 \rightarrow f' = 3$ cycling transition. The intensity of MOT beams

is ~ 30 times saturation making the scattering rate insensitive to small fluctuations in the intensity. Since the MOT beams use a $\sigma^+ - \sigma^-$ configuration coming from six directions on three orthogonal axes, the polarization is effectively isotropic. Therefore the scattering rate is in principle m_f state independent. However a small (6%) difference in the scattering rates of $m_f = \pm 1$ is noted, possibly caused by spatial variation of the repump intensity. Background subtraction is performed by taking 100 images using the experimental sequence with the dipole force trapping beams extinguished so that no atoms are trapped. From these images, an average background is computed along with the standard deviation of the background counts in order to estimate the scattered light noise contribution to the counting noise. This contribution is ~ 0.3 atoms/superpixel which for the ~ 1600 superpixels in the counting regions results in a noise floor of ~ 13 atoms for determination of the total atom number and magnetization.

In order to calibrate the atom detection, the populations for RF rotations from the $m_f = 0$ state are measured for various RF pulse lengths and hence number of atoms transferred to $m_f = \pm 1$ [110,133]. The initial $m_f = 0$ state is a z polar state with $\sqrt{N}$ fluctuations in the transverse magnetizations L_x and L_y and no fluctuations in L_z. An RF rotation about L_y rotates the z polar state into an x polar state where the populations are equally distributed between N_1 and N_{-1} and the $\sqrt{N}$ fluctuations are in L_y and L_z. In between the fluctuations in L_z go as $\sqrt{N_1 + N_{-1}}$. This allows the calibration of the imaging system using this noise since the photo-electron counts scale as $N_1 + N_{-1}$ but the fluctuations of L_z scale as $\sqrt{N_1 + N_{-1}}$. This noise is sometimes called quantum projection noise (QPN). Using the RF calibration data the small difference in scattering rate between $m_f = \pm 1$ noted above is corrected by fitting the mean line of all the points of magnetization versus number transferred. More details of the calibration are in Appendix E.

Using the calibration factor, the number of atoms the m_f states from the images of the Stern-Gerlach separated clouds are counted. From these numbers, the mean and variance

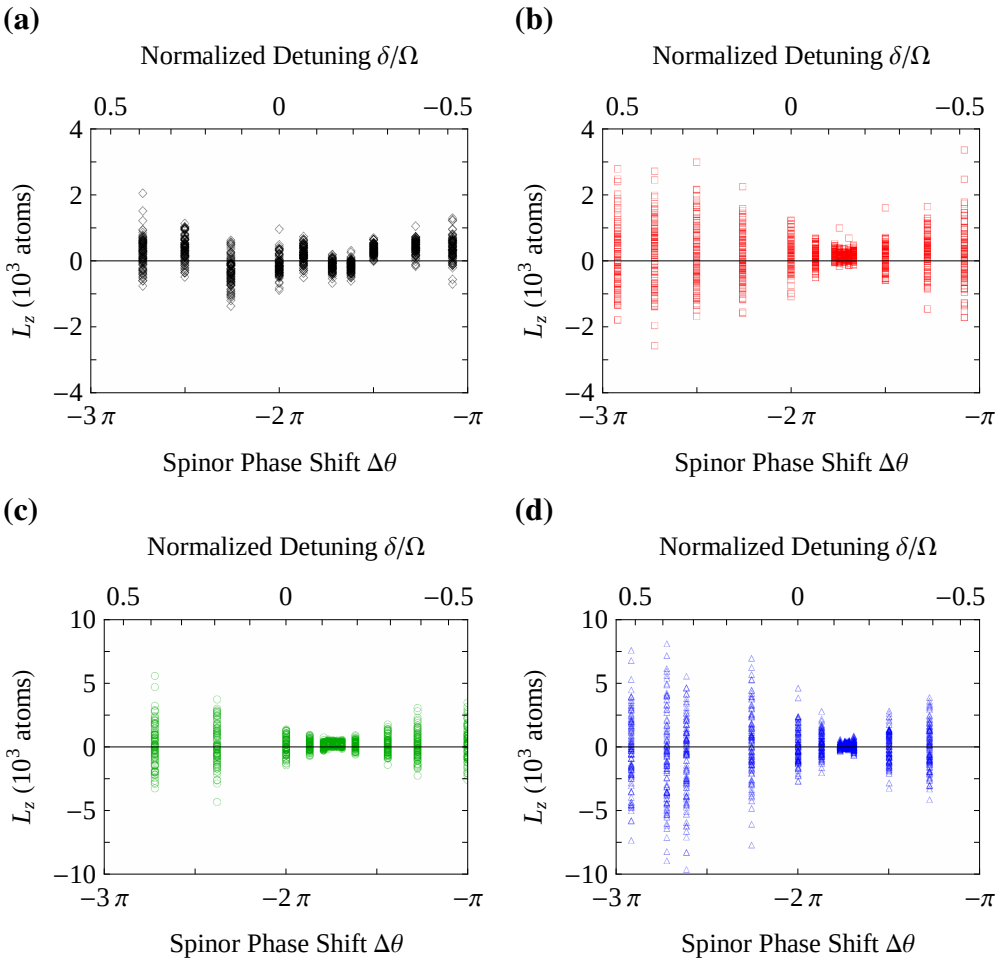

Figure 5.3: Squeezing measurement data for **(a)** 15 ms, **(b)** 30 ms, **(c)** 45 ms, and **(d)** 65 ms of evolution after the quench.

for the total number of atoms is calculated as well as the mean and variance for the magnetization of the atoms. The estimated error of the magnetization variance depends on the number of samples and is calculated according to $\sigma_{VAR} = VAR\sqrt{2/(N_{samp}-1)}$ [136]. To calculate the squeezing parameter, the magnetization variance is divided by the SQL which is just the mean number of atoms.

5.2 Experimental Results and Comparison

We now turn to the experiment to measure spin-nematic squeezing. The experiment begins with a condensate in the $m_f = 0$ state purified during evaporation discussed in Chapter 2.

Spin-mixing dynamics are initiated with the quenching the condensate by lowering the magnetic field from 2 G to its final value of 210 mG. The atoms are then allowed to evolve freely for a set time, varied from 15 ms to 65 ms, during which spin-nematic squeezing develops. The measurement protocol is initiated 500 μs before the atoms are released from the trap to rotate the squeezing quadratures into L_z. The atoms are then released from the dipole force trap for 22 ms of TOF expansion. The Stern-Gerlach field is ramped up 1 ms after the trap is released and remains on for 20 ms to separate the m_f projections. After the 22 ms TOF, the separated clouds of atoms are fluorescently imaged with a 400 μs exposure.

The fluctuations of the measured magnetization and how they vary with spinor phase shift is the signal of spin-nematic squeezing. The magnetization fluctuations are measured for several spinor phase shifts for four different times. For each combination of evolution time and phase shift the experiment cycle is repeated 100 times to collect statistics of the measured magnetization. The data collection is an extensive process with each measurement requiring the creation and destructive imaging of a condensate with an experimental cycle time of $\sim$20 s. These runs generated the raw data which consists of 5500 images from the squeezing measurements, another 900 images for the RF calibration, and another 1100 images for the spin-mixing data discussed at the end of the chapter. These data runs, along with periodically devoting experimental runs to acquiring background images, checking the Rabi rates of the microwave and RF transitions, checking the center frequency of the RF transition, and just keeping the experiment taking good data, required running the experiment for 24 hours a day for a week. This task involved three graduate students working in shifts to acquire all the data. The collated results of the magnetization data are shown in Figure 5.3.

In Figure 5.4, the measured noise tomography signals are shown compared to the quantum theoretical calculation. For the data, the estimated error for both the squeezing parameter and the phase shift are approximately the size of the symbols. In Figure 5.4(a), the signal clearly has noise reduced below the SQL for certain quadrature phases and has increased

noise π spinor phase away. Figure 5.4(b) shows a the detail of the most squeezed phase shift for each of the times separately. Only the squeezing from one spin-nematic SU(2) subspace is measured, but because of the action of the Larmor precession this samples the squeezing for both degenerate subspaces. After ~ 30 ms of evolution the measurement of squeezing is limited by a combination of light scattered by the apparatus and the photo-electron shot noise (PSN). The PSN limit is indicated by the gray lines in Figure 5.4 and 5.5. The maximum observed squeezing is $-8.3^{+0.6}_{-0.7}$ dB. When corrected for the PSN, this gives an inferred squeezing of $-10.3^{+0.7}_{-0.9}$ dB. This measurement is the main result of this thesis.

The data is compared to calculations of the spin-nematic quadrature squeezing from the quantum simulation, shown as solid lines in Figure 5.4. For this calculation the spinor dynamical rate of $c = -2\pi\hbar \times 8$ Hz has been chosen such that the simulation anti-squeezing amplitudes match experimental values, but is also a good fit to the long time evolution of the populations as well as calculations from the trap frequencies and N. This is the only free parameter for the simulation used to fit the experimental data. The phase of maximum squeezing also evolves in time converging to the spinor phase of the separatrix given by $\cos\theta_s \to -q/c - 1$ as $N_0 \to N$. There is ~ 150 mrad discrepancy between the theoretical prediction and measured position of maximum squeezing. In Figure 5.4(b), the phase of the data has been shifted to match the theoretical phase in order to highlight the match of the basic shapes and the sensitivity of the phase measurement. As squeezing increases the phases where the squeezing parameter is less than the SQL narrows and the feature sharpens. This can be understood by considering that it is the projection of the uncertainty ellipse, which becomes increasingly more eccentric as squeezing increases. Figure 5.5 shows the time evolution of the minimum and maximum quadratures and compared to the theoretical predications.

The measured squeezing does not go to the -12.5 dB limit established by the PSN, likely due to technical noise sources. The number of atoms in a given data run fluctuates 3 –

(a)

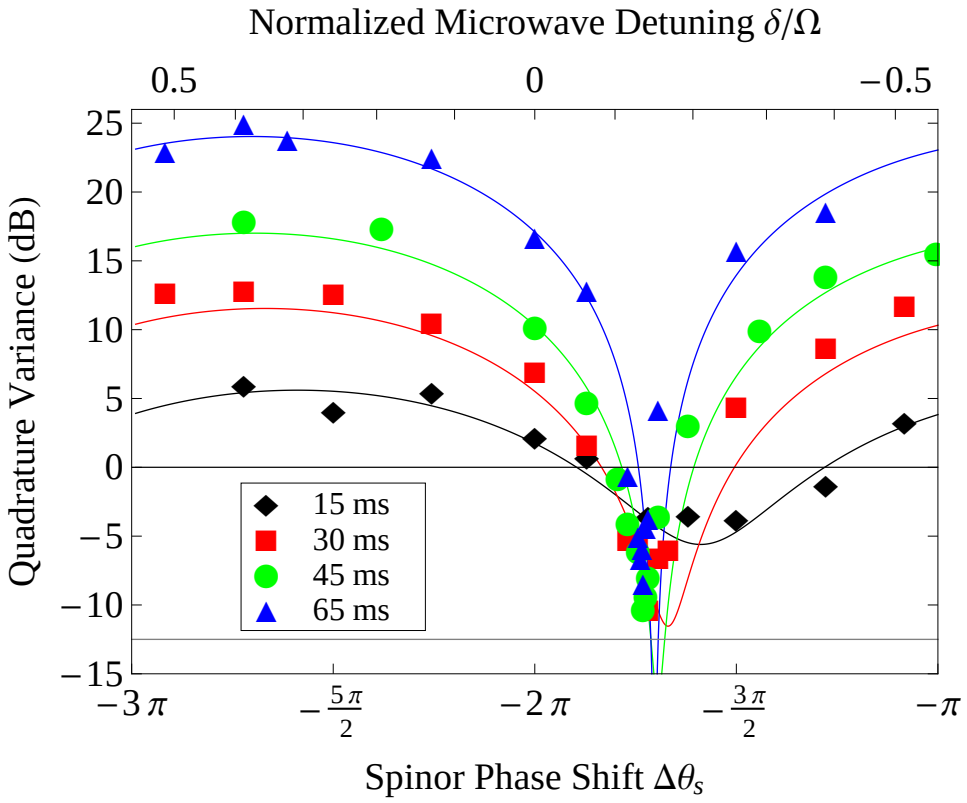

(b)

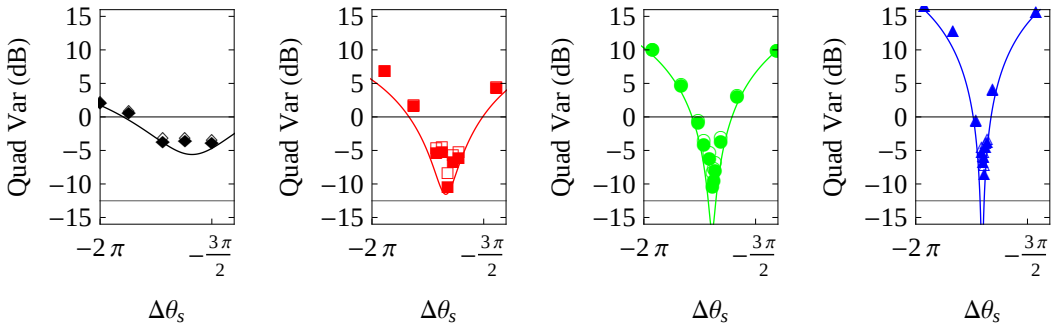

Figure 5.4: Comparison of quantum simulation to measured data for 45,000 atoms, a spinor dynamical rate of $-2\pi \times 8$ Hz, and a magnetic field decay modeled from the experiment. Estimated errors are approximately the size of the marker for both phase and variance. The gray line is the estimated imaging limit due to PSN. Open markers are statistics of the raw data, filled markers have been corrected for PSN. **(a)** Measurement of the quadrature variances for various times and spinor phase shifts. **(b)** Detail for each time. The data has been shifted to highlight the match of the curve shape with the data.

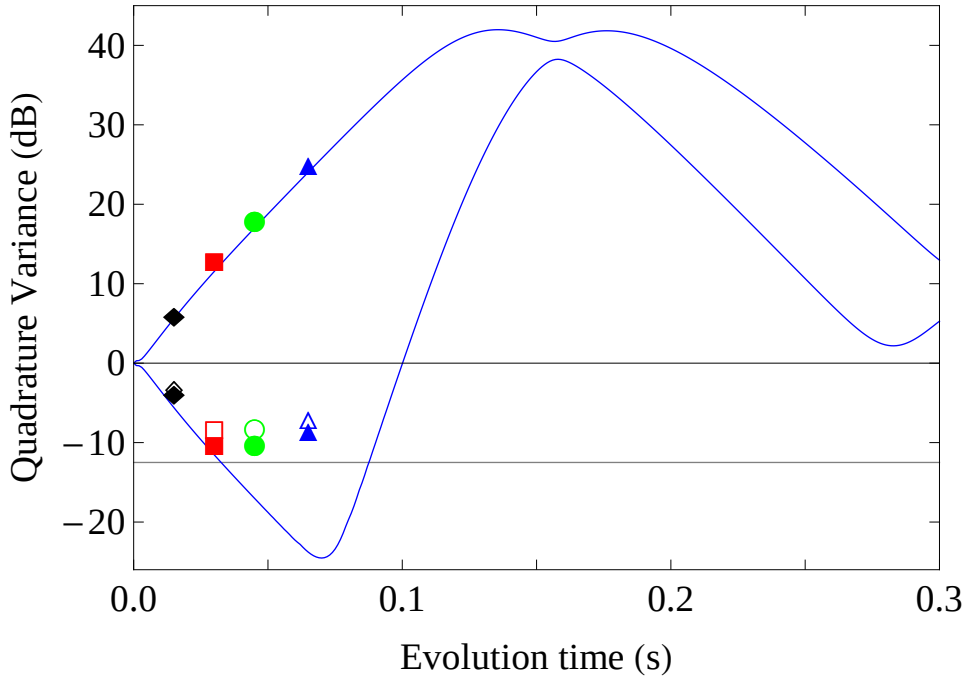

Figure 5.5: The maximum and minimum quadrature variances as a function of time.

10%. The location of the narrow range of the phase of the maximally squeezed quadrature is very sensitive to the spinor dynamical rate which varies as $N^{2/5}$. So as the total number fluctuates, effectively several nearby phase quadratures are sampled which blurs the signal. The spinor dynamical rate also depends on the trap frequencies and thus the details of the optical trapping potential. One such detail is the intersection of the cross beam, which is sensitive to small changes in alignment. Changes in this alignment are observed as changes of the aspect ratio of the imaged atom cloud fluctuating around its nominal spherical shape when observed with absorptive imaging. Another potential noise source is fluctuations of the spinor phase shift. This noise source was analyzed for both magnetic field fluctuations affecting the detuning for the $|f_{1,0}\rangle \rightarrow |f_{2,\pm1}\rangle$ transitions, which has a small effect on the phase shift, and variations of the on-resonance Rabi rate (See Appendix A). The dominant noise source of these was determined to be the Rabi rate fluctuation for which the 2π pulse varies 5 μs out of 130 μs, resulting in deviations of the expected phase shift of 50 mrad. Finally the measurements are very sensitive to noise in the microwave amplification. A

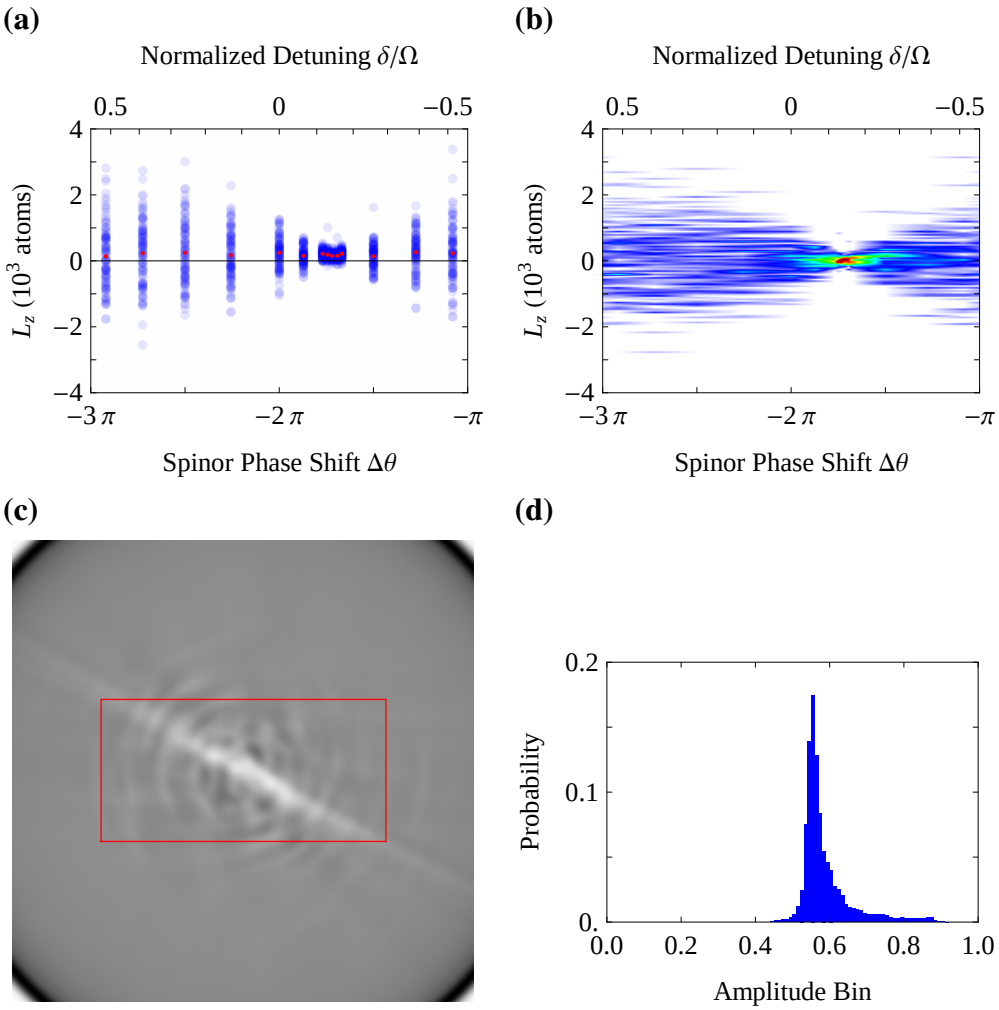

Figure 5.6: Reconstruction sequence for 30 ms data: **(a)** Plot of the data points (blue) for the measured value of L_z versus the spinor phase shift (bottom axis) calculated from the normalized microwave detuning (top axis). The red points are the mean for each phase's data set. **(b)** Linear interpolation of the data after the means are subtracted out and the resulting data is binned in 50 atoms bins. **(c)** The image from the inverse Radon transformation (Shown in gray scale) with circular edge artifacts in the corners. The red rectangle is the cropped region. **(d)** Histogram of the reconstructed data from the cropped region of part (c).

malfunction of the high power amplifier added sidebands ~ 60 dB smaller than the carrier at an offset frequency of 150 kHz. Even this small noise was enough to completely obscure the squeezing. It was only after replacement with another amplifier that the ability to measure squeezing was restored.

5.3 Phase Space Reconstruction

A reconstruction of the phase space distribution of the squeezing is also done for each time. The magnetization versus spinor phase shift data for 30 ms of evolution is shown in Figure 5.6(a). Each blue dot is the magnetization of a single run and the red dots are the means of all the runs for a given phase shift. In order to reconstruct the phase space distribution, this data is binned and interpolated, and then an inverse Radon transform is performed. The limited data needs to be conditioned for the transform. First, there is a slow drift in the imaging background that causes the mean value of the measured magnetization drift a few hundred atoms over the course of a day. While this is not a problem for noise measurements lasting an hour each, it presents a difficulty for the reconstruction which uses data from up to twenty hours. So for each 100 point data set used for the reconstruction, the mean of the points is subtracted. Then each data set is binned such that there are approximately 10 non-zero bins of $\langle L_z \rangle$ for the largest standard deviation set and 2-3 non-zero bins for the smallest. These bins along with the phase shift estimates are linearly interpolated to fill in the projection image (Figure 5.6(b)). Then an inverse Radon transform (Figure 5.6(c)) is performed with high frequency cutoff of $\sim 1/(150 \text{ atoms})$ ($\sim 1/(300 \text{ atoms})$ for the last two times) in order to smooth out artifacts from the finite data set, without widening the squeezed axis. From here, the circular edge artifacts are cropped and the image is rescaled from minimum to maximum to a range of 0 to 1. The zero value for the rescaling is determined by the peak of the histogram of the data points (Figure 5.6(d)), ensuring that the Gaussian noise of the background averages to zero. The actual probability distribution of the reconstruction is in the high count tail of the histogram. Once this background is subtracted out, the probability density is normalized by dividing by the sum of pixel values. The final reconstructions are shown in Figure 5.7. Figure 5.7 parts (a) and (b) are qualitatively similar to Figure 4.5 parts (b) and (c) respectively. The uncertainty ellipse from the quantum simulation is shown for comparison. The final parts are limited by the PSN of the measurement. While part (c) is similar to part (d) of Figure 4.5, the PSN makes it more

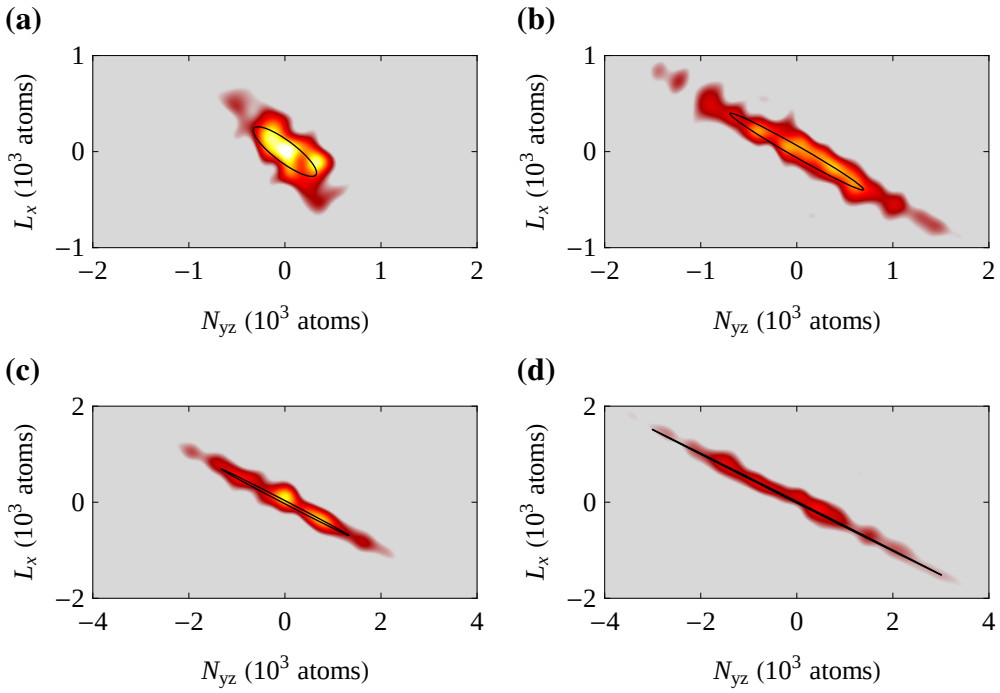

Figure 5.7: Reconstructions of the phase space for the investigated times after the beginning of the quench: **(a)** 15 ms, **(b)** 30 ms, **(c)** 45 ms, and **(d)** 65 ms. For the last two times the scale of L_x and N_{yz} are half the scale of the first two times. The black trace in each is the calculated $1/\sqrt{e}$ uncertainty ellipse from the quantum simulation.

difficult to compare. However, it is clear in Figure 5.7 parts (c) and (d) that the maximum quadrature squeezing parameter continues to grow similar to the theoretical plots.

5.4 Comparison of Theoretical Population Dynamics to Experiment

One of the goals for the theoretical simulations was to provide a more complete description of population dynamics and their fluctuations. With the two theoretical approaches in such good agreement, the simulations are now compared to the measured population dynamics from the experiment. In Figure 5.8(a) the mean (solid blue line) and the mean plus and minus standard deviation (light blue shaded region) of the fractional population of ρ_0 from the theoretical predications of Chapter 3 is shown again. On top of the theory plot are experimental measurements determined by the statistics of 30 runs shown as the mean with standard deviation error bars. The only free parameter used for the theory is the spinor

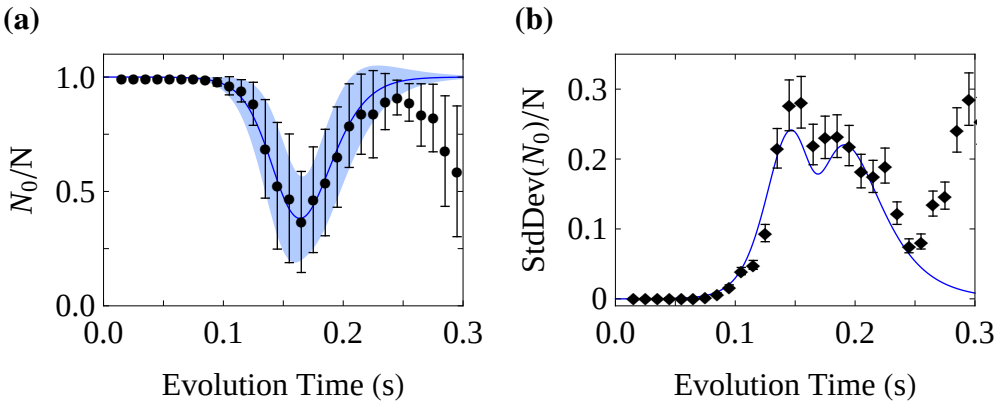

Figure 5.8: Time evolution of the population of $\bar{N}_0$ experimental values. **(a)** Fractional population in $m_f = 0$ for 45000 atoms $c = -2\pi\hbar \times 7.5$ Hz and a magnetic field that ramps to 210 mG. **(b)** The standard deviation of N_0 as a function of time.

dynamical rate chosen here as $c = -2\pi\hbar \times 7.5$ Hz to match the time of the minimum mean value. These match extremely well, both mean value and noise up to about 250 ms where clear deviations begin. However by this time 20% of the atoms have been lost due to the BEC lifetime of 1 s, which likely explains the deviation. Figure 5.8(b) shows the time evolution of the standard deviation as a measurement of the noise. The error bars are the error propagation estimate of the noise of the standard deviation depending on the value and the number of samples [136]. Though the noise by itself is not as good of a match, there is still evidence of the double peaked feature predicted theoretically. Once again at about 250 ms there are clear deviations.

5.5 Conclusion

This chapter describes the observation of quadrature squeezing in the spin-nematic subspaces of the spin-1 system. One of the squeezed subspaces is manipulated into the measurement basis by two SU(3) rotations implemented using microwave and RF oscillating magnetic fields. The measurement basis of L_z is detected by counting the atoms in Stern-Gerlach separated clouds of m_f projections using low noise fluorescence imaging. The maximum observed squeezing is $-8.3^{+0.6}_{-0.7}$ dB ($-10.3^{+0.7}_{-0.9}$ dB corrected for the PSN) limited

by detection noise. This measurement is the main result of this thesis. The measurement is compared to the quantum theoretical model developed in previous chapters with good agreement. The measured magnetization values are also used to reconstruct the phase space probability density which provide qualitative agreement with Figure 4.5. Finally the time evolution of the populations are measured and compared to theoretical predictions beyond the low-depletion limit imposed for the squeezing measurements. There is a good quantitative match for considerably longer than any other comparison in the literature, but eventually diverges likely due to atom loss.

CHAPTER VI

PHOTOASSOCIATION OF A SPIN-1 BEC

In this chapter, the measurements of spin dependent photo-association spectroscopy of a spin-1 BEC are described. Chronologically these measurements occured before the squeezing measurements and resulted in the publication of Ref. [57]. However these results were marginal for the goal of altering spinor population dynamics in a measureable way and have not led to further experimental studies. This topic is thus relegated to a secondary result of this thesis. This chapter closely follows Ref. [57] with some additional background information on molecular structure.

As was shown in Chapter 3, the magnetic properties of a spin-1 BEC depend on the sign of the difference of the two s-wave scattering lengths. For $a_2 - a_0 < 0$ the condensate is ferromagnetic and for $a_2 - a_0 > 0$ the condensate is anti-ferromagnetic. Further study of magnetic quantum gases could be greatly aided by the ability to control their magnetic properties. Since these properties are determined by the s-wave scattering lengths, they can in principle be tuned using Feshbach resonances which are a modification of the scattering length by near-resonant coupling to a bound state. Both magnetic [28, 52, 137] and optical [53–55] Feshbach resonances have been employed to dynamically change atomic s-wave scattering lengths. Unfortunately, for ^{87}Rb, the locations of the magnetic Feshbach resonances require a magnetic field larger than several Gauss, which has been shown to suppress spinor dynamics [16, 138]. However, Jack and Yamashita suggest using multiple photo-association lines from a vibrational level with a rich hyperfine structure, which would allow parameters that depend on spin dependent scattering lengths to be enhanced between lines from different scattering channels [56]. Specifically, variation of the spin dependent interaction strength could be optimized if there are adjacent molecular states that occur

through different scattering channels. In order to identify the existence of such lines, collision channel selective spectroscopy needs to be performed. This requires extensive control over the atomic hyperfine states and the Zeeman states of the colliding atoms which is not available for photo-association spectra from magneto-optical traps [57]. Although the effects of the hyperfine levels of the colliding atoms on the photo-association spectrum have been previously observed [139, 140], there had not previously been any photo-association spectroscopy that is directly selective of the collision channel of atoms.

The molecular states investigated in this thesis are a dimer of ^{87}Rb near the $5S_{1/2}$-$5P_{3/2}$ atomic dissociation limit. The states are in the $v = 152$ vibration level of a potential with 1_g symmetry dissociating to that limit. The binding energy of this level is only 24.1 cm^{-1} or $2\pi\hbar\times 723$ GHz below the D_2 line which marks the dissociation limit. This level was chosen since it is well known, has a good Franck-Condon overlap, has the prerequisite hyperfine structure, and is easily accessible by tuning the same diode lasers used for atom trapping. It has been studied before [141, 142], but here a spinor perspective is added.

In order to explain the experimental results, a quick overview of the relevant molecular structure is needed including the hyperfine structure along with a spinor analysis of the photo-association process. Then the experimental measurements are presented fit to the energies of the theoretical hyperfine structure. Finally an analysis of the experimental data to access the possibility of using optical Feshbach resonances to change spinor dynamics is presented.

6.1 Molecular Structure

Molecular states have a complicated level structure and classification. Here the focus will be only on the structure of homo-nuclear dimers near the dissociation limit where the molecule breaks into free atoms. These are sometimes called “physicist’s molecules” because of being near the limit of free atoms which greatly simplifies the understanding of their structure [143]. Molecules studied by other techniques are often near the ground state

vibrationally but are highly excited rotationally. The molecules made by photo-association of cold atoms are typically at the other extreme of high vibrational excitation[1] but minimal rotational. "Physicist's molecules" are very near the free atom limit and are typically only bound by a few tens of cm^{-1} while the ground states have binding energies in the several thousands of cm^{-1}.

6.1.1 Hund's Cases

The two extremes of vibrational energy above are linked by the Born-Oppenheimer adiabatic potentials which approximate the binding energy as a function of internuclear separation from deeply bound states to free atoms. The Born-Oppenheimer approximation treats the nuclei as relatively stationary as far as the electrons are concerned and solves for the electronic wave-functions of the continuously variable internuclear separation [144]. After the electronic wave-functions determine the potential for the nuclei, their rotational and vibrational energy is added in. These energies are dependent on the electronic state. As the average internuclear distance varies, so does the angular momentum couplings of the molecule. The Hund's cases classify the ways in which these angular momenta couple and their hierarchy of energies. The important energies are the spin-orbit interaction $|A|$ of the electrons, (L-S coupling); the spin-rotation interaction, whose magnitude is determined by the rotational constant $B = \frac{\hbar}{2\mu R^2}$ (where μ is the reduced mass of the nuclei); and the electrostatic interaction between electrons and the nuclei usually constraining the former to rotate with the latter. The electrostatic interaction is characterized by the difference in energy between adjacent electronic levels with different values of $\Lambda(\Omega)$[2] annotated as $|\Delta E|$. Almost all alkali dimer states can be classified as Hund's case (a), (b), or (c). It should

[1] Though in some cases they can be excited to the ground vibrational level. This is especially true of certain potentials whose only minima are at large internuclear separation such as the 0_g^- and 1_u dissociating to $P_{3/2}$.

[2] Due to the cylindrical symmetry of the molecule, the electronic orbital angular momentum L is not a good quantum number, but its projection onto the internuclear axis denoted by Λ is a good quantum number. For Hund's case (c), the L-S coupling is so strong that Λ is not a good quantum number and is replaced by the projection of the total electronic angular momentum Ω (Fig.6.1).

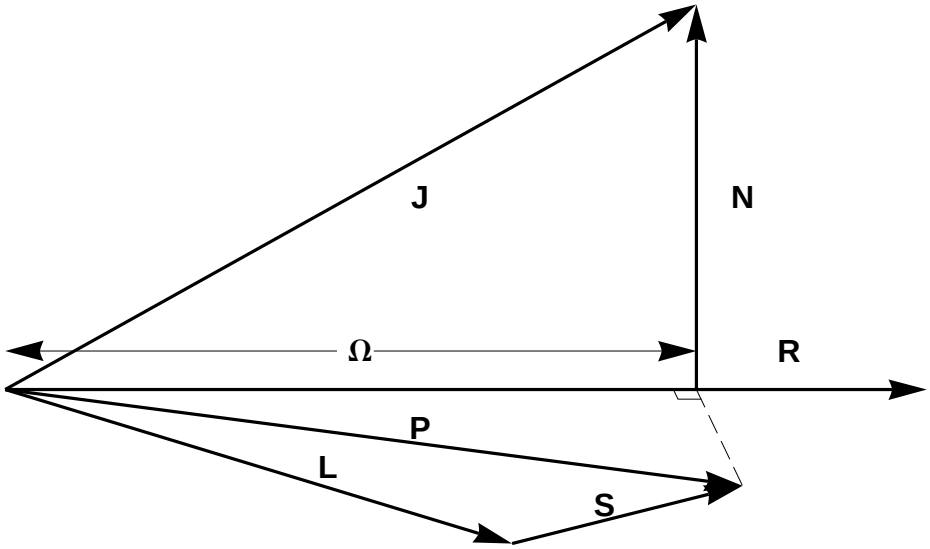

Figure 6.1: For Hund's case (c) the value of Ω is the projection of the rotational angular momentum, $\boldsymbol{J}$, onto the internuclear axis, $\boldsymbol{R}$. $\boldsymbol{J}$ includes the nuclear orbital angular momentum, $\boldsymbol{N}$, the total electronic angular momentum, $\boldsymbol{P}$, which itself is the coupling of the total electronic orbital angular momentum, $\boldsymbol{L}$, and total electronic spin, $\boldsymbol{S}$. Ω is also the projection of $\boldsymbol{P}$ onto the internuclear axis since the nuclear rotation vector is perpendicular to the internuclear axis by definition.

be noted that the Hund's cases are idealizations that molecular states only approximately conform to and continuously vary from one to another. The hierarchy of energies are as follows:

$$\begin{aligned} &\text{Hund's case (a)} && |\Delta E| \gg |A| \gg B \\ &\text{Hund's case (b)} && |\Delta E| \gg B \gg |A| \\ &\text{Hund's case (c)} && |A| \gg |\Delta E| \gg B. \end{aligned}$$

There are a few symmetries that further characterize the molecular states. Reflecting the electronic spatial wave function through a plane containing the inter-nuclear axis gives an overall sign of ± 1 to the wave function and is annotated with a superscripted + or $-$. This spatial parity symmetry is only valid for $\Lambda = 0$ states or when Λ-doubling makes the + or $-$ projections of $\boldsymbol{L}$ no longer degenerate. For homo-nuclear molecules, reflecting the molecular wave function through the center of charge multiplies the overall wave function by ± 1 giving gerade (even) and ungerade (odd) symmetries signified by a subscript g or u.

The states studied here are of the Hund's case (c) coupling scheme (Fig. 6.1). The parity symmetry of $\boldsymbol{L}$ does not work for Hund's case (c) since L is not a good quantum number. However, this symmetry is replaced by the parity of the overall electronic wave function including spin. Similar to the spatial parity case, it is only meaningful for states with $\Omega = 0$. The nomenclature of our symmetry, 1_g signifies that for the chosen level the projection of the total electronic angular momentum has a projection $|\Omega| = 1$ and the total wave-function has even symmetry.

6.1.2 Hyperfine-Rotation Hamiltonian

The energy due to the rotational angular momentum is related to $\boldsymbol{J}^2$ by the the R dependent constant B_v. However there is another angular momentum to consider, the total nuclear spin, $\boldsymbol{I}$. This is of the form of a standard magnetic interaction between the magnetic fields generated by the electronic motion and the due to the nuclear spin. Due to the cylindrical symmetry imposed, the coupling of $\boldsymbol{I}$ is not to the rapidly precessing $\boldsymbol{J}$ but its constant projection on the internuclear axis represented by $\boldsymbol{\Omega} = \Omega\,\hat{\boldsymbol{R}}$. This energy is proportional to $\boldsymbol{I}\cdot\boldsymbol{\Omega}$ related by the R dependent constant a_v. This hyperfine rotation Hamiltonian is written as the first line of Eq. (6.1). Unfortunately, for this particular case, J is not a good quantum number and so the operator $\boldsymbol{J}^2$ must be rewritten in terms of $\boldsymbol{F}^2$, $\boldsymbol{I}^2$, $\bar{F}_+$, $\bar{F}_-$, $\bar{I}_+$, $\bar{I}_-$, $F_{\bar{z}}$, and $I_{\bar{z}}$; where the projection, raising, and lowering operators for $\boldsymbol{F}$ and $\boldsymbol{I}$ are defined relative to the internuclear axis labeled here as $\bar{z}$.

For the 1_g potential, the molecular hyperfine energy is comparable to the rotational energy of the state. The effective Hamiltonian for the 1_g rotation-hyperfine structure can be written as [145]

$$\begin{aligned} H_{H-R} &= a_v\,\boldsymbol{I}\cdot\boldsymbol{\Omega} + B_v\,\boldsymbol{J}^2 \\ &= a_v\,I_{\bar{z}}\,\Omega + B_v\,\{\boldsymbol{F}^2 + \boldsymbol{I}^2 - 2\,\boldsymbol{J}\cdot\boldsymbol{I}\} \\ &= a_v\,I_{\bar{z}}\,\Omega + B_v\,\{\boldsymbol{F}^2 + \boldsymbol{I}^2 - 2\,(\boldsymbol{F}-\boldsymbol{I})\cdot\boldsymbol{I}\} \\ &= a_v\,I_{\bar{z}}\,\Omega + B_v\,\{\boldsymbol{F}^2 + \boldsymbol{I}^2 - 2\,F_{\bar{z}}I_{\bar{z}} - \bar{F}_+\bar{I}_- - \bar{F}_-\bar{I}_+\}. \end{aligned} \tag{6.1}$$

A matrix representation of this Hamiltonian is composed of fourteen 2×2 block diagonal sections and four diagonal states. Since the 2×2 block diagonal sections only mix states with the same values of F and I, the matrix can also be broken up by these quantum numbers. Furthermore, since changing the signs of $F_{\bar{z}}$, $I_{\bar{z}}$, and Ω results in a degenerate state, labeling of the states by F, $F_{\bar{z}}$, I, and $I_{\bar{z}}$, uses the convention that their sign relative to the sign of Ω is given. Removing these redundant degeneracies gives matrices for the $I = 1$, $F = 1$; $I = 3$, $F = 1$; $I = 3$, $F = 2$; and $I = 3$, $F = 3$ which are 2×2; 3×3; 5×5; and 6×6, respectively. The eigenvalues of the Hamiltonian for each combination of F and I are obtained by diagonalizing its corresponding matrix in the $|F, F_{\bar{z}}, I, I_{\bar{z}}\rangle$ basis set. The coupling is sufficiently weak that labeling the final states by the almost good quantum numbers of $F_{\bar{z}}$ and $I_{\bar{z}}$ is justified. Fig. 6.2 shows the Hamiltonian matrix broken up by the F and I quantum numbers. The diagonal elements are connected by arrows to their corresponding eigenvalues in the stick spectrum, which are labeled by the basis states. The parameters a_v, B_v used are from the later fit to data. The stick spectrum is labeled according to the dominant part of the corresponding eigenvectors.

6.1.3 Spinor Photo-association

In order to predict selection rules to aid in the analysis a spinor model of photo-association is adopted. In this model, the atoms are undergoing a spinor collision when the photo-association occurs. This is consistent with the standard model of photo-association since the transition rate depends on the square of the overlap of the scattering and excited state molecular wave-functions known as the Franck-Condon factor [143]. This factor is only significant for separations approximately between the classical turning points which in turn is on the order of the scattering length of the atoms. For two identical spin-1 bosons, the allowed s-wave collision channels are $F = 2$ or 0. Addition of the angular momentum of the colliding atoms and the PA photon specifies the possible total angular momentum, F, of the available molecular states for each scattering channel. Photo-association through the

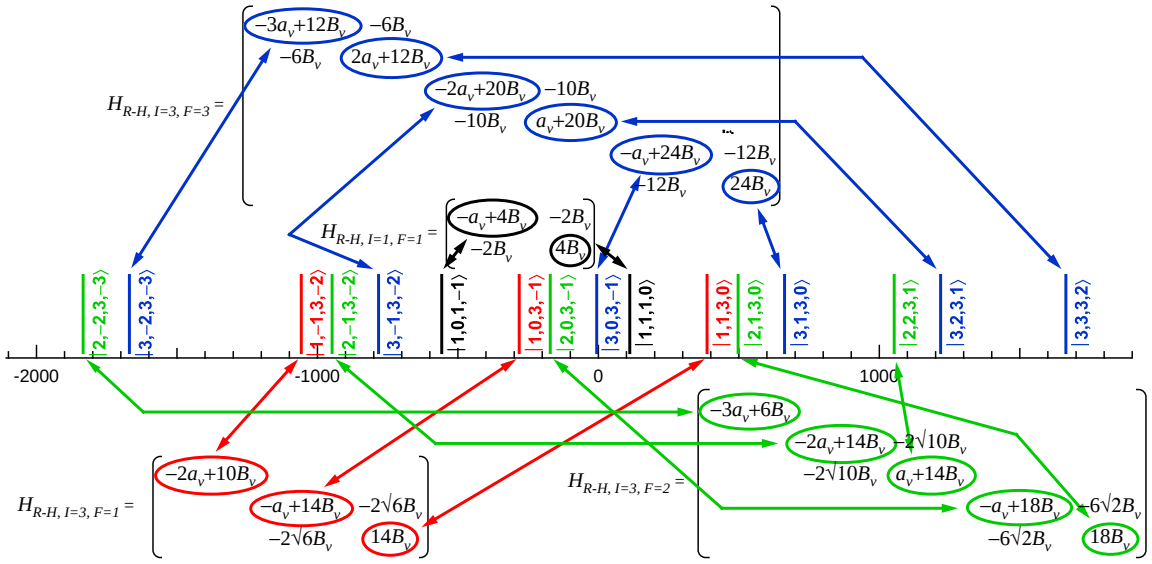

Figure 6.2: The hyperfine-rotation Hamiltonian is composed of 7 2×2 block diagonal elements and 2 states which do not mix. Here the sections of the matrix are sorted by the quantum numbers F and I. The diagonal elements are connected to their approximate eigenvalues by arrows. The eigenvalues in the spectrum are labeled by the $|F, F_{\bar{z}}, I, I_{\bar{z}}\rangle$ basis states of the Hamiltonian.

	$S=0,$ $I=2$	$S=0,$ $I=0$	$S=1,$ $I=3$	$S=1,$ $I=1$
$\lvert F, M_F\rangle = \lvert 0,0\rangle$	0	$\frac{3}{8}$	0	$\frac{5}{8}$
$\lvert F, M_F\rangle = \lvert 2,-2\rangle$	$\frac{3}{16}$	0	$\frac{63}{80}$	$\frac{1}{40}$
$\lvert F, M_F\rangle = \lvert 2,-1\rangle$	$\frac{3}{16}$	0	$\frac{63}{80}$	$\frac{1}{40}$
$\lvert F, M_F\rangle = \lvert 2,0\rangle$	$\frac{3}{16}$	0	$\frac{63}{80}$	$\frac{1}{40}$

Table 6.1: Probability of total S and I states for selected scattering channels of identical $f = 1$ atoms for s-wave scattering.

total spin 2 scattering channel gives excited state molecular F numbers of 1, 2, and 3 while the total spin 0 scattering channel restricts F to 1 [57], (See Fig. 6.3).

Photo-association is an electric dipole allowed transition which means it follows these selection rules as well. A simple model is that the electric dipole interaction acts only on the orbital angular momentum of the valence electrons and thus all the other angular momenta

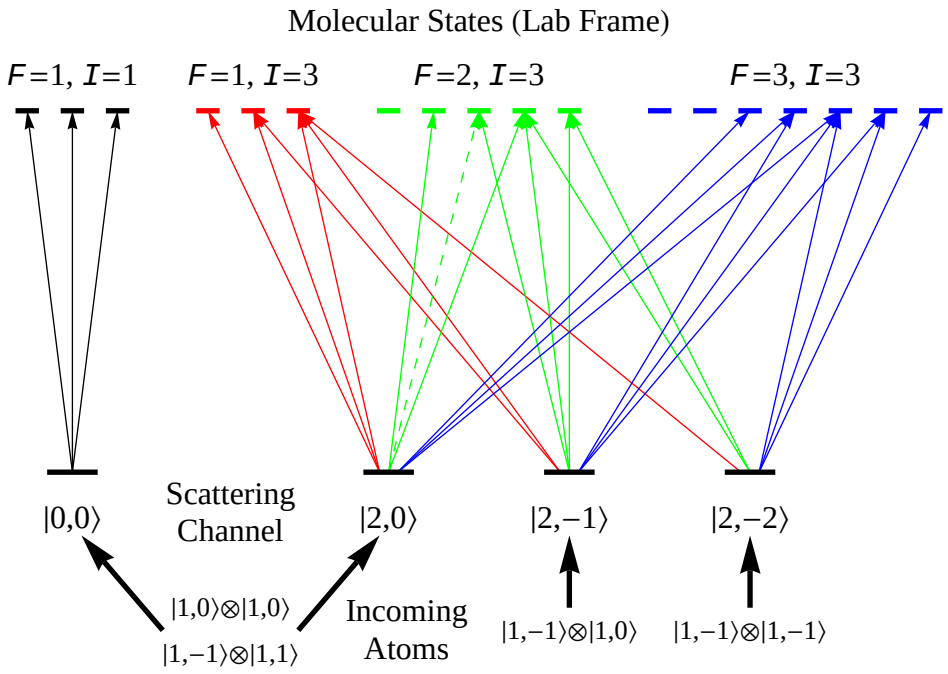

Figure 6.3: Spin dependent photo-association. The possible scattering channels of two colliding spin-1 atoms are shown for selected combinations of incoming atoms. Each channel may absorb a PA photon and transit to a bound excited molecular state $|F, M_F\rangle$. All Zeeman projections are in the lab frame relative to a quantization axis defined by an external magnetic field. The $\Delta F = 0$, $\Delta M_F = 0$ transition indicated by the dashed line is forbidden by the dipole selection rule.

at the time of the transition are unaffected. This allows an analysis of the combinations of the nuclear and electronic spins from the scattering channels of the ground state atoms to apply to the excited molecular states as well. When the $|F, M_F\rangle$ scattering channels are decomposed into their $|i, m_i\rangle$ and $|s, m_s\rangle$ components and recombined into $|I, M_I\rangle$ and $|S, M_S\rangle$ it is found that each scattering channel is at least dominantly associated with only one total nuclear spin. The results of this analysis are given in Table 6.1. Due to the gerade symmetry of the excited state and s-wave scattering, only $I = 1, 3$ are allowed. As seen in Eq. (6.1) the energy of the excited molecular state depends on $\boldsymbol{I}^2$, predicting that we can influence each scattering channel differently due to this spectroscopic difference. Molecular transitions also add another parity selection rule in that gerade and ungerade symmetry has to be different between the states of the transition. This is less important in the case of

colliding ground state atoms since they are a mixture of molecular ground potential states dissociating to $5S_{1/2} + 5S_{1/2}$ and have mixed parity with regard to this symmetry. However the electric dipole selection rule expressed as $\Delta F = \pm 1$ if $F = F'$ is significant to our analysis. Because of this the $|F_{2,0}\rangle$ scattering channel to $|F_{2,0}\rangle$ molecular state transition indicated by the dashed line in Fig. 6.3 is forbidden by the dipole selection rule and gives an experimental means to identify excited molecular states with $F = 2$ [57].

6.2 Measured Spectrum and Fit

The experiment is performed on ^{87}Rb condensates created directly in an optical trap [13]. After a condensate is formed, laser light is used to couple colliding atoms to excited molecular levels, which are subsequently lost from the trap. To measure the spectrum of the molecular excited states, the condensate population losses are measured for different frequencies of the photo-association (PA) light. The PA laser has a focused waist of 80 μm, and its frequency is actively stabilized with an accuracy ~5 MHz using a transfer cavity locked to a stabilized diode laser.

Figure 6.4 shows the observed photo-association spectrum taken using condensates with $|f_{1,-1}\rangle$ and $|f_{1,0}\rangle$ spin states. A portion of the $|f_{1,-1}\rangle$ spectrum was observed in [142]. To avoid mechanical excitation of the condensate, the PA light is ramped up to 3.8 mW in 50 ms, after which it remains on for 100 ms. Successive data points are separated by 5 MHz. The weaker lines identified by κ through π have been confirmed using higher intensity and longer probe time but are shown here under the same conditions as the stronger lines for consistency. The inset shows a line too weak to be made out in the larger scan. In order to enhance the visibility of this line, the PA light power is increased to 11 mW and left on for 300 ms, and it has been averaged over four scans. For each data point, an absorptive image of the condensate is taken 12 ms after the PA and trapping lasers are turned off. The condensate population is counted and normalized to an average value taken under the same conditions but with the PA light frequency detuned far from any of the molecular lines

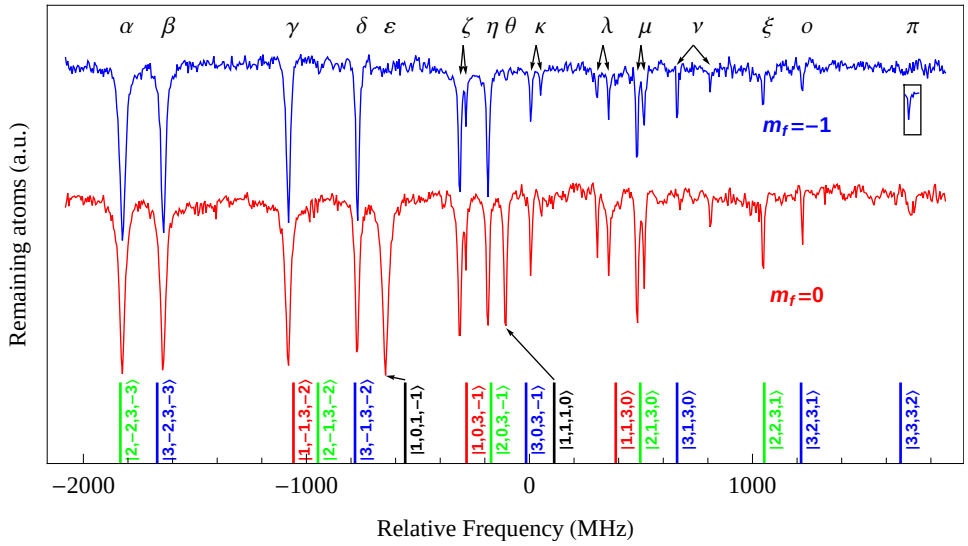

Figure 6.4: Observed photo-association spectrum of the $1_g(P_{3/2})$ $v = 152$ state for $m_f = -1$ (upper) and $m_f = 0$ (lower). These spectra are obtained after 150 ms of exposing a BEC to a PA light with 3.8 mW and 80 micron beam waist. The inset box for $m_f = -1$ is obtained using 350 ms and 11 mW with averaging to enhance visibility of this weaker line. Plots are offset for clarity. The origin of the hyperfine-rotation Hamiltonian fit is used as the zero point for the plot. A stick spectrum with approximate $|F, F_{\bar{z}}, I, I_{\bar{z}}\rangle$ labels is given.

observed in Figure 6.4.

6.2.1 Analysis of Excited Molecular States from Experimental Parameters

The experimental properties of the photo-association spectrum are used to identify the quantum numbers for the observed molecular lines. The most striking difference between the two PA spectra in Fig. 6.4 is that the lines ε and θ appear only for the condensate of the $m_f = 0$ spin state. As discussed before, two $m_f = -1$ atoms can only scatter through the total spin 2 channel, while two $m_f = 0$ atoms access both the total spin 2 and 0 channels, predicting that these lines occur through the total spin 0 scattering channel. If a condensate has a mixture of $m_f = -1$ and $m_f = 1$ they should also participate in the total spin 0 channel photo-association, while neither of these spin states should photo-associate on these lines if they coexist in the condensate only with an $m_f = 0$ spin state. To illustrate these predictions, PA spectra across the lines ε and θ are taken with condensates containing

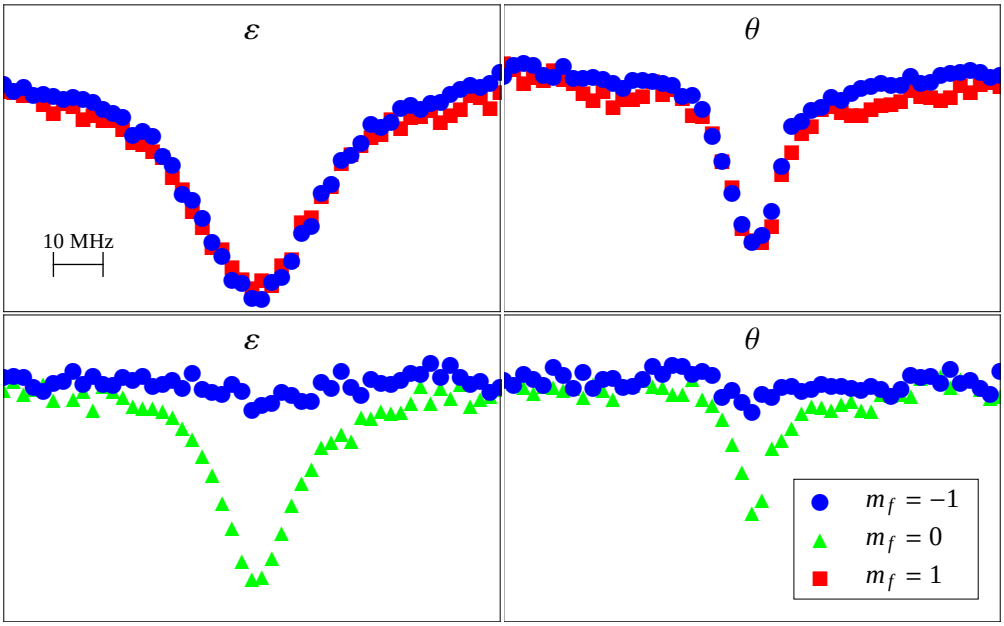

Figure 6.5: Photo-association spectroscopy of ε and θ with different mixtures of spin states. (Top) Lines ε and θ for mixture of $m_f = -1$ and $m_f = 1$ spin states. (Bottom) For mixture of $m_f = -1$ and $m_f = 0$. The observed data points corresponding to $m_f = (-1, 0, 1)$ spin states are represented by circles, triangles, and squares respectively.

different mixtures of spin states as shown in Figure 6.5.

The data shown in Figure 6.5(a) and (b) are taken with similar conditions to Figure 6.4, whereas in Figure 6.5(c) and (d) the photo-association power is decreased to 1.5 mW to reduce the mechanical effects on the $m_f = -1$ atoms caused by the rapid loss of the $m_f = 0$ atoms from the trap. The spin state combinations are prepared using microwave manipulation [16]. The populations of different m_f states are counted by spatially separating them using a Stern-Gerlach field during the time of flight. The observed data in this figure shows that the $m_f = -1$ and $m_f = 1$ spin states participate in the photo-association for the lines ε and θ if both of them coexist in the condensate, whereas if the $m_f = -1$ spin state coexists with the $m_f = 0$ spin state it does not participate in the photo-association process. This observation matches the analysis based on scattering channels and confirms that $F = 1$ for lines ε and θ.

To identify $F = 2$ PA lines the analysis that a $\Delta F = 0$, $\Delta M_F = 0$ transition from a

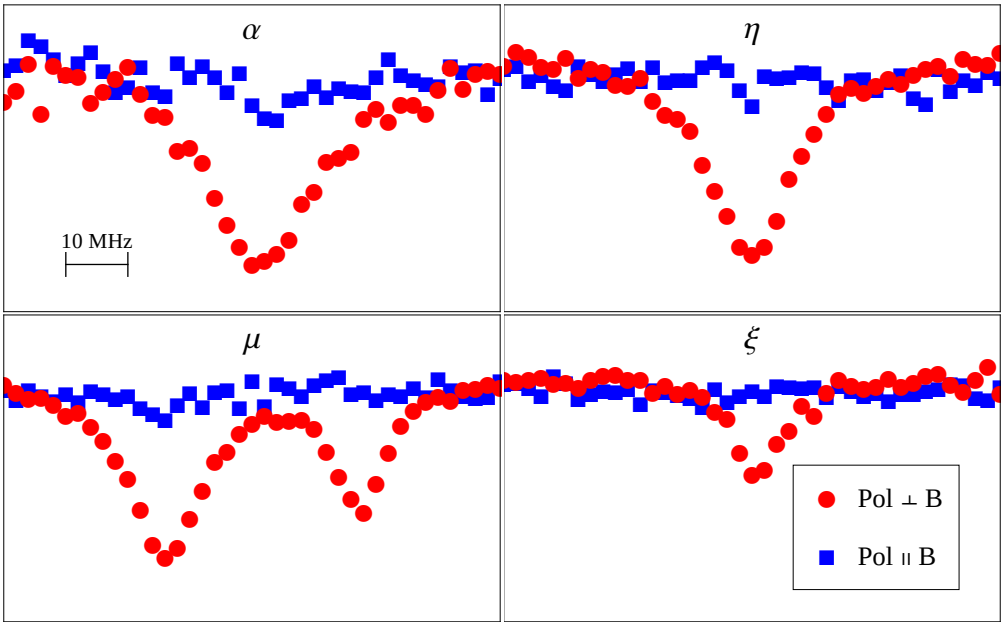

Figure 6.6: Photo-association spectroscopy through lines α, η, μ, and ξ for an $m_f = 0$ spin state condensate to an $F = 2$ molecular state. The data points are taken with the polarization vector of the PA light along (squares) and perpendicular to (circles) an external magnetic field.

two-atom collisional spin state $|F_{2,0}\rangle$ to a bound molecular state $|F_{2,0}\rangle$ is forbidden by the electric dipole selection rule is used as indicated in Figure 6.3. Therefore the lines with $F = 2$ are suppressed for an $m_f = 0$ spin state condensate with π-polarized PA light. Such lines are found by taking a PA spectrum of a pure $m_f = 0$ condensate in the presence of an external B-field of 1 G along the polarization of the PA light. The observed data for this case, shown in Figure 6.6, indicates that the lines α, η, μ, and ξ are absent. By changing the polarization of the PA light perpendicular to the quantization axis defined by the applied B-field, all of these lines reappear in the spectrum. The data shown in Figure 6.6 confirms $F = 2$ as a good quantum number for these lines. Figure 6.6(c) also indicates that the line μ is split into two $F = 2$ components.

From these observations and the spacing of the lines F and I are assigned for the observed lines. For the possible values of $F = 1$, 2, and 3 the eigenvalues of $\boldsymbol{F}^2$ are 2, 6, and 12. Therefore the separation between molecular states with $F = 1$ and 2 should be

2/3 of the frequency separation between the lines with $F = 2$ and 3. F numbers for the remaining lines are readily deduced by their spacing and order in each hyperfine grouping. The total nuclear spin for these lines is determined by the analysis of the decomposition of the scattering channels. Table 6.2 gives the assigned values of F and I for the observed lines.

6.2.2 Fit to Hyperfine-Rotation Hamiltonian

Now the energy separations of the observed spectrum of the $m_f = -1$ condensate of Figure 6.4 are fit to the hyperfine-rotation Hamiltonian using a least squares approach. Fitting parameters a_v, B_v, and the frequency offset ω_{offset}, are used in the thirteen equations generated by setting the diagonalization of the $I = 3$ matrices shown in Figure 6.2 equal to the energies in the spectrum. In the case of split lines, the stronger one is used for fitting. The least squares fit of these equations specifies a_v and B_v to be 667(5) and 27.6(1.3) MHz, respectively. The positions of the resulting eigenvalues are shown as a stick spectrum in Figure 6.4, which produces good agreement with the observed lines in the PA spectrum. The stick spectrum is labeled according to the dominant part of the corresponding eigenvectors, which is in agreement with the assigned quantum numbers in Table 6.2.

A few general comments should be made for the observed as well as predicted spectra. First, the molecular state corresponding to the $|F_{2,-1}, I_{3,-2}\rangle$ eigenstate is not observed under any experimental condition. This line is also absent in a scan of the $v = 153$ vibrational level. Second, predicted locations of the lines ε and θ corresponding to the $F = 0$ scattering channel are in poorer agreement with their observed locations compared to the other lines.

Table 6.2: Assigned total angular momentum and nuclear spin of the molecular states appearing in the PA spectra of Figure 6.4.

	α	β	γ	δ	ε	ζ	η	θ	κ	λ	μ	ν	ξ	o	π
F	2	3	1	3	1	1	2	1	3	1	2	3	2	3	3
I	3	3	3	3	1	3	3	1	3	3	3	3	3	3	3

These two lines are connected by arrows to their assumed eigenvalues in Figure 6.4. The separation of these lines is not simply a_v as the Hamiltonian indicates. Also the origin of the Hamiltonian for these lines appears to be different than for the $F = 2$ scattering channel lines. It is unclear as to whether different fit parameters or a revision to the Hamiltonian is needed to correct these deviations. Last, it is noted that some of the lines appear to be split on the order of 30 to 160 MHz. These split lines are connected to their labels in Figure 6.4 for clarity. The Hamiltonian presented in Eq. (6.1) predicts that all lines should be doubly degenerate and does not account for this splitting. This points to an additional interaction not considered in this simple model. These discrepancies could be useful for refinement of the molecular potential theory especially coupled with a systematic study of many vibrational levels.

6.3 Optical Feshbach Resonances and Changing c_2

The primary motivation for studying this system is to assess the suitability of multiple nearby optical Feshbach resonances to manipulate spin-dependent properties of a condensate. In an $f = 1$ spinor condensate, the magnetic properties are determined by the difference of the s-wave scattering lengths, $\Delta a = a_{F=2} - a_{F=0}$. The magnitude of Δa is proportional to the rate of spin changing collisions while its sign signifies whether the overall behavior is ferromagnetic or anti-ferromagnetic ($-$ or $+$ respectively). To determine the change in Δa due to the photo-association light, the observed data from Figure 6.4 is fitted to a theoretical formula for the inelastic loss rate (K_{inel}) in order to find the width and amplitude for each line as discussed in Ref. [54]. These fit parameters, along with the condensate density (n_0) and the measured field-free value for Δa of $-1.45(32)$ a_B [16], are then used to calculate the estimated change in Δa as shown in Figure 6.8(a).

In order to determine Δa from the spectrum, a few simplifying assumptions are made. For a given line, it is assumed that the effect on its associated scattering channel can be reduced to merely the measured photo-association spectrum of the line. The PA laser

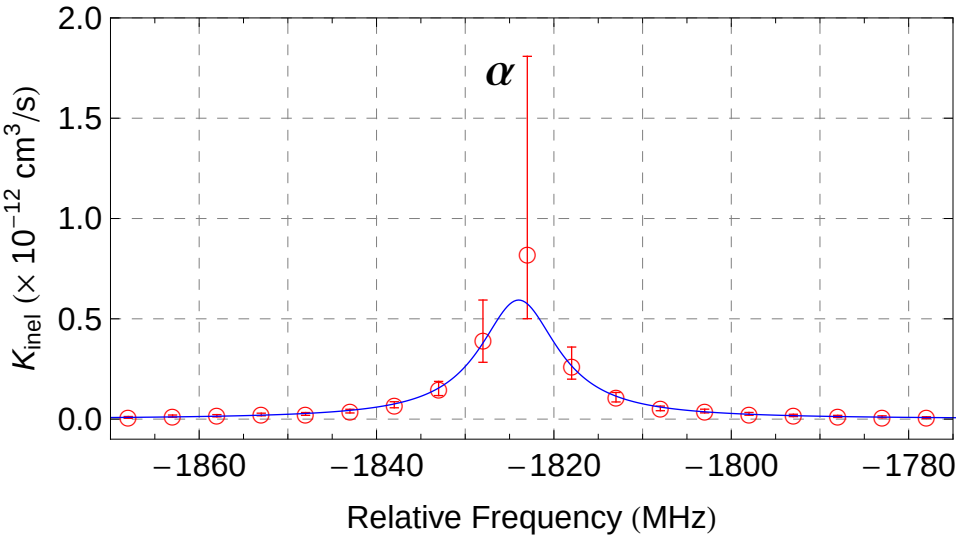

Figure 6.7: Sample of data fitting for K_{inel}. (Circles) Plot of the solution to Eq. (6.2) for the data on line α with error bars using estimated counting error of 5%. (Solid) Plot of Eq. (6.3) where the weighted least squares fit values are $A = 1.59 \times 10^{-12}\text{cm}^3$, $\Gamma_{\text{spon}} = 10.7\text{MHz}$, and $\omega_{\text{offset}} = -1824\text{MHz}$.

polarization has not produced an observable effect apart from suppressing the forbidden $|F_{2,0}\rangle \rightarrow |F_{2,0}\rangle$ transition used to identify the $F = 2$ molecular states. Since each line can comprise both π and σ transitions to the molecular states, this observation implies that the net effect of polarization is minimal. This can be understood by noting that the lab and molecular frames rarely coincide. Therefore, a given transition can see a definite polarization in one frame but mixed polarization in the other one. The polarization significantly affects the photo-association rate only if the transition is forbidden in one of the frames. It is therefore assumed that the measured line shapes for an $m_f = 0$ condensate are sufficient to determine their effects on the associated scattering channel.

6.3.1 Description of the Line Shape Fit

To calculate Δa from the spectrum, the data is fit to theoretical equations describing the fractional atom number in terms of the condensate density, pulse time, and the inelastic scattering rate. Since the rate depends on density, which lowers as the condensate is depleted, it is necessary to relate the fraction of remaining atoms to the inelastic scattering

rate by the equation [142, 146]:

$$\begin{aligned}\frac{N(\eta)}{N(0)} &= \frac{15}{2}\eta^{-5/2} \\ &\times(\eta^{1/2} + \tfrac{1}{3}\eta^{3/2} - (1+\eta)^{1/2}\tanh^{-1}\sqrt{\eta/(1+\eta)})\end{aligned} \tag{6.2}$$

where $\eta = 2K_{\text{inel}}n_0t$. By solving Eq. (6.2) for each point of the spectrum, we derive K_{inel} as a function of PA laser frequency. A peak condensate density of $n_0 = 10^{14}$ cm^{-3} is assumed, which is typical for this experiment. To estimate the error of this solution, Eq. (6.2) is also solved for the data point plus and minus the estimated counting error of 5%. This solution and the corresponding error bars for the α line are shown in Figure 6.7. The error bars for the points with the smallest fraction of atoms remaining are quite large. Because of this large error in the central points, a weighted fit is used for K_{inel}. Weights are determined by the inverse of the variance, which is approximated by squaring the 5% errors. This technique weights the points in the wings of the Lorentzian more heavily than the center. The data is fit for each line in the spectrum to determine parameters for calculating the change in Δa, where the following equations for a single line are used [54]:

$$K_{\text{inel}} = \frac{2\pi\hbar}{m}\frac{1}{k_i}\frac{\Gamma_{\text{stim}}\Gamma_{\text{spon}}}{\Delta^2 + (\Gamma_{\text{spon}}/2)^2} \tag{6.3}$$

$$a = a_{\text{bg}} + \frac{1}{2k_i}\frac{\Gamma_{\text{stim}}\Delta}{\Delta^2 + (\Gamma_{\text{spon}}/2)^2} \tag{6.4}$$

The parameter k_i is the wavenumber of the atoms in the condensate. These equations already assume that $\Gamma_{\text{stim}} \ll \Gamma_{\text{spon}}$ and thus that the PA intensity contributes negligibly to the line widths. The data for each line's K_{inel} are fit with Γ_{spon}, ω_{offset} ($\Delta = \omega_{\text{PA}} - \omega_{\text{offset}}$), and $A = \frac{2\pi\hbar}{m}\frac{1}{k_i}\Gamma_{\text{stim}}$ used as fitting parameters. Similar to the case of trap depth and inelastic scattering for near resonant atom trapping [112, 115], the change in scattering length varies as $1/\Delta$ while the inelastic collision rate varies as $1/\Delta^2$. A sample fit result for line α is shown in Figure 6.7, which demonstrates a good overlap between the fit and the calculated values of K_{inel}. In the following analysis we will use the values of K_{inel} deduced from this

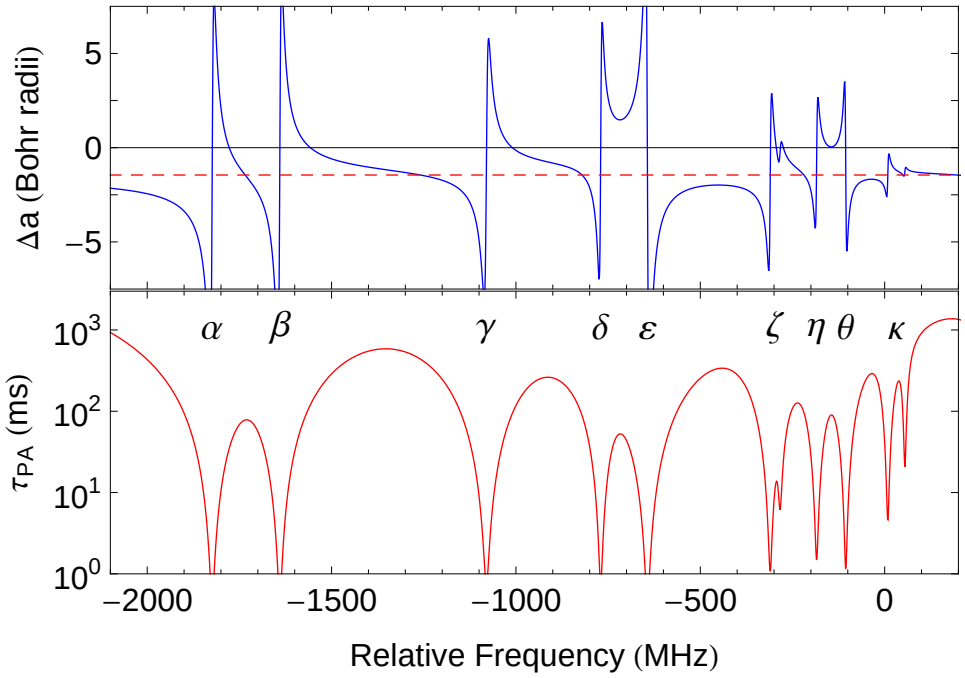

Figure 6.8: Calculated values for Δa and for the PA limited half-life of the BEC. The dotted line in top plot is the nominal value of Δa, which is $-1.45(32)$ Bohr radii for ^{87}Rb [16]. The intensity here is 33 times that used to take the spectra in Figure 6.4.

fitting technique instead of simply calculating K_{inel} from the observed data, since the fit is considered more reliable.

To obtain the total effect on K_{inel} and on Δa, it is assumed that for each scattering channel the effects of the PA laser can be calculated by summing the contributions from each photo-association feature associated with the channel. The total effect on a given channel's scattering length and the total inelastic scattering rate for both channels is given by

$$a_F(\omega_{\mathrm{PA}}) = a_{\mathrm{bg},F} + \sum_i \frac{m}{4\pi\hbar} A_{F,i} \frac{\omega_{\mathrm{PA}} - \omega_{\mathrm{offset},F,i}}{(\omega_{\mathrm{PA}} - \omega_{\mathrm{offset},F,i})^2 + (\Gamma_{\mathrm{spon},F,i}/2)^2} \tag{6.5}$$

$$K_{\mathrm{inel}}(\omega_{\mathrm{PA}}) = \sum_{F,i} A_{F,i} \frac{\Gamma_{\mathrm{spon},F,i}}{(\omega_{\mathrm{PA}} - \omega_{\mathrm{offset},F,i})^2 + (\Gamma_{\mathrm{spon},F,i}/2)^2} \tag{6.6}$$

6.3.2 Prospects for Changing the Magnetic Properties

Controlling the magnetic properties of ^{87}Rb condensates has three potential goals; changing the interaction from ferromagnetic to anti-ferromagnetic, reducing the spinor interaction to zero, and increasing the strength of the ferromagnetic interaction. Figure 6.8 shows the calculated values for making the condensate anti-ferromagnetic. In Figure 6.8, Δa and the photo-association induced loss-limited half-life, $\tau_{PA} = (K_{\text{inel}} \times n_0)^{-1}$, are plotted for different detunings for a PA intensity of 1250 W/cm^2, which is 33 times higher than used in our experiments. The photo-association limited lifetime is the time during which spin dependent dynamics can be observed before the condensate is depleted by the photo-association driven atom loss. With respect to changing the sign of Δa and hence magnetic nature of the condensate, one of the more promising frequency ranges is between lines δ and ε, which are associated with different scattering channels. Here the influences of the two lines reinforce each other producing a large positive change in Δa. In this region, as the intensity of the PA light increases, the atom loss rate increases continuously, while $|\Delta a|$ initially lowers to zero and then raises on the anti-ferromagnetic side. At $\approx$ 33 times the spectroscopy intensity, spinor dynamics occur at the same rate as the nominal value of $2\pi\times$4.3(3) rad/s [16], but with opposite sign. The PA limited half-life between lines δ and ε for this intensity is 50 ms. While 50 ms is a short half-life, the ratio of the spinor dynamical time to the PA limited half-life is $\approx$ 1.3 rad/halflife which is marginally sufficient to observe the effect in population dynamics.

The goal of reducing the spinor dynamical rate to zero can also be accomplished in this region. With an intensity $\approx$ 17 times the spectroscopy intensity, Δa goes to zero with a half-life of 100 ms. Regions a few 100 MHz to the blue of the $a_{F=2}$ lines are also promising for reducing Δa to zero with good lifetimes. To enhance the ferromagnetic nature of the condensate, the region between lines ε and ζ is promising. These lines are also from different scattering channels, but in the opposite order. Here the dynamical rate can be doubled with an intensity of 90 times the spectroscopic value, while maintaining a PA limited half-life

of 100 ms.

In principle it is possible to produce these effects simply by detuning 1 to 2 GHz to the blue or red of the entire vibrational level, while increasing the intensity. However, this is challenging for several reasons. First, the laser power needed exceeds several Watts which is a few thousand times the spectroscopic power. Second, at these detunings and intensities, other molecular states become important. Between the 1_g, 0_g^-, and 0_u^+ symmetries, resonant features can be found approximately every 10 GHz. Finally, the tensor light shift, which causes an effect similar to magnetic fields, is expected to be significant at these intensities [115, 147]. Even at the lower intensities proposed above, the effects of the tensor light shift warrants further study.

6.4 Conclusion

In conclusion, we have performed photo-association spectroscopy on a spin-1 condensate. This work identifies for the first time photo-association which distiguishes between total spin scattering channels for the same atomic states. The spin dependent photo-association spectrum was used to identify good quantum numbers for some of the molecular states, which are in agreement with theoretical predictions of a hyperfine-rotation Hamiltonian. The results of this study provide a test case to answer general questions about how to model molecular potentials in the presence of hyperfine and rotation interactions. The spectrum is also used to predict the photo-association limited lifetime and change in Δa. It is shown that optical Feshbach resonances to a molecular state with hyperfine structure can be used to alter the spin dependent mean-field interaction energy to change the spinor dynamics of the condensate with limited viability.

CHAPTER VII

CONCLUSION

The primary study of this thesis has been spin-nematic squeezing in a spin-1 condensate. The measurement of spin-nematic squeezing builds on the success of previous experiments of spin-mixing together with advances in low noise atom counting. The major contributions of this thesis have been linking theoretical models to experimental results and the development of the intuition and tools to address the squeezed subspaces. Understanding how spin-nematic squeezing is generated and how to measure it has required a review of several theoretical models of spin-mixing as well as extending these existing models. This extension reveals that the squeezing is between quadratures of a spin moment and a nematic (quadrapole) moment in abstract subspaces of the SU(3) symmetry group of the spin-1 system. The identification of the subspaces within the SU(3) symmetry allowed the development of techniques using RF and microwave oscillating magnetic fields to manipulate the phase space in order to measure the spin-nematic squeezing. Spin-mixing from a classically meta-stable state, the phase space manipulation, and low noise atom counting form the core of the experiment to measure spin-nematic squeezing. Spin-nematic squeezing is also compared to its quantum optics analogue, two-mode squeezing generated by four-wave mixing.

The attention paid to previous theoretical models and the extension of them has also increased the understanding of spin-mixing. The modeling of spin-mixing in the presence of a finite magnetic field based on the SU(3) symmetry was crucial. Extensive simulation from a fully quantum model and a semi-classical model using quasi-probability distributions was required to illuminate the dynamics which led to spin-nematic squeezing picture.

These simulations model dynamics beyond just the squeezing and give population dynamics as well. For the first time a quantum model and a semi-classical model of dynamics gave very similar results. Furthermore these simulations had detailed quantitative agreement with experimental measurements of the populations including non-Gaussian distributions in the population dynamics.

The other experimental study in this thesis was performing spin-dependent photo-association spectroscopy. Spin-mixing is known to depend on the difference of the strengths of the scattering channels of the atoms. Optical Feshbach resonances have been shown to be able to alter these scattering lengths but with prohibitive losses of atoms near the resonance. The possibility of using multiple nearby resonances from different scattering channels had been proposed to overcome this limitation. However there was no spectroscopy in the literature which analyzes for the different scattering channels of atoms for the same initial states. Through analysis of the initial atomic states, this thesis studied how the spin state of the atoms affects what photo-association resonances are available to the colliding atoms based on their scattering channel and how this affects the optical Feshbach resonances. From this analysis a prediction was made for the extent of alteration of spin-mixing achievable as well as the impact on the atom loss rate.

7.1 Spinor Theory

The spinor theory in this thesis has brought new insight primarily by combining previous theoretical work from several sources into a more complete whole. The quantum techniques are largely a review of the literature on the topic. However, inclusion of the effect of the quadratic Zeeman, which had been seldom done previously, turned out to be critical. More recent theoretical work that goes beyond the mean-field also includes this effect. The semi-classical mean-field technique is also largely a review, but with the addition of a quasi-probability distribution determined by the commutation relations of the su(3) Lie algebra of the spin-1 system. This semi-classical approach is validated by comparison to the exact

quantum technique with calculations that match to within 0.5% for population dynamics.

Using multiple theoretical approaches has greatly added to the understanding of this system. The formulation presented in this thesis predicts that the under-damped oscillation of populations observed experimentally is more due to dispersion than dissipation as previously put forward. From the semi-classical picture this dispersion is strongest near the separatrix, the feature of the phase space which marks the infinite period orbits and separates the oscillating spinor phase dynamical solutions form the solutions where the spinor phase winds. The states disperse due to the different evolution rates of nearby energy contours. This is important because the $m_f = 0$ state in a ferromagnetic condensate straddles the separatrix and thus has maximal dispersion. As this evolution proceeds, the spinor phase converges towards the separatrix and the probability distribution starts to evolve along it yielding population dynamics. The theory also predicts that for states away from the separatrix, the dispersion will have less influence and more steady oscillations will be observed. With the manipulation techniques developed, it will be possible to prepare states centered on any point in the mean-field phase space allowing detailed studies of the spinor dynamical rate and dispersion as a function of spinor energy.

In terms of the phase space, much of the previous work has been focused on the ground states and their symmetries rather than the covering symmetry of the spin-1 system. So the picture of the phase space and order parameter was extended to encompass the full SU(3) nature of the spin-1 system. This picture includes both polar and ferromagnetic order parameters. This picture also gives categories of the subspaces such as the familiar spin subspace composed of dipole moments and the unfamiliar nematic phase subspace composed of quadrupole moments. This analysis led to a fuller understanding of the dipole moments and quadrupole moments of the density matrix. Even more important was the su(3) commutator structure of the full phase space. The commutation relations trivially answer many questions about fluctuations of states and where squeezing can be observed. This picture allowed a broader comprehension of manipulations, going beyond simple spin

space rotations into quadrupole rotations such as the spinor phase shift. This analysis demonstrated how the mean values and distributions of the initial state moves around as it is manipulated. This picture could be a useful guide for future work including using these properties of the spin-1 BEC as a model for other systems.

7.1.1 Future Explorations of Spinor Dynamics

The experimental results described in this thesis all begin with a non-equilibrium spin configuration created by quenching an unmagnetized spin-1 system through a quantum phase transition. Although this thesis has focused on the squeezing that develops in this system, investigations of the dynamics and in particular the paths to equilibrium of closed quantum systems such as these are a very active area of theoretical research [148, 149], stimulated in part by experimental work in strongly interacting quantum gases [150]. Many of these investigations focus on the nature of the relaxation of an initially pure state, which is a particular interesting problem when the system is brought though a quantum phase transition such as the ferromagnetic quench.

In the course of the squeezing work, a considerable effort was devoted to developing the theoretical tools needed to be able to compare the results to theory. This work has paid extra benefits, providing a qualitative picture for spin-mixing and squeezing in a spin-1 system previously lacking. It also provides the ability to quantitatively compare experimental results of evolution. This evolution was analyzed for an initial non-equilibrium state of $m_f = 0$ with subsequent population dynamics after a ferromagnetic quench. The only free parameter used for the theory was the spinor dynamical rate chosen to match the time of the minimum mean value of the fractional population of the $m_f = 0$ component during the first oscillation.

The excited non-equilibrium spin configurations created by quenching the spin system is an interesting system to explore. Although some of these issues have been studied in

earlier experiments [15, 33–35], up to now none of the experiments have shown quantitative agreement with full quantum calculations, except in the perturbative limit explored at very early times. In this thesis, the mean and standard deviation of the fractional populations were measured as an experimental check of our model. Both the mean value and the standard deviation show excellent agreement with the calculation through most of the first oscillation. But these calculations also provide the amazing insight that the mean value and standard deviation are not sufficient to fully capture the highly non-Gaussian statistics of the evolved states. The experimental measurement of these predictions is already providing follow-on work. These results point the way to a host of fascinating explorations of out-of-equilibrium quantum systems [148, 149, 151–153], of which just the first glimpse is seen in this thesis.

Eventually the observed dynamics diverge from the model that has no dissipation, but on the well-motivated time scale of atom loss. By the time significant deviations are noted, 20% of the atoms have been lost, an effect which has been largely ignored in this thesis. The incorporation of atom loss as a model for dissipation into the theory discussed in this thesis will likely explain the dynamics even at longer times. Potential methods of including the atom loss are by taking into account its effects on the spinor dynamical rate for the semi-classical and quantum models and by using a quantum Monte-Carlo approach of anihilation operators on the Fock basis of the quantum simulation.

7.2 Spin-Nematic Squeezing

This thesis described the observation of quadrature squeezing in the spin-nematic subspaces of a spin-1 system. One of the squeezed subspaces was manipulated into the measurement basis of L_z by two SU(3) rotations implemented using microwave and RF oscillating magnetic fields. L_z was detected by counting the atoms in Stern-Gerlach separated clouds of m_f projections using low noise fluorescence imaging. The maximum observed squeezing is $-8.3^{+0.6}_{-0.7}$ dB ($-10.3^{+0.7}_{-0.9}$ dB corrected for the photo-electron shot noise) below the standard

quantum limit for the variance of the squeezing quadratures. This measurement is the main result of this thesis. The measurement was compared to a quantum theoretical model with good agreement. The measured magnetization values were also used to reconstruct the phase space probability density which provide qualitative agreement with the predictions of a semi-classical calculation.

The theoretical extensions discussed earlier were motivated by a need to understand and make quantitative predictions for the development of spin-nematic squeezing through spin-mixing from and initial state of $m_f = 0$. The perfect classical field $m_f = 0$ state does not evolve in the mean-field but it does for quantum solutions. This is because quantum fluctuations dominate for the classically meta-stable initial state of $m_f = 0$. These quantum fluctuations are key to the generation of squeezing in the spin-nematic subspaces. In the semi-classical picture the quantum fluctuations give a distribution about the $m_f = 0$ state which lies on the separatrix. Dispersion along the separatrix occcurs in each of two spin-nematic subspaces which are defined by the SU(3) symmetry of the spin-1 system. It is this dispersion which generates squeezing in the semi-classical view. In the lab frame, the system does not confine itself to either of the squeezed subspaces but rather undergoes rapid Larmor precession which transfers one subspace to the other. However, because the squeezing is identical in both subspaces, and the precession of the spin moments and quadrapole moments is synchronized, it is not necessary to track the precession in order to measure squeezing. The SU(3) picture also demonstrates how to manipulate the subspaces so that they can be measured.

The theory developed is also applicable to anti-ferromagnetic interactions since it is just a change of sign of the spinor dynamical rate. Anti-ferromagnetic condensates starting in pure $m_f = 0$ are also predicted to exhibit spin-nematic squeezing. However for similar magnitude of spinor dynamical rate and magnetic field the amplitude is not as large as the ferromagnetic case, but still large enough to stretch the limits of measurement. It does have the interesting feature that the population dynamics never leave the low depletion regime.

This results in the phase space being cyclically squeezed and un-squeezed.

7.2.1 Future Squeezing Work

Spin-nematic squeezing is a new type of squeezing for atomic systems. The generated squeezing could be used as a resource for other experiments. A principle motivation for creating squeezed states in the laboratory is to enable more precise measurements of important quantities such a frequency, magnetic fields, etc. Although the experimental work in this thesis has demonstrated record levels of squeezing, the path to improved precision in real-world measurements is not clear, just as the demonstration of a qubit does not necessarily point the way to a useful quantum computer. Just as spin-squeezing has been used to enhance both magnetometry and clock performance, perhaps spin-nematic squeezing can find similar application, but maybe in ways not possible for spin-squeezing. The simplest version is just to manipulate the phase space to turn the spin-nematic squeezing into spin-squeezing. However it may be that a way can be found to take advantage of the SU(3) symmetry of the system. The SU(3) analysis here will enable designing proof-of-principle experiments to demonstrate its metrological uses.

A strength of squeezing in this system is that it is robust to magnetic field noise. The observation of this insensitivity to Larmor rotation would seem to be a poor starting point for a magnetometer. However, it is simple to rotate the spin-nematic squeezing into a magnetically sensitive orientation. This transfer is field sensitive, and a subsequent measurement of N_0 provides a measurement of the field that will be noise limited by the quadratures of the squeezed state. Furthermore by transferring between field sensitive and insensitive states the interaction may be more precisely controlled thus reducing the technical noise.

Squeezed states in SU(3) is largely uncharted territory, which could be explored in greater depth. Although this thesis has discussed the quadrature squeezing from the perspective of spin-nematic degrees of freedom, it also admits description (in the low depletion limit) in the language of two-mode squeezing familiar from quantum optics, in which the

$m = \pm 1$ states are the signal and idler and the $m = 0$ state serves as the pump and the local oscillator. It will be possible to draw upon the extensive work with optical squeezed states in order to guide further explorations in investigations of entanglement and related studies of quantum information with continuous variables protocols including EPR correlations, quantum teleportation, etc [154]. Quantum teleportation is normally done with photons, but there are proposals to do these experiments with matter waves [155–157]. This raises the interesting possibility of teleportation of quantum states completely with atoms. Finally, the fact that the squeezing is explicitly in nematic variables provide potential avenues to make important connections to (itinerant) condensed matter quantum magnet systems.

7.3 Photo-association Spectroscopy

The other group of experiments in this thesis was spin-dependent photo-association spectroscopy. This was done to assess the possibility of using multiple optical Feshbach resonances from different scattering channels to change the nature of spin-mixing. The basic required structure was identified spectroscopically in that there exist photo-association lines that occur for only one of the two scattering channels. Unfortunately in the end, the analysis indicated that the technique was marginal since the lifetime due to off-resonant photo-association was still reduced too much compared to the time for population dynamics to see the effect. While the investigated vibrational level was marginal, a spectroscopic search of many levels may yet provide a better candidate. What is needed is a similar hyperfine structure, but with stronger lines, narrower lines, or a more favorable spacing of the lines. It may be better to consider the 1_g potential dissociating to the $P_{1/2}$ instead of the $P_{3/2}$ since it does not pre-dissociate. This would be a rather extensive spectroscopic project, but would have other benefits to molecular spectroscopy and atomic physics. One of the early drives to do photo-association spectroscopy was the determination of the scattering length for Bose-Einstein condensate feasibility calculations. The analysis of the hyperfine-rotation energies to find the zero offset from many vibrational levels could improve the accuracy

the measurement of the scattering length by reducing the uncertainty of the rotationless potential. Since there are lines for both the total spin 0 and 2 scattering channels, this may even allow a more accurate determination of the difference of the scattering lengths.

The improvements in the understanding of the phase space and state preparation techniques developed later for the squeezing measurements may revitalize the effort to change spinor dynamics. With proper state preparation, population dynamics are immediate. More importantly with a well-chosen prepared state the question of whether the dynamics are ferromagnetic or anti-ferromagnetic can be answered in 10-20 ms merely by observing if the population of $m_f = 0$ in the prepared state decreases or increases. Another interesting idea that does not require intensities that make for challenging lifetimes is a small modulation of the spinor dynamical rate. Several proposals based on this technique have been put forth [158–165]. Similarly, using the AC shift of off resonant microwaves could be used to modulate the quadratic Zeeman effect. These ideas may make it possible to observe an internal state analogue of the the AC Josephson effect found by Shapiro [166, 167].

7.4 Problems and Potential Improvements

Like any experimental system, ours has problems that are found out after construction that must be worked around until the apparatus can be rebuilt. Summarized here are a few problems that could be solved in a new generation of the experimental apparatus.

The long wait of 15 s to saturate the MOT is the longest wait time in the experimental cycle of $\sim$ 20 s. Reduction of this wait would significantly improve the data taking ability and allow overcoming some of the problems from slow drifts while taking the data. One solution being explored is using a cold atomic beam from a 2D MOT to load the 3D MOT for the experiment. It is expected to reduce the loading time to less than 1 s while also reducing the background vapor pressure from the unused ^{85}Rb isotope. This also removes problems caused by the getter. Currently its glow in the near infrared is a time varying background to the imaging.

Another problem is in the construction of the vacuum chamber. The zero-length windows on the octagon use Kovar, an iron-nickel alloy, for the transition between the glass and the stainless steel flange. This transition sleeve is ferromagnetic and causes several hysteresis problems as well as semi-permanent magnetization of the chamber. This is exacerbated by having the bias coils directly wrapped onto some of these windows. This has been worked around this for some time, mainly by running the experiment for hours before sensitive data to get the magnetic fields into a stable hysteresis pattern. In order to solve these problems, the solution is a rebuild without ferromagnetic parts, either the same stainless steel chamber with non-magnetic windows or even further to a glass cell with no metallic parts at all.

The largely organic growth of the experiment over the years has resulted in a somewhat haphazard addition of electronic components. Because of this, the power distribution and grounding have suffered which results in an experiment that has problems with ground loops. The most common effect is the small fluctuation of many parameters at 60 Hz and its harmonics. Synchronizing the experimental sequence trigger with the AC line has been needed to get consistent results. It is likely that the only solution is to rebuild the experiment from the ground up while paying careful attention to these issues. This would require taking the experiment off-line for a few months or the construction of a new completely independent apparatus.

APPENDIX A

^{87}RB HYPERFINE GROUND STATES IN STATIC AND OSCILLATORY MAGNETIC FIELDS

Key to understanding several of the energies and techniques used in this thesis is the interaction of ^{87}Rb atoms in the ground electronic state, $5^2S_{1/2}$, with internal and external magnetic fields. The internal magnetic interaction results in the hyperfine splitting of the ground electronic state. The external interactions describe the Zeeman shifts of the states in magnetic fields including the RF and microwave transitions used to manipulate states, the spinor energy due to static magnetic fields, and phases imparted by magnetic fields. The sections on hyperfine splitting and interactions with static magnetic fields principally summarizes the relevant portions of Ref. [113] of similar title. The transitions section extends this work and incorporates elements of Refs. [112, 113, 129] to formulate a relatively simple set of solutions for the magnetic dipole transitions between various states in the electronic ground state hyperfine manifold. For the microwave transitions this is extended further to the dressed state picture to describe relatively far off-resonant energy shifts and rapid near resonance phase shifts of individual components.

A.1 Ground State Hyperfine Splitting

In hydrogen, it is relatively easy to calculate the magnetic interaction between the nuclear spin and electronic spin resulting in the ground state hyperfine splitting. The appropriate constant for the magnitude can be calculated from simple known values. In the alkalies, the form is similar and it is possible to estimate the appropriate constants for the interaction. However the calculation of the constant is done with some difficulty and so here the form will be used with the measured value for the constant. Calculation of the hyperfine splitting

of the ^{87}Rb electronic ground state follows the standard formulation where the nuclear and electronic angular momenta add to form a composite particle $\boldsymbol{F} = \boldsymbol{I} + \boldsymbol{S}$ [1] and the energy of the interaction is proportional to the dot product of the two. The Hamiltonian of the interaction is [113]:

$$H_{hfs} = A_{hfs}\, \boldsymbol{I} \cdot \boldsymbol{S} \tag{A.1}$$

where A_{hfs} is a measured constant with value $\hbar \times 3.417$ GHz. Since $\boldsymbol{I} \cdot \boldsymbol{S} = \frac{1}{2}(\boldsymbol{F}^2 - \boldsymbol{I}^2 - \boldsymbol{S}^2)$ this has eigenvalues $\frac{1}{2}\, A_{hfs}\, (F(F+1) - I(I+1) - S(S+1))$. For $F = 1$ and $F = 2$ this evaluates to $-\frac{5}{4}\, A_{hfs}$ and $\frac{3}{4}\, A_{hfs}$ respectively for a total splitting of $2\, A_{hfs}$. Thus ^{87}Rb has a ground state hyperfine splitting of $\hbar \times 6.834$ GHz which is in the microwave regime.

A.2 Static and Slowly Varying Magnetic Fields

To calculate the effect of a static external magnetic field chosen along z, it is necessary to add the energy [113]:

$$H_B = \mu_B\, \boldsymbol{B} \cdot (g_I\, \boldsymbol{I} + g_S\, \boldsymbol{S}) = \mu_B\, B_z\, (g_I\, I_z + g_S\, S_z) \tag{A.2}$$

to the Hamiltonian. The interaction is scaled by the Lande g factors g_I and g_S (g_I is a measured value for the ^{87}Rb nucleus). Since this Hamiltonian is not in the same basis as H_{hfs} one must be treated as a perturbation to the other or the combined Hamiltonian must be diagonalized, usually in the $|F, F_z\rangle$ basis. See Table A.1.

For low fields, H_B is the perturbation, and g_F can be calculated for each F manifold such that:

$$H_B \cong \mu_B\, B_z\, g_F\, F_z \tag{A.3}$$

$$g_F = g_S \frac{F(F+1) - I(I+1) + S(S+1)}{2F(F+1)} + g_I \frac{F(F+1) + I(I+1) - S(S+1)}{2F(F+1)} \tag{A.4}$$

The two g_F values are nearly identical in magnitude but opposite in sign. The splittings of the energies of the m_F within a manifold have frequencies commonly associated with the

[1] In this appendix, uppercase symbols are used to represent total atomic parameters similar to most elementary texts. Unlike elsewhere in this thesis, there is no chance of confusion with many particle states since everything in this appendix describes single atom interactions with magnetic fields. Also note that the single valence electron is in an S state, therefore $L = 0$ and $J = S = 1/2$.

Table A.1: Decomposition of $|F, F_z\rangle$ into $|I, I_z, S, S_z\rangle$ components.

$$
\begin{aligned}
|F_{1,-1}\rangle &= \sqrt{\tfrac{1}{4}}\ |I_{3/2,-1/2}S_{1/2,-1/2}\rangle - \sqrt{\tfrac{3}{4}}\ |I_{3/2,-3/2}S_{1/2,1/2}\rangle \\
|F_{1,0}\rangle &= \sqrt{\tfrac{1}{2}}\ |I_{3/2,1/2}S_{1/2,-1/2}\rangle - \sqrt{\tfrac{1}{2}}\ |I_{3/2,-1/2}S_{1/2,1/2}\rangle \\
|F_{1,1}\rangle &= \sqrt{\tfrac{3}{4}}\ |I_{3/2,3/2}S_{1/2,-1/2}\rangle - \sqrt{\tfrac{1}{4}}\ |I_{3/2,1/2}S_{1/2,1/2}\rangle \\
|F_{2,-2}\rangle &= |I_{3/2,-3/2}S_{1/2,-1/2}\rangle \\
|F_{2,-1}\rangle &= \sqrt{\tfrac{3}{4}}\ |I_{3/2,-1/2}S_{1/2,-1/2}\rangle + \sqrt{\tfrac{1}{4}}\ |I_{3/2,-3/2}S_{1/2,1/2}\rangle \\
|F_{2,0}\rangle &= \sqrt{\tfrac{1}{2}}\ |I_{3/2,1/2}S_{1/2,-1/2}\rangle + \sqrt{\tfrac{1}{2}}\ |I_{3/2,-1/2}S_{1/2,1/2}\rangle \\
|F_{2,1}\rangle &= \sqrt{\tfrac{1}{4}}\ |I_{3/2,3/2}S_{1/2,-1/2}\rangle + \sqrt{\tfrac{3}{4}}\ |I_{3/2,1/2}S_{1/2,1/2}\rangle \\
|F_{2,2}\rangle &= |I_{3/2,3/2}S_{1/2,1/2}\rangle
\end{aligned}
$$

radio frequency (RF) regime. This low field regime is known as the *anomalous Zeeman effect*.

The nuclear part of Eq. (A.4) is often neglected, however it makes the g_F differ in magnitude by $\sim 0.5\%$. It is responsible for the splitting of two nearly degenerate pairs in the microwave spectrum. At one Gauss the 2 pairs of $\pm\Delta$ transtions in Fig. are $\sim \pm 700$ kHz from the clock transition, but each pair is split by ~ 3 kHz due to the nuclear contribution to the energy which makes them easily resolvable.

For high fields, the $g_S S_z$ part of the interaction dominates and the states are grouped by S_z. This regime is know as the *Paschen-Back effect* or *normal Zeeman Effect* for hyperfine structure [113].

For intermediate values, it is necessary to diagonalize the full Hamiltonian. The eigenvalues give the famous *Breit-Rabi formulas* [113] that are approximately linear for small magnetic fields where F_z is a good quantum number (Zeeman regime), and approximately

linear for larger fields where I_z and S_z become the good quantum numbers, but non-linear in between. These eigenvalues are typically expanded in a power series. At low fields the energies are represented as linear in magnetic field and the shifts are called the linear Zeeman effect. The next order term, quadratic in magnetic field, is called the quadratic Zeeman effect. This is not to be confused with Hamiltonians where the energy is quadratic in magnetic field. The quadratic term in the power series expansion is responsible for the well known "clock shift" experienced by Rb atomic clocks in finite magnetic fields.

In order to calculate the intermediate values, H_B must be added to the diagonal H_{hfs} and diagonalized for the chosen B_z. In the $|F, F_z\rangle$ basis we have

$$H_B = \mu_B B_z \times \begin{pmatrix} \frac{g_S - 5g_I}{4} & 0 & 0 & 0 & \frac{-\sqrt{3}g_S + \sqrt{3}g_I}{4} & 0 & 0 & 0 \\ 0 & 0 & 0 & 0 & 0 & \frac{-g_S + g_I}{2} & 0 & 0 \\ 0 & 0 & \frac{-g_S + 5g_I}{4} & 0 & 0 & 0 & \frac{-\sqrt{3}g_S + \sqrt{3}g_I}{4} & 0 \\ 0 & 0 & 0 & \frac{-g_S - 3g_I}{2} & 0 & 0 & 0 & 0 \\ \frac{-\sqrt{3}g_S + \sqrt{3}g_I}{4} & 0 & 0 & 0 & \frac{-g_S - 3g_I}{4} & 0 & 0 & 0 \\ 0 & \frac{-g_S + g_I}{2} & 0 & 0 & 0 & 0 & 0 & 0 \\ 0 & 0 & \frac{-\sqrt{3}g_S + \sqrt{3}g_I}{4} & 0 & 0 & 0 & \frac{g_S + 3g_I}{4} & 0 \\ 0 & 0 & 0 & 0 & 0 & 0 & 0 & \frac{g_S + 3g_I}{2} \end{pmatrix} \tag{A.5}$$

$$H = H_{hfs} + H_B \tag{A.6}$$

Both the electronic spin and nuclear have contributions to the energy, but the nuclear is much smaller and can often be ignored. However the near degeneracy of the linear approximation of the shifts of the $F = 1$ and $F = 2$ can readily be resolved in fields around a Gauss. See Figure A.1.

Spinor energies and phases. The magnetic field energy is important to spinor dynamics as well. Since spinor dynamics in the $F = 1$ manifold can convert two $m_F = 0$ atoms into

one each in $m_F = 1$ and $m_F = -1$ and vice versa, the difference in magnetic energies determines the bias with which these reactions go. The linear part of the magnetic interaction is equal and opposite for the latter combination and so cancels out. However, the quadratic term has the same sign and contributes $\sim \hbar \times 72$ Hz/G^2 per atom.

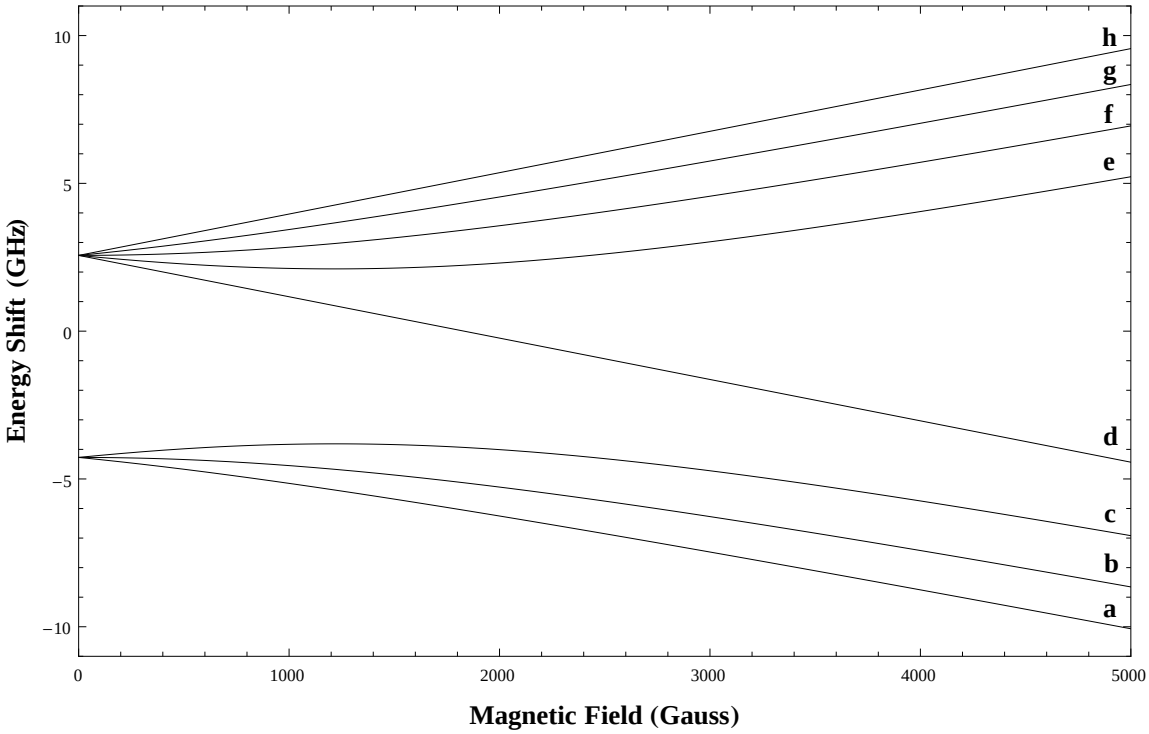

Figure A.1: Plot of energy levels in ^{87}Rb ground hyperfine manifold as a function of magnetic field. These energies are obtained by diagonalizing Eq. (A.6). The letters follow the normal nomenclature to describe scattering channels for Feshbach resonances: a, $|F_{1,1}\rangle$; b, $|F_{1,0}\rangle$ c, $|F_{1,-1}\rangle$; d, $|F_{2,-2}\rangle$; e, $|F_{2,-1}\rangle$; f, $|F_{2,0}\rangle$; g, $|F_{2,1}\rangle$; h, $|F_{2,2}\rangle$. (See text.)

A.3 Oscillatory Magnetic Fields

Since $\Delta L = 0$, transitions between states in the hyperfine ground state are forbidden to electric dipole interactions. However, many are allowed with the weaker magnetic dipole transitions where oscillating magnetic fields are important. In order to analyze the effects of oscillatory magnetic fields, the model of the spin flip transition will be used. The effect on the nuclear magnetic moment will be neglected due to it weakness and consequently slow dynamics relative to the electron spin. The oscillatory field will be treated as a perturbation on the quantizing field B_z. By treating the problem as a spin flip, the quantum mechanics reduces simply to several copies of the spin-1/2 in an oscillatory magnetic field problem. Some authors treat the aptly named RF rotation part of this problem with a classical rotation matrix approach along with classical spin precession in a rotating frame for the microwave regime [122]. Using the spin flip model for all unifies the RF and microwave portions under one semi-classical formalism.

A.3.1 Spin Flip Transitions

Key to the spin flip model is the interaction of the oscillating magnetic field with the spin of the valence electron. Like the static magnetic field problem, the interaction Hamiltonian is $H'_B = \mu_B g_S \boldsymbol{B}' \cdot \boldsymbol{S}$ where $\boldsymbol{B}' = \boldsymbol{B}'_0 \cos \omega_B t$. However, since the perturbing field does not set the quantization axis, we must consider fields in the x, y, and z axes. Fortunately, there is already an easy formalism for dealing with this in the Pauli spin matrices where $S_i = \frac{\hbar}{2}\sigma_i$. Defining the reduced Rabi rate for a given component B'_i, $\Omega_{red} = \frac{\mu_B g_S B'_i}{2\hbar}$ (If B'_i is along the z axis then $\Omega_{red} \equiv \Omega_{clock}$), then $H'_B = \hbar\, \Omega_{red}\, \sigma_i \cos \omega_B t$, with

$$\sigma_x = \begin{pmatrix} 0 & 1 \\ 1 & 0 \end{pmatrix} \quad \sigma_y = \begin{pmatrix} 0 & -i \\ i & 0 \end{pmatrix} \quad \sigma_z = \begin{pmatrix} 1 & 0 \\ 0 & -1 \end{pmatrix}.$$

These matrices and the $|I, I_z, S, S_z\rangle$ decompositions listed in Table A.1 are easily used to generate the matrix representation of the perturbing Hamiltonian for the 8 $|F, F_z\rangle$ states of the hyperfine manifold for each field orientation individually. Evaluation of these operators

follows from a projection of the $|F, F_z\rangle$ on to the $|I, I_z, S, S_z\rangle$ basis states. A convenient order is to go first by I_z and then by S_z so that the operator becomes 4 block diagonal copies of the Pauli spin matrix. With these operators an arbitrary field direction can be made by linear combinations. Two important linear combinations are $\sigma_\pm = \frac{1}{\sqrt{2}}\left(\sigma_x \pm i\sigma_y\right)$. These represent rotating fields transverse to the quantization axis or circular polarization. However since the experimental sources are typically linearly polarized, the focus here will be on the Cartesian forms. Furthermore, since the component of the oscillatory field perpendicular to the bias can be chosen as the x axis, there is no need to separately consider σ_y.

$$\begin{aligned}\langle F, F_z|\sigma_i|F, F_z\rangle &= \left(\sum \langle F, F_z|I, I_z, S, S_z\rangle\langle I, I_z, S, S_z|\right) \\ &\quad \times\sigma_i\left(\sum |I, I_z, S, S_z\rangle\langle I, I_z, S, S_z|F, F_z\rangle\right)\end{aligned} \tag{A.7a}$$

$$\langle F, F_z|\sigma_x|F, F_z\rangle = \left(\begin{array}{ccc|ccccc} 0 & -\frac{1}{2\sqrt{2}} & 0 & -\frac{\sqrt{3}}{2} & 0 & \frac{1}{2\sqrt{2}} & 0 & 0 \\ -\frac{1}{2\sqrt{2}} & 0 & -\frac{1}{2\sqrt{2}} & 0 & -\frac{1}{2}\sqrt{\frac{3}{2}} & 0 & \frac{1}{2}\sqrt{\frac{3}{2}} & 0 \\ 0 & -\frac{1}{2\sqrt{2}} & 0 & 0 & 0 & -\frac{1}{2\sqrt{2}} & 0 & \frac{\sqrt{3}}{2} \\ \hline -\frac{\sqrt{3}}{2} & 0 & 0 & 0 & \frac{1}{2} & 0 & 0 & 0 \\ 0 & -\frac{1}{2}\sqrt{\frac{3}{2}} & 0 & \frac{1}{2} & 0 & \frac{1}{2}\sqrt{\frac{3}{2}} & 0 & 0 \\ \frac{1}{2\sqrt{2}} & 0 & -\frac{1}{2\sqrt{2}} & 0 & \frac{1}{2}\sqrt{\frac{3}{2}} & 0 & \frac{1}{2}\sqrt{\frac{3}{2}} & 0 \\ 0 & \frac{1}{2}\sqrt{\frac{3}{2}} & 0 & 0 & 0 & \frac{1}{2}\sqrt{\frac{3}{2}} & 0 & \frac{1}{2} \\ 0 & 0 & \frac{\sqrt{3}}{2} & 0 & 0 & 0 & \frac{1}{2} & 0 \end{array}\right) \tag{A.7b}$$

$$\langle F, F_z|\sigma_z|F, F_z\rangle = \left(\begin{array}{ccc|ccccc} \frac{1}{2} & 0 & 0 & 0 & -\frac{\sqrt{3}}{2} & 0 & 0 & 0 \\ 0 & 0 & 0 & 0 & 0 & -1 & 0 & 0 \\ 0 & 0 & -\frac{1}{2} & 0 & 0 & 0 & -\frac{\sqrt{3}}{2} & 0 \\ \hline 0 & 0 & 0 & -1 & 0 & 0 & 0 & 0 \\ -\frac{\sqrt{3}}{2} & 0 & 0 & 0 & -\frac{1}{2} & 0 & 0 & 0 \\ 0 & -1 & 0 & 0 & 0 & 0 & 0 & 0 \\ 0 & 0 & -\frac{\sqrt{3}}{2} & 0 & 0 & 0 & \frac{1}{2} & 0 \\ 0 & 0 & 0 & 0 & 0 & 0 & 0 & 1 \end{array}\right) \tag{A.8}$$

In these matrices, the basis states are in the same order as Table 1. The inserted lines are to help the reader separate out the RF and microwave portions of the matrices. The upper left and lower right block diagonal are RF transitions in the $F = 1$ and $F = 2$ manifolds respectively. The other two sections go together in describing microwave transitions between the manifolds. From these matrices, the selection rules become readily apparent. For $B_\omega \parallel B_z$, $\Delta F = \pm 1$ and $\Delta F_z = 0$; and for $B_\omega \perp B_z$, $\Delta F = 0, \pm 1$ and $\Delta F_z = \pm 1$. Note that the diagonal terms in the σ_z matrix represent the states phase evolution in the Schröedinger picture. Also note that for a non-rotating B_ω the component of the field perpendicular to B_z can be chosen along the x direction without loss of generality.

Now having a form for the perturbing Hamiltonian, it is expedient to adopt the interaction picture of quantum mechanics which is commonly done in transition problems [129]. For the low fields generally used, the diagonal form of Eq. (A.3) is sufficient for H_0 with B_z being the non-oscillating bias field.

$$H''_B = \exp^{iH_0 t/\hbar} \cdot H'_B \cdot \exp^{-iH_0 t/\hbar} \tag{A.9}$$

Transferring the phase evolution to the states gives complicated Hamiltonians with most terms being sums of exponentials. To simplify it is useful to also apply the rotating wave

approximation (RWA) where only states near a resonance have significant impact due to a near cancellation of the oscillation frequency. The other rapidly oscillating terms contribute only small amplitudes ($\sim \frac{1}{\omega}$) to the evolution and are dropped. Here we will keep the terms that for some positive value of ω_B makes a given argument of the exponential small. These exist in two major sets which are in the microwave and RF regimes.

A.3.2 Microwave Transitions

Transitions connecting between $F = 1$ and $F = 2$ are separated by the hyperfine splitting and are in the microwave regime. In finite magnetic fields above a few milli-Gauss and driving fields that give Rabi rates of at least a kiloHertz, they are well resolved and each one is essentially its own independent two-level system with a simple pattern given in Figure A.2. The transitions are approximately evenly spaced from -3Δ to 3Δ with 0 being the clock transition. Two sets of near degeneracies exist, but they each connect distinct pairs of states. These nearly degenerate transitions give rise to the linear splitting of the spectrum of the $\pm\Delta$ transitions mentioned above. The microwave transitions are particularly useful to measure the magnitude of the magnetic field the atoms are experiencing.

Here we will solve the two level system between the states $|F_{1,-1}\rangle$ and $|F_{2,-1}\rangle$ as a general example of the microwave transitions. The initial Hamiltonian is

$$H_0 = \hbar \begin{pmatrix} \frac{3}{8}\omega_{hfs} - \Delta & 0 \\ 0 & -\frac{5}{8}\omega_{hfs} + \Delta \end{pmatrix} \tag{A.10}$$

with $\omega_{hfs} = 2A_{hfs}$ and $\Delta = \frac{1}{2}\mu_B B_z$. This transition occurs through the B_z projection of the oscillating magnetic field with

$$H'_B = \hbar\, \Omega_{red} \cos\omega_B t \begin{pmatrix} \frac{1}{2} & -\frac{\sqrt{3}}{2} \\ -\frac{\sqrt{3}}{2} & -\frac{1}{2} \end{pmatrix}. \tag{A.11}$$

Going to the interaction picture,

$$H''_B = \hbar\, \Omega_{red} \cos\omega_B t \begin{pmatrix} \frac{1}{2} & -\frac{\sqrt{3}}{2}\exp^{i(\omega_{hfs}-2\Delta)t} \\ -\frac{\sqrt{3}}{2}\exp^{-i(\omega_{hfs}-2\Delta)t} & -\frac{1}{2} \end{pmatrix}. \tag{A.12}$$

Expanding the cosine into exponentials and making the RWA gives

$$H_B'' = \frac{\hbar\,\Omega_{red}}{2}\begin{pmatrix} 0 & -\frac{\sqrt{3}}{2}\exp^{-i\delta t} \\ -\frac{\sqrt{3}}{2}\exp^{i\delta t} & 0 \end{pmatrix}. \tag{A.13}$$

where the detuning $\delta = \omega_B - (\omega_{hfs} - 2\Delta)$ is the difference between the microwave angular frequency and the resonance. While we could have kept the full 8×8 matrix for completeness, the RWA at this point would have rendered all other matrix elements 0. For simplicity, we will use the actual Rabi rate of this transition $\Omega_{-2\Delta} = \frac{\sqrt{3}}{2}\Omega_{red}$. Substituting this interaction Hamiltonian into the Schrödinger equation results in the standard two level Rabi problem. Representing the states with complex coefficients ($|F_{1,-1}\rangle \rightarrow c_g(t)$ and $|F_{2,-1}\rangle \rightarrow c_e(t)$) give the coupled differential equations:

$$i\hbar\frac{\partial c_g(t)}{\partial t} = -\frac{\hbar\,\Omega_{-2\Delta}}{2}\,c_e(t)\exp^{-i\delta t} \tag{A.14a}$$

$$i\hbar\frac{\partial c_e(t)}{\partial t} = -\frac{\hbar\,\Omega_{-2\Delta}}{2}\,c_g(t)\exp^{i\delta t} \tag{A.14b}$$

This form of the equations is suitable for numerical integration which is useful for simulating Ω or δ as functions of time such as used for pulse shaping or adiabatic rapid passage. If these parameters are constant over the desired evolution, then further solution is possible. The standard solution to these equations is to decouple them by differentiation and substitution to turn them into two uncoupled second order differential equations and solve each one separately as is done in Ref. [112]. On resonance, they can be easily solved exactly and using time-independent perturbation theory.

A.3.3 RF Transitions

Transitions connecting states in the same hyperfine manifold are in the radio frequency regime. These are often known as RF rotations. In small magnetic fields up to a few Gauss they can be described by classical rotation matrices acting on the magnetic moment of the atoms. One group acts in the $F = 1$ manifold with 3 levels and another in the $F = 2$ manifold with 5 levels. In larger fields the quadratic Zeeman energies split each of these manifolds into their own collection of two-level systems.

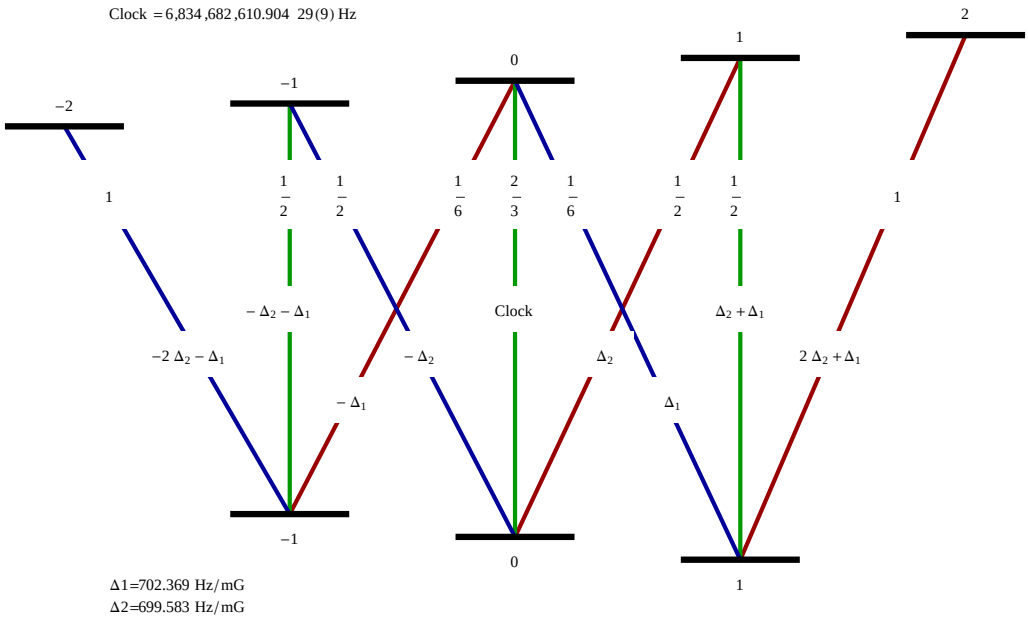

Figure A.2: Diagram of energy levels and microwave transitions in ^{87}Rb ground hyperfine manifold. Given on the lines are the linearized detunings from the Clock transition and linestrengths for σ_-, σ_z, and σ_+ transitions. (See text.)

For the RF transitions, we will look at the simpler of the two, the three-level system in the $F = 1$ manifold. Unlike the two-level system of the microwaves, the quadratic Zeeman shift does more that shift the central frequency, it interferes with the phase matching of the separate transitions in and out of $|F_{1,0}\rangle$. We will keep it as much as is practical. Thus the initial Hamiltonian is:

$$H_0 = \hbar \begin{pmatrix} -\frac{5}{8}\omega_{hfs} - \Delta + \delta & 0 & 0 \\ 0 & -\frac{5}{8}\omega_{hfs} & 0 \\ 0 & 0 & -\frac{5}{8}\omega_{hfs} + \Delta + \delta \end{pmatrix} \tag{A.15}$$

RF transitions only occur through the transverse component of the oscillating magnetic field and so the perturbing Hamiltonian is the B_x portion of the oscillating magnetic field.

$$H'_B = \hbar\, \Omega_{red} \cos \omega_B t \begin{pmatrix} 0 & -\frac{1}{2\sqrt{2}} & 0 \\ -\frac{1}{2\sqrt{2}} & 0 & -\frac{1}{2\sqrt{2}} \\ 0 & -\frac{1}{2\sqrt{2}} & 0 \end{pmatrix} \tag{A.16}$$

Once again we will use the interaction picture.

$$H_B'' = \hbar\,\Omega_{red}\cos\omega_B t \begin{pmatrix} 0 & -\frac{1}{2\sqrt{2}}\exp^{-i(\Delta-\delta)t} & 0 \\ -\frac{1}{2\sqrt{2}}\exp^{i(\Delta-\delta)t} & 0 & -\frac{1}{2\sqrt{2}}\exp^{-i(\Delta+\delta)t} \\ 0 & -\frac{1}{2\sqrt{2}}\exp^{i(\Delta+\delta)t} & 0 \end{pmatrix} \tag{A.17}$$

Again we expand the cosine and make the RWA. We will use $\delta_\pm = \omega_B - \Delta \pm \delta$ to make the expression simpler.

$$H_B'' = \frac{\hbar\,\Omega_{red}}{2} \begin{pmatrix} 0 & -\frac{1}{2\sqrt{2}}\exp^{i\delta_+ t} & 0 \\ -\frac{1}{2\sqrt{2}}\exp^{-i\delta_+ t} & 0 & -\frac{1}{2\sqrt{2}}\exp^{i\delta_- t} \\ 0 & -\frac{1}{2\sqrt{2}}\exp^{-i\delta_- t} & 0 \end{pmatrix} \tag{A.18}$$

We set $\Omega_{RF} = \frac{1}{4}\Omega_{red}$ and substitute. This value is chosen because it is the real Rabi rate of the rotation of a ferromagnetic state (rotations of $|F_{1,-1}\rangle$).

$$i\hbar\frac{\partial c_-(t)}{\partial t} = -\frac{\hbar\,\Omega_{RF}}{\sqrt{2}}\,c_0(t)\exp^{i\delta_+ t} \tag{A.19a}$$

$$i\hbar\frac{\partial c_0(t)}{\partial t} = -\frac{\hbar\,\Omega_{RF}}{\sqrt{2}}\,c_-(t)\exp^{-i\delta_+ t} - \frac{\hbar\,\Omega_{RF}}{\sqrt{2}}\,c_+(t)\exp^{i\delta_- t} \tag{A.19b}$$

$$i\hbar\frac{\partial c_+(t)}{\partial t} = -\frac{\hbar\,\Omega_{RF}}{\sqrt{2}}\,c_0(t)\exp^{-i\delta_- t} \tag{A.19c}$$

Similar to the two level case these equations are suitable for numerical integration. Since the coefficients are time dependent, solution is accomplished by separation. However, separation is algebraically complex for a quadratic Zeeman, so the problem will be simplified further by assuming it is negligible and $\delta_\pm = \delta = \omega_B - \Delta$. Substituting into Eq. (A.19a)-A.19c and dividing through by $i\hbar$ gives:

$$\frac{\partial c_-(t)}{\partial t} = i\frac{\Omega_{RF}}{\sqrt{2}}\,c_0(t)\exp^{i\delta t} \tag{A.20a}$$

$$\frac{\partial c_0(t)}{\partial t} = i\frac{\Omega_{RF}}{\sqrt{2}}\,c_-(t)\exp^{-i\delta t} + i\frac{\Omega_{RF}}{\sqrt{2}}\,c_+(t)\exp^{i\delta t} \tag{A.20b}$$

$$\frac{\partial c_+(t)}{\partial t} = i\frac{\Omega_{RF}}{\sqrt{2}}\,c_0(t)\exp^{-i\delta t} \tag{A.20c}$$

Differentiating Eq. (A.20b) and substituting,

$$\begin{aligned}\frac{\partial^2 c_0(t)}{\partial t^2} &= i\frac{\Omega_{RF}}{\sqrt{2}}\frac{\partial c_-(t)}{\partial t}\exp^{-i\delta t} + i\frac{\Omega_{RF}}{\sqrt{2}}\frac{\partial c_+(t)}{\partial t}\exp^{i\delta t} \\ &\quad + \delta\frac{\Omega_{RF}}{\sqrt{2}}\,c_-(t)\exp^{-i\delta t} - \delta\frac{\Omega_{RF}}{\sqrt{2}}\,c_+(t)\exp^{i\delta t} \\ &= -\Omega_{RF}^2 c_0(t) + \delta\frac{\Omega_{RF}}{\sqrt{2}}\,c_-(t)\exp^{-i\delta t} - \delta\frac{\Omega_{RF}}{\sqrt{2}}\,c_+(t)\exp^{i\delta t}. \end{aligned} \tag{A.21}$$

Again differentiating Eq. (A.21) and substituting,

$$\begin{aligned}\frac{\partial^3 c_0(t)}{\partial t^3} &= -\Omega_{RF}^2\frac{\partial c_0(t)}{\partial t} + \delta\frac{\Omega_{RF}}{\sqrt{2}}\frac{\partial c_-(t)}{\partial t}\exp^{-i\delta t} - \delta\frac{\Omega_{RF}}{\sqrt{2}}\frac{\partial c_+(t)}{\partial t}\exp^{i\delta t} \\ &\quad - i\delta^2\frac{\Omega_{RF}}{\sqrt{2}}\,c_-(t)\exp^{-i\delta t} - i\delta^2\frac{\Omega_{RF}}{\sqrt{2}}\,c_+(t)\exp^{i\delta t} \\ &= -\Omega_{RF}^2\frac{\partial c_0(t)}{\partial t} - \delta^2\frac{\partial c_0(t)}{\partial t} \\ &= -\left(\Omega_{RF}^2 + \delta^2\right)\frac{\partial c_0(t)}{\partial t}. \end{aligned} \tag{A.22}$$

The first order δ terms cancel without a quadratic Zeeman leading to the final line of Eq. (A.22) which has the solution:

$$c_0(t) = \alpha\exp^{i\sqrt{\Omega_{RF}^2+\delta^2}t} + \beta\exp^{-i\sqrt{\Omega_{RF}^2+\delta^2}t} + \delta\gamma \tag{A.23a}$$

The final arbitrary constant is conveniently chosen to simplify determining the constants when $\delta = 0$. Substituting Eq. (A.23a) into Eq. (A.20a) and Eq. (A.20c) and integrating gives:

$$c_-(t) = \frac{\Omega_{RF}}{\sqrt{2}}\left(\frac{\alpha}{\delta + \sqrt{\Omega_{RF}^2+\delta^2}}\exp^{i\sqrt{\Omega_{RF}^2+\delta^2}t} + \frac{\beta}{\delta - \sqrt{\Omega_{RF}^2+\delta^2}}\exp^{-i\sqrt{\Omega_{RF}^2+\delta^2}t} + \gamma\right)\exp^{i\delta t} \tag{A.23b}$$

$$c_+(t) = \frac{\Omega_{RF}}{\sqrt{2}}\left(\frac{\alpha}{-\delta + \sqrt{\Omega_{RF}^2+\delta^2}}\exp^{i\sqrt{\Omega_{RF}^2+\delta^2}t} + \frac{\beta}{-\delta - \sqrt{\Omega_{RF}^2+\delta^2}}\exp^{-i\sqrt{\Omega_{RF}^2+\delta^2}t} - \gamma\right)\exp^{-i\delta t} \tag{A.23c}$$

Using the complex values for $c_i(0)$ allows the three complex coefficients α, β, and γ to be uniquely determined.

Of course with no quadratic Zeeman and no detuning, the time dependence of H_B'' is removed and it is relatively easy to solve

$$\psi(t) = \exp^{-\frac{i}{\hbar}H_B''t}\psi(0). \tag{A.24}$$

Odd and even terms of the exponentiation are simply given by

$$\sum_{n=1,nodd}^{\infty}\frac{1}{n!}\left(i\frac{\Omega_{RF}t}{\sqrt{2}}\right)^n\begin{pmatrix}0 & \sqrt{2}^{n-1} & 0\\ \sqrt{2}^{n-1} & 0 & \sqrt{2}^{n-1}\\ 0 & \sqrt{2}^{n-1} & 0\end{pmatrix} = \frac{i}{\sqrt{2}}\sin\Omega_{RF}t\begin{pmatrix}0 & 1 & 0\\ 1 & 0 & 1\\ 0 & 1 & 0\end{pmatrix} \tag{A.25}$$

and

$$\sum_{n=2,neven}^{\infty}\frac{1}{n!}\left(i\frac{\Omega_{RF}t}{\sqrt{2}}\right)^n\begin{pmatrix}\sqrt{2}^{n-2} & 0 & \sqrt{2}^{n-2}\\ 0 & 2\sqrt{2}^{n-2} & 0\\ \sqrt{2}^{n-2} & 0 & \sqrt{2}^{n-2}\end{pmatrix} = -\frac{1}{2}(1-\cos\Omega_{RF}t)\begin{pmatrix}1 & 0 & 1\\ 0 & 2 & 0\\ 1 & 0 & 1\end{pmatrix} \tag{A.26}$$

respectively. Adding the initial identity matrix thus gives the solution

$$\psi(t) = \begin{pmatrix}\frac{1}{2}(1+\cos\Omega_{RF}t) & \frac{i}{\sqrt{2}}\sin\Omega_{RF}t & -\frac{1}{2}(1-\cos\Omega_{RF}t)\\ \frac{i}{\sqrt{2}}\sin\Omega_{RF}t & \cos\Omega_{RF}t & \frac{i}{\sqrt{2}}\sin\Omega_{RF}t\\ -\frac{1}{2}(1-\cos\Omega_{RF}t) & \frac{i}{\sqrt{2}}\sin\Omega_{RF}t & \frac{1}{2}(1+\cos\Omega_{RF}t)\end{pmatrix}\psi(0) \tag{A.27}$$

which is the same as Ref. [122] up to the phases due to the rotation being about the x axis instead of the y axis.

For two simple examples, we choose resonance and so $\delta = 0$. The first is a rotation of $|F_{1,-1}\rangle$ (ferromagnetic state). This rotation cycles through the zero field ferromagnetic spinor ground states as the magnetization varies sinusoidally. The second is a rotation of $|F_{1,0}\rangle$ (polar state). This rotation varies the population in $|F_{1,0}\rangle$ sinusoidally while populating with equal probability $|F_{1,\pm1}\rangle$. While it appears to go twice as fast as the ferromagnetic rotation, this is due to the phase matching involved on resonance and the peak at $\Omega_{RF}t = \pi$ will vary in amplitude for small detuning while it will still return to all $|F_{1,0}\rangle$ at $\Omega_{RF}t = 2\pi$.

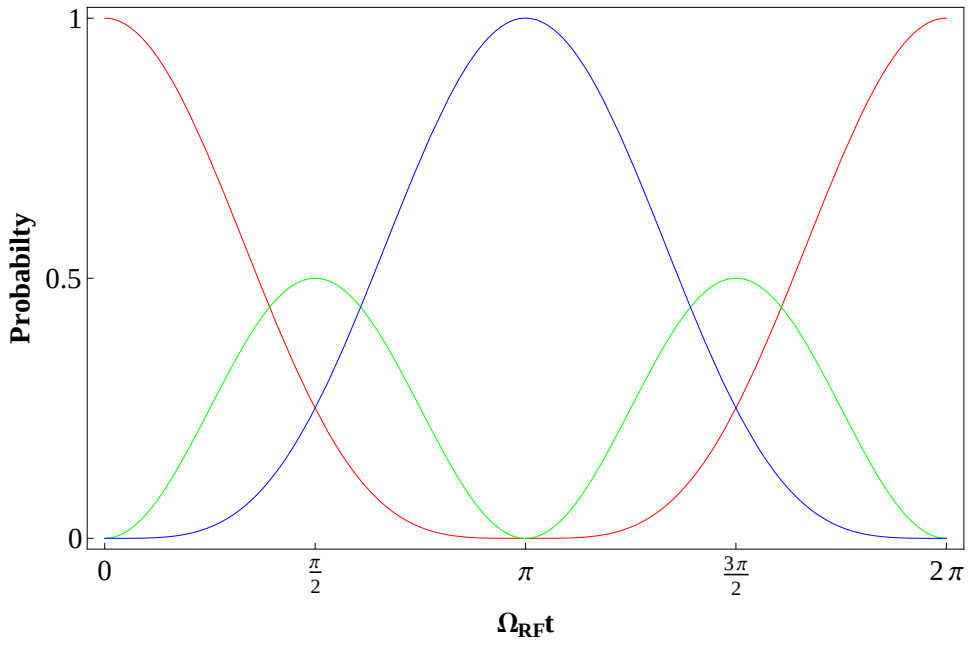

Figure A.3: RF rotation of a ferromagnetic state, $|F_{1,-1}\rangle$. The probability for measuring each m_F state is shown as a function of time. Red $|F_{1,-1}\rangle$, Green $|F_{1,0}\rangle$, and Blue $|F_{1,1}\rangle$. (See text.)

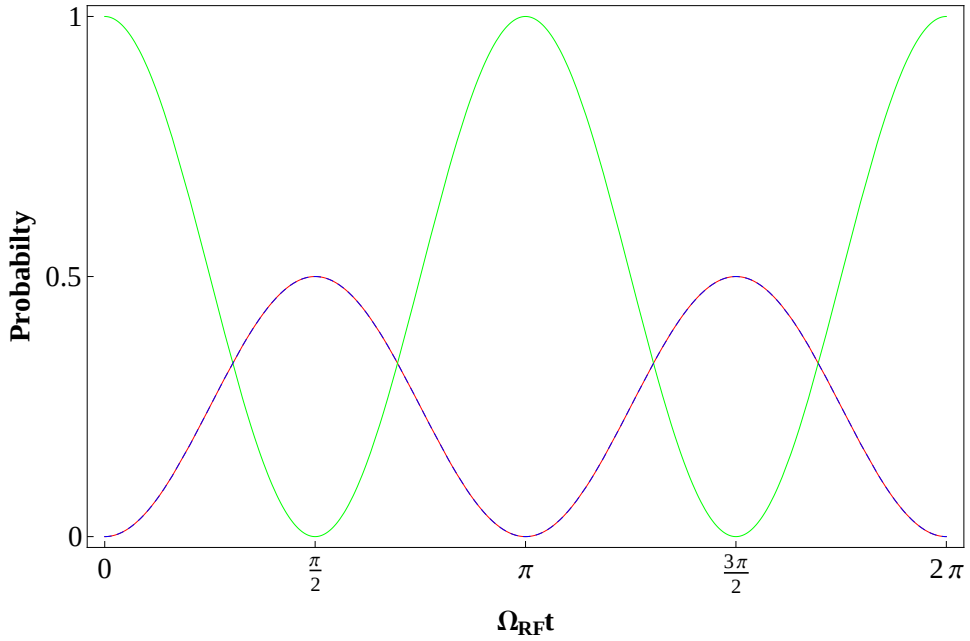

Figure A.4: RF rotation of a polar state, $|F_{1,0}\rangle$. The probability for measuring each m_F state is shown as a function of time. Red $|F_{1,-1}\rangle$, Green $|F_{1,0}\rangle$, and Dashed Blue $|F_{1,1}\rangle$. (See text.)

A.3.4 Microwave Phase Shifts

We begin with the solution to the Rabi two level problem,

$$c_e(t) = i\frac{\Omega}{\Omega'}\sin\frac{\Omega' t}{2}\, e^{i\delta t/2} \tag{A.28a}$$

$$c_g(t) = \left(\cos\frac{\Omega' t}{2} - i\frac{\delta}{\Omega'}\sin\frac{\Omega' t}{2}\right) e^{i\delta t/2} \tag{A.28b}$$

with $\Omega' = \sqrt{\Omega^2 + \delta^2}$. We are interested in a 2π pulse slightly off resonant such that none remains in the excited state and the resulting phase shift. Therefore we need

$$\begin{aligned} \frac{\Omega' t}{2} &= \pi \\ t &= \frac{2\pi}{\Omega'} \end{aligned} \tag{A.29}$$

Substituting into Eq. (A.28b) we get

$$\begin{aligned} c_g &= \cos\pi\, e^{i\pi\delta/\Omega'} \\ &= -e^{i\pi\delta/\Omega'} \\ &= e^{i\pi(1+\delta/\Omega')} \end{aligned} \tag{A.30}$$

This is the clock transition contribution to the phase shift of the zero component for the microwaves slightly detuned from the clock. However there exists other microwave transitions which will perturb this result. We will assume that we can treat each contribution as an independent two level system. We return to Eq. (A.28b), but we will look at the regime where $\delta \gg \Omega$. First we expand the trigonometric functions as exponentials.

$$\begin{aligned} c_g(t) &= \frac{1}{2}\left(e^{i\Omega' t/2} + e^{-i\Omega' t/2} - \frac{\delta}{\Omega'}e^{i\Omega' t/2} + \frac{\delta}{\Omega'}e^{-i\Omega' t/2}\right) e^{i\delta t/2} \\ &= \frac{1}{2}\left(1 - \frac{\delta}{\Omega'}\right) e^{i(\delta+\Omega')t/2} + \frac{1}{2}\left(1 + \frac{\delta}{\Omega'}\right) e^{i(\delta-\Omega')t/2} \end{aligned} \tag{A.31}$$

Since $\delta \gg \Omega$, $\Omega' \approx \delta$ and so to lowest order the amplitude of one term goes to zero while the argument of the exponential goes to zero for the other term resulting in no phase shift. Which term for each case depends on the sign of δ but the resulting equation is the same.

To expand into the next order we drop the approximately zero amplitude term and expand the small argument of the remaining exponential. With $\Omega' = \sqrt{\Omega^2 + \delta^2} \approx \delta(1 + \frac{1}{2}\frac{\Omega^2}{\delta^2})$, then Eq. (A.31) reduces to

$$c_g(t) = e^{\text{sign}[\delta] i \frac{\Omega^2}{4\delta} t} \tag{A.32}$$

Since $t \approx 2\pi/\Omega$ the residual phase shift is $\sim \frac{\pi}{2}\frac{\Omega}{\delta}$. For our typical experimental parameters of $\Omega = 7500$Hz and $\delta = 150$kHz this gives a phase shift of ~ 25 milli-radians. The Rabi rate will vary some from transition to transition but is usually within a factor of 2 of each other. By symmetry the contributions are expected to tend to cancel one another.

APPENDIX B

EXACT SOLUTIONS OF SPINOR DYNAMICS

B.1 Angular Momentum

Evolution from the spin-mixing Hamiltonian for no magnetic field can easily be solved exactly. Here we construct the angular momentum eigenstates in a Fock basis using the following operators.

$$\hat{L}_{\pm}|L,M\rangle = \sqrt{L(L+1)-M(M\pm 1)}\,|L,M\pm 1\rangle \tag{B.1}$$

$$\hat{L}_{+} = \sqrt{2}\left(\hat{a}_1^{\dagger}\hat{a}_0 + \hat{a}_0^{\dagger}\hat{a}_{-1}\right) \tag{B.2}$$

$$\hat{L}_{-} = \sqrt{2}\left(\hat{a}_0^{\dagger}\hat{a}_1 + \hat{a}_{-1}^{\dagger}\hat{a}_0\right) \tag{B.3}$$

$$M = \hat{L}_z = \hat{a}_1^{\dagger}\hat{a}_1 - \hat{a}_{-1}^{\dagger}\hat{a}_{-1} \tag{B.4}$$

We start with $|L_{N,-N}\rangle = |N,0,0\rangle$. The solution below is for $N = 4$. The construction is performed by applying the raising operator $\hat{L}_{+}$ to both sides.

$$\begin{aligned}
\hat{L}_{+}|L_{4,-4}\rangle &= \hat{L}_{+}|4,0,0\rangle \\
\sqrt{20-12}\,|L_{4,-3}\rangle &= \sqrt{2}\,\sqrt{4}\,\sqrt{1}\,|3,1,0\rangle \\
|L_{4,-3}\rangle &= |3,1,0\rangle
\end{aligned}$$

Construction continues with another application of the raising operator. At this point we can also construct the $M = -2$ state of total angular momentum $L = 2$ by its orthogonality

with $|L_{4,-2}\rangle$.

$$\begin{aligned}
\hat{L}_+|L_{4,-3}\rangle &= \hat{L}_+|3,1,0\rangle \\
\sqrt{20-6}\,|L_{4,-2}\rangle &= \sqrt{2}\,\sqrt{3}\,\sqrt{2}\,|2,2,0\rangle + \sqrt{2}\,\sqrt{1}\,\sqrt{1}\,|3,0,1\rangle \\
|L_{4,-2}\rangle &= \sqrt{\frac{6}{7}}\,|2,2,0\rangle + \sqrt{\frac{1}{7}}\,|3,0,1\rangle
\end{aligned}$$

$$|L_{2,-2}\rangle = -\sqrt{\frac{1}{7}}\,|2,2,0\rangle + \sqrt{\frac{6}{7}}\,|3,0,1\rangle$$

Construction continues with application of the raising operator to both $|L_{4,-2}\rangle$ and $|L_{2,-2}\rangle$.

$$\begin{aligned}
\hat{L}_+|L_{4,-2}\rangle &= \hat{L}_+\sqrt{\frac{6}{7}}\,|2,2,0\rangle + \hat{L}_+\sqrt{\frac{1}{7}}\,|3,0,1\rangle \\
\sqrt{20-2}\,|L_{4,-1}\rangle &= \sqrt{\frac{6}{7}}\,\sqrt{2}\,\sqrt{2}\,\sqrt{3}\,|1,3,0\rangle + \sqrt{\frac{6}{7}}\,\sqrt{2}\,\sqrt{2}\,\sqrt{1}\,|2,1,1\rangle \\
&+ \sqrt{\frac{1}{7}}\,\sqrt{2}\,\sqrt{3}\,\sqrt{1}\,|2,1,1\rangle \\
|L_{4,-1}\rangle &= \frac{2}{\sqrt{7}}\,|1,3,0\rangle + \sqrt{\frac{3}{7}}\,|2,1,1\rangle
\end{aligned}$$

$$\begin{aligned}
\hat{L}_+|L_{2,-2}\rangle &= -\hat{L}_+\sqrt{\frac{1}{7}}\,|2,2,0\rangle + \hat{L}_+\sqrt{\frac{6}{7}}\,|3,0,1\rangle \\
\sqrt{6-2}\,|L_{2,-1}\rangle &= -\sqrt{\frac{1}{7}}\,\sqrt{2}\,\sqrt{2}\,\sqrt{3}\,|1,3,0\rangle - \sqrt{\frac{1}{7}}\,\sqrt{2}\,\sqrt{2}\,\sqrt{1}\,|2,1,1\rangle \\
&+ \sqrt{\frac{6}{7}}\,\sqrt{2}\,\sqrt{3}\,\sqrt{1}\,|2,1,1\rangle \\
|L_{2,-1}\rangle &= -\sqrt{\frac{3}{7}}\,|1,3,0\rangle + \frac{2}{\sqrt{7}}\,|2,1,1\rangle
\end{aligned}$$

Construction continues with another application of the raising operator. At this point we can also construct the $M = 0$ state of total angular momentum $L = 0$ by its orthogonality

with $|L_{4,0}\rangle$ and $|L_{2,0}\rangle$.

$$\begin{aligned}
\hat{L}_+|L_{4,-1}\rangle &= \hat{L}_+\frac{2}{\sqrt{7}}\,|1,3,0\rangle + \hat{L}_+\sqrt{\frac{3}{7}}\,|2,1,1\rangle \\
\sqrt{20}\,|L_{4,0}\rangle &= \frac{2}{\sqrt{7}}\sqrt{2}\sqrt{1}\sqrt{4}\,|0,4,0\rangle + \frac{2}{\sqrt{7}}\sqrt{2}\sqrt{3}\sqrt{1}\,|1,2,1\rangle \\
&+ \sqrt{\frac{3}{7}}\sqrt{2}\sqrt{2}\sqrt{2}\,|1,2,1\rangle + \sqrt{\frac{3}{7}}\sqrt{2}\sqrt{1}\sqrt{2}\,|2,0,2\rangle \\
|L_{4,0}\rangle &= \frac{2\sqrt{2}}{\sqrt{35}}\,|0,4,0\rangle + \frac{2\sqrt{6}}{\sqrt{35}}\,|1,2,1\rangle + \frac{\sqrt{3}}{\sqrt{35}}\,|2,0,2\rangle
\end{aligned}$$

$$\begin{aligned}
\hat{L}_+|L_{2,-1}\rangle &= -\hat{L}_+\sqrt{\frac{3}{7}}\,|1,3,0\rangle + \hat{L}_+\frac{2}{\sqrt{7}}\,|2,1,1\rangle \\
\sqrt{6}\,|L_{2,0}\rangle &= -\sqrt{\frac{3}{7}}\sqrt{2}\sqrt{1}\sqrt{4}\,|0,4,0\rangle - \sqrt{\frac{3}{7}}\sqrt{2}\sqrt{3}\sqrt{1}\,|1,2,1\rangle \\
&+ \frac{2}{\sqrt{7}}\sqrt{2}\sqrt{2}\sqrt{2}\,|1,2,1\rangle + \frac{2}{\sqrt{7}}\sqrt{2}\sqrt{1}\sqrt{2}\,|2,0,2\rangle \\
|L_{2,0}\rangle &= -\frac{2\sqrt{3}}{\sqrt{21}}\,|0,4,0\rangle + \frac{1}{\sqrt{21}}\,|1,2,1\rangle + \frac{2\sqrt{2}}{\sqrt{21}}\,|2,0,2\rangle
\end{aligned}$$

$$\begin{aligned}
|L_{0,0}\rangle &= \det\begin{pmatrix} |0,4,0\rangle & |1,2,1\rangle & |2,0,2\rangle \\ \frac{2\sqrt{2}}{\sqrt{35}} & \frac{2\sqrt{6}}{\sqrt{35}} & \frac{\sqrt{3}}{\sqrt{35}} \\ -\frac{2\sqrt{3}}{\sqrt{21}} & \frac{1}{\sqrt{21}} & \frac{2\sqrt{2}}{\sqrt{21}} \end{pmatrix} \\
&= \left(\frac{2\sqrt{6}}{\sqrt{35}}\frac{2\sqrt{2}}{\sqrt{21}} - \frac{1}{\sqrt{21}}\frac{\sqrt{3}}{\sqrt{35}}\right)|0,4,0\rangle \\
&- \left(\frac{2\sqrt{2}}{\sqrt{35}}\frac{2\sqrt{2}}{\sqrt{21}} + \frac{2\sqrt{3}}{\sqrt{21}}\frac{\sqrt{3}}{\sqrt{35}}\right)|1,2,1\rangle \\
&+ \left(\frac{2\sqrt{2}}{\sqrt{35}}\frac{1}{\sqrt{21}} + \frac{2\sqrt{3}}{\sqrt{21}}\frac{2\sqrt{6}}{\sqrt{35}}\right)|2,0,2\rangle \\
&= \frac{\sqrt{3}}{\sqrt{15}}\,|0,4,0\rangle - \frac{2}{\sqrt{15}}\,|1,2,1\rangle + \frac{2\sqrt{2}}{\sqrt{15}}\,|2,0,2\rangle
\end{aligned}$$

This completes our construction of the angular momentum $M = 0$ states in a Fock basis. The angular momentum states have eigenenergies of [44]

$$E_l^a = \lambda'_a\,[l(l+1) - 2N] \tag{B.5}$$

Now to analyze the evolution we use the following equation [44].

$$|\psi(t)\rangle = \exp^{-i\theta_N(t)} \sum_{l=0}^{N} C_l \exp^{-i\lambda'_a l(l+1)t} |l, m_l\rangle \tag{B.6}$$

We then project our intial $|0, 4, 0\rangle$ Fock state onto this basis and substitute. Ignoring overall phase we have the solution

$$\begin{aligned}
|\psi'(t)\rangle &= \sum_{l=0}^{N} C_l \exp^{-i\lambda'_a l(l+1)t} |l, m_l\rangle \\
&= \sqrt{\frac{3}{15}} \exp^{-i\lambda'_a(0)t} |L_{0,0}\rangle - \sqrt{\frac{12}{21}} \exp^{-i\lambda'_a(6)t} |L_{2,0}\rangle + \sqrt{\frac{8}{35}} \exp^{-i\lambda'_a(20)t} |L_{4,0}\rangle \\
&= \left(\frac{21}{105} + \frac{60}{105} \exp^{-i\lambda'_a(6)t} + \frac{24}{105} \exp^{-i\lambda'_a(20)t}\right) |0, 4, 0\rangle \\
&\quad + \left(-\frac{14\sqrt{3}}{105} - \frac{10\sqrt{3}}{105} \exp^{-i\lambda'_a(6)t} + \frac{24\sqrt{3}}{105} \exp^{-i\lambda'_a(20)t}\right) |1, 2, 1\rangle \\
&\quad + \left(\frac{14\sqrt{6}}{105} - \frac{20\sqrt{6}}{105} \exp^{-i\lambda'_a(6)t} + \frac{6\sqrt{6}}{105} \exp^{-i\lambda'_a(20)t}\right) |2, 0, 2\rangle.
\end{aligned}$$

B.2 Tridiagonal Matrix

An alternative route for evolution is in [46] by treating the Fock state as a number of pairs of ± 1 in a vacuum state of atoms with $m = 0$. The spin-mixing operator then acts as a hopping Hamiltonian jumping between numbers of pairs and can be represented by a tridiagonal matrix.

$$\begin{aligned}
\tilde{H}_{k,k'} &= 2\lambda'_a \{k(2(N-2k)-1)\delta_{k,k'} \\
&+ (k'+1)\sqrt{(N-2k')(N-2k'-1)}\delta_{k,k'+1} \\
&+ k'\sqrt{(N-2k'+1)(N-2k'+2)}\delta_{k,k'-1}\}
\end{aligned}$$

For four atoms this gives the matrix

$$H = \lambda'_a \begin{pmatrix} 0 & 4\sqrt{3} & 0 \\ 4\sqrt{3} & 6 & 4\sqrt{2} \\ 0 & 4\sqrt{2} & -4 \end{pmatrix} \tag{B.7}$$

where the basis vectors are the Fock states $|0,4,0\rangle$, $|1,2,1\rangle$, and $|2,0,2\rangle$. Calcuating the eigenvalues gives $-8\lambda'_a$, $-2\lambda'_a$, and $12\lambda'_a$. The normalized eigenvectors are $(\frac{2\sqrt{2}}{\sqrt{35}}, \frac{2\sqrt{6}}{\sqrt{35}}, \frac{\sqrt{3}}{\sqrt{35}})^T$, $(-\frac{2\sqrt{3}}{\sqrt{21}}, \frac{1}{\sqrt{21}}, \frac{2\sqrt{2}}{\sqrt{21}})^T$, and $(\frac{\sqrt{3}}{\sqrt{15}}, -\frac{2}{\sqrt{15}}, \frac{2\sqrt{2}}{\sqrt{15}})^T$; the same as the angular momentum states above. These are the same eigenvalues as Eq. (B.5). Exact evolution is accomplished in the same fashion, exponetials of the eigenvalues with the projections of the intial state onto the eigenvectors.

APPENDIX C

SIMULATION CODE

Included in this appendix are stripped down versions of the the code written for Mathematica® to run the simulations and make nice plots of the results. Currently an undergrad in our group, Ben Land, is porting this to the C programing language and compiling in such a way that the simulations can be run hundreds of times faster through MathLink®, but still use the power of Mathematica® for plotting and analysis.[1]

While the notation here is largely consistent with the rest of the thesis, it has been changed a few times and so a few variables are likely different. Some cells are commented, especially with references to the dynamical equations.

C.1 Fourth Order Runge-Kutta Numerical Integration

For the numerical integration a fourth order Runge-Kutta technique is used [168]. The setup is for the initial value problem given as

$$y' = f(t, y) \tag{C.1a}$$

$$y(t_0) = y_0. \tag{C.1b}$$

The steps of the numerical integration are given by

$$y_{n+1} = y_n + \frac{1}{6}(k_1 + 2k_2 + 2k_3 + k_4) \tag{C.2a}$$

$$t_{n+1} = t_n + h \tag{C.2b}$$

[1] Mathematica and MathLink are registered trademarks of Wolfram Research, Inc. The simulations are ran on Version 7.0 and Version 8.0 through the Georgia Tech site license.

with y_{n+1} is the approximation of $y(t_{n+1}$. The intermediate slopes are defined as

$$k_1 = hf(t_n, y_n) \tag{C.3a}$$

$$k_2 = hf(t_n + \frac{1}{2}h, y_n + \frac{1}{2}k_1) \tag{C.3b}$$

$$k_3 = hf(t_n + \frac{1}{2}h, y_n + \frac{1}{2}k_2) \tag{C.3c}$$

$$k_4 = hf(t_n + h, y_n + k_3). \tag{C.3d}$$

At the beginning of the numerical simulation these are defined, but the functional form of y' must also be defined for use.

C.2 Fock State Simulation

For the quantum simulation the wavefunction is represented as a vector of coefficients for the Fock state basis. The Hamiltonian being numerically integrated is

$$\begin{aligned}\tilde{H}_{k,k'} &= \{2\lambda_a' k(2(N-2k)-1)+2q\}\delta_{k,k'} \\ &+ 2\lambda_a'\{(k'+1)\sqrt{(N-2k')(N-2k'-1)}\delta_{k,k'+1} \\ &+ k'\sqrt{(N-2k'+1)(N-2k'+2)}\delta_{k,k'-1}\}.\end{aligned}$$

This is a fairly simple tridiagonal matrix. There are numerical techniques to exactly solve this in an efficient manner. However in order to match the experiment better, the simulation uses an initial magnetic quench. With the Hamiltonian having a time dependence due to the varying magnetic field it is no longer exactly solvable and thus numerical integration is the only reasonable approach.

Evolution is accomplished by numerical integration of the Schrödinger equation

$$i\hbar\frac{\partial\psi}{\partial t} = \tilde{H}\psi \tag{C.4}$$

with the wavefunction represented as a vector of complex coefficients for each number of pairs k. The size of the vector scales with N while the Hamiltonian matrix scales with N^2. However the number of non-zero matrix elements also scales with N due to the matrix being tridiagonal. This greatly simplifies the numerical integration by evaluating only the products with non-zero matrix elements. For a typically constant mean field spinor dynamical rate, $c = 2N\lambda_a'/\hbar$, the eigen-frequencies of the Hamiltonian also scale as N necessitating finer integration steps to adequately capture the full evolution. So overall the calculation scales roughly as N^2.

Also included in this file are several samples of the calculation of expectation values and the spinor phase shift for making plots.

```
SetDirectory[NotebookDirectory[]];

(* Wikipedia Runge-Kutta methods *)
(* You must define Ydot[Yn,t] *)
(* For multiple parameters, Yn & Ydot should be vectors *)
k1 = Function[{Yn, t, Δt}, Ydot[Yn, t]];
k2 = Function[{Yn, t, Δt}, Ydot[Yn + Δt/2 k1[Yn, t, Δt], t + Δt/2]];
k3 = Function[{Yn, t, Δt}, Ydot[Yn + Δt/2 k2[Yn, t, Δt], t + Δt/2]];
k4 = Function[{Yn, t, Δt}, Ydot[Yn + Δt * k3[Yn, t, Δt], t + Δt]];
Ynplus1 =
  Function[{Yn, t, Δt}, Yn + 1/6 Δt (k1[Yn, t, Δt] + 2 k2[Yn, t, Δt] +
      2 k3[Yn, t, Δt] + k4[Yn, t, Δt])];

(* This section is to calculate the magnetic field
 ramp with a control value and decay constant. *)
Bcon = Function[{t}, (2 - 0.210) * UnitStep[2 * 10^-3 - t] -
    (2 - 0.210)/(2 * 10^-3) UnitStep[t] UnitStep[2 * 10^-3 - t] t + 0.210];
τB = 1 * 10^-3;
BzDot = Function[{Bz, t}, 1/τB (-Bz + Bcon[t])];
Hold[Plot[Bcon[t], {t, 0, 10 * 10^-3}, PlotRange → {0, 2}]];
RunTime = 0.015; (* Total simulated time in seconds *)
Δt = 0.001 * 10^-3; (* Simulation time step in seconds *)
ΔT = 1 * 10^-3; (* Simulation output step in seconds *)
iter = Round[RunTime / Δt]
Ydot = Function[{Yn, t}, N[BzDot[Yn, t]]];
Bi = Bcon[0];
BList = {Bi};
For[i = 1, i ≤ iter, i++,
  newB = N[Ynplus1[Bi, i Δt, Δt] , 50];
  Bi = newB;
  BList = Append[BList, Bi];
  If[Mod[i, Round[ΔT / Δt]] == 0, Print[i * Δt]];
 ];
Bz = Function[{t},
   If[Round[t / Δt] < Length[BList], BList[[Round[t / Δt]]], 0.21]];
Plot[Bz[t], {t, 0, 20 * 10^-3}, PlotRange → {0, 2}]
```

```
(* Fock Vector is {k0,k1,...} where |N_-1,N_0,N_1⟩=|k-ml,
  N-2k+ml,k⟩ and k runs from 0 to
 IntegerPart[(N+ml)/2], ml is assumed negative *)

(* Here I am using the mean-field definition of c =
 N*c2∫|η(r)|^4 d^3r with η normalized to 1. *)
YdotTriDiagC = Compile[{{c, _Real}, {δ, _Real},
    {Yn, _Complex, 1}, {NumAtoms, _Integer}},
   Table[((c/(2 NumAtoms)) 2 (i - 1) (2 (NumAtoms - 2 (i - 1)) - 1) + δ (i - 1))
      Yn[[i]], {i, 1, Length[Yn]}] +
    (c/(2 NumAtoms)) Prepend[Table[2 ((i - 2) + 1)
       √((NumAtoms - 2 (i - 2)) (NumAtoms - 2 (i - 2) - 1)) Yn[[i - 1]],
      {i, 2, Length[Yn]}], 0] + (c/(2 NumAtoms))
     Append[Table[2 i √((NumAtoms - 2 i + 1) (NumAtoms - 2 i + 2))
       Yn[[i + 1]], {i, 1, Length[Yn] - 1}], 0]];

DateString[] (* This is to keep
 track of how long the simulation takes. *)
c = -2 π * 8; (* Spinor dynamical rate *)
NumAtoms = 45 000;
(* The program assumes an even number of atoms *)
RunTime = 0.3; (* Total simulated time in seconds *)
Δt = 0.001 * 10^-3; (* Simulation time step in seconds *)
ΔT = 1 * 10^-3; (* Simulation output step in seconds *)
iter = Round[RunTime / Δt]
Ydot = Function[{Yn, t},
   N[-i * YdotTriDiagC[c, 2 π * 144 * Bz[t]^2, Yn, NumAtoms], 50]];
Fock0 = Prepend[Table[0, {IntegerPart[NumAtoms/2]}], 1];
FockList = {Fock0};
ψi = Fock0;
For[i = 1, i ≤ iter, i++,
  ψi = N[Ynplus1[ψi, i Δt, Δt] ];
  If[Mod[i, Round[ΔT / Δt]] == 0,
   FockList = Append[FockList, ψi]];
  If[Mod[i, Round[10 ΔT / Δt]] == 0, Print[i * Δt]];
 ];
DateString[]
Beep[]
Speak["Calculation Complete"]
```

```
(* Use this section to save the simulation
 run in Hierarchical Data Format version 5. *)
Hold[
  Export["QuantumSim.h5", {Re[Chop[FockList]],
    Im[Chop[FockList]]}, {"Datasets", "TimeSequence"}]];
(* Use this section to load a saved simulation run. *)
Hold[
  c = -2 π * 8; (* Spinor dynamical rate *)
  NumAtoms = 45 000;
  RunTime = 0.30; (* Total simulated time in seconds *)
  Δt = 0.001 * 10^-3; (* Simulation time step in seconds *)
  ΔT = 1 * 10^-3; (* Simulation output step in seconds *)
  FockDataSet =
   Import["QuantumSim.h5", {"Datasets", "TimeSequence"}];
  FockList = FockDataSet[[1]] + i * FockDataSet[[2]];
  Remove[FockDataSet];];
(* Functions for plotting expectation values. *)
kExpValueC =
  Compile[{{FockVect, _Complex, 1}, {NumAtoms, _Integer}},
   Sum[k * Conjugate[FockVect[[k + 1]]] * FockVect[[k + 1]],
    {k, 0, IntegerPart[NumAtoms/2]}]];
kSqrExpValueC = Compile[{{FockVect, _Complex, 1},
    {NumAtoms, _Integer}},
   Sum[k^2 * Conjugate[FockVect[[k + 1]]] * FockVect[[k + 1]],
    {k, 0, IntegerPart[NumAtoms/2]}]];
n0ExpValueC = Compile[{{FockVect, _Complex, 1},
    {NumAtoms, _Integer}}, Sum[
    (NumAtoms - 2 k) * Conjugate[FockVect[[k + 1]]] * FockVect[[k + 1]],
    {k, 0, IntegerPart[NumAtoms/2]}]];
n0SqrExpValueC = Compile[{{FockVect, _Complex, 1},
    {NumAtoms, _Integer}},
   Sum[(NumAtoms - 2 k)^2 * Conjugate[FockVect[[k + 1]]] *
     FockVect[[k + 1]], {k, 0, IntegerPart[NumAtoms/2]}]];
n0VarExpValue = Function[{FockVect, NumAtoms},
   Re[n0SqrExpValueC[FockVect, NumAtoms]] -
```

```
    Re[n0ExpValueC[FockVect, NumAtoms]]^2];
FxSqrExpC = Compile[{{FockVect, _Complex, 1},
    {NumAtoms, _Integer}}, 1/2 Sum[
      (2 (i - 1) (NumAtoms - 2 (i - 1) + 1) + 2 i (NumAtoms - 2 (i - 1))) *
       Conjugate[FockVect[[i]]] * FockVect[[i]],
      {i, 1, Length[FockVect]}] +
    Sum[(i - 1) Sqrt((NumAtoms - 2 i + 3) (NumAtoms - 2 i + 4))
      Conjugate[FockVect[[i - 1]]] * FockVect[[i]],
     {i, 2, Length[FockVect]}] +
    Sum[i Sqrt((NumAtoms - 2 i + 2) (NumAtoms - 2 i + 1))
      Conjugate[FockVect[[i + 1]]] * FockVect[[i]],
     {i, 1, Length[FockVect] - 1}]];
NyzSqrExpC = Compile[{{FockVect, _Complex, 1},
    {NumAtoms, _Integer}}, 1/(2 NumAtoms^2) Sum[
      (2 (i - 1) (NumAtoms - 2 (i - 1) + 1) + 2 i (NumAtoms - 2 (i - 1))) *
       Conjugate[FockVect[[i]]] * FockVect[[i]],
      {i, 1, Length[FockVect]}] - (1/NumAtoms)^2
     Sum[(i - 1) Sqrt((NumAtoms - 2 i + 3) (NumAtoms - 2 i + 4))
      Conjugate[FockVect[[i - 1]]] * FockVect[[i]],
      {i, 2, Length[FockVect]}] - (1/NumAtoms)^2
     Sum[i Sqrt((NumAtoms - 2 i + 2) (NumAtoms - 2 i + 1))
      Conjugate[FockVect[[i + 1]]] * FockVect[[i]],
     {i, 1, Length[FockVect] - 1}]];
qShiftC = Compile[{{θ, _Real}, {FockVect, _Complex, 1}},
   Table[E^(-i*(i-1) θ) FockVect[[i]], {i, 1, Length[FockVect]}]];
```

```
(* The remainder is sample plots using the functions above. *)
kExpectationList =
  Table[{(i - 1) ΔT, kExpValueC[FockList[[i]], NumAtoms] / NumAtoms},
   {i, 1, Length[FockList]}];
n0ExpectationList = Table[{(i - 1) ΔT,
    (NumAtoms - 2 kExpValueC[FockList[[i]], NumAtoms]) / NumAtoms},
   {i, 1, Length[FockList]}];
n0StdDevList = Table[{(i - 1) ΔT,
    √n0VarExpValue[FockList[[i]], NumAtoms] / NumAtoms},
   {i, 1, Length[FockList]}];
FxStdDevExpectationList = Table[
   {(i - 1) ΔT, √FxSqrExpC[FockList[[i]], NumAtoms]},
   {i, 1, Length[FockList]}];
Show[ListPlot[kExpectationList, Joined → True,
  PlotStyle → {Thick, Blue}], ListPlot[n0ExpectationList,
  Joined → True, PlotStyle → {Thick, Green}],
 PlotRange → {0, 1.1}, Frame → True]
ListPlot[FxStdDevExpectationList, Joined → True, Frame → True]
ListPlot[n0StdDevList, Joined → True, Frame → True]

n0PolyPlotList =
  Join[Table[{n0ExpectationList[[i, 1]], n0ExpectationList[[i, 2]] +
      n0StdDevList[[i, 2]]}, {i, 1, Length[n0ExpectationList]}],
   Reverse[Table[{n0ExpectationList[[i, 1]],
      n0ExpectationList[[i, 2]] - n0StdDevList[[i, 2]]},
     {i, 1, Length[n0ExpectationList]}]]];
Show[Graphics[{LightBlue, Polygon[n0PolyPlotList]}],
 ListPlot[n0ExpectationList, Joined → True,
  PlotStyle → {Thick, Blue}], PlotRange → {0, 1.1}, Frame → True]

ϕRotList = Table[Join[
    Table[{θ, √FxSqrExpC[qShiftC[θ, FockList[[it]]], NumAtoms]},
     {θ, 0, 3 π / 2 - π / 100, π / 100}],
    Table[{θ, √FxSqrExpC[qShiftC[θ, FockList[[it]]], NumAtoms]},
     {θ, 3 π / 2, 2 π, π / 500}]], {it, {1, 16, 31, 46, 66}}];
ListPlot[ϕRotList, Joined → True, Frame → True]

ϕRotListdB =
  Table[{ϕRotList[[i, j, 1]], 10 Log[10, ϕRotList[[i, j, 2]]^2 / NumAtoms]},
   {i, 1, Length[ϕRotList]}, {j, 1, Length[ϕRotList[[1]]]}];
ListPlot[ϕRotListdB, Joined → True, Frame → True]
```

C.3 Mean Field Simulation

The semi-classical simulation uses the classical field state vector $(\zeta_1, \zeta_0, \zeta_{-1})^T$ to represent the individual states. In order to regain the same statistics as the quantum simulation, many samples are used with a distribution calculated as in Chapter 3. Each of these are numerically integrated using the following dynamical equations:

$$\begin{aligned} i\hbar\dot{\zeta}_1 &= E_1\zeta_1 + c[(\rho_1 + \rho_0 - \rho_{-1})\zeta_1 + \zeta_0^2\zeta_{-1}^*] \\ i\hbar\dot{\zeta}_0 &= E_0\zeta_0 + c[(\rho_1 + \rho_{-1})\zeta_0 + 2\zeta_1\zeta_{-1}\zeta_0^*] \\ i\hbar\dot{\zeta}_{-1} &= E_{-1}\zeta_{-1} + c[(\rho_{-1} + \rho_0 - \rho_1)\zeta_{-1} + \zeta_0^2\zeta_1^*] \end{aligned}$$

The magnetic quench is simulated in this form as well. Also included in this file are several samples of the calculation of expectation values and the spinor phase shift for making plots.

```
SetDirectory[NotebookDirectory[]];

(* Wikipedia Runge-Kutta methods *)
(* You must define Ydot[Yn,t] *)
(* For multiple parameters, Yn & Ydot should be vectors *)
k1 = Function[{Yn, t, Δt}, Ydot[Yn, t]];
k2 = Function[{Yn, t, Δt}, Ydot[Yn + Δt/2 k1[Yn, t, Δt], t + Δt/2]];
k3 = Function[{Yn, t, Δt}, Ydot[Yn + Δt/2 k2[Yn, t, Δt], t + Δt/2]];
k4 = Function[{Yn, t, Δt}, Ydot[Yn + Δt * k3[Yn, t, Δt], t + Δt]];
Ynplus1 =
  Function[{Yn, t, Δt}, Yn + 1/6 Δt (k1[Yn, t, Δt] + 2 k2[Yn, t, Δt] +
      2 k3[Yn, t, Δt] + k4[Yn, t, Δt])];

(* Spinor Dynamics  MSC thesis eqn 5.25 *)
(* ħ removed so E1, E0, En1, c in angular frequency *)
ℊDot1C = Compile[{{E1, _Real}, {c, _Real},
    {ℊ1, _Complex}, {ℊ0, _Complex}, {ℊn1, _Complex}},
   -i (E1 * ℊ1 + c * (ℊ1 * Conjugate[ℊ1] + ℊ0 * Conjugate[ℊ0] -
         ℊn1 * Conjugate[ℊn1]) ℊ1 + c * ℊ0^2 Conjugate[ℊn1])];
ℊDot0C = Compile[{{E0, _Real}, {c, _Real}, {ℊ1, _Complex},
    {ℊ0, _Complex}, {ℊn1, _Complex}},
   -i (E0 * ℊ0 + c * (ℊ1 * Conjugate[ℊ1] + ℊn1 * Conjugate[ℊn1]) ℊ0 +
      2 c * ℊ1 * ℊn1 * Conjugate[ℊ0])];
ℊDotn1C = Compile[{{En1, _Real}, {c, _Real}, {ℊ1, _Complex},
    {ℊ0, _Complex}, {ℊn1, _Complex}},
   -i (En1 * ℊn1 + c * (ℊn1 * Conjugate[ℊn1] + ℊ0 * Conjugate[ℊ0] -
         ℊ1 * Conjugate[ℊ1]) ℊn1 + c * ℊ0^2 Conjugate[ℊ1])];
ℤDot2 = Function[{E1, E0, En1, c, ℊ1, ℊ0, ℊn1},
   N[{ℊDot1C[E1, c, ℊ1, ℊ0, ℊn1], ℊDot0C[E0, c, ℊ1, ℊ0, ℊn1],
     ℊDotn1C[En1, c, ℊ1, ℊ0, ℊn1]}, 50]];
```

```
(* This section is to calculate the magnetic field
 ramp with a control value and decay constant. *)
Bcon = Function[{t}, (2 - 0.210) * UnitStep[2 * 10^-3 - t] -
     (2 - 0.210)/(2 * 10^-3) UnitStep[t] UnitStep[2 * 10^-3 - t] t + 0.210];
τB = 1 * 10^-3;
BzDot = Function[{Bz, t}, 1/τB (-Bz + Bcon[t])];
Hold[Plot[Bcon[t], {t, 0, 10 * 10^-3}, PlotRange → {0, 2}]];
RunTime = 0.015; (* Total simulated time in seconds *)
Δt = 0.001 * 10^-3; (* Simulation time step in seconds *)
ΔT = 1 * 10^-3; (* Simulation output step in seconds *)
iter = Round[RunTime / Δt]
Ydot = Function[{Yn, t}, N[BzDot[Yn, t]]];
Bi = Bcon[0];
BList = {Bi};
For[i = 1, i ≤ iter, i++,
  newB = N[Ynplus1[Bi, i Δt, Δt] , 50];
  Bi = newB;
  BList = Append[BList, Bi];
  If[Mod[i, Round[ΔT / Δt]] == 0, Print[i * Δt]];
 ];
Bz = Function[{t},
   If[Round[t / Δt] < Length[BList], BList[[Round[t / Δt]]], 0.21]];
Plot[Bz[t], {t, 0, 20 * 10^-3}, PlotRange → {0, 2}]

c = -8; (* Spinor dynamical rate in Hz *)
NumAtoms = 45 000;
NumSamps = 500;

FxDist =
  RandomReal[NormalDistribution[0, Sqrt[1/NumAtoms]], NumSamps];

NyzDist = RandomReal[NormalDistribution[0, Sqrt[1/NumAtoms]],
   NumSamps];

FyDist = RandomReal[NormalDistribution[0, Sqrt[1/NumAtoms]],
   NumSamps];
```

```
NxzDist = RandomReal[NormalDistribution[0, Sqrt[1/NumAtoms]],
    NumSamps];
χplusDist = Table[If[FxDist[[i]] + NxzDist[[i]] > 0,
     ArcTan[-(FyDist[[i]] + NyzDist[[i]])/(FxDist[[i]] + NxzDist[[i]])],
     ArcTan[-(FyDist[[i]] + NyzDist[[i]])/(FxDist[[i]] + NxzDist[[i]])] + π], {i, NumSamps}];
χminusDist = Table[If[FxDist[[i]] - NxzDist[[i]] > 0,
     ArcTan[(FyDist[[i]] - NyzDist[[i]])/(FxDist[[i]] - NxzDist[[i]])],
     ArcTan[(FyDist[[i]] - NyzDist[[i]])/(FxDist[[i]] - NxzDist[[i]])] + π], {i, NumSamps}];
ρ0Dist = Table[1/2 + 1/2 Sqrt[(1 - 4 ((FxDist[[i]] + NxzDist[[i]])^2/(8 Cos[χplusDist[[i]]]^2) +
          (FxDist[[i]] - NxzDist[[i]])^2/(8 Cos[χminusDist[[i]]]^2)))], {i, NumSamps}];
mDist = Table[1/ρ0Dist[[i]] ((FxDist[[i]] + NxzDist[[i]])^2/(8 Cos[χplusDist[[i]]]^2) -
       (FxDist[[i]] - NxzDist[[i]])^2/(8 Cos[χminusDist[[i]]]^2)), {i, NumSamps}];
ψξ = Function[{χ1, χn1, ρ0, M}, {e^(i*χ1) Sqrt[(1 - ρ0 + M)/2],
     Sqrt[ρ0], e^(i*χn1) Sqrt[(1 - ρ0 - M)/2]}];
ψξ0List = Table[ψξ[χplusDist[[i]], χminusDist[[i]],
    ρ0Dist[[i]], mDist[[i]]], {i, NumSamps}];
```

```
DateString[]
Δt = 0.01 * 10^-3;
RunTime = 0.07;
ΔT = 1 * 10^-3;
iter = Round[RunTime / Δt]
Ydot = Function[{Yn, t}, ZDot2[2 π * 72 Bz[t]^2,
     0, 2 π * 72 Bz[t]^2, 2 π * c, Yn[[1]], Yn[[2]], Yn[[3]]]];
Ψ = {ψζ0List};
ψi = ψζ0List;
For[i = 1, i ≤ iter, i++,
  newψList =
   Table[N[Ynplus1[ψi[[j]], i Δt, Δt] ], {j, 1, NumSamps}];
  If[Mod[i, Round[ΔT / Δt]] == 0, Ψ = Append[Ψ, newψList]];
  If[Mod[i, Round[10 ΔT / Δt]] == 0, Print[i * Δt]];
  ψi = newψList;];
Speak["Simulation run complete."]
DateString[]
```

```
(* Use this section to save the simulation
 run in Hierarchical Data Format version 5. *)
Hold[Export["SemiClassicalSim.h5",
   {Re[Chop[Ψ]], Im[Chop[Ψ]]}, {"Datasets", "TimeSequence"}]
 ];
```

```
(* Use this section to load a saved simulation run. *)
Hold[
  c = -8; (* Spinor dynamical rate *)
  NumAtoms = 45000;
  RunTime = 0.07; (* Total simulated time in seconds *)
  Δt = 0.01 * 10^-3; (* Simulation time step in seconds *)
  ΔT = 1 * 10^-3; (* Simulation output step in seconds *)
  DataSet =
   Import["SemiClassicalSim.h5", {"Datasets", "TimeSequence"}];
  Ψ = DataSet[[1]] + i * DataSet[[2]];
  Remove[DataSet];];
```

```
P0 = DiagonalMatrix[{0, 1, 0}];
qShift = Function[ϕ, DiagonalMatrix[{1, e^(i*ϕ/2), 1}]];
```

$$\text{RFy} = \text{Function}\left[\beta, \begin{pmatrix} \frac{1}{2}(1+\text{Cos}[\beta]) & \frac{1}{\sqrt{2}}\text{Sin}[\beta] & \frac{1}{2}(1-\text{Cos}[\beta]) \\ -\frac{1}{\sqrt{2}}\text{Sin}[\beta] & \text{Cos}[\beta] & \frac{1}{\sqrt{2}}\text{Sin}[\beta] \\ \frac{1}{2}(1-\text{Cos}[\beta]) & -\frac{1}{\sqrt{2}}\text{Sin}[\beta] & \frac{1}{2}(1+\text{Cos}[\beta]) \end{pmatrix}\right];$$

```
(* M-S C thesis, Fz basis *)
fx = 1/Sqrt[2] {{0, 1, 0}, {1, 0, 1}, {0, 1, 0}};
fy = i/Sqrt[2] {{0, -1, 0}, {1, 0, -1}, {0, 1, 0}};
fz = {{1, 0, 0}, {0, 0, 0}, {0, 0, -1}};
Mean$\rho$0$\psi\xi$ = Function[{$\psi\xi$List},
    Mean[Table[Conjugate[$\psi\xi$List[[i]]].P0.$\psi\xi$List[[i]],
      {i, 1, Length[$\psi\xi$List]}]]];
StdDev$\rho$0$\psi\xi$ = Function[{$\psi\xi$List}, StandardDeviation[
     Table[Conjugate[$\psi\xi$List[[i]]].P0.$\psi\xi$List[[i]],
      {i, 1, Length[$\psi\xi$List]}]]];
FxStdDev = Function[Ψ, StandardDeviation[
     Table[Conjugate[Ψ[[i]]].fx.Ψ[[i]], {i, 1, Length[Ψ]}]]];
ΨMeas = Function[{Ψ, Meas}, Table[Meas.Ψ[[i]], {i, 1, Length[Ψ]}]];
n0ExpectationList =
  Table[{(i - 1) ΔT, Mean$\rho$0$\psi\xi$[Ψ[[i]]]}, {i, 1, Length[Ψ]}];
n0StdDevList = Table[{(i - 1) ΔT, StdDev$\rho$0$\psi\xi$[Ψ[[i]]]},
    {i, 1, Length[Ψ]}];
ListPlot[n0ExpectationList, Joined → True,
 PlotStyle → {Thick, Green}]
ListPlot[n0StdDevList, Joined → True, Frame → True]
n0PolyPlotList =
  Join[Table[{n0ExpectationList[[i, 1]], n0ExpectationList[[i, 2]] +
      n0StdDevList[[i, 2]]}, {i, 1, Length[n0ExpectationList]}],
   Reverse[Table[{n0ExpectationList[[i, 1]],
      n0ExpectationList[[i, 2]] - n0StdDevList[[i, 2]]},
     {i, 1, Length[n0ExpectationList]}]]];
Show[Graphics[{LightBlue, Polygon[n0PolyPlotList]}],
 ListPlot[n0ExpectationList, Joined → True,
  PlotStyle → {Thick, Blue}], PlotRange → {0, 1.1}, Frame → True]
$\phi$RotList = Table[
    Join[Table[{$\theta$, NumAtoms * FxStdDev[ΨMeas[Ψ[[it]], qShift[$\theta$]]]},
      {$\theta$, 0, 3 π / 2 - π / 100, π / 100}],
     Table[{$\theta$, NumAtoms * FxStdDev[ΨMeas[Ψ[[it]], qShift[$\theta$]]]},
      {$\theta$, 3 π / 2, 2 π, π / 500}]], {it, {1, 16, 31, 46, 66}}];
ListPlot[$\phi$RotList, Joined → True, Frame → True]
```

```
ϕRotListdB =
  Table[{ϕRotList[[i, j, 1]], 10 Log[10, ϕRotList[[i, j, 2]]^2 / NumAtoms]},
   {i, 1, Length[ϕRotList]}, {j, 1, Length[ϕRotList[[1]]]}];
ListPlot[ϕRotListdB, Joined → True, Frame → True]
```

APPENDIX D

QUANTUM OPTICS ANALOGY

We saw in Chapter 4 that spin-mixing dynamics has an analogy with four-wave-mixing of quantum optics (Figure D.1). The process of two incoming $m_f = 0$ atoms becoming one each of $m_f = \pm 1$ is mathematically the same process as FWM generating two outgoing modes with opposite momenta and frequency shift generated by a strong pump in a non-linear crystal with a χ_3 term. Similar to the quantum optics case of a strong pump that can be treated classically, the low-depletion limit simplifies understanding of the squeezing generated. The FWM generates the two-mode squeezing. Our measurement protocol can also be compared to optics processes. The spinor phase shift varies the phase of the local oscillator that is used to detect the squeezing. The RF rotation acts as two beam splitters which take in the three modes of b_1, b_0', and b_{-1} and gives three output modes. The output mode associated with $m_f = 0$ is just the sum(difference)[1] of b_1 and b_{-1}. The output modes for $m_f = \pm 1$ are the difference(sum) of b_1 and b_{-1} combined with the phase shifted local oscillator b_0' for a heterodyne measurement. This heterodyne signal is the difference of $m_f = \pm 1$ or the magnetization L_z. While the exact phase relationship is partly random, the fluctuations depend on the phase shift of the local oscillator relative to the non-random part of the phase of $m_f = \pm 1$. The final detector is the fluorescence detection of the Stern-Gerlach separated components, allowing us to count the quanta of the modes.

[1] Both the sum and difference modes are squeezed. Which one the RF rotation gives depends on whether the rotation is about the x or y axis.

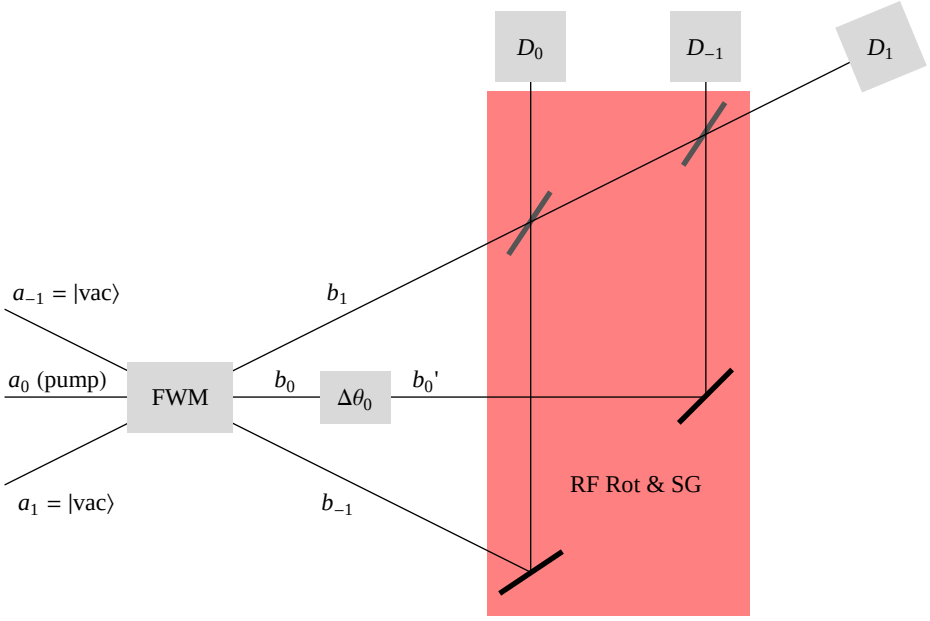

Figure D.1: Quantum optics version of the spin mixing experiment and measurement protocol.

APPENDIX E

IMAGING CALIBRATION

There is some subtlety using the QPN calibration technique. The calibration is performed in conditions similar to the actual squeezing experiment, significant evolution of the quadrature has already occurred giving an extra ~ 1.5 dB of noise over the SQL. The reason for the wait is that the RF rotation requires high stability of the magnetic field to be effective and easily interpreted, but because of the finite time to lower the magnetic field it takes ~ 15ms to ensure sufficient stability. In order to account for this extra noise, the analysis of the quantum projection noise is reviewed. The expected total counts of the $m_f = \pm 1$ clouds and variance of the difference of the counts of the $m_f = \pm 1$ clouds is expected to be $\alpha(N_1 + N_{-1})$ and $\alpha^2(N_1 + N_{-1})$ respectively, where α is the calibration constant to be determined. From the numerical simulation the actual expected variance is determined to be ~ 1.5 dB higher. This does not affect the total counts, but adds a factor into the variance which is now $\alpha^2\beta^2(N_1 + N_{-1})$, where β^2 is the 1.5 dB factor. So now the slope of the variance versus the number is $\alpha\beta^2$. In order to determine this slope the RF calibration data is binned according to total counts in the $m_f = \pm 1$ clouds and the variance of the difference of the $m_f = \pm 1$ components is computed. The total transferred counts and variance of the difference computed is shown with estimated error bars in Figure E.1 [136]. A fit weighted with the inverse of the point estimated errors is performed to determine the slope of the line. With the fitted slope of 102(5), α is found to be 72(4) counts per atoms (CPA). However $\alpha = CPA_{PE} \times GAIN_{preamp}$ where the pre-amp gain is set to 4. So the photo-electron CPA is 18(1) (the pre-amp gain is taken to be noiseless). This number sets the fundamental limit of the squeezing that can be measured to -12.5 dB because of the photo-electron shot noise. The photo-electron shot noise for 45000 atoms contributes ~ 50 atoms noise to the

total number of atoms and magnetization.

Counting of the atoms is performed using a Stern-Gerlach separation of the m_f states during time of flight (TOF) followed by fluorescence imaging. The imaging system consists of a 50 mm focal high aperture laser objective (HALO) lens inside the vacuum chamber, a 250 mm focal achromat, and an Andor Ikon-M camera. The numerical aperture of the objective is 0.3. The quantum efficiency of the camera is > 90% with a 16-bit depth. We bin the signal 8×8 in order to minimize the readout noise, but still not saturate the analog to digital conversion with our maximum signal. The atoms are fluoresced for 400 μs using the magneto-optical trap (MOT) beams that have been apertured down to 12 mm diameter to reduce the background scattered light and tuned to $\sim$ 6 MHz red of resonance. The intensity of MOT beams is $\sim$ 30 times saturation making the scattering rate insensitive to small fluctuations in the intensity. We perform background subtraction by taking 100 images using the experimental sequence, except that the dipole force trapping beams are extinguished. From these 100 images we compute an average background for background subtraction and compute the standard deviation in order to estimate the scattered light noise contribution to our counting noise. This contribution is $\sim$ 0.3 atoms/superpixel which for the $\sim$ 1600 superpixels in the counting regions results in $\sim$ 13 atoms noise on the calculated total number and magnetization measurements. In order to calibrate the counting of atoms, we perform RF rotations from the pure $m_f = 0$ state measured for various RF pulse lengths and hence number of atoms transferred to $m_f = \pm 1$. Due to coming from multiple directions, the polarization from the MOT beams is effectively isotropic. Therefore the scattering rate is ideally m_f state independent. However we note a small (6%) difference in the scattering rates of $m_f = \pm 1$, possibly caused by spatial variation of the repump intensity. Using the RF calibration data we find this small difference by fitting the line of all the points of magnetization versus number transferred having zero slope. This one linear correction is effective for all conditions.

The overall imaging calibration factor is measured using the quantum projection noise.

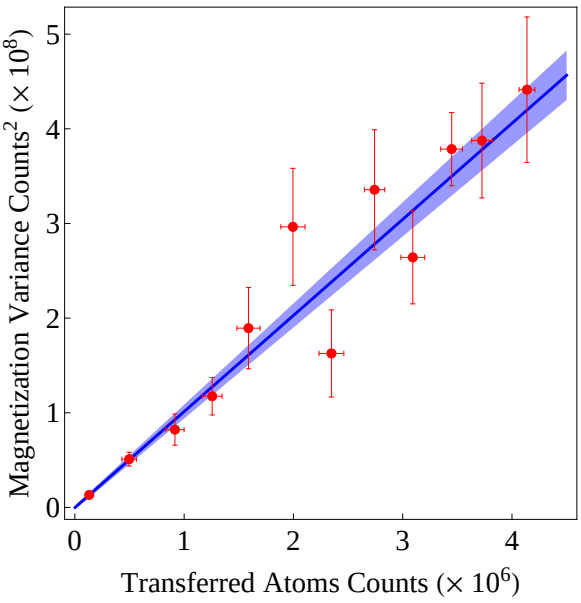

Figure E.1: RF Calibration Data and Fit.

Although the technique has been used in several papers, there is some subtlety in our case. Because we perform the calibration in conditions similar to the experimental data, significant evolution of the quadrature has already occurred giving an extra $\sim$ 1.5 dB of noise over the SQL. This can be seen in the main paper Fig. 2b. The black trace is from this earliest time and for zero phase shift there is clearly added noise on the quadrature. The reason for the wait is that the RF rotation requires high stability of the magnetic field to be effective and easily interpreted, but because of the finite time to lower the magnetic field it takes $\sim$ 15ms to ensure sufficient stability. In order to account for this extra noise, we review the analysis of the quantum projection noise. For an RF rotation of a pure $m_f = 0$ coherent state the mean populations of the transferred $m_f = \pm 1$ atoms are expected to be equal on average with both the sum and difference (L_z) having N_T variance where N_T is the total number of atoms transferred. We use the difference since it is insensitive to background fluctuations. From here the expected total counts and variance for the transferred $m_f = \pm 1$ is expected to be αN_T and $\alpha^2 N_T$ respectively, where α is the calibration constant to be determined. From the numerical simulation the actual expected variance is determined to be

$\sim$ 1.5 dB higher. This does not affect the total counts, but adds a factor into the variance which is now $\alpha^2\beta^2 N_T$, where β^2 is the 1.5 dB factor. So now the slope of the variance versus the number is $\alpha\beta^2$. In order to determine this slope we use the RF calibration data and bin the results according to total counts. From these the total transferred counts and variance of the difference is computed which is shown with estimated error bars in Fig. E.1 [136]. A fit weighted with the inverse of the point estimated errors is performed to determine the slope of the line. With the fitted slope of 102(5), we find α to be 72(4) counts per atoms (CPA). However $\alpha = CPA_{PE} \times GAIN_{preamp}$ where the pre-amp gain is set to 4. So the photo-electron CPA is 18(1) (the pre-amp gain is taken to be noiseless). This number sets the fundamental limit of the squeezing that can be measured to -12.5 dB because of the photo-electron shot noise. This noise limit is shown as a gray line in Fig.2 of main paper. The photo-electron shot noise for 45000 atoms contributes $\sim$ 50 atoms noise to the total number of atoms and magnetization.

REFERENCES

[1] M. H. Anderson, J. R. Ensher, M. R. Matthews, C. E. Wieman, and E. A. Cornell, "Observation of Bose-Einstein Condensation in a Dilute Atomic Vapor," *Science* **269**, pp. 198 (1995).

[2] C. C. Bradley, C. A. Sackett, J. J. Tollett, and R. G. Hulet, "Evidence of Bose-Einstein Condensation in an Atomic Gas with Attractive Interactions," *Phys. Rev. Lett.* **75**, 1687 (1995).

[3] K. B. Davis, M. O. Mewes, M. R. Andrews, N. J. van Druten, D. S. Durfee, D. M. Kurn, and W. Ketterle, "Bose-Einstein Condensation in a Gas of Sodium Atoms," *Phys. Rev. Lett.* **75**, 3969 (1995).

[4] B. DeMarco and D. S. Jin, "Onset of Fermi degeneracy in a trapped atomic gas," *Science* **285**, 1703 (1999).

[5] F. Schreck, L. Khaykovich, K. L. Corwin, G. Ferrari, T. Bourdel, J. Cubizolles, and C. Salomon, "Quasipure Bose-Einstein Condensate Immersed in a Fermi Sea," *Phys. Rev. Lett.* **87**, 080403 (2001).

[6] A. G. Truscott, K. E. Strecker, W. I. McAlexander, G. B. Partridge, and R. G. Hulet, "Observation of Fermi pressure in a gas of trapped atoms," *Science* **291**, 2570 (2001).

[7] M. R. Andrews, C. G. Townsend, H.-J. Miesner, D. S. Durfee, D. M. Kurn, and W. Ketterle, "Observation of Interference between Two Bose Condensates," *Science* **275**, pp. 637 (1997).

[8] I. Bloch, T. W. Hänsch, and T. Esslinger, "Measurement of the spatial coherence of a trapped bose gas at the phase transition," *Nature* **403**, 166 (2000).

[9] M.-O. Mewes, M. R. Andrews, D. M. Kurn, D. S. Durfee, C. G. Townsend, and W. Ketterle, "Output Coupler for Bose-Einstein Condensed Atoms," *Phys. Rev. Lett.* **78**, 582 (1997).

[10] I. Bloch, T. W. Hänsch, and T. Esslinger, "Atom Laser with a cw Output Coupler," *Phys. Rev. Lett.* **82**, 3008 (1999).

[11] M. Greiner, O. Mandel, T. Esslinger, T. W. Hänsch, and I. Bloch, "Quantum phase transition from a superfluid to a Mott insulator in a gas of ultracold atoms," *Nature* **415**, 39 (2002).

[12] D. M. Stamper-Kurn, M. R. Andrews, A. P. Chikkatur, S. Inouye, H.-J. Miesner, J. Stenger, and W. Ketterle, "Optical Confinement of a Bose-Einstein Condensate," *Phys. Rev. Lett.* **80**, 2027 (1998).

[13] M. D. Barrett, J. A. Sauer, and M. S. Chapman, "All-Optical Formation of an Atomic Bose-Einstein Condensate," *Phys. Rev. Lett.* **87**, 010404 (2001).

[14] E. A. Cornell, D. S. Hall, M. R. Matthews, and C. E. Wieman, "Having It Both Ways: Distinguishable Yet Phase-Coherent Mixtures of Bose-Einstein Condensates," *Journal of Low Temperature Physics* **113**, 151 (1998), 10.1023/A:1022513609071.

[15] M.-S. Chang, C. D. Hamley, M. D. Barrett, J. A. Sauer, K. M. Fortier, W. Zhang, L. You, and M. S. Chapman, "Observation of Spinor Dynamics in Optically Trapped *Rb*87 Bose-Einstein Condensates," *Phys. Rev. Lett.* **92**, 140403 (2004).

[16] M.-S. Chang, Q. Qin, W. Zhang, and M. S. Chapman, "Coherent spinor dynamics in a spin-1 Bose condensate," *Nature Physics* **1**, 111 (2005).

[17] E. M. Bookjans, C. D. Hamley, and M. S. Chapman, "Strong Quantum Spin Correlations Observed in Atomic Spin Mixing," *Phys. Rev. Lett.* **107**, 210406 (2011).

[18] J. Stenger, S. Inouye, D. M. Stamper-Kurn, H.-J. Miesner, and W. Ketterle, "Spin domains in ground-state Bose-Einstein condensates," *Nature* **396**, 345 (1998).

[19] S. Inouye, M. R. Andrews, J. Stenger, H.-J. Miesner, D. M. Stamper-Kurn, and W. Ketterle, "Observation of Feshbach resonances in a Bose-Einstein condensate," *Nature* **392**, 151 (1998).

[20] H.-J. Miesner, D. M. Stamper-Kurn, J. Stenger, S. Inouye, A. P. Chikkatur, and W. Ketterle, "Observation of Metastable States in Spinor Bose-Einstein Condensates," *Phys. Rev. Lett.* **82**, 2228 (1999).

[21] D. M. Stamper-Kurn, H.-J. Miesner, A. P. Chikkatur, S. Inouye, J. Stenger, and W. Ketterle, "Quantum Tunneling across Spin Domains in a Bose-Einstein Condensate," *Phys. Rev. Lett.* **83**, 661 (1999).

[22] A. Lamacraft, "Quantum Quenches in a Spinor Condensate," *Phys. Rev. Lett.* **98**, 160404 (2007).

[23] H. Schmaljohann, M. Erhard, J. Kronjäger, M. Kottke, S. van Staa, L. Cacciapuoti, J. J. Arlt, K. Bongs, and K. Sengstock, "Dynamics of $F = 2$ Spinor Bose-Einstein Condensates," *Phys. Rev. Lett.* **92**, 040402 (2004).

[24] J. Kronjäger, C. Becker, M. Brinkmann, R. Walser, P. Navez, K. Bongs, and K. Sengstock, "Evolution of a spinor condensate: Coherent dynamics, dephasing, and revivals," *Phys. Rev. A* **72**, 063619 (2005).

[25] J. Kronjäger, C. Becker, P. Navez, K. Bongs, and K. Sengstock, "Magnetically Tuned Spin Dynamics Resonance," *Phys. Rev. Lett.* **97**, 110404 (2006).

[26] A. T. Black, E. Gomez, L. D. Turner, S. Jung, and P. D. Lett, "Spinor Dynamics in an Antiferromagnetic Spin-1 Condensate," *Phys. Rev. Lett.* **99**, 070403 (2007).

[27] A. Widera, F. Gerbier, S. Fölling, T. Gericke, O. Mandel, and I. Bloch, "Coherent Collisional Spin Dynamics in Optical Lattices," *Phys. Rev. Lett.* **95**, 190405 (2005).

[28] L. E. Sadler, J. M. Higbie, S. R. Leslie, M. Vengalattore, and D. M. Stamper-Kurn, "Spontaneous symmetry breaking in a quenched ferromagnetic spinor Bose-Einstein condensate," *Nature* **443**, 312 (2006).

[29] M. Vengalattore, S. R. Leslie, J. Guzman, and D. M. Stamper-Kurn, "Spontaneously Modulated Spin Textures in a Dipolar Spinor Bose-Einstein Condensate," *Phys. Rev. Lett.* **100**, 170403 (2008).

[30] C. Klempt, O. Topic, G. Gebreyesus, M. Scherer, T. Henninger, P. Hyllus, W. Ertmer, L. Santos, and J. J. Arlt, "Multiresonant Spinor Dynamics in a Bose-Einstein Condensate," *Phys. Rev. Lett.* **103**, 195302 (2009).

[31] L. S. Leslie, A. Hansen, K. C. Wright, B. M. Deutsch, and N. P. Bigelow, "Creation and Detection of Skyrmions in a Bose-Einstein Condensate," *Phys. Rev. Lett.* **103**, 250401 (2009).

[32] E. M. Bookjans, A. Vinit, and C. Raman, "Quantum Phase Transition in an Antiferromagnetic Spinor Bose-Einstein Condensate," *Phys. Rev. Lett.* **107**, 195306 (2011).

[33] Y. Liu, E. Gomez, S. E. Maxwell, L. D. Turner, E. Tiesinga, and P. D. Lett, "Number Fluctuations and Energy Dissipation in Sodium Spinor Condensates," *Phys. Rev. Lett.* **102**, 225301 (2009).

[34] S. R. Leslie, J. Guzman, M. Vengalattore, J. D. Sau, M. L. Cohen, and D. M. Stamper-Kurn, "Amplification of fluctuations in a spinor Bose-Einstein condensate," *Phys. Rev. A* **79**, 043631 (2009).

[35] C. Klempt, O. Topic, G. Gebreyesus, M. Scherer, T. Henninger, P. Hyllus, W. Ertmer, L. Santos, and J. J. Arlt, "Parametric Amplification of Vacuum Fluctuations in a Spinor Condensate," *Phys. Rev. Lett.* **104**, 195303 (2010).

[36] C. D. Hamley, C. S. Gerving, T. M. Hoang, E. M. Bookjans, and M. S. Chapman, "Spin-Nematic Squeezing in a Quantum Gas,", arXiv:1111.1694v1 submitted to *Nature* 2011.

[37] B. Lücke, M. Scherer, J. Kruse, L. Pezzé, F. Deuretzbacher, P. Hyllus, O. Topic, J. Peise, W. Ertmer, J. Arlt, L. Santos, A. Smerzi, and C. Klempt, "Twin Matter Waves for Interferometry Beyond the Classical Limit," *Science* **334**, 773 (2011).

[38] C. J. Myatt, E. A. Burt, R. W. Ghrist, E. A. Cornell, and C. E. Wieman, "Production of Two Overlapping Bose-Einstein Condensates by Sympathetic Cooling," *Phys. Rev. Lett.* **78**, 586 (1997).

[39] T.-L. Ho, "Spinor Bose Condensates in Optical Traps," *Phys. Rev. Lett.* **81**, 742 (1998).

[40] T. Ohmi and K. Machida, "Bose-Einstein Condensation with Internal Degrees of Freedom in Alkali Atom Gases," *Journal of the Physical Society of Japan* **67**, 1822 (1998).

[41] W. Zhang, S. Yi, and L. You, "Mean field ground state of a spin-1 condensate in a magnetic field," *New Journal of Physics* **5**, 77 (2003).

[42] W. Zhang, D. L. Zhou, M.-S. Chang, M. S. Chapman, and L. You, "Coherent spin mixing dynamics in a spin-1 atomic condensate," *Phys. Rev. A* **72**, 013602 (2005).

[43] K. Murata, H. Saito, and M. Ueda, "Broken-axisymmetry phase of a spin-1 ferromagnetic Bose-Einstein condensate," *Phys. Rev. A* **75**, 013607 (2007).

[44] C. K. Law, H. Pu, and N. P. Bigelow, "Quantum Spins Mixing in Spinor Bose-Einstein Condensates," *Phys. Rev. Lett.* **81**, 5257 (1998).

[45] H. Pu, C. K. Law, S. Raghavan, J. H. Eberly, and N. P. Bigelow, "Spin-mixing dynamics of a spinor Bose-Einstein condensate," *Phys. Rev. A* **60**, 1463 (1999).

[46] G. I. Mias, N. R. Cooper, and S. M. Girvin, "Quantum noise, scaling, and domain formation in a spinor Bose-Einstein condensate," *Phys. Rev. A* **77**, 023616 (2008).

[47] D. R. Romano and E. J. V. de Passos, "Population and phase dynamics of $F = 1$ spinor condensates in an external magnetic field," *Phys. Rev. A* **70**, 043614 (2004).

[48] M. Luo, C. Bao, and Z. Li, "Evolution of the average populations of spin components of spin-1 Bose-Einstein condensates beyond mean-field theory," *Phys. Rev. A* **77**, 043625 (2008).

[49] Q. Zhai, L. Chang, R. Lu, and L. You, "Number fluctuation dynamics of a spin-1 atomic condensate," *Phys. Rev. A* **79**, 043608 (2009).

[50] J. Heinze, F. Deuretzbacher, and D. Pfannkuche, "Influence of the particle number on the spin dynamics of ultracold atoms," *Phys. Rev. A* **82**, 023617 (2010).

[51] Z. Chen, C. Bao, and Z. Li, "Effect of a Magnetic Field on the Spin Evolution of ^{87}Rb Bose–Einstein Condensates with Zero Polarization," *Journal of the Physical Society of Japan* **78**, 114002 (2009).

[52] S. L. Cornish, N. R. Claussen, J. L. Roberts, E. A. Cornell, and C. E. Wieman, "Stable 85Rb Bose-Einstein Condensates with Widely Tunable Interactions," *Phys. Rev. Lett.* **85**, 1795 (2000).

[53] F. K. Fatemi, K. M. Jones, and P. D. Lett, "Observation of Optically Induced Feshbach Resonances in Collisions of Cold Atoms," *Phys. Rev. Lett.* **85**, 4462 (2000).

[54] M. Theis, G. Thalhammer, K. Winkler, M. Hellwig, G. Ruff, R. Grimm, and J. H. Denschlag, "Tuning the Scattering Length with an Optically Induced Feshbach Resonance," *Phys. Rev. Lett.* **93**, 123001 (2004).

[55] J. L. Bohn and P. S. Julienne, "Prospects for influencing scattering lengths with far-off-resonant light," *Phys. Rev. A* **56**, 1486 (1997).

[56] M. W. Jack and M. Yamashita, "Maximal entanglement of two spinor Bose-Einstein condensates," *Phys. Rev. A* **71**, 033619 (2005).

[57] C. D. Hamley, E. M. Bookjans, G. Behin-Aein, P. Ahmadi, and M. S. Chapman, "Photoassociation spectroscopy of a spin-1 Bose-Einstein condensate," *Phys. Rev. A* **79**, 023401 (2009).

[58] M. Blume and Y. Y. Hsieh, "Biquadratic Exchange and Quadrupolar Ordering," *J. App. Phys.* **40**, 1249 (1969).

[59] P.-G. de Gennes and J. Prost, *The Physics of Liquid Crystals* (Clarendon Press, 1995).

[60] H. H. Chen and P. M. Levy, "Quadrupole Phase Transitions in Magnetic Solids," *Phys. Rev. Lett.* **27**, 1383 (1971).

[61] H. Tsunetsugu and M. Arikawa, "Spin Nematic Phase in $S = 1$ Triangular Antiferromagnets," *J. Phys. Soc. Jpn* **75**, 083701 (2006).

[62] K. Penc and A. M. Läuchli, "Spin Nematic Phases in Quantum Spin Systems,", in *Introduction to Frustrated Magnetism*, edited by C. Lacroix, P. Mendels, and F. Mila volume 164 of *Springer Series in Solid-State Sciences* pp. 331–362 Springer Berlin Heidelberg 2011.

[63] S. Fujimoto, "Spin Nematic State as a Candidate of the Hidden Order Phase of URu_2Si_2," *Phys. Rev. Lett.* **106**, 196407 (2011).

[64] L. W. Harriger, H. Q. Luo, M. S. Liu, C. Frost, J. P. Hu, M. R. Norman, and P. Dai, "Nematic spin fluid in the tetragonal phase of $BaFe_2As_2$," *Phys. Rev. B* **84**, 054544 (2011).

[65] D. Podolsky and E. Demler, "Properties and detection of spin nematic order in strongly correlated electron systems," *New J. Phys.* **7**, 59 (2005).

[66] H.-A. Bachor and T. C. Ralph, *A guide to experiments in quantum optics* (Wiley-VCH, 2004).

[67] C. M. Caves, "Quantum-mechanical noise in an interferometer," *Phys. Rev. D* **23**, 1693 (1981).

[68] R. Schnabel, N. Mavalvala, D. E. McClelland, and P. K. Lam, "Quantum metrology for gravitational wave astronomy," *Nat Commun* **1**, 121 (2010), 10.1038/ncomms1122.

[69] K. Hammerer, A. S. Sørensen, and E. S. Polzik, "Quantum interface between light and atomic ensembles," *Rev. Mod. Phys.* **82**, 1041 (2010).

[70] C. Gross, T. Zibold, E. Nicklas, J. Estève, and M. K. Oberthaler, "Nonlinear atom interferometer surpasses classical precision limit," *Nature* **464**, 1165 (2010).

[71] M. F. Riedel, P. Böhi, Y. Li, T. W. Hänsch, A. Sinatra, and P. Treutlein, "Atom-chip-based generation of entanglement for quantum metrology," *Nature* **464**, 1170 (2010).

[72] C.-S. Chuu, F. Schreck, T. P. Meyrath, J. L. Hanssen, G. N. Price, and M. G. Raizen, "Direct Observation of Sub-Poissonian Number Statistics in a Degenerate Bose Gas," *Phys. Rev. Lett.* **95**, 260403 (2005).

[73] J. Esteve, C. Gross, A. Weller, S. Giovanazzi, and M. K. Oberthaler, "Squeezing and entanglement in a Bose-Einstein condensate," *Nature* **455**, 1216 (2008).

[74] A. Itah, H. Veksler, O. Lahav, A. Blumkin, C. Moreno, C. Gordon, and J. Steinhauer, "Direct Observation of a Sub-Poissonian Number Distribution of Atoms in an Optical Lattice," *Phys. Rev. Lett.* **104**, 113001 (2010).

[75] S. Whitlock, C. F. Ockeloen, and R. J. C. Spreeuw, "Sub-Poissonian Atom-Number Fluctuations by Three-Body Loss in Mesoscopic Ensembles," *Phys. Rev. Lett.* **104**, 120402 (2010).

[76] C. Orzel, A. K. Tuchman, M. L. Fenselau, M. Yasuda, and M. A. Kasevich, "Squeezed States in a Bose-Einstein Condensate," *Science* **291**, 2386 (2001).

[77] M. Greiner, C. A. Regal, J. T. Stewart, and D. S. Jin, "Probing Pair-Correlated Fermionic Atoms through Correlations in Atom Shot Noise," *Phys. Rev. Lett.* **94**, 110401 (2005).

[78] S. Fölling, F. Gerbier, A. Widera, O. Mandel, T. Gericke, and I. Bloch, "Spatial quantum noise interferometry in expanding ultracold atom clouds," *Nature* **434**, 481 (2005).

[79] A. Öttl, S. Ritter, M. Köhl, and T. Esslinger, "Correlations and Counting Statistics of an Atom Laser," *Phys. Rev. Lett.* **95**, 090404 (2005).

[80] M. Schellekens, R. Hoppeler, A. Perrin, J. V. Gomes, D. Boiron, A. Aspect, and C. I. Westbrook, "Hanbury Brown Twiss Effect for Ultracold Quantum Gases," *Science* **310**, 648 (2005).

[81] T. Rom, T. Best, D. van Oosten, U. Schneider, S. Fölling, B. Paredes, and I. Bloch, "Free fermion antibunching in a degenerate atomic Fermi gas released from an optical lattice," *Nature* **444**, 733 (2006).

[82] T. Jeltes, J. M. McNamara, W. Hogervorst, W. Vassen, V. Krachmalnicoff, M. Schellekens, A. Perrin, H. Chang, D. Boiron, A. Aspect, and C. I. Westbrook, "Comparison of the Hanbury Brown-Twiss effect for bosons and fermions," *Nature* **445**, 402 (2007).

[83] A. Perrin, H. Chang, V. Krachmalnicoff, M. Schellekens, D. Boiron, A. Aspect, and C. I. Westbrook, "Observation of Atom Pairs in Spontaneous Four-Wave Mixing of Two Colliding Bose-Einstein Condensates," *Phys. Rev. Lett.* **99**, 150405 (2007).

[84] X. Wang and B. C. Sanders, "Relations between bosonic quadrature squeezing and atomic spin squeezing," *Phys. Rev. A* **68**, 033821 (2003).

[85] J. Hald, J. L. Sørensen, C. Schori, and E. S. Polzik, "Spin Squeezed Atoms: A Macroscopic Entangled Ensemble Created by Light," *Phys. Rev. Lett.* **83**, 1319 (1999).

[86] A. Kuzmich, L. Mandel, and N. P. Bigelow, "Generation of Spin Squeezing via Continuous Quantum Nondemolition Measurement," *Phys. Rev. Lett.* **85**, 1594 (2000).

[87] T. Takano, M. Fuyama, R. Namiki, and Y. Takahashi, "Spin Squeezing of a Cold Atomic Ensemble with the Nuclear Spin of One-Half," *Phys. Rev. Lett.* **102**, 033601 (2009).

[88] I. D. Leroux, M. H. Schleier-Smith, and V. Vuletić, "Implementation of Cavity Squeezing of a Collective Atomic Spin," *Phys. Rev. Lett.* **104**, 073602 (2010).

[89] Z. Chen, J. G. Bohnet, S. R. Sankar, J. Dai, and J. K. Thompson, "Conditional Spin Squeezing of a Large Ensemble via the Vacuum Rabi Splitting," *Phys. Rev. Lett.* **106**, 133601 (2011).

[90] M. Koschorreck, M. Napolitano, B. Dubost, and M. W. Mitchell, "Sub-Projection-Noise Sensitivity in Broadband Atomic Magnetometry," *Phys. Rev. Lett.* **104**, 093602 (2010).

[91] W. Wasilewski, K. Jensen, H. Krauter, J. J. Renema, M. V. Balabas, and E. S. Polzik, "Quantum Noise Limited and Entanglement-Assisted Magnetometry," *Phys. Rev. Lett.* **104**, 133601 (2010).

[92] J. Appel, P. J. Windpassinger, D. Oblak, U. B. Hoff, N. Kjærgaard, and E. S. Polzik, "Mesoscopic atomic entanglement for precision measurements beyond the standard quantum limit," *Proceedings of the National Academy of Sciences* **106**, 10960 (2009).

[93] A. Louchet-Chauvet, J. Appel, J. J. Renema, D. Oblak, N. Kjaergaard, and E. S. Polzik, "Entanglement-assisted atomic clock beyond the projection noise limit," *New Journal of Physics* **12**, 065032 (2010).

[94] M. Kitagawa and M. Ueda, "Squeezed spin states," *Phys. Rev. A* **47**, 5138 (1993).

[95] D. J. Wineland, J. J. Bollinger, W. M. Itano, and D. J. Heinzen, "Squeezed atomic states and projection noise in spectroscopy," *Phys. Rev. A* **50**, 67 (1994).

[96] R. E. Slusher, L. W. Hollberg, B. Yurke, J. C. Mertz, and J. F. Valley, "Observation of Squeezed States Generated by Four-Wave Mixing in an Optical Cavity," *Phys. Rev. Lett.* **55**, 2409 (1985).

[97] D. F. Walls and G. J. Milburn, *Quantum optics* (Springer, Berlin ; New York :, 1994).

[98] B. R. Mollow and R. J. Glauber, "Quantum Theory of Parametric Amplification. II," *Phys. Rev.* **160**, 1097 (1967).

[99] L. Deng, E. W. Hagley, J. Wen, M. Trippenbach, Y. Band, P. S. Julienne, J. E. Simsarian, K. Helmerson, S. L. Rolston, and W. D. Phillips, "Four-wave mixing with matter waves," *Nature* **398**, 218 (1999).

[100] J. M. Vogels, K. Xu, and W. Ketterle, "Generation of Macroscopic Pair-Correlated Atomic Beams by Four-Wave Mixing in Bose-Einstein Condensates," *Phys. Rev. Lett.* **89**, 020401 (2002).

[101] V. Krachmalnicoff, J.-C. Jaskula, M. Bonneau, V. Leung, G. B. Partridge, D. Boiron, C. I. Westbrook, P. Deuar, P. Ziń, M. Trippenbach, and K. V. Kheruntsyan, "Spontaneous Four-Wave Mixing of de Broglie Waves: Beyond Optics," *Phys. Rev. Lett.* **104**, 150402 (2010).

[102] D. Pertot, B. Gadway, and D. Schneble, "Collinear Four-Wave Mixing of Two-Component Matter Waves," *Phys. Rev. Lett.* **104**, 200402 (2010).

[103] Y. Liu, S. Jung, S. E. Maxwell, L. D. Turner, E. Tiesinga, and P. D. Lett, "Quantum Phase Transitions and Continuous Observation of Spinor Dynamics in an Antiferromagnetic Condensate," *Phys. Rev. Lett.* **102**, 125301 (2009).

[104] J.-C. Jaskula, M. Bonneau, G. B. Partridge, V. Krachmalnicoff, P. Deuar, K. V. Kheruntsyan, A. Aspect, D. Boiron, and C. I. Westbrook, "Sub-Poissonian Number Differences in Four-Wave Mixing of Matter Waves," *Phys. Rev. Lett.* **105**, 190402 (2010).

[105] L.-M. Duan, J. I. Cirac, and P. Zoller, "Quantum entanglement in spinor Bose-Einstein condensates," *Phys. Rev. A* **65**, 033619 (2002).

[106] O. E. Müstecaplıoğlu, M. Zhang, and L. You, "Spin squeezing and entanglement in spinor condensates," *Phys. Rev. A* **66**, 033611 (2002).

[107] J. D. Sau, S. R. Leslie, M. L. Cohen, and D. M. Stamper-Kurn, "Spin squeezing of high-spin, spatially extended quantum fields," *New Journal of Physics* **12**, 085011 (2010).

[108] M. D. Barrett, *A QUEST for BEC: an all optical alternative*, PhD thesis Georgia Institute of Technology 2002.

[109] M.-S. Chang, *Coherent Spin Dynamics of a Spin-1 Bose-Einstein Condensate*, PhD thesis Georgia Institute of Technology 2006.

[110] E. M. Bookjans, *Relative Number Squeezing in a Spin-1 Bose-Einstein Condensate*, PhD thesis Georgia Institute of Technology 2010.

[111] C. Klempt, T. van Zoest, T. Henninger, O. Topic, E. Rasel, W. Ertmer, and J. Arlt, "Ultraviolet light-induced atom desorption for large rubidium and potassium magneto-optical traps," *Phys. Rev. A* **73**, 013410 (2006).

[112] H. J. Metcalf and P. van der Straten, *Laser Cooling and Trapping* (Springer-Verlag, New York, 1999).

[113] D. A. Steck, "Rubidium 87 D Line Data,", available online at http://steck.us/alkalidata 2008.

[114] W. Demtröder, *Laser spectroscopy: basic concepts and instrumentation*Advanced texts in physics (Springer, 2003).

[115] R. Grimm, M. Weidermüller, and Y. B. Ovchinnikov, "Optical Dipole Traps for Neutral Atoms," *Adv. Atom Mol. Opt. Phys.* **42**, 95 (1999).

[116] J. Jackson, *Classical electrodynamics* (Wiley, 1999).

[117] E. V. Goldstein and P. Meystre, "Quantum theory of atomic four-wave mixing in Bose-Einstein condensates," *Phys. Rev. A* **59**, 3896 (1999).

[118] S. Yi, O. E. Müstecaplıoğlu, and L. You, "Dynamics of quantum phases in a spinor condensate," *Phys. Rev. A* **68**, 013613 (2003).

[119] C. Pethick and H. Smith, *Bose-Einstein condensation in dilute gases* (Cambridge University Press, 2002).

[120] L. Pitaevskiĭ and S. Stringari, *Bose-Einstein condensation*International series of monographs on physics (Clarendon Press, 2003).

[121] M. Yasunaga and M. Tsubota, "Internal Josephson effects in spinor dipolar Bose-Einstein condensates," *Phys. Rev. A* **81**, 023624 (2010).

[122] D. Budker, D. F. Kimball, and D. P. DeMille, *Atomic Physics: An Exploration Through Problems and Solutions* (Oxford University Press, 2004).

[123] I. Carusotto and E. J. Mueller, "Imaging of spinor gases," *Journal of Physics B: Atomic, Molecular and Optical Physics* **37**, S115 (2004).

[124] Y. Di, Y. Wang, and H. Wei, "Dipole-quadrupole decomposition of two coupled spin 1 systems," *Journal of Physics A: Mathematical and Theoretical* **43**, 065303 (2010).

[125] G. Ramachandran and K. S. Mallesh, "'Oriented' Spin Systems," *Nuclear Physics A* **422**, 327 (1984).

[126] S. Sirsi, "Spin squeezing, entanglement and correlations," *Journal of Optics B: Quantum and Semiclassical Optics* **6**, 437 (2004).

[127] D. J. Wineland, J. J. Bollinger, W. M. Itano, F. L. Moore, and D. J. Heinzen, "Spin squeezing and reduced quantum noise in spectroscopy," *Phys. Rev. A* **46**, R6797 (1992).

[128] D. J. Griffiths, *Introduction to Quantum Mechanics* (Prentice Hall, Inc, Upper Saddle River, New Jersey, 1995).

[129] J. J. Sakurai, *Modern Quantum Mechanics: Revised Edition* (Addison-Wesley Publishing Company, New York, 1994).

[130] K. Wódkiewicz and J. H. Eberly, "Coherent states, squeezed fluctuations, and the SU(2) and SU(1,1) groups in quantum-optics applications," *J. Opt. Soc. Am. B* **2**, 458 (1985).

[131] L. Mandel and E. Wolf, *Optical coherence and quantum optics* (Cambridge University Press, 1995).

[132] S. R. A. Leslie, *On Spinor Condensates as Amplifiers, Sensors and Tunable Quantum Playgrounds for Studies of Spin*, PhD thesis University of California, Berkeley 2008.

[133] E. M. Bookjans, C. D. Hamley, and M. S. Chapman, "Strong Quantum Spin Correlations Observed in Atomic Spin Mixing,", arXiv:1109.2185v1 to appear in *Phys. Rev. Lett.* 2011.

[134] F. Gerbier, A. Widera, S. Fölling, O. Mandel, and I. Bloch, "Resonant control of spin dynamics in ultracold quantum gases by microwave dressing," *Phys. Rev. A* **73**, 041602 (2006).

[135] E. M. Bookjans, A. Vinit, and C. Raman, "Quantum Phase Transition in an Antiferromagnetic Spinor Bose-Einstein Condensate,", arXiv:1109.1012v1 2011.

[136] J. R. Taylor, *An Introduction to Error Analysis*, Second ed. (University Science Books, 1997).

[137] E. Tiesinga, B. J. Verhaar, and H. T. C. Stoof, "Threshold and resonance phenomena in ultracold ground-state collisions," *Phys. Rev. A* **47**, 4114 (1993).

[138] H. Schmaljohann, M. Erhard, J. Kronjäger, K. Sengstock, and K. Bongs, "Dynamics and thermodynamics in spinor quantum gases," *Appl. Phys. B* **79**, 1001 (2004).

[139] E. R. I. Abraham, W. I. McAlexander, H. T. C. Stoof, and R. G. Hulet, "Hyperfine structure in photoassociative spectra of *Li*26 and *Li*27," *Phys. Rev. A* **53**, 3092 (1996).

[140] E. Tiesinga, K. M. Jones, P. D. Lett, U. Volz, C. J. Williams, and P. S. Julienne, "Measurement and modeling of hyperfine- and rotation-induced state mixing in large weakly bound sodium dimers," *Phys. Rev. A* **71**, 052703 (2005).

[141] J. D. Miller, R. A. Cline, and D. J. Heinzen, "Photoassociation spectrum of ultracold Rb atoms," *Phys. Rev. Lett.* **71**, 2204 (1993).

[142] M. Theis, *Optical Feshbach Resonances in a Bose-Einstein Condensate*, PhD thesis University of Innsbruck 2005.

[143] K. M. Jones, E. Tiesinga, P. D. Lett, and P. S. Julienne, "Ultracold photoassociation spectroscopy: Long-range molecules and atomic scattering," *Rev. Mod. Phys.* **78**, 483 (2006).

[144] B. Bransden and C. Joachain, *Physics of atoms and molecules*Pearson Education (Prentice Hall, 2003).

[145] X. Wang, H. Wang, P. L. Gould, W. C. Stwalley, E. Tiesinga, and P. S. Julienne, "Observation of the pure long-range $1u$ state of an alkali-metal dimer by photoassociative spectroscopy," *Phys. Rev. A* **57**, 4600 (1998).

[146] C. McKenzie, J. Hecker Denschlag, H. Häffner, A. Browaeys, L. E. E. de Araujo, F. K. Fatemi, K. M. Jones, J. E. Simsarian, D. Cho, A. Simoni, E. Tiesinga, P. S. Julienne, K. Helmerson, P. D. Lett, S. L. Rolston, and W. D. Phillips, "Photoassociation of Sodium in a Bose-Einstein Condensate," *Phys. Rev. Lett.* **88**, 120403 (2002).

[147] M. V. Romalis and E. N. Fortson, "Zeeman frequency shifts in an optical dipole trap used to search for an electric-dipole moment," *Phys. Rev. A* **59**, 4547 (1999).

[148] J. Dziarmaga, "Dynamics of a quantum phase transition and relaxation to a steady state," *Advances in Physics* **59**, 1063 (2010).

[149] A. Polkovnikov, K. Sengupta, A. Silva, and M. Vengalattore, "*Colloquium*: Nonequilibrium dynamics of closed interacting quantum systems," *Rev. Mod. Phys.* **83**, 863 (2011).

[150] I. Bloch, J. Dalibard, and W. Zwerger, "Many-body physics with ultracold gases," *Rev. Mod. Phys.* **80**, 885 (2008).

[151] W. H. Zurek, U. Dorner, and P. Zoller, "Dynamics of a Quantum Phase Transition," *Phys. Rev. Lett.* **95**, 105701 (2005).

[152] B. Damski and W. H. Zurek, "Dynamics of a Quantum Phase Transition in a Ferromagnetic Bose-Einstein Condensate," *Phys. Rev. Lett.* **99**, 130402 (2007).

[153] B. Damski and W. H. Zurek, "How to fix a broken symmetry: quantum dynamics of symmetry restoration in a ferromagnetic BoseŰEinstein condensate," *New Journal of Physics* **10**, 045023 (2008).

[154] S. L. Braunstein and P. van Loock, "Quantum information with continuous variables," *Rev. Mod. Phys.* **77**, 513 (2005).

[155] H. Pu and P. Meystre, "Creating Macroscopic Atomic Einstein-Podolsky-Rosen States from Bose-Einstein Condensates," *Phys. Rev. Lett.* **85**, 3987 (2000).

[156] L.-M. Duan, A. Sørensen, J. I. Cirac, and P. Zoller, "Squeezing and Entanglement of Atomic Beams," *Phys. Rev. Lett.* **85**, 3991 (2000).

[157] T. Opatrný and G. Kurizki, "Matter-Wave Entanglement and Teleportation by Molecular Dissociation and Collisions," *Phys. Rev. Lett.* **86**, 3180 (2001).

[158] H. Jing, J. Fu, Z. Geng, and W.-M. Liu, "Coherent two-color photoassociation in a spinor-1 Bose-Einstein condensate: Single-spin versus mixed-spin cases," *Phys. Rev. A* **79**, 045601 (2009).

[159] J. Cheng, "Regular and irregular spin-mixing dynamics in coupled spin-1 atomic and molecular Bose-Einstein condensates," *Phys. Rev. A* **80**, 023608 (2009).

[160] H. Jing, Y. Jiang, and P. Meystre, "Magneto-optical control of atomic spin mixing in dipolar spinor Bose-Einstein condensates," *Phys. Rev. A* **80**, 063618 (2009).

[161] H. Jing, Y. Jiang, W. Zhang, and P. Meystre, "Laser-catalyzed spin-exchange process in a Bose-Einstein condensate," *Phys. Rev. A* **81**, 031603 (2010).

[162] W. Zhang, B. Sun, M. S. Chapman, and L. You, "Localization of spin mixing dynamics in a spin-1 Bose-Einstein condensate," *Phys. Rev. A* **81**, 033602 (2010).

[163] J. Zhang, T. Li, and Y. Zhang, "Interspecies singlet pairing in a mixture of two spin-1 Bose condensates," *Phys. Rev. A* **83**, 023614 (2011).

[164] H. Jing, Y. Deng, and P. Meystre, "Spinor atom-molecule conversion via laser-induced three-body recombination," *Phys. Rev. A* **83**, 043601 (2011).

[165] B.-Y. Ning, J. Zhuang, J. Q. You, and W. Zhang, "Enhancement of spin coherence in a spin-1 Bose-Einstein condensate by dynamical decoupling approaches," *Phys. Rev. A* **84**, 013606 (2011).

[166] S. Shapiro, "Josephson Currents in Superconducting Tunneling: The Effect of Microwaves and Other Observations," *Phys. Rev. Lett.* **11**, 80 (1963).

[167] H. Pu, S. Raghavan, and N. Bigelow, "Manipulating spinor condensates with magnetic fields: Stochastization, metastability, and dynamical spin localization," *Phys. Rev. A* **61**, 023602 (2000).

[168] "Runge-Kutta methods,", http://en.wikipedia.org/wiki/Runge-Kutta_methods accessed March 2010.